

**IMPERIAL COLLEGE OF SCIENCE, TECHNOLOGY
AND MEDICINE**

University of London

**Development of Valid FE Models for
Structural Dynamic Design**

by

Daniel Wesley Fotsch

A thesis submitted to the University of London

for the Degree of Doctor of Philosophy

Department of Mechanical Engineering

Imperial College of Science, Technology and Medicine

London SW7

April 2001

Dedicated to my wife,

Anita,

and children:

Bradley, Erika and Kevin,

*for their patience, understanding and
immeasurable support during the course
of this work*

Abstract

The ability to perform vibration analysis of complex industrial structures using finite element analysis (FEA) has led to a critical role for the finite element (FE) model in the design process of such structures. However, the conventional design process rarely allows for the experimental validation of the model within the time frame of the design cycle. This is because the building of the physical hardware is usually not completed until very late in the cycle. This thesis addresses this problem with a proposed improvement to the overall model validation process and with developments for the specific validation tasks of generating the FE model and determining how well it correlates with test data.

The proposed improvement to the model validation process is to replace the test data with another FE model called a "super-model", which can be produced at a much earlier stage than any hardware for testing. The intention is to validate the modelling method, instead of the model, by showing that a "super-model" can reproduce the test data very accurately. For assemblies of components that are too large for current computer capacity a physical model reduction method is proposed that will produce a design model with about one tenth the DOFs of the "super-model" while retaining a reasonable estimate of its modal characteristics. A new method that allows the simultaneous display of both the mode shape correlation and the frequency comparison is presented along with new correlation methods for both mode shapes and FRFs.

The effectiveness of these developments is demonstrated with a case study for an assembly of two components of a real industrial structure. The ability to replace the modal test data with the results from an analysis using a "super-model" is clearly demonstrated along with the advantages of the physical model reduction technique and the new correlation methods. However, it is concluded that further research is needed to improve the robustness of the reduction technique—at least until available computer power allows for an analysis of an assembly of "super-models".

Acknowledgements

I would like to thank Rolls-Royce for funding the research with particular recognition of Bernard Staples, Bob Dewhurst, Rob Tuley, Ian Poccachard and Jeff Green for their support and valued input throughout. Also, thanks to Dr. Malcolm Hall for his assistance in bringing me to Imperial College.

If not for the initial persistence and countless efforts of Professor David Ewins this research would not have been possible, for this I am extremely grateful. Also, the valued input of Dr. Mehmet Imregrun is much appreciated.

Much gratitude goes to Liz Savage and Margaret Wright who made literally every day easier by helping me in various ways, both big and small.

Thanks are extended to my office-mates, Götz von Groll, Gan Chen, Wenjie Liu and Suresh Nayagam, who shared their experiences and insights with me on numerous occasions.

To my wife, Anita, and children: Bradley, Erika and Kevin, who shared every success and every failure but remained rock solid in their support—you guys are the best. Also, many thanks and hugs to Betty and Hans Kosel who efficiently managed all our affairs on the other side of the Atlantic—no small feat.

Contents

Nomenclature	vii
Standard Abbreviations	x
List of Figures	xii
1 Introduction	1
1.1 The Structural Dynamic Design Process	2
1.2 Finite Element Model Validation	4
1.3 The Essential Problem with the Model Validation Process in Practice	6
1.4 FE Modelling and Correlation	7
1.5 Research Objectives	8
1.6 Thesis Overview	9
2 New Strategy for Model Validation	12
2.1 Introduction	12
2.2 The Improved Model Validation Process	13
2.3 Replacing Test Data with a Super Model	15
2.4 Conclusions	23
3 Finite Element Modelling Methods	25
3.1 Introduction	25

3.2	Classification of a Structure	26
3.3	Different Model Levels	27
3.4	Basic Finite Element Types and Usage	29
3.4.1	The Beam Element	32
3.4.2	The Shell Element	32
3.4.3	The Solid Element	35
3.5	Modelling with Shells and Beams	37
3.6	Other Modelling Considerations	42
3.6.1	Element Order	42
3.6.2	Element Distortion	45
3.6.3	Mesh Density	47
3.7	Basic Finite Element Modelling	48
3.7.1	Solid-Element Model	51
3.7.2	Combined Shell and Solid-Element Model: Hybrid	51
3.7.3	Shell-Element Model	53
3.7.4	Combined Beam and Shell-Element Model	55
3.8	Basic Detail Feature Modelling	57
3.8.1	Flanges	58
3.8.2	Channels	63
3.8.3	Scallops	66
3.8.4	Holes	69
3.8.5	Bosses	73
3.9	Closing Remarks	76
4	Assemblies of Components	78
4.1	Introduction	78
4.2	Joints	80
4.2.1	Basic Joint Types	81
4.2.2	Overview of Basic Joint Modelling Methods	84

4.2.3	Modelling Joints with Beam and Shell Element Flange Models	86
4.3	Interface Effects	88
4.3.1	Example of the Interface Effect Problem	88
4.3.2	Mode Tracking	96
4.4	Model Reduction	97
4.4.1	Overview of Matrix Model Reduction Methods	98
4.4.2	Physical Model Reduction	99
4.5	Conclusions	108
5	Model Correlation	110
5.1	Introduction	110
5.2	Overview of Correlation Methods	111
5.2.1	Vector Correlation	112
5.2.2	Orthogonality	118
5.2.3	Frequency Response Function Correlation	121
5.2.4	Examples	124
5.3	MAC in the Frequency Domain	128
5.3.1	Evolution of the FMAC: MAC Plot with Frequency Scales .	129
5.3.2	Frequency Domain Correlation	136
5.3.3	Case Study: Combustor Casing	138
5.4	Axisymmetric Structures	143
5.4.1	Mode Shape Rotation	144
5.4.2	Fourier Decomposition	144
5.4.3	Case Study: Assembly of Two Turbine Engine Casings	147
5.5	Conclusions	155
6	Case Study	157
6.1	Combustor Casing	158

6.2	Turbine Casing	166
6.3	Assembly of Combustor and Turbine Casings	173
6.3.1	Mode Tracking	177
6.4	Effects of Features on Modal Characteristics	179
6.4.1	Combustor Casing	180
6.4.2	Turbine Casing	185
6.4.3	Assembly of Combustor and Turbine Casings	187
6.4.4	Summary of Feature Effect Results	192
6.5	Physical Model Reduction of Engine Casings	193
6.5.1	Combustor Casing Model Reduction	194
6.5.2	Turbine Casing Model Reduction	199
6.5.3	Assembly of the Reduced Component Models	203
6.6	Residual Modes and Reduced Assemblies	205
6.7	Conclusions	208
6.7.1	Super Models	208
6.7.2	Effects of Features on Correlation	208
6.7.3	Physical Model Reduction	209
7	Conclusions and Future Work	210
7.1	Conclusions	211
7.1.1	New Model Validation Strategy	211
7.1.2	FE Modelling	211
7.1.3	Physical Model Reduction	212
7.1.4	Model Correlation	212
7.2	Summary of Contributions	213
7.3	Suggestions for Future Work	216
7.4	Closure	217
8	References	218

Nomenclature

Basic Terms, Dimensions and Subscripts

R	radial coordinate
Z	axial coordinate
θ	circumferential coordinate/location
N	total number of degrees of freedom/coordinates
n	number of primary/master/measured degrees of freedom
NE	element number
m	number of included/effective modes
L	number of correlated mode pairs
r	current mode number
i, j, k, l	integers
a	Fourier sine coefficients
b	Fourier cosine coefficients
u	modal strain energy density per element
U	modal average strain energy density per element
w_r	weighting factor for mode r

Matrices, Vectors and Scalars

$[\]$	matrix
$[\]^T$	transpose of a matrix
$[\]^{-1}$	inverse of a matrix
$[\]^+$	generalised or pseudo inverse of a matrix
$[\]^*$	complex conjugate of matrix
	column vector
T	transpose of column vector, row vector
$*$	complex conjugate of vector
$[I]$	identity matrix
A	vector of Fourier coefficients
$[S]$	weighting matrix for SMAC
$[W]$	weighting matrix for FRSF

Spatial Model Properties

$[M]$	mass matrix
$[M_A]$	analytical mass matrix
A	area
I_{xx}	area moment of inertia about x axis, same as J for a beam
I_{yy}	area moment of inertia about y axis
I_{zz}	area moment of inertia about z axis
I_{yz}	area product of inertia for y and z axes
J	beam torsional stiffness constant
v	element volume

Modal and Response Properties

ω	eigenvalue, rad/s
ω_a	analytical eigenvalue
ω_x	experimental eigenvalue
ω_r	natural frequency of r th mode, rad/s
$[\phi]$	mass normalized eigenvector matrix
$[\psi]$	eigenvector matrix
$[\phi^a], [\phi^x]$	analytical, experimental mass normalized eigenvector matrix
$[\psi^a], [\psi^x]$	analytical, experimental eigenvector matrix
ϕ_r	r^{th} mode of mass normalized eigenvector
ψ_r	r^{th} mode of eigenvector
ϕ_{jr}	j^{th} element of r^{th} mode of mass normalized eigenvector
ψ_{jr}	j^{th} element of r^{th} mode of eigenvector
$H_{jk}(\omega)$	individual frequency response element
$[H(\omega)]$	frequency response matrix

Standard Abbreviations

CMP	correlated mode pair
COMAC	coordinate modal assurance criterion
COMEF	coordinate modal error function
CORTHOG	cross orthogonality check
DD	detailed design
DOF(s)	degree(s) of freedom
DP	distortion parameter
ECOMAC	extended coordinate modal assurance criterion
FD	final design
FDAC	frequency domain assurance criterion
FE	finite element
FEA	finite element analysis
FEM	finite element method
FMAC	frequency scaled modal assurance criterion
FRAC	frequency response assurance criterion
FRF	frequency response function
FRSF	frequency response scale factor
ID	inside diameter
IMAC	inverse modal assurance criterion
MAC	modal assurance criterion

MASED	modal average strain energy density
MFAC	modal FRF assurance criterion
MSF	modal scale factor
NCO	normalized cross orthogonality
OD	outside diameter
ODS	operating deflection shape
PD	preliminary design
PCO	pseudo orthogonality check
SCO	SEREP normalized cross orthogonality
SEREP	system equivalent reduction expansion
SMAC	scaled modal assurance criterion
WEM	whole engine model
2-D	two dimensional
3-D	three dimensional
n-D	n nodal diameter (diametral) pattern, n can be any integer

List of Figures

1.1	Structural Dynamic Design	2
1.2	Model Validation	5
2.1	Improved Model Validation Process	14
2.2	Super Model Component Validation	14
2.3	Cross-section of Turbine Engine Casing	17
2.4	View A of the Bolt Holes and Scallops for the Aft Flange	17
2.5	View B of the Bolt Holes for the Forward Flange	17
2.6	Cross-section of Initial FE Model for the Turbine Engine Casing .	18
2.7	Initial FE Model for the Turbine Engine Casing	19
2.8	FMAC for Initial Turbine Engine Casing Model	20
2.9	Cross-section of Refined FE Model for the Turbine Engine Casing	21
2.10	Refined FE Model for the Turbine Engine Casing	21
2.11	FMAC for Refined Turbine Engine Casing Model	22
2.12	FMAC for Initial and Refined Turbine Engine Casing Model . . .	23
3.1	Cross-section of Engine Casing	27
3.2	Preliminary Design FE Model	28
3.3	Detailed Design FE Model	29
3.4	Final Design FE Model	29
3.5	Basic 3-D Structural Finite Element Types	31
3.6	Beam Element Geometry Definition	32

3.7	4-noded Shell Element Geometry Definition	33
3.8	Section of Engine Casing Modelled with Shells and Beams	34
3.9	Section of Engine Casing Modelled with Shells Only	35
3.10	Section of Engine Casing Modelled with Solids (hexahedron) . . .	36
3.11	Section of Engine Casing Modelled with Solids and Shells (Hybrid)	37
3.12	Cross-section Geometry for Three Basic Junctions	38
3.13	Shell Fe Model and Corresponding Area for L-shaped Junction .	39
3.14	Shell Fe Models for T-shaped Junction	40
3.15	Shell Fe Models for Cross-shaped Junction	41
3.16	Order of Basic 3-D Structural Finite Element Types	44
3.17	Primary Element Distortion Types for the 4-noded Shell	46
3.18	Cross-section of Generic Turbine Engine Casing	50
3.19	Cross-section of Solid Model for Generic Turbine Engine Casing .	51
3.20	Cross-section of Hybrid Model for Generic Turbine Engine Casing	52
3.21	FMAC for Hybrid Model of Generic Turbine Engine Casing . . .	53
3.22	Cross-section of Shell Model for Generic Turbine Engine Casing .	54
3.23	FMAC for Shell and Hybrid Models of Generic Turbine Engine Casing	54
3.24	Cross-section of Shell/Beam Model for Generic Turbine Engine Casing	55
3.25	FMAC plot for Shell/Beam, Shell and Hybrid Models for Turbine Engine Casing	56
3.26	Cross-section of Geometry for Three Basic Flanges	58
3.27	Solid FE Models for the Three Basic Flanges	59
3.28	Shell FE Models for the Three Basic Flanges	60
3.29	Shell/Beam FE Models for the Three Basic Flanges: Approach 1	61
3.30	Shell/Beam FE Models for the Three Basic Flanges: Approach 2	62
3.31	Shell/Beam FE Models for the Three Basic Flanges: Approach 3	62
3.32	Cross-sections of Geometry for Three Basic Channels	63

3.33	Solid FE Models for the Three Basic Channels	64
3.34	Shell FE Models for the Three Basic Channels	65
3.35	Shell/Beam FE Models for the Three Basic Channels	65
3.36	Geometry for some Basic Scallop	67
3.37	Shell FE Model for the Scalloped Flange	68
3.38	Solid FE Model for the Gear	69
3.39	Solid FE Model for the Complex Scallop	69
3.40	Geometry for some Basic Holes	70
3.41	Three Mesh Densities for a Basic Hole	71
3.42	FE Models for the Basic Holes	72
3.43	Two Types of Basic Bosses	73
3.44	FE Models for Two Types of Basic Bosses	74
3.45	Coarse FE Model for Piping Boss	75
4.1	Joint Cross-section, Heeling and Toeing	80
4.2	Basic Joint Types	82
4.3	Basic Flange Joint Shell Models	86
4.4	Cross-section FE Model and FMAC for Aft-turbine Casing	90
4.5	Cross-section FE Model and FMAC for Forward-turbine Casing .	91
4.6	Cross-section FE Model for the Assembly	92
4.7	Interface of the Forward and Aft-casing Cross-section FE Models	93
4.8	FMAC for Assembly using Bolt Only Joint Model	94
4.9	FMAC for Assembly using Bolt and ID Joint Model	95
4.10	FMAC Comparing Component Analytical Modes to Experimental Assembly Modes	97
4.11	Initial Flat Plate 40x40 Shell-Element FE Model	102
4.12	Flat Plate Modal Average Strain Energy Density for 10 Modes .	103
4.13	Reduced 11x11 Shell-Element FE Model	104
4.14	FMAC for Reduced 11x11 Element FE Model	105

4.15	Reduced 6x6 Shell-Element FE Model	106
4.16	FMAC for Reduced 6x6 Element FE Model	107
4.17	FMAC Comparing 11x11 Reduced Mesh with 6x6 Reduce Mesh	108
5.1	Vector Correlation Examples	124
5.2	Vector Correlation Examples (Continued)	125
5.3	Orthogonality Examples	126
5.4	FRF Correlation Examples	127
5.5	Original MAC plot	129
5.6	Frequency Comparison	130
5.7	Auto-MAC of Experimental Modes	131
5.8	The New MAC plot	132
5.9	FMAC: MAC plot with frequency scales	133
5.10	FMAC with natural frequency difference on the y-axis	134
5.11	FMAC with natural frequency difference on the y-axis and mea- sured mode number on the x-axis	135
5.12	MSC/NASTRAN Model of Combustor Casing	139
5.13	FMAC plot for Combustor Casing	140
5.14	New Plot Format for FDAC of FRFs	141
5.15	MFAC of Mode Shapes versus FRFs	142
5.16	One ring of measured DOFs separated into groups by DOF type .	146
5.17	MSC/NASTRAN Model for Assembly of Two Casings	148
5.18	Fourier indices for the analytical modes	149
5.19	Fourier indices for the experimental modes	151
5.20	Comparison of MAC versus MAC with mode shape rotation . . .	152
5.21	Comparison of MAC versus Fourier MAC using 2 indices	153
5.22	Comparison of MAC versus Fourier MAC using 2 indices plus ro- tation	154
6.1	Cross-section of Combustor Casing Geometry	158

6.2	Combustor Casing Feature Geometry	160
6.3	Combustor Casing Super Model	161
6.4	FMAC Plot for Combustor Casing Super Model	163
6.5	Cross-section of Combustor Casing Refined Super Model	164
6.6	Refined Combustor Casing 3-D Super Model	164
6.7	FMAC Plot for Initial and Refined Combustor Casing Super Models	165
6.8	Cross-section of Turbine Casing Geometry	166
6.9	Turbine Casing Feature Geometry	167
6.10	Turbine Casing Super Model	168
6.11	FMAC Plot for Turbine Casing Super Model	170
6.12	Refined Turbine Casing Super Model	171
6.13	FMAC Plot for Initial and Refined Turbine Casing Super Models	172
6.14	Assembly Cross-section Super Model	173
6.15	Assembly 3-D Super Model	174
6.16	Assembly Cross-section Joint Model at the Mating Flanges	175
6.17	FMAC Plot for Assembly Super Model	176
6.18	FMAC Plot for Mode Tracking Component Modes to Assembly .	178
6.19	FMAC Plot for the Combustor Casing: No Features	180
6.20	FMAC Plot for the Combustor Casing with Flange Holes	181
6.21	FMAC Plot for the Combustor Casing with Scallops	182
6.22	FMAC Plot for the Combustor Casing with Holes and Bosses . .	183
6.23	FMAC Plot for the Combustor Casing: None and All Features . .	184
6.24	FMAC Plot for the Turbine Casing: No Features	185
6.25	FMAC Plot for the Turbine Casing with Flange Holes	186
6.26	FMAC Plot for the Assembly: No Features	187
6.27	FMAC Plot for the Assembly with Flange Holes	188
6.28	FMAC Plot for the Assembly with Scallops	189
6.29	FMAC Plot for the Assembly with Holes and Bosses	190
6.30	FMAC Plot for the Assembly: None and All Features	191

6.31	Summary of the Feature Effect Results	192
6.32	MASED for Combustor Casing Super Model	195
6.33	Combustor Casing Cross-section Super Model Reduction Zones . .	196
6.34	Combustor Casing: Cross-section of Reduced and Super Models .	196
6.35	Combustor Casing Reduced Beam/Shell 3-D Model	197
6.36	FMAC Plot for the Combustor Casing Reduced and Super Models	198
6.37	MASED for Turbine Casing Super Model	199
6.38	Turbine Casing: Cross-section of Reduced and Super Models . . .	200
6.39	Turbine Casing Reduced Beam/Shell 3-D Model	201
6.40	FMAC Plot for Turbine Casing Reduced and Super Models . . .	202
6.41	Cross-section of Joint Model for the Reduced Assembly	203
6.42	FMAC Plot for Assembly Reduced and Super Models	204
6.43	FMAC: Combustor Casing Reduced and Super Models, Higher Modes	206
6.44	FMAC: Turbine Casing Reduced and Super Models, Higher Modes	207

Chapter 1

Introduction

The design process for industrial structures generally includes three primary environmental quantities: static loads, temperatures and dynamic loads. This research is concerned with the most complex of these issues: the dynamic load environment or the specific area of structural vibration.

The highly competitive environment for the design and manufacture of industrial structures has led to the demand for ever shorter design cycles for such structures. This reduction in time for the design has put increased pressure on the primary tool used to aid the design—the finite element (FE) model. Because of this, the FE model used for design must be generated much more quickly and to a much higher standard than ever before. Further, in order to be able to use a valid model—one that has been correlated with test data from the real structure—the model validation process must also be completed much more rapidly.

The primary focus of this thesis is the development of valid FE models within the direct design cycle loop. A central feature to achieving this is an improvement in the overall model validation process. Additionally, two of the key tasks within the model validation process—generating the initial FE model and determining how well it correlates with the test data—are addressed.

While the developments presented in this thesis can be generalized to most industrial structures, the concentration here is on the design and analysis of the

non-rotating components of gas turbine engines. Accordingly, the structural dynamic design process and finite element modelling discussions are tailored to gas turbine engine components. Although the model validation and correlation topics are presented for general structures, the case studies presented are for gas turbine engine components and assemblies of components.

1.1 The Structural Dynamic Design Process

In general the structural dynamic design process for industrial structures is made up of three chronological stages: *(i)* preliminary design, *(ii)* detailed design and *(iii)* final design. Figure 1.1 shows the details of activities for both design and analysis for each of the three stages. The finite element analyses (FEA) that accompany each design stage are: *(i)* preliminary design (PD) analysis, *(ii)* detailed

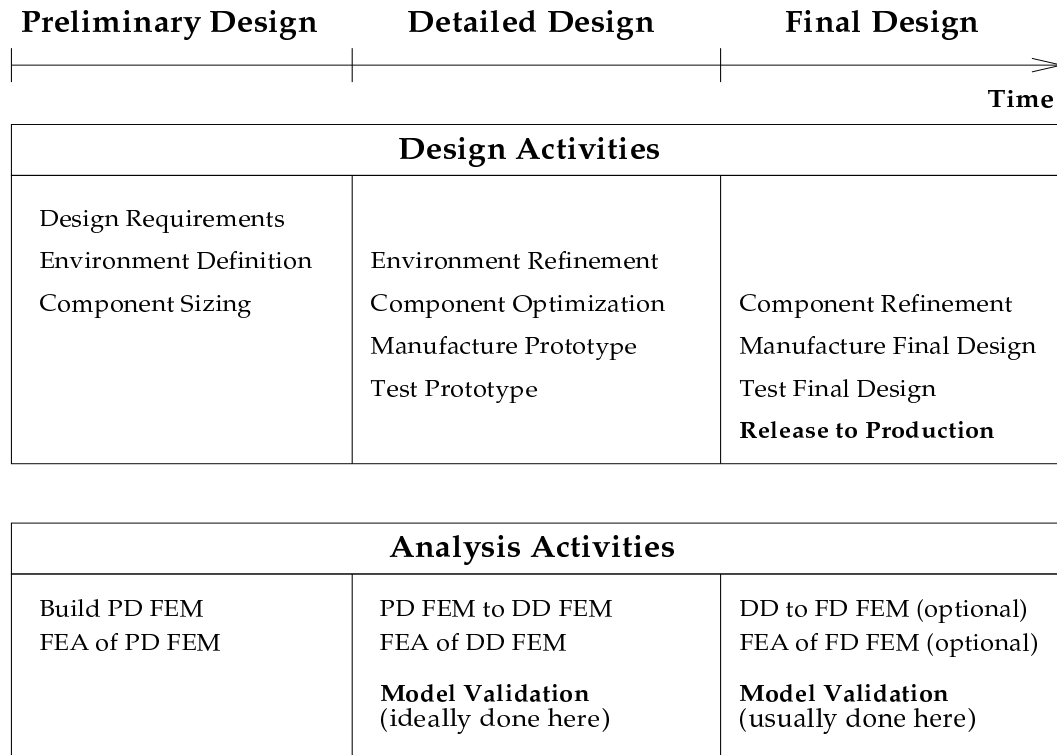


Figure 1.1: Structural Dynamic Design

design (DD) analysis and (iii) final design (FD) analysis for which there are three corresponding FE models.

The design activities generally precede the analysis activities, since the design generates input data for the analysis. As a particular design progresses through the three stages, the analyses generally progress as well with the FE model being modified to incorporate any environmental or design changes that have been made. At the end of the detailed design stage the design and corresponding FE model are usually considered to be "final". Accordingly, the design geometry and corresponding FE model are deemed unchangeable or "frozen" so that the design may be manufactured to the final specifications. This is necessary since in general it may take from a few weeks to several months to manufacture the design depending on many factors—some of which are: the complexity of the geometry; the ability to form the material; and the manufacturing method(s) (machine, forge, weld, braze or cast). With the design frozen, the final design stage is in general for the manufacture and release to production of the design. However, occasionally refinements are made to the design at this stage in order to address any unforeseen issues that arise from either analysis or manufacturing. The final design stage is also used to trouble-shoot any unforeseen vibration problems that are discovered during development testing of the design. Accordingly, the design may be changed at this stage to alleviate such undesirable vibration problems.

The validation of the FE model is ideally done in the detailed design stage but it is often not performed until the final design stage due to the significant amount of time required to manufacture the design which is necessary to furnish the required test data. Performing the model validation this late in the design process significantly limits the benefit of using a validated model to guide the design away from potential vibration problems. Furthermore, once the design has been manufactured, making design changes may be very expensive to implement and may cause significant delay in the release of the design to production. For these reasons, a new strategy to improve the model validation process is warranted.

1.2 Finite Element Model Validation

The ability to perform vibration analysis of complex industrial structures using finite element analysis (FEA) has led to a critical role for the finite element (FE) model in the design process of such structures. The recent growth in the capabilities of FEA has led to the replacement of a small percentage of vibration testing with FEA. However, the requirement remains that critical components must be shown, by test, to be acceptable from a vibration standpoint. Furthermore, before FE models for such components can be used to assess design modifications, they must first be validated using test data.

The validation of an FE model for vibration analyses has proven to be a significant contributor to cost reduction of vibration testing, since once validation is achieved the FE model may be used to avoid further costly vibration tests. In fact, often the first step in a field failure investigation is to assess the integrity of the FE model used for the design against all the available vibration data. Although this is not a rigorous validation of the FE model, it is done to determine if another test—usually a modal test—is necessary. This often proves inconclusive since the data available is usually operational engine response data for a very limited number of transducers. This renders the task of model validation very difficult since the forcing functions in a running engine are largely unknown and difficult to simulate. Further, trying to correlate frequency response functions (FRFs), or in this case operating deflection shapes (ODSs), can be much more difficult than correlating mode shapes due to the nature and amount of damping that must be assumed for the analytical model and the frequency shifts between the test and analytical responses. Accordingly, a modal test is usually required in order to validate the FE model. Since the total expense for a combination of FE analyses and modal test(s) is far less than that for a single "build and run the engine test", the validation of the FE model using modal test data is logically the preferred course of action. After the FE model is validated it can then be used to guide the necessary design

changes.

The complete model validation process consists of the tasks shown in Figure 1.2. The process begins with a design which can be either for a component or

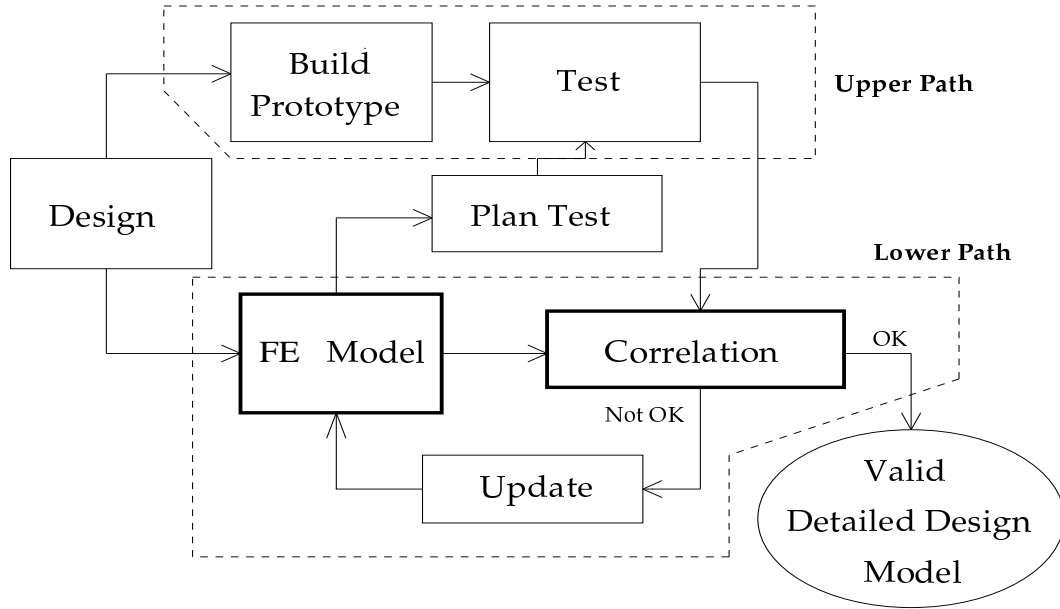


Figure 1.2: Model Validation

for an assembly of components. Ideally, the upper path of the process—build and test—and the lower path—model, correlate and update—are performed in parallel. However, it is often deemed too costly to build a prototype during the design cycle and therefore the final design is used instead although this is usually available only at the very end of the cycle. The test that is performed is generally a modal test, as previously mentioned. The FE model that was used to guide the design is also used to plan the modal test. This is referred to as "test planning" and involves the selection of the transducer locations, the excitation locations and the suspension locations. In the past, the test planning task was performed by an experienced test engineer. However, recent research has automated test planning by providing a computer program to assist the test engineer in much of the work [2, 3, 4]. Once the modal test has been completed, the degree of correlation between the

FE model and the test data can be assessed. This is usually done using modal data but can also be done using FRFs (see Chapter 5). Depending on the degree of correlation between the FE model and the test data, the FE model may need to be changed or updated in order to improve the correlation. Although this may be done manually, a significant amount of research has been done to develop automated model updating procedures [5, 6].

In the past decade or so, there has been a significant amount of research focused on the individual model validation procedures of modal testing, test planning and model updating. Therefore, the focus of the research presented here is on improving the overall model validation strategy and process as well as the tasks within the process for modelling and correlation.

1.3 The Essential Problem with the Model Validation Process in Practice

The problem with the conventional model validation process is that often the build and modal test tasks require such a significant amount of the design cycle time that the final design is manufactured prior to the first opportunity to perform the model correlation and updating tasks. In such circumstances, the knowledge acquired from updating (in the form of the areas of weakness in the model) comes so late in the process that it is often not used to help improve the FE models or FE modelling techniques. Furthermore, there is no way of knowing before manufacturing the design how accurately the initial FE model, which was used to assess and to guide the design, really represented the actual vibration characteristics of the physical structure. The initial FE model might, in fact, be a poor representation of the physical structure and therefore might provide misleading information about the potential for in-service vibration problems. Worse, the ability to assess risk for vibration, which is a major goal for flight-worthy structures, might be significantly

and adversely affected. Because of the significant amount of time consumed in building the hardware, it is often the case that only when vibration problems arise during final design testing can the FE model correlation and updating tasks be completed. The validated FE model is then used to help determine the necessary design modifications so that the vibration problem is alleviated.

There is a clear need for a new model validation strategy or process which will allow for the completion of the FE model correlation and updating tasks **within** the design cycle time, thereby providing a validated model in time for it to have an impact on the design of the physical structure. In this way, a design with minimal risk for vibration may be obtained.

1.4 FE Modelling and Correlation

Two important tasks in the model validation process are *(i)* the creation of the initial FE model and *(ii)* the process for determining how well it correlates with measured data. The ability to improve or update the initial FE model is strongly dependent on the effective completion of both of these tasks. The initial FE model must at least be a reasonable representation of the physical structure: that is, it must be able to predict modes close enough to the test modes so that the initial correlation is sufficient to guide the updating process. Further, the correlation tools must be capable of assessing the degree of correspondence between the analysis and test modes despite the presence of noise and other errors inherent in the testing process.

There has been a significant amount of knowledge gained over the past twenty years or so on how to create an accurate FE model. However, the focus here is on the specific area of how to model an assembly of two or more substructures with the least number of DOFs necessary to predict the required number of modes of the assembly accurately. Interest may be in the dynamics of either *(i)* one of the components, *(ii)* a portion of the assembly, or *(iii)* the entire assembly. The

latter two cases will be affected by the "interface effect" which is the change in character of the component modes after the components have been assembled. A major problem is trying to determine which of the modes of each component are important in defining the modes of the assembly. The problem areas common to all three cases are (a) the interfaces or the joints between the structures and (b) the modelling of complex geometric shapes. The difficulty with joints is in trying to create a linear model that simulates both their stiffness and damping characteristics. The complex geometric shapes pose the problem of determining how best to model them as efficiently as possible. What is needed is a methodology using existing modelling and reduction techniques that will, for any of the cases, produce a practical size (least number of DOFs) linear model with the proper modal characteristics.

The ability to determine how well the FE model correlates with the test data is a significant part of the model validation process. There has been, and continues to be, a great deal of effort spent on model correlation. The current techniques for assessing correlation can sometimes be misleading by indicating poor numerical correlation when the modes visually appear to be identical. Further, there is a need for a better way to correlate frequency response functions (FRFs) in the event that the test data are too noisy to extract the mode shapes accurately.

1.5 Research Objectives

The overall objective of the research presented in this thesis is to improve the model validation process so that the design of the structure may benefit from using a validated FE model. The specific objectives for this research were:

- (i) to develop a new strategy for model validation such that a validated model can be obtained within the design cycle time,

- (ii) to develop techniques to model, reduce and simplify an assembly of structures resulting in a model which is both adequate and practical for use in the design cycle, and
- (iii) to develop new correlation techniques to help overcome the aforementioned shortcomings of the current techniques.

1.6 Thesis Overview

The next four chapters address the specific objectives in the order they were presented above. It is important to mention that Chapter 2 is much shorter than Chapters 3, 4 and 5. This is because Chapter 2 presents the *concept* for the overall improvement of the model validation process, whereas the latter chapters present the *detail* to support the developments for specific tasks within the process. Chapter 6 brings all the developments together to demonstrate them in a case study of a real structure and Chapter 7 concludes the thesis.

Chapter 2 presents the proposed new strategy to improve the model validation process. The chapter begins with an overview of the tasks involved in the conventional model validation process. Then, the proposed new strategy for improving the model validation process—replacing the test data with a very detailed FE model called a "super-model"—is presented followed by a case study to demonstrate the feasibility of the proposal. The chapter ends with general conclusions about the advantages of the proposed new strategy.

Chapter 3 addresses basic finite element modelling methods. The chapter begins with a general introduction to FE modelling followed by the classification of engine structures and the different levels of models used. Next, a detailed discussion is presented on the different type of elements, and their respective usage with specific techniques presented for modelling with beam and shell elements. This is followed by a comparison of four different model types for a generic turbine

engine casing to illustrate the effects on the modal characteristics of the choice of model type. The chapter ends with methods for modelling different structural features of particular interest and some closing remarks.

Chapter 4 is concerned with the specific concepts involved in assembling multiple components to form a larger structure. The chapter begins with a general introduction to the problems encountered for performing dynamic analysis of assemblies of components. Then the specific topics of modelling joints and the dynamic interaction of components—interface effects—are discussed in detail. Next, a new physical model reduction technique is presented for application to each component so that after the components are assembled a model of practical size is obtained. The chapter ends with general conclusions about structural assemblies and the new model reduction method presented.

Chapter 5 discusses the techniques used to determine how well the FE model correlates with the test data. The chapter begins with a general introduction to model correlation followed by a detailed review of the currently-available correlation methods. Next, the details of correlating frequency response functions are discussed and a new method for this is presented. Then the particular difficulties encountered in performing correlation on the mode shapes for axisymmetric structures are discussed followed by a presentation of two new methods to help overcome these difficulties. The new correlation methods are demonstrated with a case study of a real structure. The chapter ends with general conclusions about the new correlation methods presented.

Chapter 6 presents a practical case study used to demonstrate the improvements this research has made to the model validation process. The case study is for an assembly of two real, relatively complex, adjacent engine casings. The study begins with super-models for each casing individually and the two assembled to demonstrate that all three models can reproduce the test data quite accurately. The validated super-models are then used to show how the different features—flange holes, scallops and casing holes affect the modal characteristics of the struc-

ture. Next, the casing super-models are reduced to demonstrate the capability of the proposed physical model reduction technique. The new correlation methods introduced in Chapter 5 are used throughout the study to demonstrate their effectiveness. The chapter ends with general conclusions about the effectiveness of the new methods contributed by this research.

Chapter 7 begins with general conclusions about the research presented in this thesis. Then a summary of the contributions of this research to the specific area of model validation is presented. The thesis is concluded with suggestions for future work followed by statements of closure.

Chapter 2

New Strategy for Model Validation

2.1 Introduction

The ability to validate an FE model of a structure—prove that the model predicts a selected number of modes accurately—has been used extensively for many years in industry. However, this ability—model validation—is all too often used so late in the design process that its effectiveness in guiding the design is significantly limited. This is generally due to the fact that the time required to build or to manufacture the physical structure is so long that there is no opportunity to validate the structure until the final stage of the design process. Occasionally, a prototype structure of a preliminary design may be built to validate critical components, but only if a strong business case can be presented to justify the cost to the program. This is because the preliminary design status of the prototype will not allow it to be used in service and, also, significant short-cuts are usually used to manufacture the prototype parts so that they can be done quickly and inexpensively while retaining the primary characteristics that are to be demonstrated by the test.

There are two consequences of the placement of the validation of the FE model

so late in the design process: *(i)* the models used for design may not be sufficiently accurate to guide the design away from vibration problems and *(ii)* the lessons learned from the validation process, in the form of modelling techniques, may not be used to improve the modelling procedure. For these reasons, it is contended that a new strategy for model validation is needed. Accordingly, a new strategy is proposed in the following section of this thesis.

2.2 The Improved Model Validation Process

The proposed new strategy for model validation, which constitutes a central feature in this thesis, is to replace the reference test data from a physical test structure (against which the FE model is compared) with another FE model called a "super-model", as shown in Figure 2.1. The test data for each component of the structure is replaced with its "super-model" and then the model correlation and updating tasks are performed using the two component FE models. The FE model of the entire structure is obtained by assembling the component FE models that were each validated using their corresponding "super-model". This approach removes the need to build a physical test structure, and to plan and perform a modal test from the validation process in the direct design cycle loop. This does not mean to

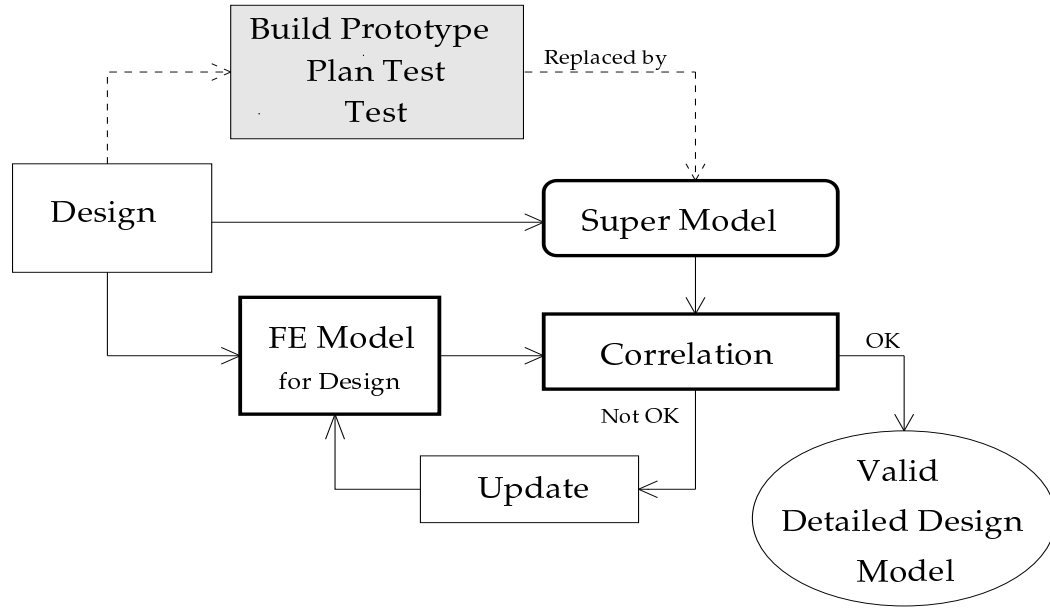


Figure 2.1: Improved Model Validation Process

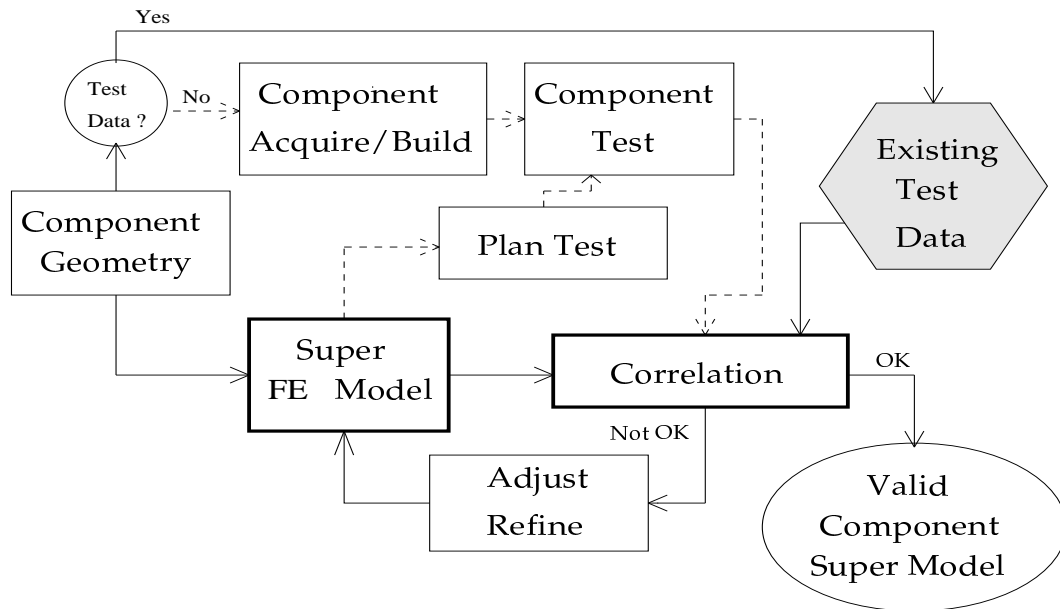


Figure 2.2: Super Model Component Validation

suggest that modal testing can or should be omitted from the whole process, only that it be removed from its present time-critical position in the model validation process so that a validated FE model may be obtained within the design cycle time. It is proposed that modal testing be used extensively **outside** the design cycle loop of the model validation process, as shown in Figure 2.2, to help learn how to model difficult features—joints and complex geometries—and then to use the lessons learned to improve the "super-model". This will enable better prediction of the potential for in-service vibration problems before the design is finalised, thereby allowing design changes to be implemented so that potential vibration problems can be avoided.

The ability to replace the test data with a "super-model" has significant advantages. Tests are often limited in frequency range and spatial resolution by the capabilities of the test equipment used and the time available for testing. Also, performing tests for multiple boundary conditions is not only time-consuming but can also be very difficult due to the interaction of the test article with the test apparatus that it is mounted on. With the capabilities of FE analysis and the currently-available (and ever-increasing) computer power one can explore much greater frequency ranges as well as multiple boundary conditions with relative ease. Further, the model updating problem, which has historically been under-determined due to the fact that the number of measured DOFs is necessarily relatively small when compared with the number of analysis DOFs, will now be over-determined because the number of (pseudo) measured DOFs can be very large when compared with the number of analysis DOFs [5].

2.3 Replacing Test Data with a Super Model

In order to be able to replace the test data—natural frequencies and mode shapes—with those from the eigensolution of a super-model, it must be shown that a super-model can reproduce or correlate with the test data with sufficient accuracy. For

the purpose of this exercise, "sufficient accuracy", for all the modes to be included, is defined as natural frequency differences of less than 3 % and MAC values greater than 0.9.

Consider the cross-section geometry for the turbine casing shown in Fig. 2.3. The figure shows that the section of the casing is conical with forward and aft flanges, both of which have bolt holes for attaching to adjacent casings. Two important features to note are the additional bolt holes on the inner side of the casing. The first hole is a short distance aft of the forward flange and the second hole is just forward of the aft flange. The areas around both bolt holes are scalloped in the circumferential direction, as shown in Figure 2.4, which is a view looking aft to forward down the engine axis of a circumferential section of the casing. Similarly, Figure 2.5 is a view looking forward to aft of a circumferential section of the casing. The flange holes for the aft and forward flanges are shown in Figure 2.4 and Figure 2.5 respectively. The case studies in Chapter 6 will show that these features—bolt holes and scallops—can be very important to obtaining good correlation.

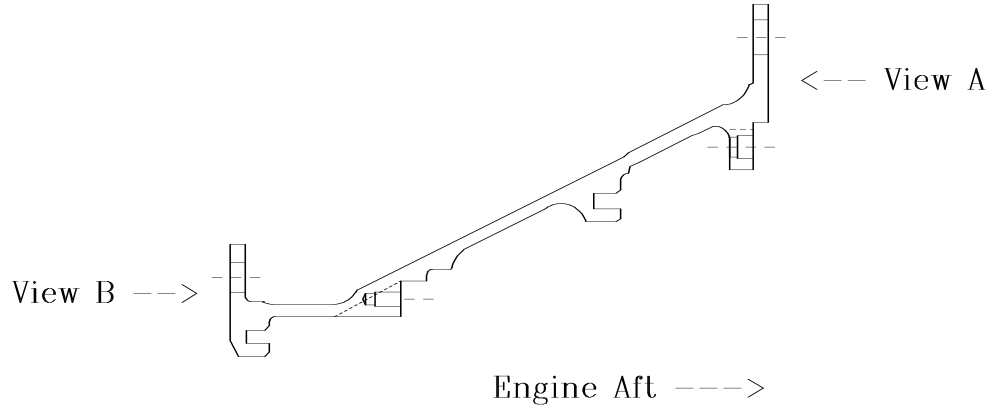


Figure 2.3: Cross-section of Turbine Engine Casing

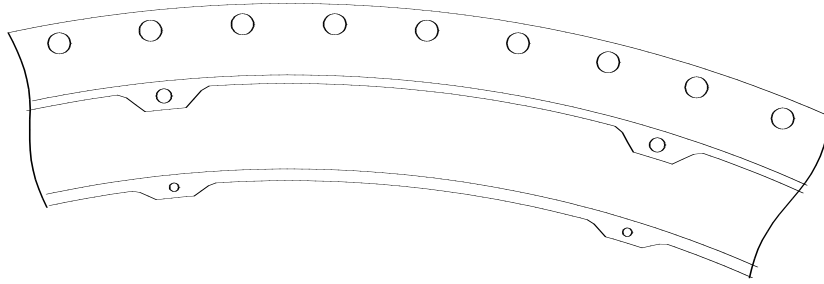


Figure 2.4: View A of the Bolt Holes and Scallops for the Aft Flange

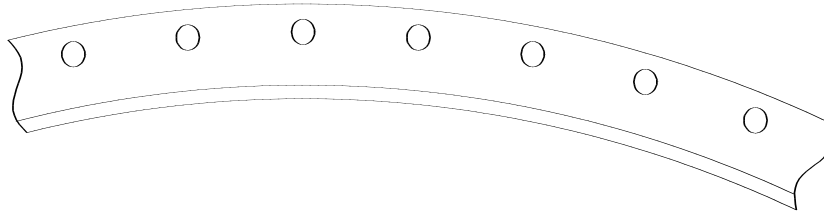


Figure 2.5: View B of the Bolt Holes for the Forward Flange

The test data (provided by Rolls-Royce) for this casing were taken for the free-

free condition and consisted of 18 measurements of radial accelerations equally-spaced about the circumference at 2 axial locations (near the forward and aft flanges). The test frequency range was between 0 and 700 Hertz for which the modal analysis produced 9 modes.

The cross-section of the initial FE model for the turbine casing is shown in Figure 2.6. The model was generated from the design drawings using the nominal dimensions. The cross-section model consisted of 124 nodes and 69 elements which

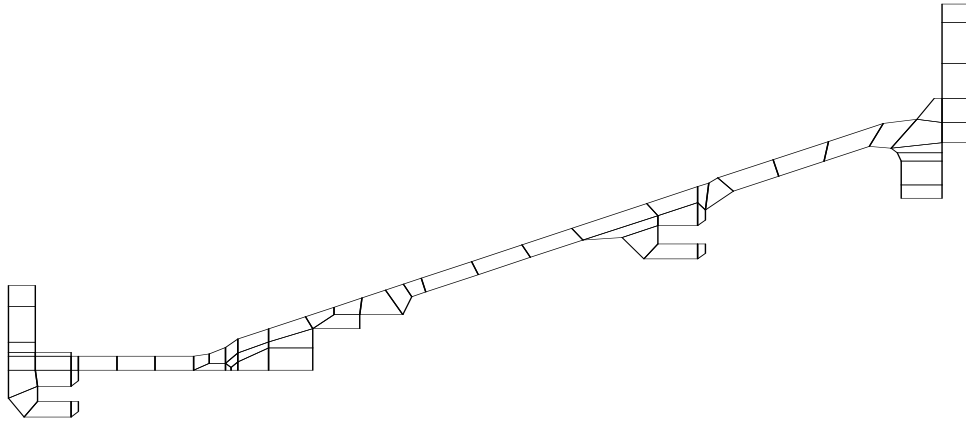


Figure 2.6: Cross-section of Initial FE Model for the Turbine Engine Casing

was then spun about the axis of symmetry with 216 elements in the circumferential direction. The significant number of elements in the circumferential direction were necessary in order to model the bolt holes and scallops. The result was the 3-D, 8-noded, hexahedron solid model with 26,784 nodes, 14,904 elements and 80,352 DOFs shown in Figure 2.7. The commercial program MSC/NASTRAN was used to obtain the free-free natural frequencies and mode shapes for the first 20 modes.

The correlation between the test data and the analysis was assessed using the modal assurance criterion (MAC) but with a new way of simultaneously displaying the frequency correspondence and mode shape correlation. The new method is

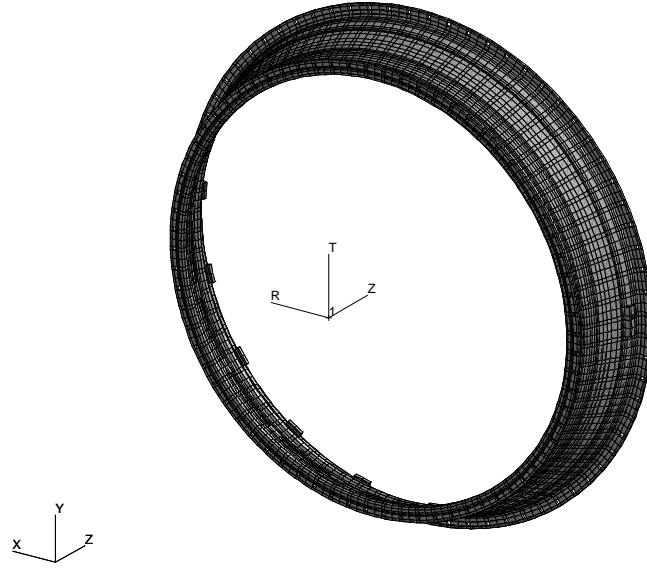


Figure 2.7: Initial FE Model for the Turbine Engine Casing

called the frequency-scaled MAC (FMAC) and is presented and discussed in detail in Chapter 5. The FMAC is obtained by plotting circles whose diameters are proportional to the MAC values. This is done for both the experimental auto-MAC and the MAC matrices which are overlaid on the same plot using black and red circles respectively. The FMAC in this case is plotted with the percentage frequency difference between analysis and test on the y axis and the experimental mode number on the x axis. In this way the difference between the size of the circles for the auto-MAC (perfect MAC=1) and the MAC provides a visual scale to assess the mode shape correlation and the percentage frequency difference (on the y axis) shows the degree of frequency correspondence.

The correlation for the initial FE model for the turbine casing is shown by the FMAC plot in Figure 2.8. The experimental auto-MAC is shown by the black circles and the MAC is shown by the red circles. The correlation is seen to be very good with MAC values very close to 1.0 and frequency differences between about

+1.5% and +5.5% for all 9 of the experimental modes. It is important to mention the consistency of the frequency differences with about a $\pm 2\%$ variation about an average at +3.5%.

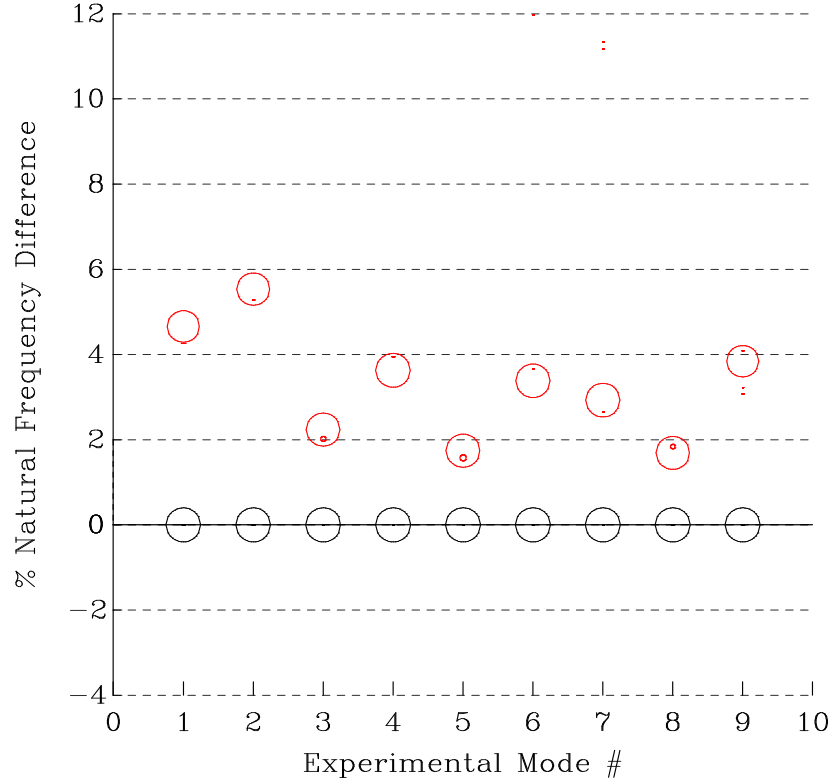


Figure 2.8: FMAC for Initial Turbine Engine Casing Model

Although the correlation for the initial FE model was very good, the goal of 3% for natural frequency differences was not met for all modes. Further, it is common practice to check the convergence of the FE model by refining the model—by increasing the number of nodes and elements—while holding the geometry and material properties constant. Accordingly, the initial cross-section FE model mesh was refined, as shown in Figure 2.9, increasing the number of nodes and elements in the cross-section to 238 and 163, respectively.

The cross-section model was again spun about the axis of symmetry with 216 elements in the circumferential direction. The resulting 3-D, 8-noded, solid model

is shown in Figure 2.10 with 51,408 nodes, 35,208 elements and 154,224 DOFs.

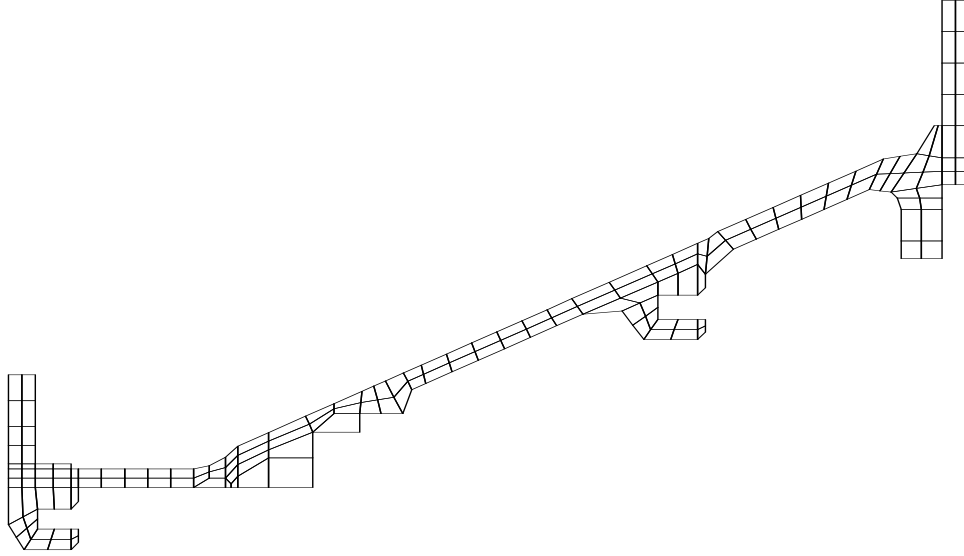


Figure 2.9: Cross-section of Refined FE Model for the Turbine Engine Casing

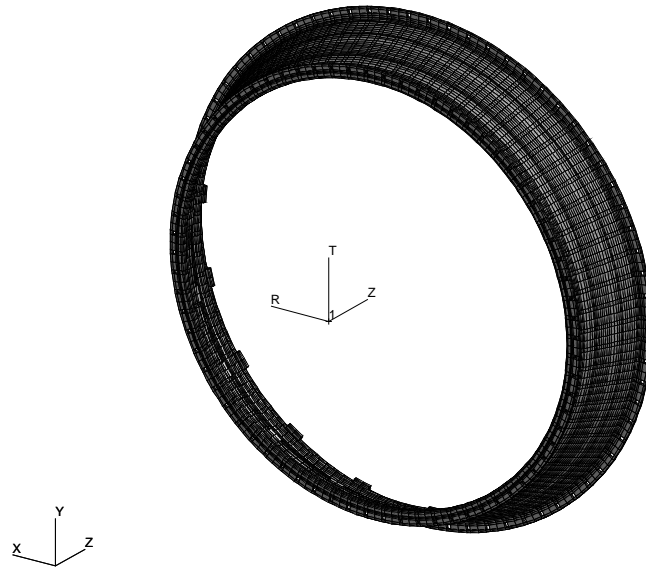


Figure 2.10: Refined FE Model for the Turbine Engine Casing

The correlation for the refined FE model for the turbine casing is shown by the FMAC plot in Figure 2.11. The experimental auto-MAC is shown by the black circles and the MAC for the refined FE model is shown by the red circles. The correlation is seen to be excellent with MAC values very close to 1.0 and natural frequency differences between about 0% and +2.5% for all 9 of the experimental modes. Note again the consistency of the natural frequency differences with about a 1.25 % variation about an average at +1.25%.

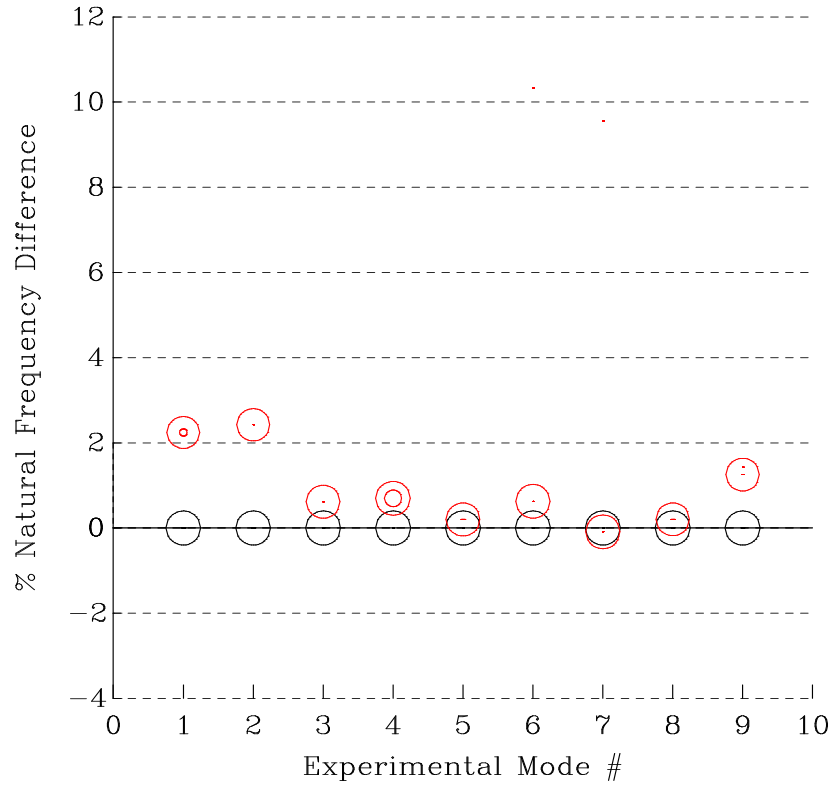


Figure 2.11: FMAC for Refined Turbine Engine Casing Model

In order to show the convergence of the model, the FMAC for the initial model and the refined model were plotted on the same plot as shown in Figure 2.12. The experimental auto-MAC is shown by the black circles, the MAC for the initial FE model is shown by the red circles and the MAC for the refined FE model is shown by the blue circles. The convergence is shown to be very good with decreases in

frequency differences from between about 1.5% for modes 3, 5 and 8 and 3.5% for mode 2 while the MAC values remained unchanged.

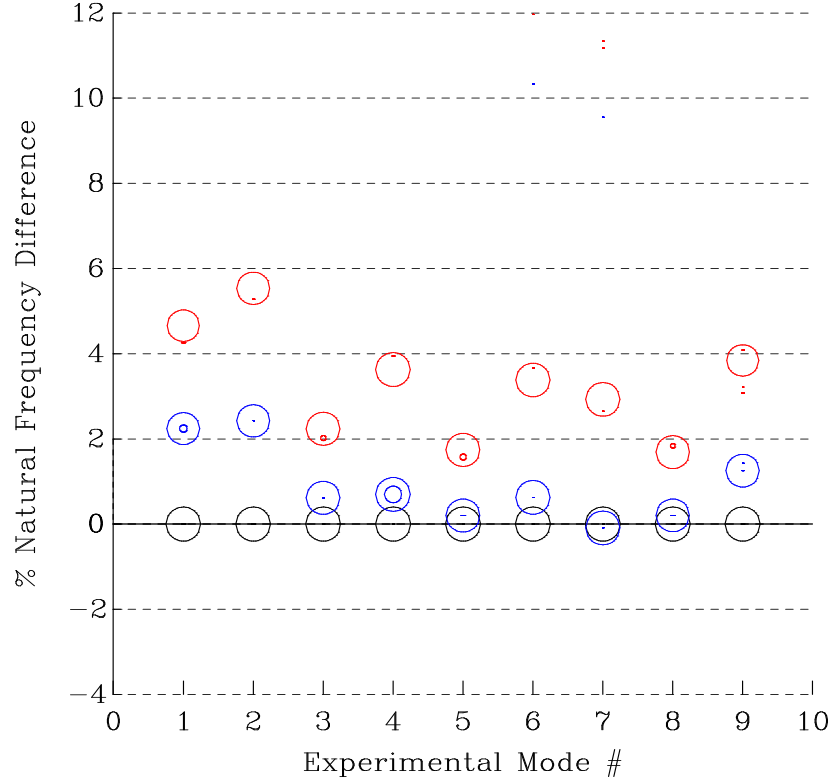


Figure 2.12: FMAC for Initial and Refined Turbine Engine Casing Model

2.4 Conclusions

In the case study presented here it has been shown that a very detailed solid element FE model called a "super-model" can match the test data from a physical structure with excellent accuracy. The consistency of the natural frequency differences is attributed to the model containing all the pertinent features of the structure, such as bolt holes and scallops, and that the FE mesh was of adequate density. Further, the actual physical geometry must have been within reasonable tolerances of the nominal dimensions that were used to create the FE model in order to obtain the

excellent correlation that was shown. This is important since it must be possible to produce an accurate super-model using only the design dimensions and without the aid of the physical structure. This is a necessary condition for the new validation strategy—replacing the test data with a super-model—to be successful.

In order to maximize the benefit from using a super-model, a review of some basic FE modelling methods will be undertaken to help determine where improvements to the super-model may be achieved.

Chapter 3

Finite Element Modelling Methods

3.1 Introduction

The topic of finite element (FE) modelling methods is quite encompassing. However, the focus here is on the methods used to represent the geometry of a structure using finite elements for linear vibration analysis. The approximate methods currently used to model the various complex geometric shapes that exist in industrial structures may eventually become obsolete—in particular for detailed design analysis. This, it is envisaged, will happen when the available computer power reaches the necessary level such that the complex geometric features may be modelled to a much higher degree of accuracy than is currently possible. The current trend is to use tetrahedron elements and commercially-available automated mesh-generating software to construct three dimensional (3-D) FE models of components [7, 8]. However, current computer power is not yet generally adequate to model, for example, an entire gas turbine engine by assembling numerous of these very detailed component models. Further, for preliminary design models, where the details and features have not yet been designed, an approximate model is considered to be

more appropriate. Accordingly, there is still a need for approximate modelling techniques and most likely will be for an estimated five years or so.

With the wealth of finite element modelling that has been performed in the past two to three decades, one might expect there to be a significant amount of literature available on FE modelling. However, the ability to generate an accurate FE model using the smallest number of degrees of freedom (DOFs) is generally considered a competitive advantage and therefore the techniques used to accomplish the feat are usually kept within the company that developed them. Accordingly, there is very little literature available on efficient geometric modelling techniques.

The following sections present the general steps required for the modelling process in a somewhat chronological order. While the actual order may vary for a given situation, it is important to focus on the decisions that are required at each step towards the goal of obtaining a sufficiently accurate and robust FE model.

3.2 Classification of a Structure

The classification of a structure is usually done by determining: (1) how critical it is to the overall function of the system and (2) the intended function of the structure within the system. The type of FE model that is to be created and the amount of detail to use in the model depends on both of these.

The desire to model every component in great detail is usually precluded by the finite amount of time available for the design process. Consequently, each component must first be ranked according to how critical it is to the overall function of the system. Accordingly, the most critical components are modelled in the most detail and the least critical components in the least detail, thereby making optimal use of the time available during the design cycle.

The characteristics—mesh density and type of element—of an FE model have a strong dependence on the structure's function. For example, one would not use the same mesh density for both a compressor fan blade and an engine casing.

This is because fan blades usually have a significant amount of twist and thickness variation requiring a large number of elements in both the radial and chordwise directions whereas casings are usually cylindrical with modest variations in dimensional features. Further, one would not necessarily use the same element type for both a compressor disk and an engine casing. This is because the relatively thick disk is better represented using solid elements whereas the relatively thin casing is better represented using shell elements, [9], page 398.

Accordingly, classifying a structure is an important first step in the modelling process and helps to ensure that the most critical components get the most modelling attention and that an FE model consistent with the intended function of the structure is generated.

3.3 Different Model Levels

The model level refers to the amount of geometric detail represented in the FE model; the mesh density or number of elements used; and, to a lesser degree, the type of element used. The level of model that is required is usually dependent on the level or type of analysis to be performed. Generally, there are three levels of analysis that are performed—one for each stage of the design process: *(i)* preliminary design (PD), *(ii)* detailed design (DD) and *(iii)* final design (FD)—for which there are three corresponding levels of model. As an example, consider the cross-section of a simplified engine casing shown in Figure 3.1.



Figure 3.1: Cross-section of Engine Casing

The first level of analysis is called "preliminary design" (PD) and usually requires a relatively coarse model that is used to make sure that the most fundamental

modes of the structure are within the desired frequency range. The coarseness of the PD model also serves the need for rapid turn around of design and analysis iterations so that an acceptable preliminary design can be obtained rapidly [10]. At this analysis level the element type is often selected to support rapid model generation. For example, shell elements may be used instead of solid elements to represent the engine casing. Figure 3.2 shows what a cross-section of a solid-element PD model might look like for the simplified engine casing shown in Figure 3.1. Note the absence of the fillets at both the front and rear flanges as well as the omission of the stiffening ring near the centre of the case. The absence of the aforementioned features may be because they had not been defined at this stage of the design or because they were deemed to have a small impact on the modal characteristics of the structure and therefore a saving in modelling time could be gained.



Figure 3.2: Preliminary Design FE Model

The second level of analysis is called "detailed design" (DD) and generally requires a more detailed model than the PD analysis and may thus include additional physical features that were omitted from the PD model. The DD model is generally the one used to confirm that the physical part meets the vibration design criteria and therefore the part may be released to production. For this reason the DD model must be of sufficient detail to be able to predict accurately all the modes within the desired frequency range. Figure 3.3 shows what a cross-section of a solid-element DD model might look like for the simplified engine casing. Note that both the front and rear flange fillets are included as well as the stiffening ring near the centre of the case. There is also a general increase in mesh density compared with that of the PD model.

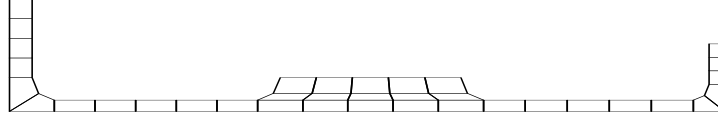


Figure 3.3: Detailed Design FE Model

The third level of analysis is called the "final design" (FD) or is sometimes referred to as the "problem solving" analysis level. This analysis type is usually only used for in-service vibration problems or to solve particularly difficult cases that have a known history of requiring a very fine and detailed model. Figure 3.4 shows what a cross-section of a solid-element FD model might look like for the engine casing. Note the greater detail in all the fillet regions as well as a significant increase in mesh density when compared with the DD model. Because of the size of the FD model, it usually requires significant computation time and therefore is precluded from use as a detailed design model. The FD model may be very similar to the proposed "super-model" but with two significant differences: (1) the "super-model" will be generated in the DD stage of the design so that it can be used to validate the DD model and (2) the "super-model" will include the lessons learned from test correlation of numerous structures (and thus might be termed a "smart model").

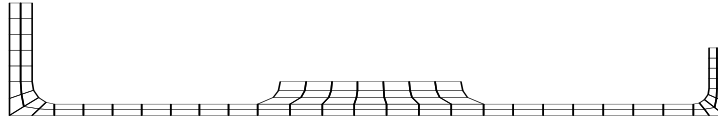


Figure 3.4: Final Design FE Model

3.4 Basic Finite Element Types and Usage

The finite element method has been the subject of numerous papers, books and other publications for many years. Accordingly, there is substantial literature available on the many different element types [9, 11, 12, 13]. The focus here is

on the basic types of 3-D structural elements and how they are used in practice to represent the different features of a structure. The intention is to present a fundamental guide to basic 3-D structural element usage and to refer the reader to the above references if a more rigorous presentation is desired.

The table in Figure 3.5 lists the basic 3-D finite element types used for structural dynamic design. The basic 3-D elements have been grouped here into the general families—beams, plates/shells and solids. Although there are many element formulations available within each group, the grouping was done to facilitate a general discussion about the merits of the different element types.

Although there are significant differences between shell and plate elements, they are grouped together here because they require very similar input information to describe them to an FE program. The primary differences between them are that, in general, the in-plane and bending displacements for plates are considered to be mutually independent whereas for shells they are considered to be coupled. Further, the geometry of a plate is flat whereas shells can be either curved or flat, [9], pages 329-331. Although not entirely correct it is relatively common practice for plate elements to be referred to as *shells*. Accordingly, from here on no distinction between plate and shell elements will be made and the term *shell* will be used to indicate either.


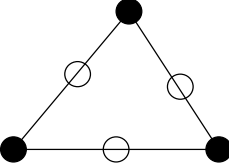
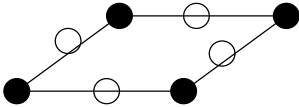
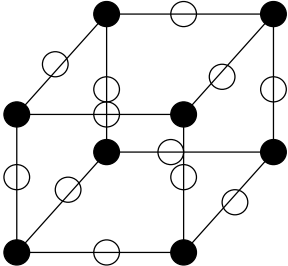
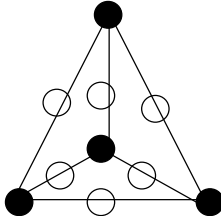
Basic 3-D Finite Element Types		
Type	Nodes/DOFs	Form
Beam	2 nodes @ 6 DOFs	
Plate/Shell Triangle	3 nodes @ 6 DOFs 6 nodes @ 6 DOFs	
Plate/Shell Quad	4 nodes @ 5 DOFs 8 nodes @ 5 DOFs	
Solid Hexahedron	8 nodes @ 3 DOFs 20 nodes @ 3 DOFs	
Solid Tetrahedron	4 nodes @ 3 DOFs 10 nodes @ 3 DOFs	

Figure 3.5: Basic 3-D Structural Finite Element Types

3.4.1 The Beam Element

The beam element, shown in Figure 3.6, is used to represent features that have one dominant dimension [14]. Some examples for using beams in gas turbine applications are for bolts, shafts, reinforcing ribs for casings and flanges for casings [15, 16].

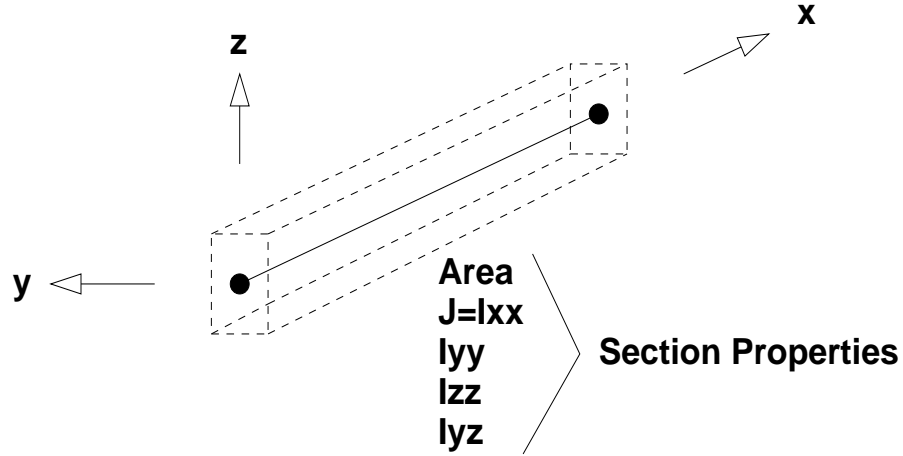


Figure 3.6: Beam Element Geometry Definition

The element geometry is specified by two nodes and a vector or third point that is used to determine the major and minor axes of the beam. Each of the nodes has 6 DOFs—3 translations in the respective orthogonal axis directions and 3 rotations, one about each orthogonal axis. Additionally, the area (A) and moments of inertia (I_{xx} , I_{yy} , I_{zz} , I_{yz}) for the beam cross-section are usually specified using the classical equations for such properties [17]. In general, the properties can be different for each end of the beam in order to model a tapered section. Also, the centroid of the beam may be offset from the actual nodes that define each end, thereby providing the user with more options for modelling complex geometries, [18], pages 511-514.

3.4.2 The Shell Element

The shell element, such as the 4-noded example shown in Figure 3.7, is used to represent features that have one dimension that is much less than the other two. As

the name implies the element is based on shell theory and is ideal for representing shell-like structures such as thin plates, hollow airfoils and engine casings [19, 20].

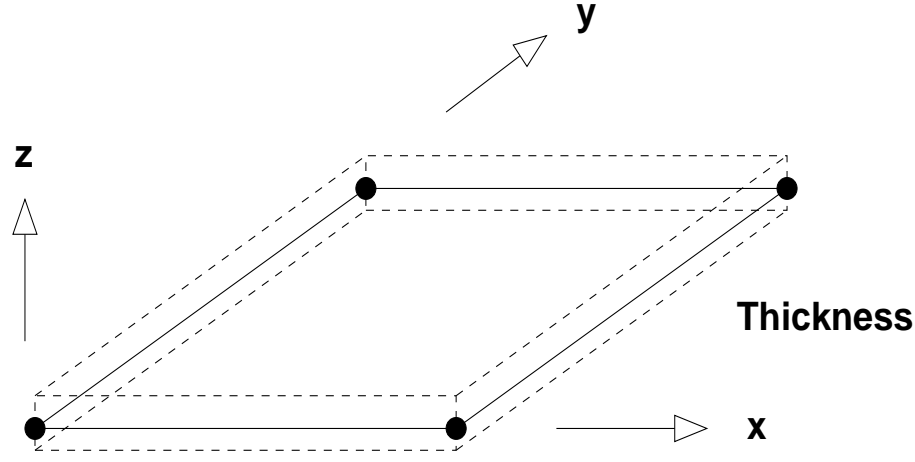


Figure 3.7: 4-noded Shell Element Geometry Definition

The element geometry is specified by at least 3 apex nodes for a triangular or 4 corner nodes for a quadrilateral, while higher-order elements may have additional nodes per edge and a node in the centre of the face for a total of 10 and 12 nodes for the triangle and quad respectively. For the triangle, each node has 6 DOFs—3 translations in the respective orthogonal axis directions and 3 rotations, one about each orthogonal axis. For the quad, each node has 5 DOFs—3 translations in the respective orthogonal axis directions and 2 rotations, one about each of the in-plane orthogonal axes. The third rotation, about the axis normal to the quad, is generally not allowed. However, there are some formulations that support a rotational DOF about the normal (sometimes called the drilling rotation), [21]. The shell thickness can either be specified for the entire element (constant for all nodes) or for each node independently in order to model a tapered section. Also, the element plane (and therefore the stiffness and inertia) may be offset in the normal direction from the geometry plane defined by the nodes, thereby providing the user with more options for modelling complex geometries, [18], pages 581-584.

Figure 3.8 shows how a casing with two flanges might be modelled by using

4-noded shell elements for the casing and beam elements for the flanges, [12], page 294. The geometry is shown by the dashed lines and the FE model by the solid lines with filled circles at the node points. Note that the beam elements use the same nodes as the shell elements at the intersections of the casing with the flanges. This is shown by the larger concentric circle around the filled circle for each shared node. In the example shown this approach reduces the number of nodes by 6, and therefore the number of DOFs by 30, compared with an all-shell element model. Because of the reduced number of DOFs, this approach is often used for large models such as a model for a whole turbine engine.

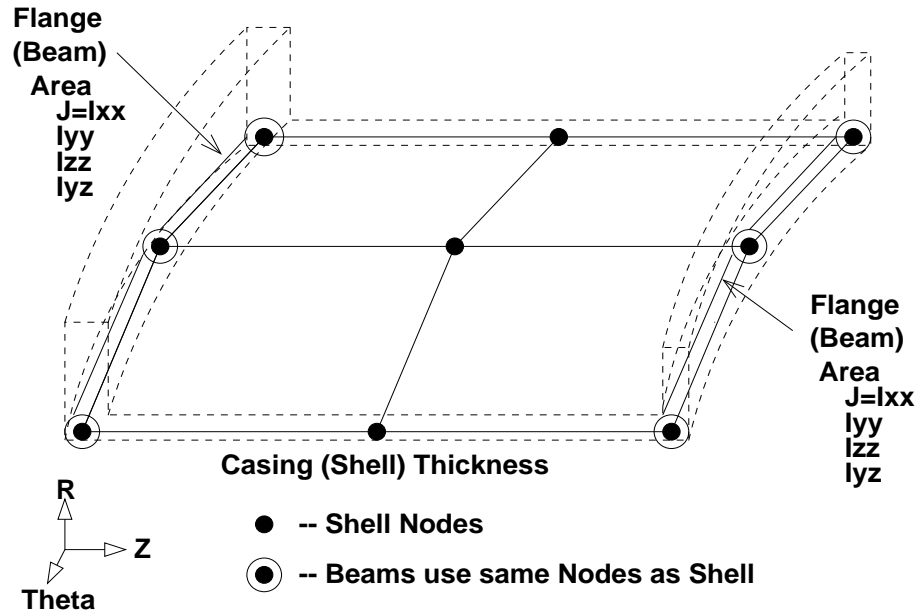


Figure 3.8: Section of Engine Casing Modelled with Shells and Beams

Figure 3.9 shows how the same casing might be modelled by using shell elements for both casing and flanges. Again, the geometry is shown by the dashed lines and the FE model by the solid lines with filled circles at the node points. Note the 6 extra nodes that are required to model the flanges resulting in 30 additional DOFs as previously mentioned.

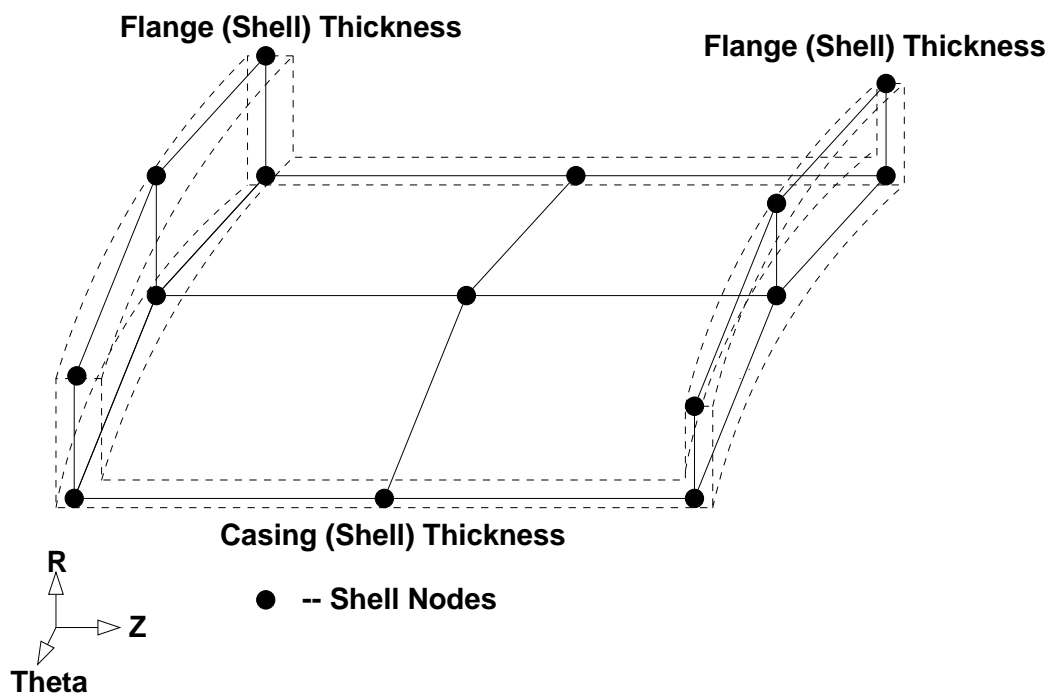


Figure 3.9: Section of Engine Casing Modelled with Shells Only

3.4.3 The Solid Element

The solid elements, shown in Figure 3.5, are used to represent features that have three dimensions of a similar order. However, with care they can be used to model thin shell-like structures as well. The element geometry is specified by at least 4 apex nodes for a tetrahedron or 8 corner nodes for a hexahedron, while higher-order elements may have additional nodes per edge and a node at the centre of each face for a total of 10 and 32 nodes for the tetrahedron and hexahedron, respectively. Each node has 3 DOFs for the 3 translations in the respective orthogonal axis

directions, [11], pages 127-128.

Figure 3.10 shows how the example casing might be modelled by using 8-noded hexahedron solid elements for both the casing and the flanges. In this figure, the geometry is shown by the red-dashed lines and the FE model by both the solid (visible) and dashed (hidden) black lines.

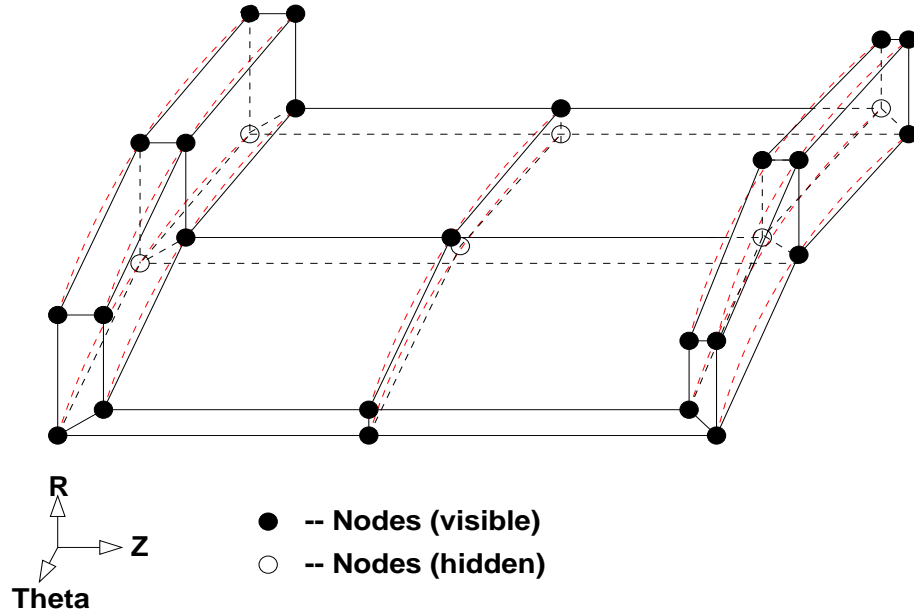


Figure 3.10: Section of Engine Casing Modelled with Solids (hexahedron)

While the example shown here is for 8-noded hexahedron solid elements, the recent trend is to use 4 or 10-noded tetrahedron elements for which there is commercial software available for generating the mesh automatically.

Figure 3.11 shows how the example casing might be modelled by using a combination of 8-noded hexahedron solid elements for both the flanges and 4-noded shell elements for the casing. This type of model is sometimes referred to as a *hybrid* model [22]. The hybrid model requires the use of constraint elements to attach the shell nodes of the casing to the face of the solid elements of the flanges [23, 24]. While this is not a trivial task there are special elements available in commercial FEA programs such as MSC/NASTRAN, [18], pages 1065-1067 and ANSYS, [25], which help to generate the appropriate constraints with minimal user input.

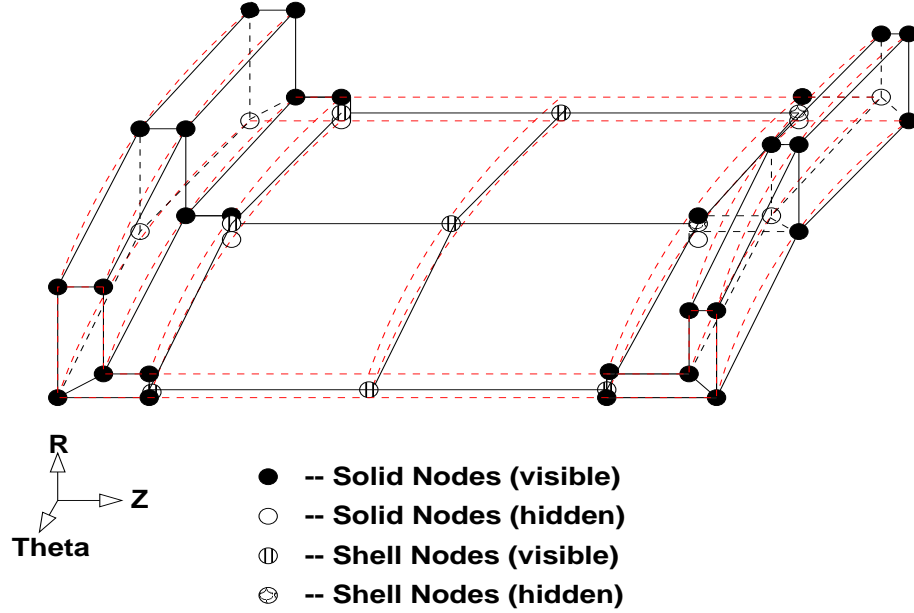


Figure 3.11: Section of Engine Casing Modelled with Solids and Shells (Hybrid)

3.5 Modelling with Shells and Beams

There are a few subtle but relatively important modelling techniques that are necessary for generating shell/beam and shell models with the maximum accuracy possible. Most of the difficulties arise in structures that have sudden changes in geometry such as flanges or junctions where two or more shell-like structures meet [26]. For such structures it can be difficult to choose the proper shell thickness. Likewise, for a shell/beam model it can be difficult to determine where it is best to terminate the shell part of the model and how much of the structure to represent with a beam.

Figure 3.12 shows the cross-section geometry for three basic shell junctions: (1) L-shaped (flange), (2) T-shaped and (3) cross-shaped. Although most junctions have fillets to provide a smooth transition between the mating parts, these have been omitted since in general fillets cannot be adequately represented with shell/beam or shell elements.

The first junction is L-shaped which is representative of most simple flanges.

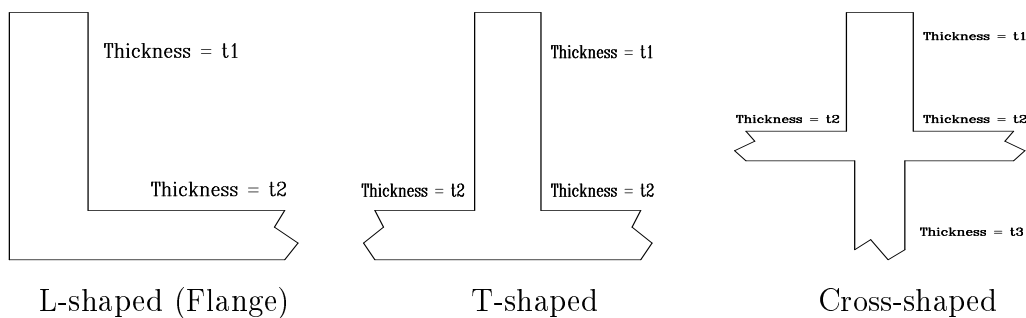


Figure 3.12: Cross-section Geometry for Three Basic Junctions

The vertical flange has thickness $t1$ and the horizontal casing has thickness $t2$. The second junction is T-shaped which could represent, say, a case stiffened by a circumferential rib. The horizontal casing has thickness $t2$ and the vertical rib has thickness $t1$. The third junction is cross-shaped which might represent a T-shaped casing section with a circumferential rib stiffener. The vertical rib above the casing has thickness $t1$, the horizontal casing has thickness $t2$ and the vertical rib below the casing has thickness $t3$.

One way to obtain better insight into the aforementioned modelling concerns is to consider how the FE analysis program interprets the geometry and thickness data input by the user. The input data consists of the element geometry and thickness, either constant for the element or at each node of the element allowing for a tapered section. Specifying an element thickness is equivalent to specifying the same thickness for each node of the element. The thickness is defined normal to each node with half the thickness in the positive normal direction and half in the negative normal direction. The goal is to obtain the proper stiffness and mass, not just for each element, but for the entire model. Accordingly, a simple but effective technique is to use the thicknesses and nodal normals to determine what the geometry of the shell element would look like by converting a 2-D area to a 3-D volume or in this case with cross-section models, a 1-D line into a 2-D area. By determining that the total area or volume of all the elements and their respective

locations are consistent with the geometry, it follows that the stiffness and mass will also be consistent with the geometry.

The L-shaped junction was modelled with shells in the conventional way—by placing nodes along the mean-line as shown in Figure 3.13. The geometry is shown by the black lines and the shell FE model by the red lines with red circles at the node locations. The problem is to determine what thickness to use at the node where the two shell elements meet, shown by the larger green circle.

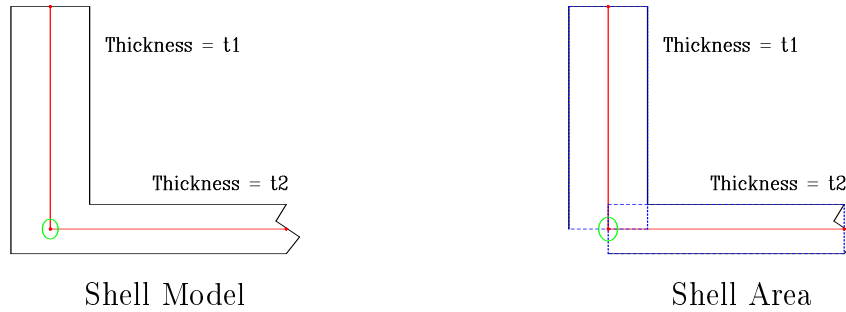


Figure 3.13: Shell Fe Model and Corresponding Area for L-shaped Junction

A method that has often been used is to select different thicknesses for each element at the common node. Accordingly, for the flange element the thickness would be t_1 and for the case element the thickness would be t_2 . The second diagram in the Figure shows with blue dashed lines how these thickness choices would be interpreted by the FE program. The blue dashed rectangle to the upper right of the common node represents an overlap in material. However, the open rectangle to the lower left of the common node represents missing material. Fortunately, in this case the amount of material or area was identical and in practice both the stiffness and mass would be correct (serendipitous). If a beam element was to be used for the vertical flange instead of the shell element then the centroid and section properties should be chosen to be consistent with the geometry from the top of the flange to the common node (green circle).

Figure 3.14 shows the geometry and shell model for the T-shaped junction. In this case the thickness needs to be determined for the node that is common to

three elements with two different thicknesses— t_1 for the vertical rib and t_2 for the horizontal casing. The common node is again shown by the larger green circle.

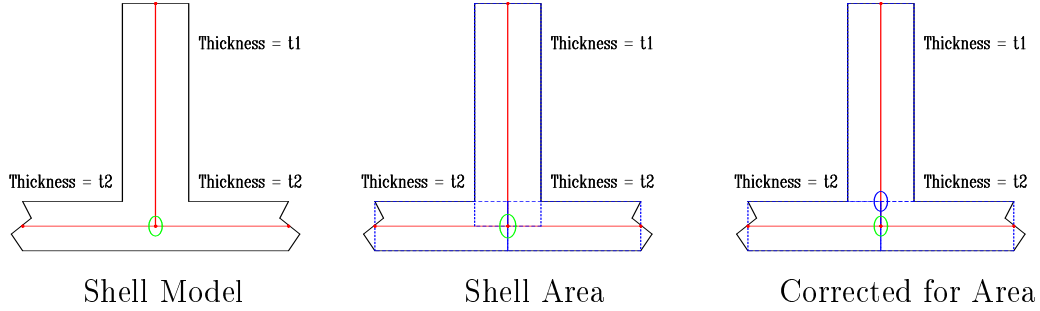


Figure 3.14: Shell Fe Models for T-shaped Junction

The selection of different thicknesses for each element at the common node would give t_1 for the vertical rib element, t_2 for the left side horizontal casing element and also t_2 for the right side horizontal casing element. The FE program's interpretation of the thickness choices is shown by the blue dashed lines in the second diagram in the Figure. The two blue dashed rectangles above the common node represent an overlap in material or area. For this case both the stiffness and mass would be over predicted. While one might think that the two effects would cancel, resulting in accurate frequencies, in practice models such as these have proven to be both too stiff and too heavy.

One solution to this over-prediction of stiffness and mass is shown in the third diagram in Figure 3.14. The geometry of the vertical rib element has been adjusted by replacing the common node with a new node shown by the large blue circle at the top of the casing. The model adjustments were completed by connecting the common node (green circle) to the new node (blue circle) with a rigid element. In this way the overlap in material was removed and the correct stiffness and mass were obtained. When using a beam element for the vertical rib instead of the shell element the centroid and section properties should be chosen to be consistent with the geometry from the top of the flange to the new node at the top of the casing (blue circle).

The geometry and shell FE model for the cross-shaped junction are shown in Figure 3.15. The thickness for this case needs to be determined for the node that is common to four elements, shown by the larger green circle, with three different thicknesses— t_1 for the vertical rib above the horizontal casing, t_2 for both the left and right sides of the horizontal casing and t_3 for the vertical casing below the horizontal casing.

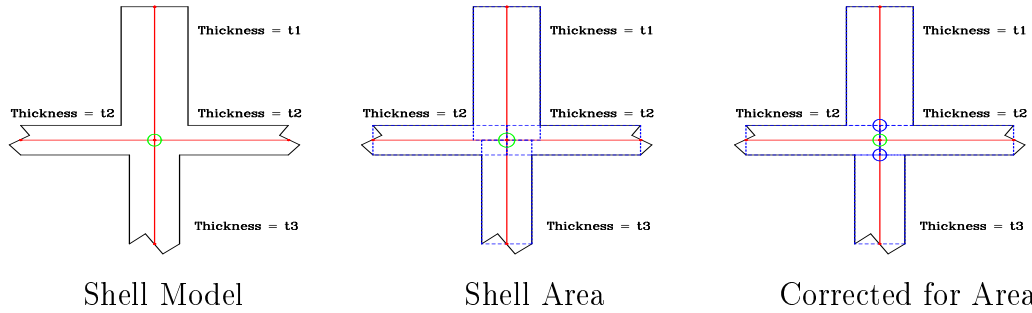


Figure 3.15: Shell Fe Models for Cross-shaped Junction

Different thicknesses were again selected for each element at the common node and were: t_1 for the vertical rib element above the horizontal casing, t_2 for both elements of the horizontal casing and t_3 for the vertical casing element below the horizontal casing. The second diagram in the figure shows how these thickness choices would be interpreted by the FE program with blue dashed lines. The four blue dashed rectangles surrounding the common node represent an over-prediction of both the stiffness and mass that in practice do not cancel each other, resulting in a model that is both too stiff and too heavy.

The third diagram in Figure 3.15 shows a solution to the stiffness and mass over-prediction again using rigid elements. The geometry of the vertical rib element was again adjusted by replacing the common node with a new node shown by the large blue circle at the top of the casing. Likewise, for the lower vertical casing, the common node was replaced with a new node at the bottom of the horizontal casing, also shown by a large blue circle. The common node (green circle) and the two new nodes (blue circles) were then attached using rigid elements to complete

the model adjustments. Accordingly, the overlap in material was removed and the correct stiffness and mass were obtained. If a beam element was to be used for the vertical rib above the casing instead of the shell element then the centroid and section properties should be chosen to be consistent with the geometry from the top of the vertical rib to the new node at the top of the case (blue circle).

Although the examples shown here were for rather simple shell junctions, it is envisaged that the techniques are applicable to the far more complex junctions found in real industrial structures.

3.6 Other Modelling Considerations

The selection of the element type—beam, shell or solid—to model a particular structure is only part of the modelling process. The analyst must also select the order of the element (number of nodes per element) and the mesh density. Further, other issues may arise during modelling complex geometries—such as: unacceptable element distortions from large aspect ratios, skew or warp—that may require the analyst to make choices. While automated mesh generators may in the near future relieve the analyst from having to make some or most of these choices, currently they are necessary, in most cases, and in particular, for models used for preliminary design. Accordingly, it is necessary to have a basic knowledge of how these factors can affect the analytical solution.

3.6.1 Element Order

Most element types are based on an assumed displacement field for which the displacement within the element is defined in terms of its nodal displacements which are represented by polynomials, [13], page 72. The order of an element is determined by the largest order term present in the polynomial. The table in Figure 3.16 lists the order of the basic elements presented in Figure 3.5.

In general the more nodes in the element, the higher the order of the polynomial. However, there are at least two exceptions to this. For example, most beam elements are based on one of the classic beam formulae such as Euler-Bernoulli [27] or Timoshenko [28] and, although they may have only two nodes, they are capable of cubic bending displacements but linear axial displacements. Further, a significant amount of research has been focused on the low-order (3 and 4-noded) shell elements in order to improve their (out-of-plane) bending properties to quadratic order while keeping the number of nodes the same [19, 29]. The improvements are usually obtained by using additional internal functions. One of the most successful methods is a combination of assumed displacements at the element boundaries with an assumed stress field within the element, [11], page 422. Formulations such as these are referred to as *mixed* for which an example is the QUAD4 in MSC/NASTRAN, [18], pages 587-590. While mixed formulation, low-order, elements can offer quadratic bending capability, their in-plane capability remains linear. Accordingly, it may be necessary to use a fully quadratic element for structures where in-plane displacements are deemed important.


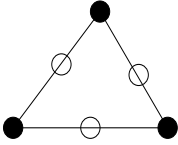
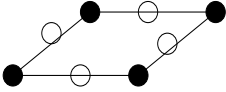
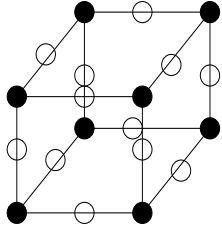
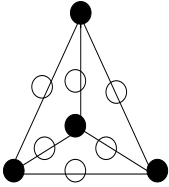
Order of Basic 3-D Finite Element Types			
Type	Nodes/DOFs	Order	Form
Beam	2 nodes @ 6 DOFs	Cubic	
Plate/Shell Triangle	3 nodes @ 6 DOFs 6 nodes @ 6 DOFs	Linear * Quadratic	
Plate/Shell Quad	4 nodes @ 5 DOFs 8 nodes @ 5 DOFs	Linear * Quadratic	
Solid Hexahedron	8 nodes @ 3 DOFs 20 nodes @ 3 DOFs	Linear Quadratic	
Solid Tetrahedron	4 nodes @ 3 DOFs 10 nodes @ 3 DOFs	Linear Quadratic	
* some formulations, linear in-plane, quadratic in bending			

Figure 3.16: Order of Basic 3-D Structural Finite Element Types

Selecting the element order, for example, 4-noded instead of 8-noded shells or 8-noded solids instead of 20-noded, may seem obvious when trying to generate a model with the least number of DOFs. However, choosing the lowest order for each element type (the one with the least number of nodes and therefore the least number of DOFs) may not be the best choice, depending on the element formulation. For example, if one were to use a 4-noded shell element of general formulation (not mixed), the order would be linear for both in-plane and bending. In general linear elements have been found to be too stiff in bending and therefore yield predicted natural frequencies that are considerably too high, [11], page 190. Accordingly, elements with quadratic order, at least in bending for shells, are usually preferred. This is substantiated, as previously mentioned, by the significant amount of research focussed on improving the low-order shell element bending capabilities so that quadratic order is obtained.

The proper selection of element order is also important for models that combine different types of elements, for example: beams and shells or shells and solids. In such cases one should choose elements of as close to the same order as possible. For example, when combining beams with shells one should choose a shell element that has at least a quadratic order in bending since the beam has cubic order in bending. Otherwise, using a shell element with linear bending might restrict the flexibility of the beam element providing an over-stiff (natural frequencies that are too high) result. Likewise, when combining shells and solids, one should take care to match the element orders. If a quadratic-order shell element is chosen, then a quadratic solid element should be used.

3.6.2 Element Distortion

An ideal element is one that has equal dimensions along all edges and equal angles at all apexes. For example, triangular shells should ideally be equilateral and quadrilateral shells should be perfectly square. This can be extended to solids

as well. However, the modelling of the various geometries that are inherent to industrial structures rarely allows for the elements to be ideally shaped. The distortion of elements can cause significant degradation to the accuracy of an FE model, [11], pages 139-142.

There are four primary forms of element distortion: (1) large aspect ratio, (2) in-plane skew, (3) out-of-plane warp and (4) excessively acute or obtuse apex angles. Figure 3.17 shows the primary types of element distortions using the 4-noded shell as an example.

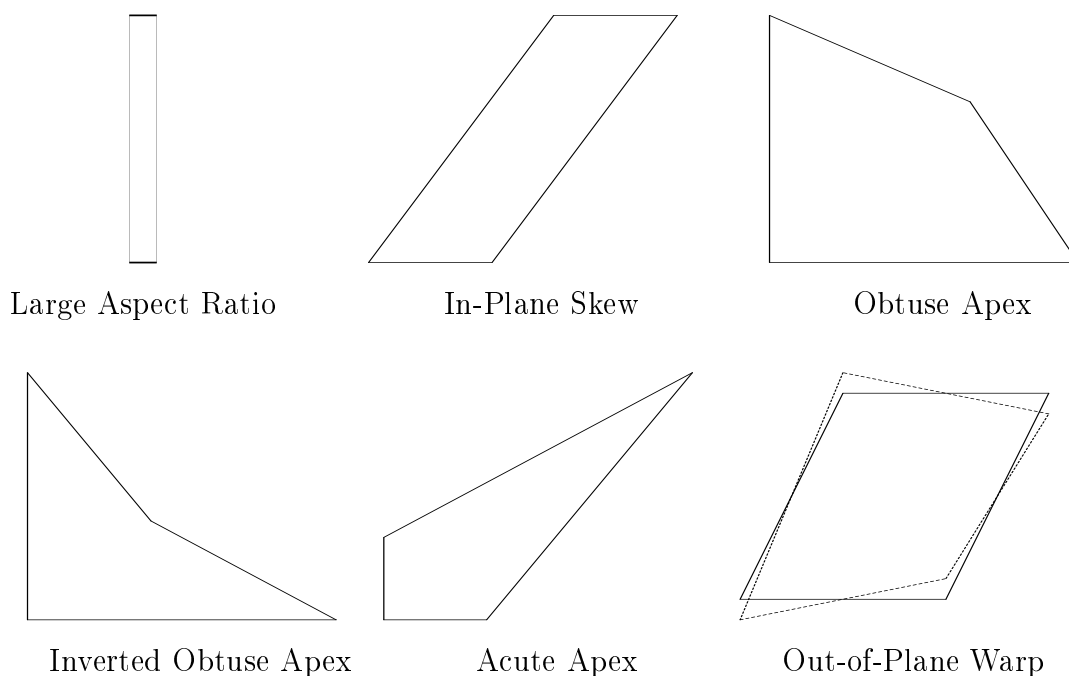


Figure 3.17: Primary Element Distortion Types for the 4-noded Shell

Fortunately most commercial FE programs provide checks for elements with excessive distortion. The aspect ratio is found by determining the ratio of the maximum and minimum lengths across the element. While a maximum aspect ratio of about 7 is recommended in, [11], page 211, the author has successfully used values as high as 10 in the models shown in Chapters 2 and 6, and for many other models. The in-plane skew and excessively acute/obtuse apex angles are

checked by determining that the angle for each apex is within a required range, such as between 45 and 135 degrees for ANSYS [25] or less than 180 degrees for MSC/NASTRAN, [18], page 583. Similarly, the nodes of each face for warped elements are checked to make sure that they are within a certain tolerance of being in the same plane. The different commercial FE programs will in general have different threshold values for aspect ratio, apex angle and warpage but will usually print warning messages if any of the thresholds are breached. However, for values that are considered too large the solution may abort.

When modelling complex geometries in practice, there may be elements within the model that exhibit a combination of the four basic types of distortion shown in Figure 3.17. For such cases, and particularly for solid elements, a more rigorous distortion check may be necessary. A distortion parameter (DP) is defined in, [11], pages 141-142, that may be used for either shell or solid elements. The distortion parameter calculation will yield DP values between -1.0 and 1.0 with DP=1.0 indicating no distortion. The DP may be zero or negative for excessive distortion but is considered acceptable for values greater than 0.20.

3.6.3 Mesh Density

It is well documented that increasing the mesh density (number of elements per unit area or volume) until the elements become infinitesimally small will produce the *real* or *correct* solution. This is assured by the element being able to pass what is called the patch test. For this test, a patch of elements is subjected to a constant strain to determine if, after the elements become infinitesimally small, the resulting stresses are exactly those that would be obtained from the constitutive behavior of the material. Elements that pass the patch test, it is argued, are guaranteed to converge to the real or correct solution [30]. Fortunately, most elements available in commercial FE programs such as MSC/NASTRAN and ANSYS are rigorously tested using the patch test as well as other tests to ensure

their robustness and that they do converge to the correct solution. Accordingly, it has become common practice to expect convergence and reliability of the elements from the aforementioned commercial FE programs.

The selected mesh density will in general depend on two factors: (1) the geometry to be modelled and (2) the goal of the analysis, in terms of the natural frequencies and mode shapes that are desired.

For the geometry it is important to determine what features are to be included in the model, particularly if there are a large number of any one type. For example, if for an engine casing there are 120 flange holes around the circumference that are to be modelled then there must be at least 240 circumferential elements for square (approximate) holes and about 3 to 5 times that many for round holes. Further, the modelling of the flange holes may also dictate the mesh density in other directions in the model due to the thresholds imposed for element aspect ratios and other distortions.

The desired number of natural frequencies and mode shapes will also affect how detailed a mesh is required. For example, if for an engine casing only the first few modes of the second nodal diameter (2-D) family are desired then the mesh in the circumferential direction can be much less dense than for say the first few modes of the sixth nodal diameter (6-D) family. This is because the mode shapes for the 2-D modes are characterised by two sine waves around the circumference whereas the 6-D mode shapes are characterised by six. Unfortunately, prior experience is often needed to determine what is required from the analysis for a given structure.

3.7 Basic Finite Element Modelling

The capability to generate FE models quickly and accurately is still only available for the most simple of structures. The desire to keep models as simple as possible and the general design requirement for quick analysis times has led to the widespread use of shell/beam or shell models for the design of large industrial structures.

Further, for certain structures a hybrid model involving a combination of shells and solids is often used. One example of this is for a bladed turbine disk for which the disk is best modelled using solids and the blade is modelled using shells. However, with the recent growth in computer power and the development of automated meshing software, complete solid models are becoming more widely used for design.

In order to illustrate the different modelling methods, a generic turbine casing was generated using similar dimensions to those of the real turbine casing shown in Chapter 2. In this way, a direct comparison of the modelling methods could be obtained without the effects of the features—flange holes, scallops, casing holes and bosses—possibly causing misleading results. The effects of the features are investigated in detail in section 3.8 (Basic Detail Feature Modelling).

Although automated mesh generation using triangle shells or tetrahedron solids is becoming more widely used, a common practice in gas turbine companies for models of axisymmetric or cyclically symmetric structures is to generate first a 2-D cross-section model, spin or replicate the cross-section model about the axis of axisymmetry into a 3-D model and then add any asymmetric features. The process of spinning or replicating a cross-section model to obtain a 3-D model in general requires that elements from the quad shell or hexahedron families be used. Using this approach, a node for a beam in the 2-D cross-section model becomes a ring of beam nodes and elements in the 3-D model. Likewise, a 2-noded shell element in 2-D becomes a ring of 4-noded shell elements in 3-D and a 4-noded quad in 2-D becomes a ring of 8-noded solids in 3-D. If higher-order elements are to be used, the 4-noded shells or 8-noded solids can be subsequently converted to higher order by adding mid-side nodes to each element.

In order to show more detail, only the 2-D cross-section of the geometry and different models are shown. This is sufficient in this case since the structure being considered is an idealised turbine casing which is perfectly axisymmetric. Accordingly, each node and element in the 2-D cross-section models corresponds to a ring of nodes or elements in the 3-D models.

Figure 3.18 shows the cross-section of the geometry for the generic turbine engine casing. The casing is seen to be conical (increasing radius from forward to aft) with forward and aft flanges of different thicknesses and radii. The centre

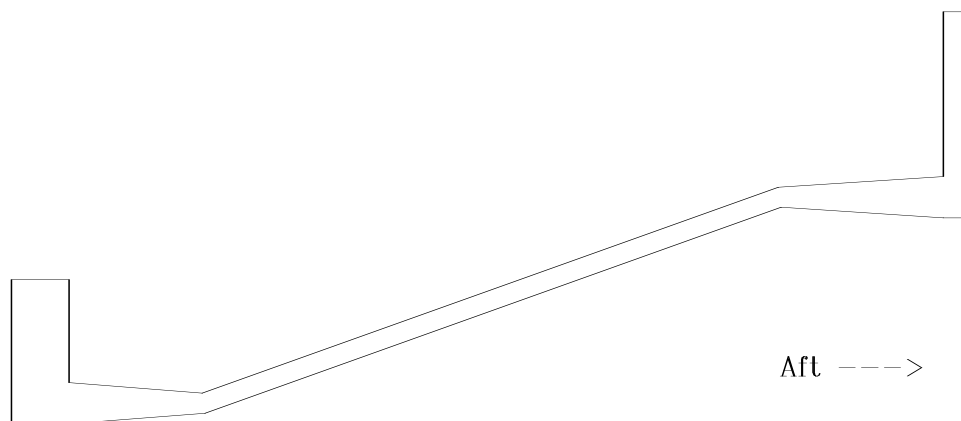


Figure 3.18: Cross-section of Generic Turbine Engine Casing

casing section has a constant thickness and connects to tapered sections at both its forward and aft ends.

The generic casing was modelled using the four element types—solids, hybrid, shells and shells/beams—discussed in section 3.4. Although two element orders are shown in Figure 3.16 for both shells and solids, the 4-noded quad and 20-noded hexahedron, respectively, were chosen for the forthcoming example. This is because MSC/NASTRAN was used for the FE analysis and therefore the mixed formulation 4-noded shell is of quadratic order in bending as is the 20-noded hexahedron solid. Building on the excellent results shown in Chapter 2 for using a detailed solid model to replace test data, the 20-noded solid model was used as the reference to which the other three model types were compared.

The FMAC introduced in Chapter 2 and presented in detail in Chapter 5 will again be used to compare the analytical predictions. The ability of the FMAC to display multiple correlations on a single plot will be used to good effect to illustrate the differences between the results from the four modelling methods.

3.7.1 Solid-Element Model

The cross-section of the hexahedron solid-element model for the turbine casing is shown in red in Figure 3.19. Since the solid model can represent the geometry exactly, the solid black lines for the geometry are hidden from view.

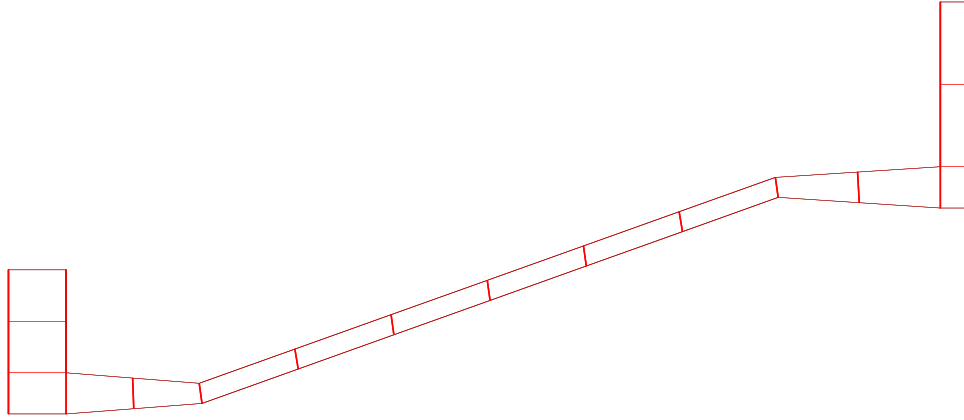


Figure 3.19: Cross-section of Solid Model for Generic Turbine Engine Casing

The cross-section model with 4 nodes per element contained 34 nodes and 16 elements which was then spun about the axis of symmetry with 72 elements in the circumferential direction. The 3-D, 8-noded, solid model was converted to a 20-noded solid model (by adding mid-side nodes to all elements) that contained 8,424 nodes, 1,152 elements and 25,272 DOFs. The commercial program MSC/NASTRAN was used to obtain the free-free natural frequencies and mode shapes for the first 20 modes.

3.7.2 Combined Shell and Solid-Element Model: Hybrid

The cross-section of the hybrid model for the turbine casing is shown in Figure 3.20. The geometry is shown by the solid black lines and the FE model by the red lines. The cross-section model contained 31 nodes and 16 elements which were then spun about the axis of symmetry with 72 nodes and 72 elements in the circumferential direction. The part of the model that was 8-noded solid hexahedrons (the flanges)

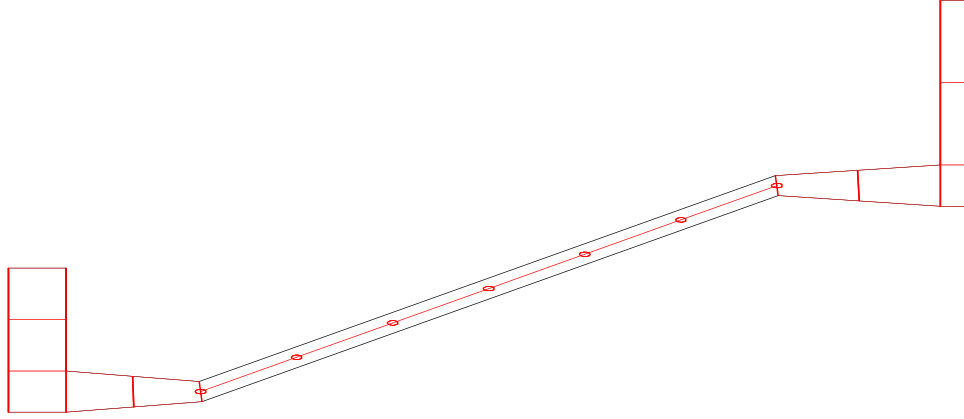


Figure 3.20: Cross-section of Hybrid Model for Generic Turbine Engine Casing

was again converted to 20-noded solids (by adding mid-side nodes to all elements). The result was a hybrid model, made of 4-noded shells and 20-noded solid hexahedrons. The 4-noded shell part of the model had 504 nodes, 432 elements and 2,520 DOFs. The 20-noded solid part of the model had 5,760 nodes, 720 elements and 17,280 DOFs. Accordingly, the model totals were 6,264 nodes, 1152 elements and 19,800 DOFs. The shell element part of the model was attached to the solid element part with constraint elements between the shell nodes which were coincident with the faces of solid elements. The commercial program MSC/NASTRAN was used to determine the free-free natural frequencies and corresponding mode shapes for the first 20 modes.

The correlation for the hybrid model compared to the reference 20-noded solid model is shown in the FMAC plot in Figure 3.21. The black circles are for the auto-MAC of the reference model and the red circles are for the hybrid model. The figure shows excellent correlation between the hybrid and reference model with MAC values very close to a perfect value of 1.0 and very consistent natural frequency differences between about -1.5% and +1.0%.

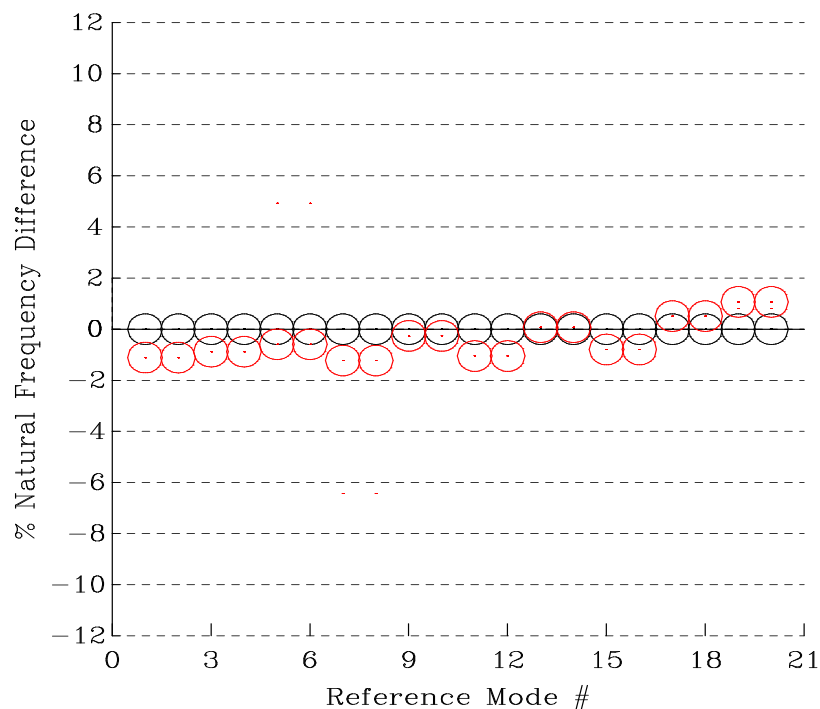


Figure 3.21: FMAC for Hybrid Model of Generic Turbine Engine Casing

3.7.3 Shell-Element Model

The cross-section of the shell model for the turbine casing is shown in Figure 3.22. The cross-section model contained 15 nodes and 14 elements which were then spun about the axis of symmetry with 72 nodes and 72 elements in the circumferential direction. The result was a 4-noded shell element model with 1,080 nodes, 1,008 elements and 5,400 DOFs. The commercial program MSC/NASTRAN was used to determine the free-free natural frequencies and corresponding mode shapes for the first 20 modes.

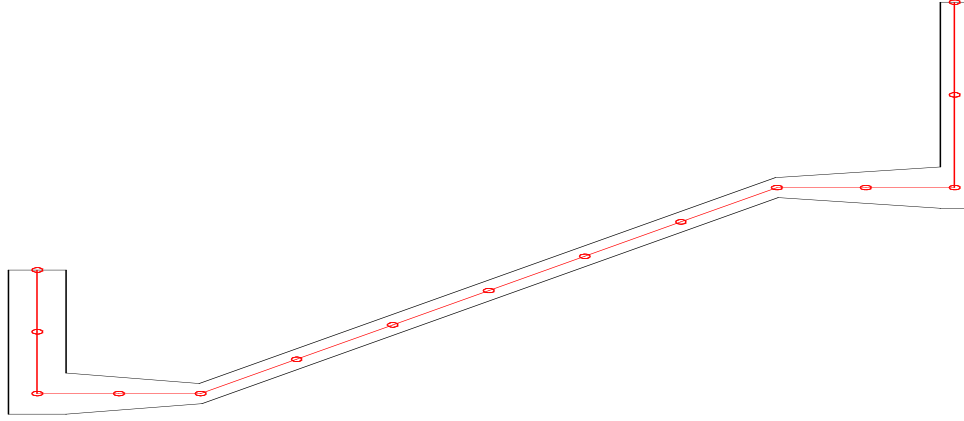


Figure 3.22: Cross-section of Shell Model for Generic Turbine Engine Casing

The correlation for both the shell and the hybrid models is shown in the FMAC plot in Figure 3.23. The black circles are for the auto-MAC of the 20-noded solid

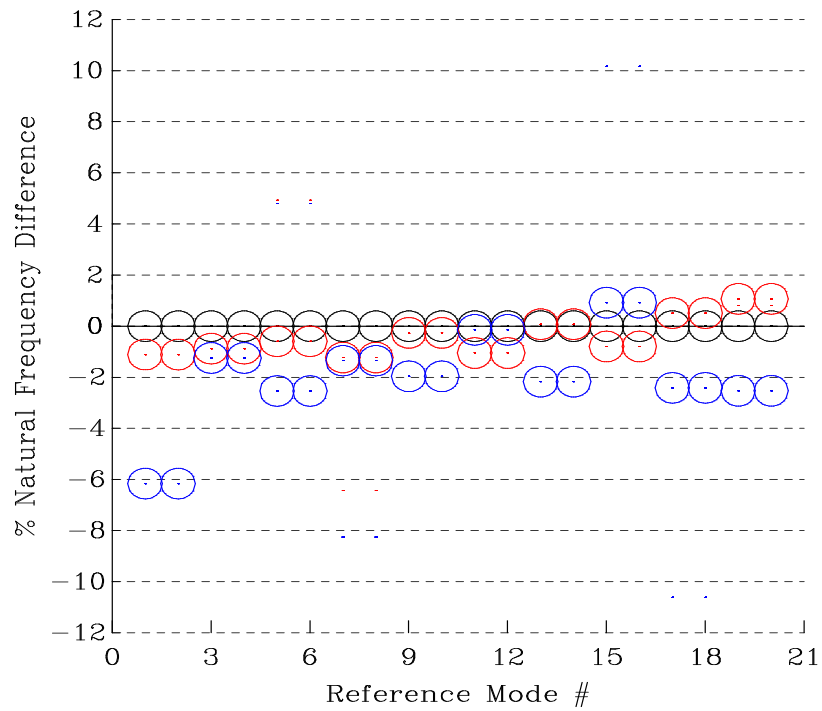


Figure 3.23: FMAC for Shell and Hybrid Models of Generic Turbine Engine Casing

reference model, the red circles are for the hybrid model and the blue circles are

for the shell model. The figure shows that the shell model did not correlate as well as the hybrid model with MAC values very close to 1.0, but with natural frequency differences between about -6% and +1%. However, except for the first two reference modes, the natural frequency differences are relatively consistent with a variation between about -2.5% and +1%.

3.7.4 Combined Beam and Shell-Element Model

The cross-section of the shell/beam model for the turbine casing is shown in Figure 3.24. The geometry is shown by the solid black lines and the FE model by the red and blue lines. The beam elements for both the forward and aft flanges were generated using nodes from the shell elements. The ability to offset the beam's centroid from the geometry was used. This is shown by the blue lines which connect the beam centroid at the blue circle to the shell/beam shared node. In this way the beam geometry is along the shell nodes but the stiffness and inertia properties are determined about the centroid with a rigid link between the two.

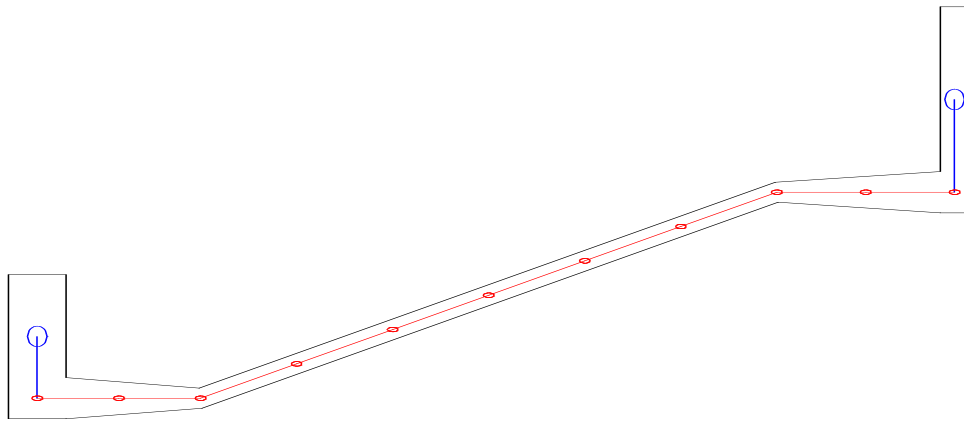


Figure 3.24: Cross-section of Shell/Beam Model for Generic Turbine Engine Casing

The cross-section model contained 11 nodes and 12 elements which were then spun about the axis of symmetry with 72 nodes and 72 elements in the circumferential direction. The result was a 4-noded shell/beam element model with 792

nodes, 864 elements and 4,104 DOFs. The commercial program MSC/NASTRAN was used to determine the free-free natural frequencies and corresponding mode shapes for the first 20 modes.

The correlation for the shell/beam, shell and hybrid models with the reference solid model is shown in the FMAC plot in Figure 3.25. The black circles are for

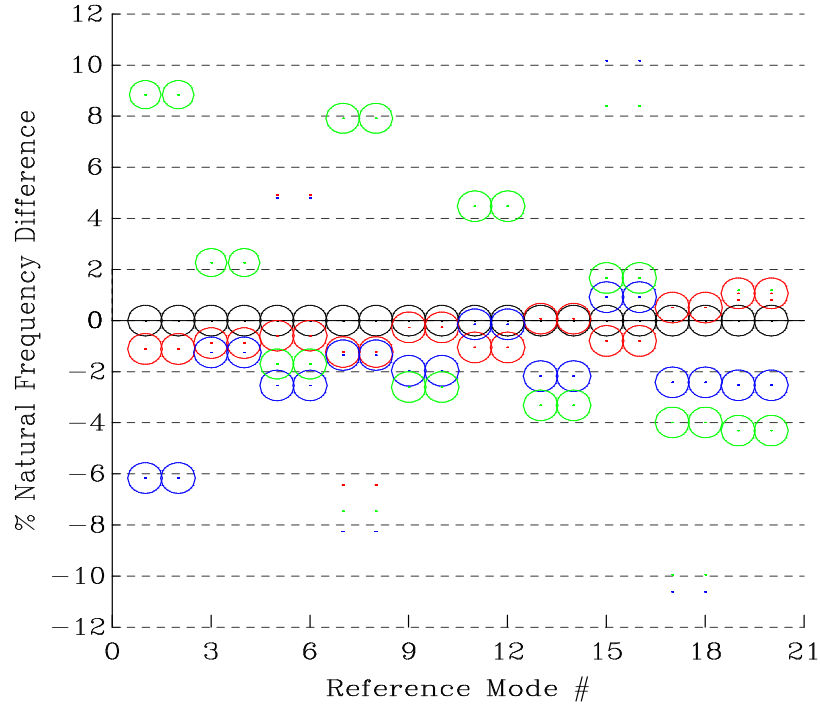


Figure 3.25: FMAC plot for Shell/Beam, Shell and Hybrid Models for Turbine Engine Casing

the auto-MAC of the reference model, the red circles are for the hybrid model, the blue circles are for the shell model and the green circles are for the shell/beam model. The figure shows that the shell/beam model did not correlate (with the solid model taken as reference) as well as either the shell or the hybrid models with MAC values very close to 1.0, but with natural frequency differences of between about -4% and +9%. Note how the natural frequency difference varies from mode to mode by more than 9% in some cases, such as from mode 6 to mode 7.

3.8 Basic Detail Feature Modelling

The modelling of the various geometric features present in industrial structures is significantly more challenging when using shell and/or beam elements than when using solid elements. This is because shell and beam elements cannot fully represent certain 3-D geometries, thereby requiring the analyst to make approximations to the geometry in the model configuration. In contrast, when using 3-D elements, there are in general no such geometric approximations to be made. There are occasions when using 3-D elements that one would use geometric approximations. For example, if the structure contained one or more very small fillets which, if modelled accurately, would yield an extremely large model for relatively little gain in modal data accuracy.

Although shell and/or beam models can only approximate certain 3-D sections, analysts have learned to use them with good success and have been doing so for many years. This is particularly evident in the gas turbine engine companies for whole engine models (WEMs) [31], the aircraft companies for airplane fuselage models [32] and the automotive industry for models of automobile bodies [33]. Even with the extrapolated growth of computer power, it is envisaged that the shell and/or beam models will remain in use for design at least until 2005, or beyond.

The modelling of the basic features is presented for the non-rotating components of gas turbine engines. However, it is envisaged that the techniques shown can be generalized for application to many other industrial structures. For example, there are flanges, holes and sometimes scallops at the perimeter of the different sections of an automobile body so that it can be assembled. Likewise, an aircraft fuselage consists of a long cylindrical casing with many circumferential reinforcing ribs that are not unlike a flange or channel.

Five basic features were considered in this study: (1) flanges, (2) channels, (3) holes, (4) scallops and (5) bosses. The first two features—flanges and channels—

were modelled using three of the four modelling methods—solids, shells and shells/beams—demonstrated in section 3.7. The last three features—scallops, holes and bosses—were modelled using shells and solids only, since beam elements cannot adequately represent such features. The hybrid method was omitted because it is generally used to characterise structures in which the features are modelled with solids and the rest of the structure with shells. The basic feature models may be combined to obtain more complex models—for example: bosses with holes, a channel with holes or a scalloped flange with holes. While the following sections present the modelling techniques for the different features, a numerical study on how the different features effect the modal characteristics of a structure is presented in Chapter 6.

3.8.1 Flanges

Flanges are used to attach adjacent engine casings together which is usually done by using bolts through holes in each of the mating flanges. Figure 3.26 shows the cross-section for three basic types of flange geometry: (1) simple or straight, (2) external spigot and (3) internal spigot. The dashed lines show the location of the bolt holes.

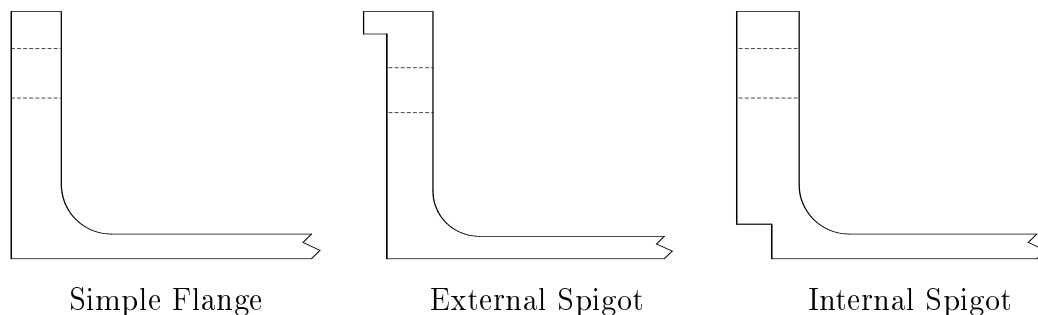


Figure 3.26: Cross-section of Geometry for Three Basic Flanges

3.8.1.1 Solid-Element Models

The solid-element models for the cross-section of the three flange types are shown in Figure 3.27. The geometry is shown in each case by the black lines and the FE models by the red lines. The red circles for the nodes at the corners of each element have been omitted since the corners are clearly visible. The element edges that form the bolt hole are shown with red dashed lines.

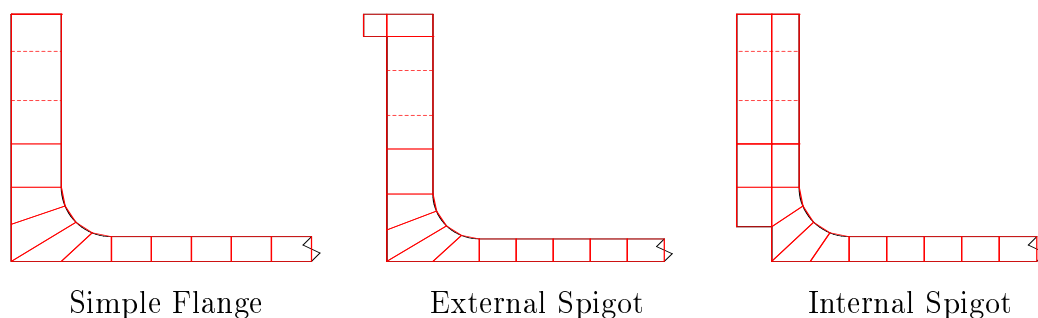


Figure 3.27: Solid FE Models for the Three Basic Flanges

The figure shows that the models include the fillet between the flange and the casing. However, it can be seen that the model geometry is not perfect in that only 5 nodes are used to represent the continuous fillet geometry. The meshes are very uniform (nearly equal-sized elements) with low aspect ratios and minimal distortion for all elements. With the mesh density used and the fillet included, the models are more representative of a detailed design model than either a preliminary design or a final design model.

3.8.1.2 Shell-Element Models

The shell models for the cross-sections of the three flange types are shown in Figure 3.28. The geometry is shown in each case by the black lines and the FE models by the red and blue lines with red and blue circles for the node locations.

The figure shows that for the simple flange and external spigot cases the shell model was generated by placing nodes along the mean-line of the flange and casing.

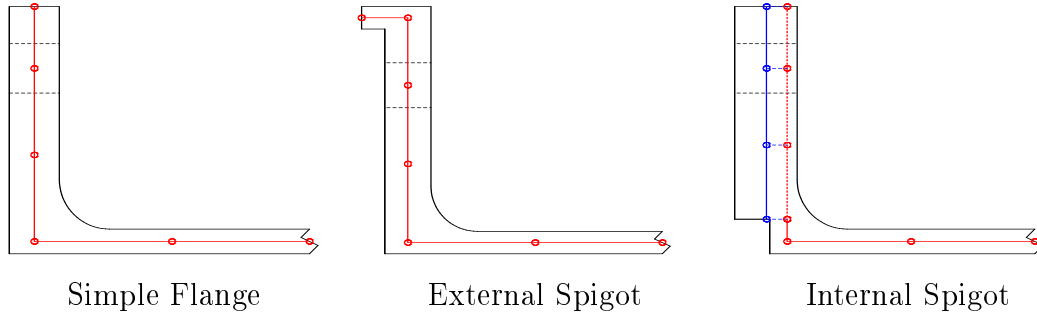


Figure 3.28: Shell FE Models for the Three Basic Flanges

The node or element thicknesses were selected by the geometric dimension normal to the shell node or element. Note that for both models a node was placed at the bolt hole centre in anticipation of connecting to an adjacent casing.

The shell model for the internal spigot was generated in a similar way, as shown in Figure 3.28. However, the nodes for the flange, shown by the red circles, were placed where the mean-line would be if the extra material for the internal spigot were removed. The top three elements that form the part of the flange with the extra material were offset to the correct mean-line of the flange which is shown by the blue lines and circles. This approach allows for the correct spatial placement of the stiffness and inertia for the flange. Further, if the nodes (red circles) were placed at the correct mean-line of the flange (blue circles), then the element where the flange meets the case would have a geometry which is not physically representative of the true geometry. Note again that a node was placed at the bolt hole centre for future connection to an adjacent casing.

3.8.1.3 Combined Beam and Shell-Element Models

Three different approaches were considered for modelling the three types of basic flange using the shell/beam method. The primary differences between the three approaches are: (i) where the node for the beam is located and (ii) whether a rigid element is required to attach the beam to the shell. However, they are math-

ematically equivalent and the choice of one over the other is a matter of analyst preference.

The shell/beam-element models for the cross-sections of the three flange types are shown in Figure 3.29 for the first approach. The geometry is shown in each case by the black lines and the FE models by the red and blue lines with circles at the node locations. The location of the beam centroid is shown by the large blue cross-hatched circle. In this approach, the beam element for the flange is generated using a node from a shell element and the ability to offset the centroid of the beam from the geometry is used. Accordingly, the beam geometry is at the shell node but the stiffness and inertia properties are determined about the centroid with an internal rigid link (supplied by the FE program as opposed to user-supplied) between the two.

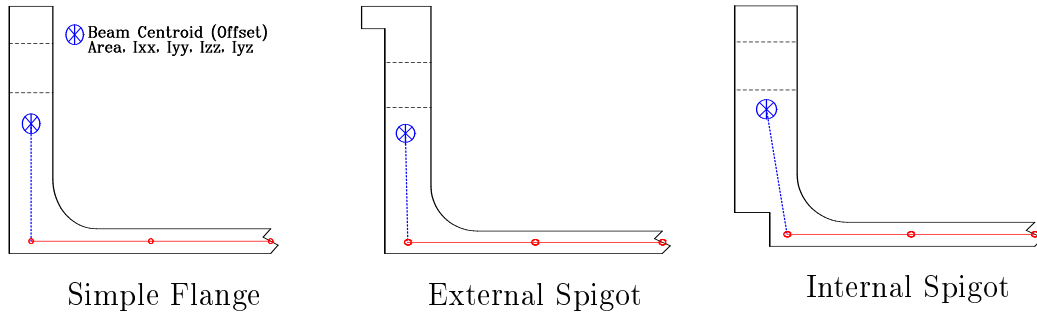


Figure 3.29: Shell/Beam FE Models for the Three Basic Flanges: Approach 1

For the second approach the shell/beam-element models for the cross-sections of the three flange types are shown in Figure 3.30. The location of the beam centroid is shown by the large blue cross-hatched circle and the nodes (shell or beam) are shown by the red circles. This approach uses a distinct node for the beam element located at the beam centroid which is attached to the appropriate shell node on the engine casing using a rigid element. Accordingly, the beam geometry, stiffness and inertia properties are defined at the node located at the beam centroid.

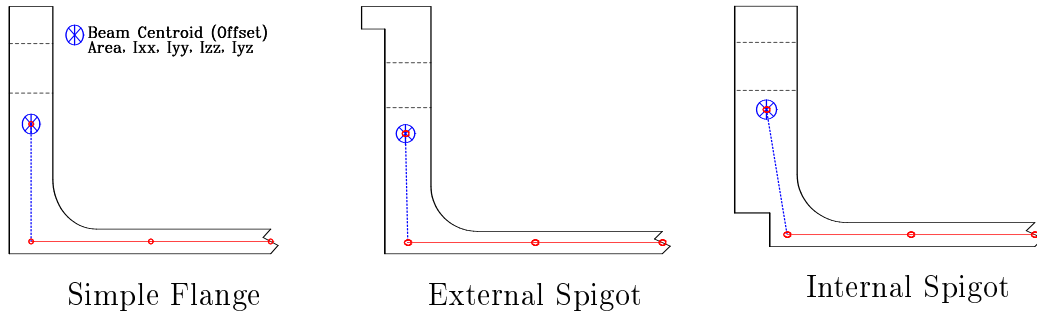


Figure 3.30: Shell/Beam FE Models for the Three Basic Flanges: Approach 2

The shell/beam-element models for the cross-sections of the three flange types are shown in Figure 3.31 for the third approach. This approach uses a distinct node for the beam element located at the bolt hole centre. The offset capability is used so that the stiffness and inertia properties are defined at the beam centroid while the geometry is at the node at the centre of the bolt circle. The FE program supplies the internal rigid link between the beam centroid and the node at the bolt hole centre, whereas the user supplies a rigid element to attach the beam node to the appropriate shell node on the engine casing.

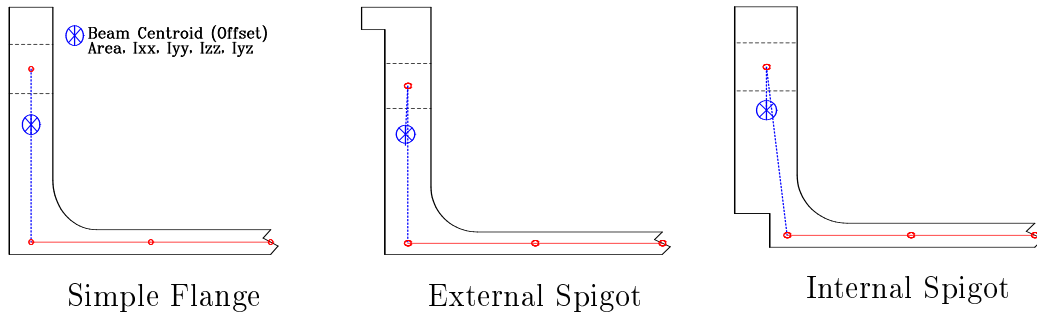


Figure 3.31: Shell/Beam FE Models for the Three Basic Flanges: Approach 3

The third approach is preferred for modelling components of an assembly so that nodes can be placed at the bolt holes for attaching to the adjacent casing. This is important since if one of the first two methods were used the attachment could not be made at the correct location which could produce misleading results.

3.8.2 Channels

Some of the uses for channels are to stiffen casings, to hold a row of turbine vanes in place and to provide a place to attach external structures. Figure 3.32 shows the cross-section for three basic types of channel geometries: (1) simple channel, (2) C or fish-mouth and (3) under-flange. The dashed lines show the location of the bolt holes for the under-flange channel.

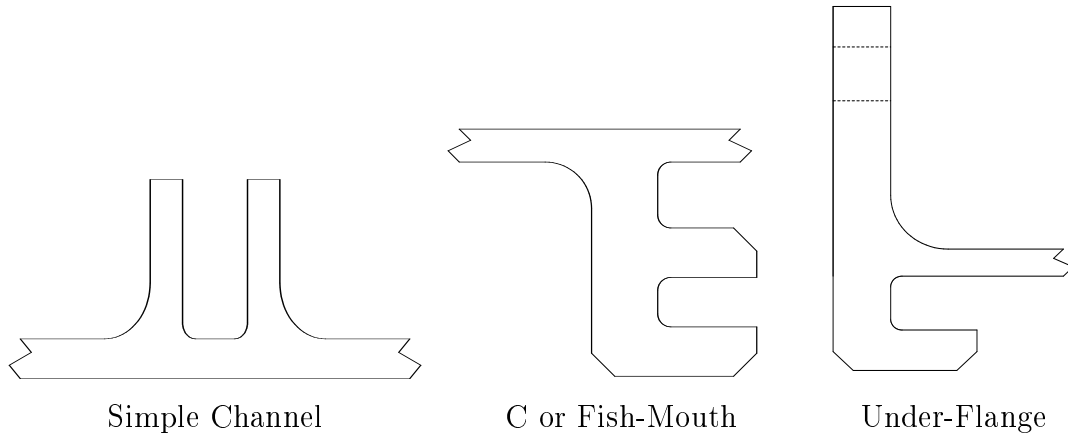


Figure 3.32: Cross-sections of Geometry for Three Basic Channels

3.8.2.1 Solid-Element Models

The solid models for the cross-sections of the three channel types are shown in Figure 3.33. The geometry is shown by the black lines and the FE models by the red lines. The red circles for the nodes at the corners of each element have been omitted since the corners are clearly visible. The element edges that form the bolt hole for the under-flange channel are shown with red dashed lines.

The figure shows that the models include the larger fillets between the channels and casings but that the smaller fillets have been omitted. However, the chamfers or bevels have been modelled. The model geometry for the larger fillets is not perfect in that only 3 nodes are used to represent them. The meshes are reasonably uniform, except in the fillet regions, with low aspect ratios and minimal distortion

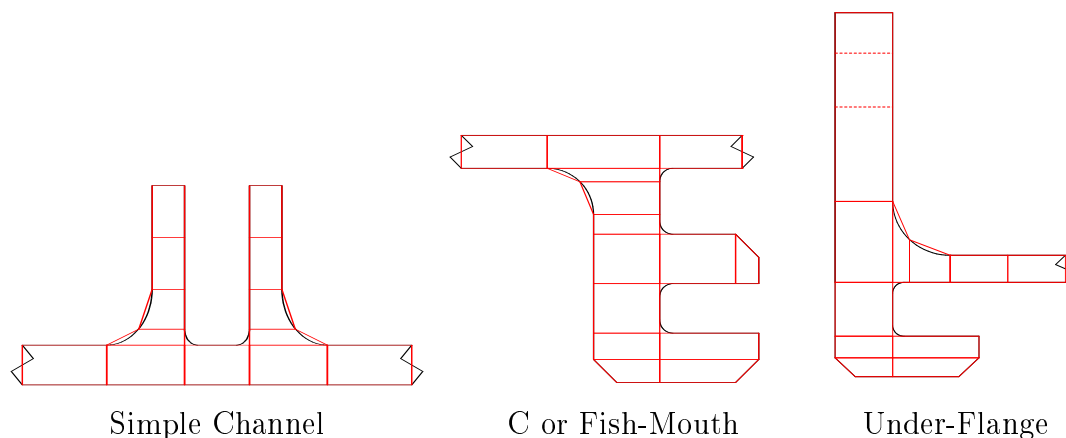


Figure 3.33: Solid FE Models for the Three Basic Channels

for all elements. With the mesh density used and the larger fillets included the models are more representative of a detailed design than a preliminary design model. However, they could also be used as a basis for a final design model. A final design model that included the smaller fillets would demand a much finer model and might be prohibitively expensive.

3.8.2.2 Shell-Element Models

The shell models for the cross-sections of the three channel types are shown in Figure 3.34. The geometry is shown by the black lines and the FE models by the red lines with red circles at the node locations.

The figure shows that the shell models were generated by placing nodes along the mean-line of each channel and casing. The node or element thicknesses were selected by the geometric dimension normal to the shell node or element. Note that for the under-flange model a node was placed at the bolt hole centre in anticipation of connecting to an adjacent casing.

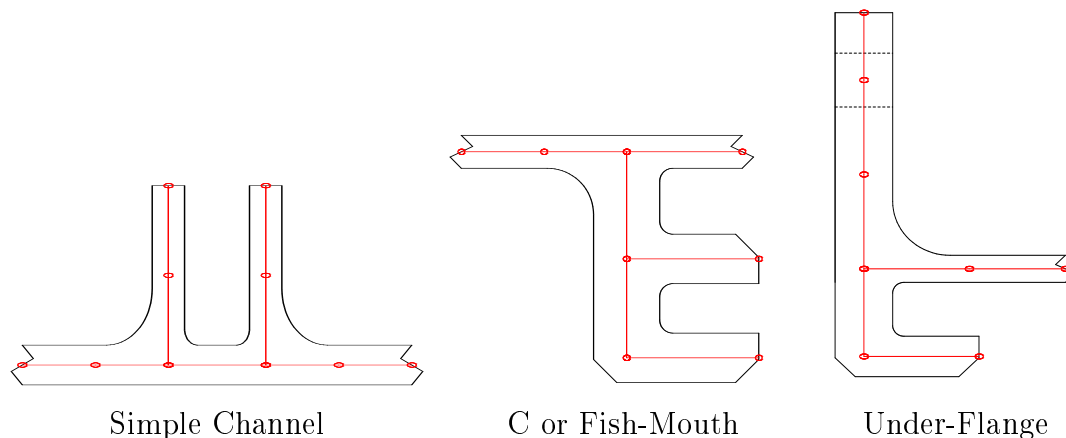


Figure 3.34: Shell FE Models for the Three Basic Channels

3.8.2.3 Combined Beam and Shell-Element Models

The shell/beam-element models for the cross-sections of the three channel types are shown in Figure 3.35. The geometry is shown by the black lines and the FE models by the red and blue lines. The location of the beam centroid is shown by the large blue cross-hatched circle and the shell nodes are shown by the red circles.

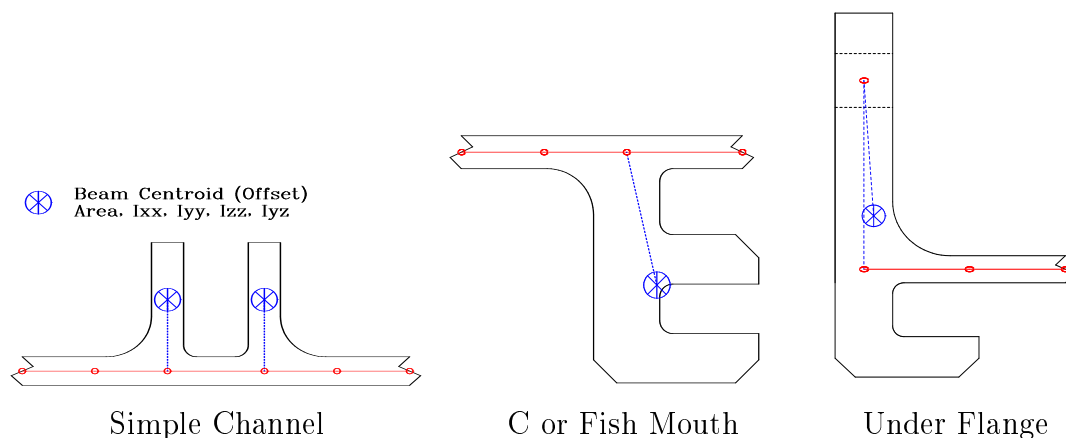


Figure 3.35: Shell/Beam FE Models for the Three Basic Channels

The casing part of the models were generated using shell elements by placing nodes along the mean-line. The node or element thicknesses were selected by the geometric dimension normal to the shell node or element. For the first two

models—simple channel and C—the beam elements for the channels were generated using a node from a shell element and the ability to offset the centroid of the beam from the geometry. Accordingly, the beam geometry is at the shell node but the stiffness and inertia properties are determined about the centroid with an internal (supplied by the FE program as apposed to user supplied) rigid link between the two. This was referred to as approach 1 in section 3.8.1.

The under-flange channel was modelled using a distinct node for the bolt hole centre with a rigid element connection to the appropriate shell node. The centroid was offset from the node at the bolt centre to the proper location. In this way the connection to an adjacent casing can be made at the bolt hole or correct location. This was referred to as approach 3 in section 3.8.1.

3.8.3 Scallops

The term scallop, as used here, refers to a structural feature that is discontinuous, and which for gas turbine engines, is usually in the circumferential direction. There are three primary uses for scallops: (1) to reduce weight, (2) to control motion such as restricting mating parts from relative rotation and (3) for load transmission like gear or spline teeth. Some basic scallop geometries are shown in Figure 3.36 with both cross-section and axial (looking along the engine axis) views. The dashed

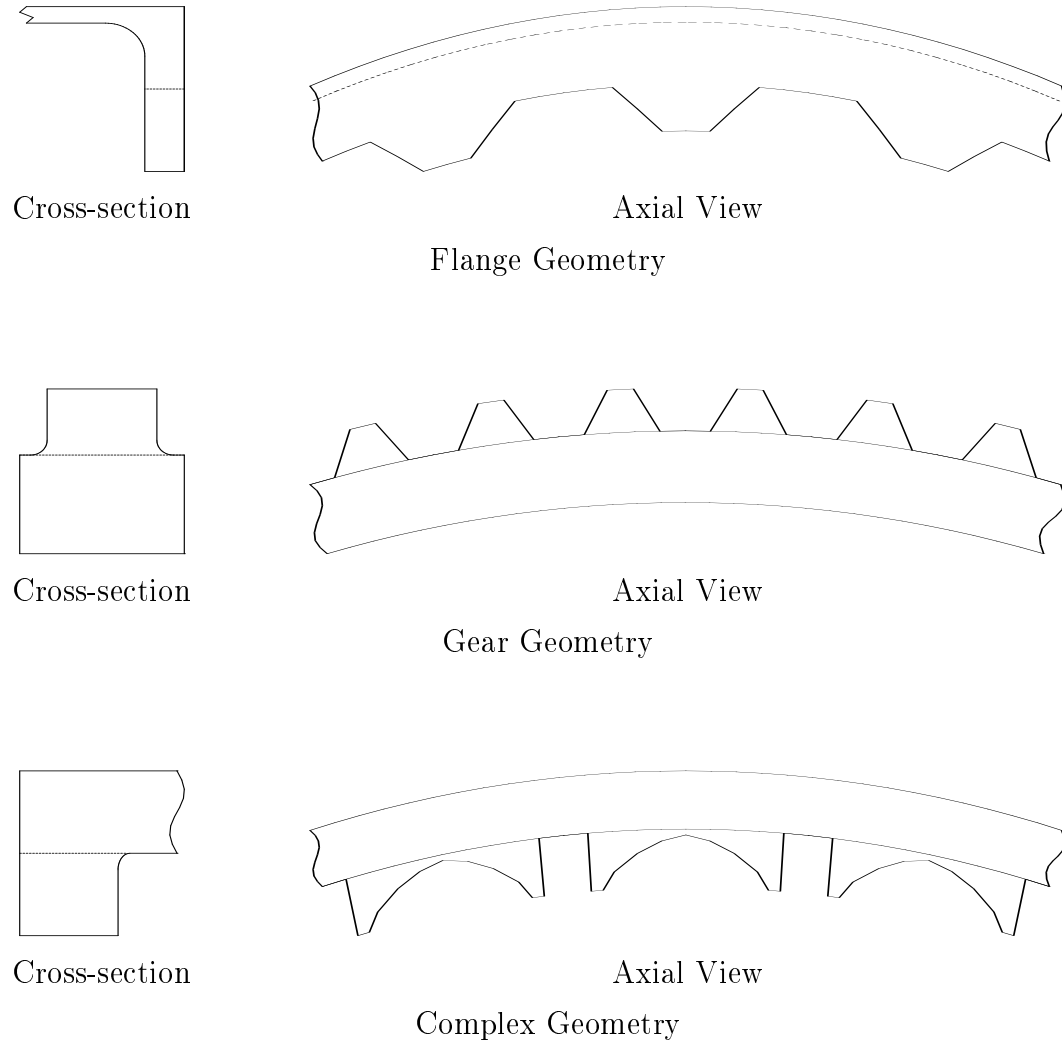


Figure 3.36: Geometry for some Basic Scallops

lines in the cross-section views show the location of the scallops whereas the axial views show the shape of the scallops in the circumferential direction.

Unless a very detailed solid model is being constructed, it is often the case that scallops are omitted from the model. This is especially true for the case of shell/beam-or shell-element models, since some scallops, such as the second and third examples in the above figure, cannot be adequately represented. However, the flange is relatively thin in one dimension compared with its other two dimensions, as shown by the cross-section, and therefore may be adequately modelled using

shell elements. The dimensions for the second and third examples are of similar magnitude in all three directions and therefore solid elements should be used. Accordingly, the first scallop example, for the flange, was modelled with shell elements and the second and third examples were modelled with solid elements. Instead of 3-D views of the 3-D models, which can inadvertently hide details, the models will be shown in 2-D with both a cross-section and axial view like the geometry was in Figure 3.36.

Figure 3.37 shows the 4-noded shell-element FE model for the scalloped flange. The cross-section view shows that the model was generated in the conventional way by selecting nodes and elements along the mean-line of the geometry. The thicknesses were selected by determining the geometric dimension normal to the shell at each node location (see section 3.5). The axial view shows how the cross-section model was spun or replicated in the circumferential direction to represent the geometry of the scallops.

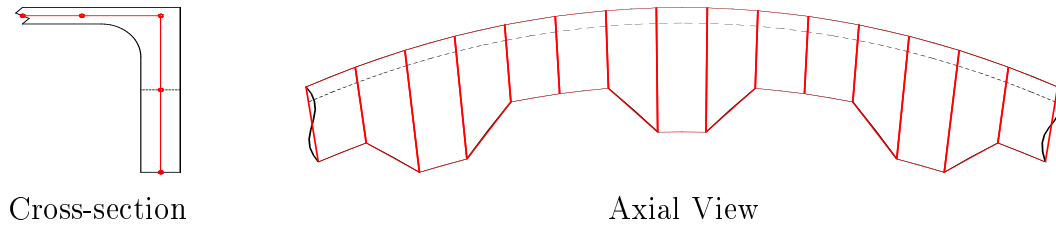


Figure 3.37: Shell FE Model for the Scalloped Flange

The hexahedron solid FE model for the gear is shown in Figure 3.38. The cross-section view shows that the fillets were modelled with 3 nodes and 2 elements which is consistent with the level of detail for a detailed design model. The axial view shows how the cross-section model was spun or replicated in the circumferential direction to represent the geometry of the gear teeth or scallops. Note that including the fillets required the teeth elements to be divided into two parts (axial view) in order to keep the aspect ratios reasonable (less than 10 at the base of the fillet). One could envisage that increasing the detail in the model of the fillet, to say 5 points, would lead to a much finer mesh in order to keep the aspect ratios of the

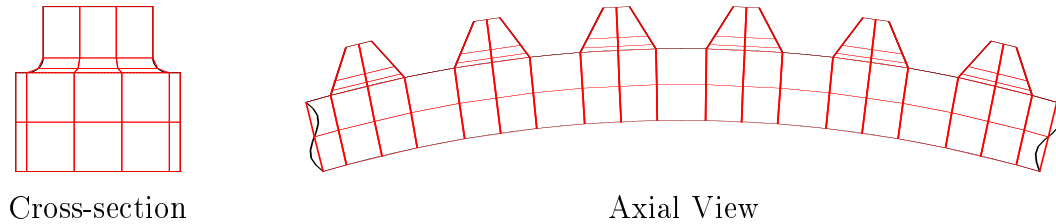


Figure 3.38: Solid FE Model for the Gear

fillet elements below 10 or so.

Figure 3.39 shows the hexahedron solid FE model for the complex scallop shape. The cross-section view shows that in this case the fillet was not modelled. The axial view shows how the cross-section model was spun or replicated in the circumferential direction to represent the complex geometry of the scallops. The fillet was

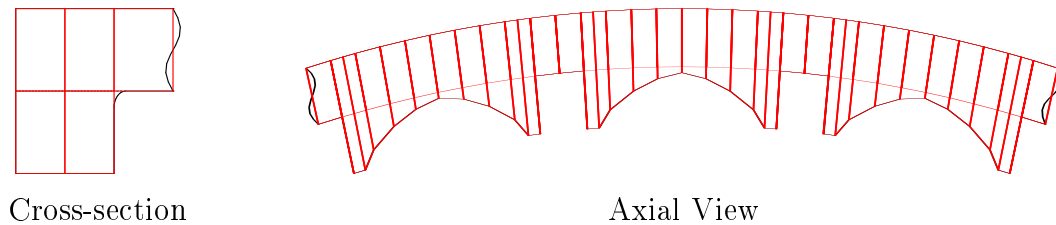


Figure 3.39: Solid FE Model for the Complex Scallop

omitted because the complex shape of the scallop in the circumferential direction would require an extremely fine mesh near the peak of each arch. However, with the amount of detail for the scallops, this model would still be considered a detailed design model.

3.8.4 Holes

Some of the many different uses for holes in structures are: (1) flange holes for attaching to adjacent structures using bolts, (2) threaded or tapped holes in bosses for mounting external components and (3) casing holes to allow internal access. For gas turbine engines there are many applications for casing holes, some of which are: (1) piping for fuel, oil or bleed air, (2) access to the flow-path for temperature

and pressure sensors and (3) access to different parts of the engine to assess internal damage using a small camera (borescope).

Figure 3.40 shows the geometry for some basic holes with both cross-section and top (looking through the hole) views. The figure shows three basic hole types: (1) a basic casing hole, (2) a counter-sunk or chamfered hole and (3) a tapped hole for a bolt (with the threads omitted).

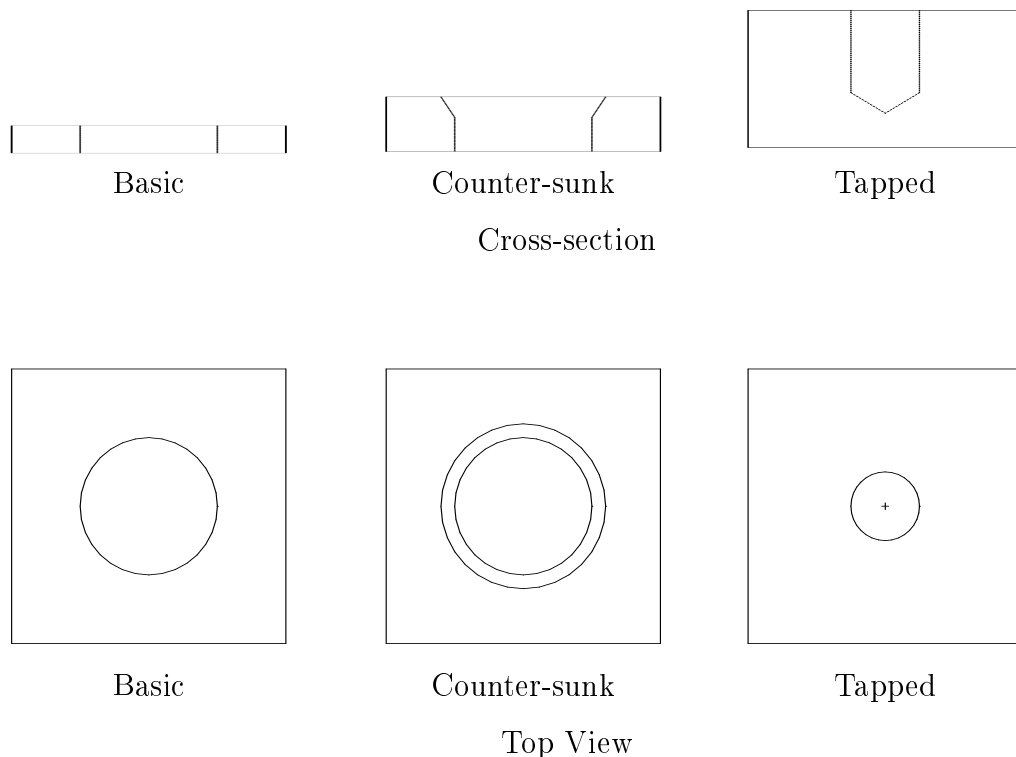


Figure 3.40: Geometry for some Basic Holes

As for the scallops, unless a very detailed solid model is being constructed, it is often the case that holes are omitted from the model. This is especially the case for shell/beam or shell models. If the holes are to be included in the model then one must decide how much detail is required for each hole.

Figure 3.41 shows a top view of three models, using 4-noded elements, for a basic casing hole with different mesh densities. The first mesh has 4 nodes around the hole perimeter (square hole) and 8 total nodes, the second has 8 nodes around

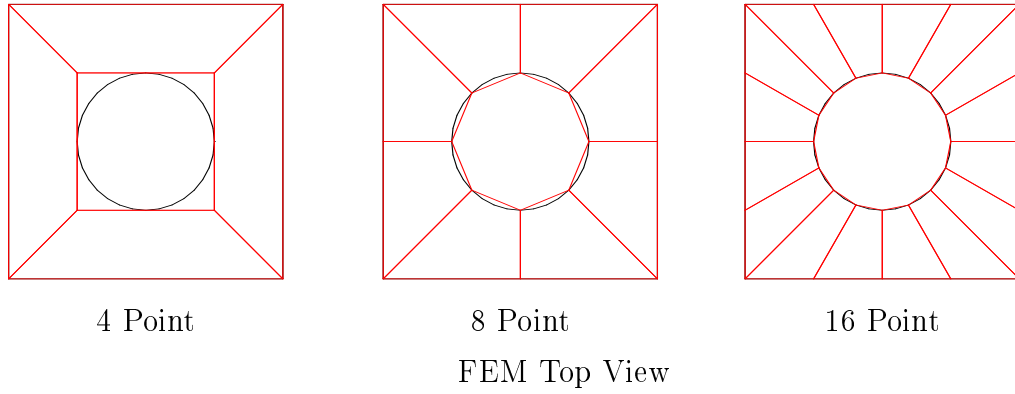


Figure 3.41: Three Mesh Densities for a Basic Hole

the hole perimeter with 16 total nodes and the third has 16 nodes around the hole perimeter and 32 total nodes. In most cases a mesh like the second example will suffice, even for a final design model, whereas a mesh like the third example is rarely required for vibration analysis. If the holes are small compared with the surrounding structure it is often found that a mesh like the first example (square hole) will produce accurate modal data. This is because, as the holes become small compared with the surrounding structure, the stiffness and mass effects become more localised and therefore have less effect on the modes of the much larger structure.

The second mesh density—8 nodes around the hole perimeter—was selected for the models of each hole type. The basic casing hole was modelled with 4-noded shell elements whereas the more complex shapes for both the conuter-sunk and tapped holes required solid elements for which hexahedrons were chosen. In order to show more detail, the 3-D models will be shown in 2-D with both a cross-section and a top view like the geometry was in Figure 3.40.

Figure 3.42 shows the FE models for the three basic hole geometries. The geometry is shown by the black lines and the FE models by the red lines. The cross-section models for each hole geometry are shown at the top of the figure and the top view of the models are shown at the bottom of the figure.

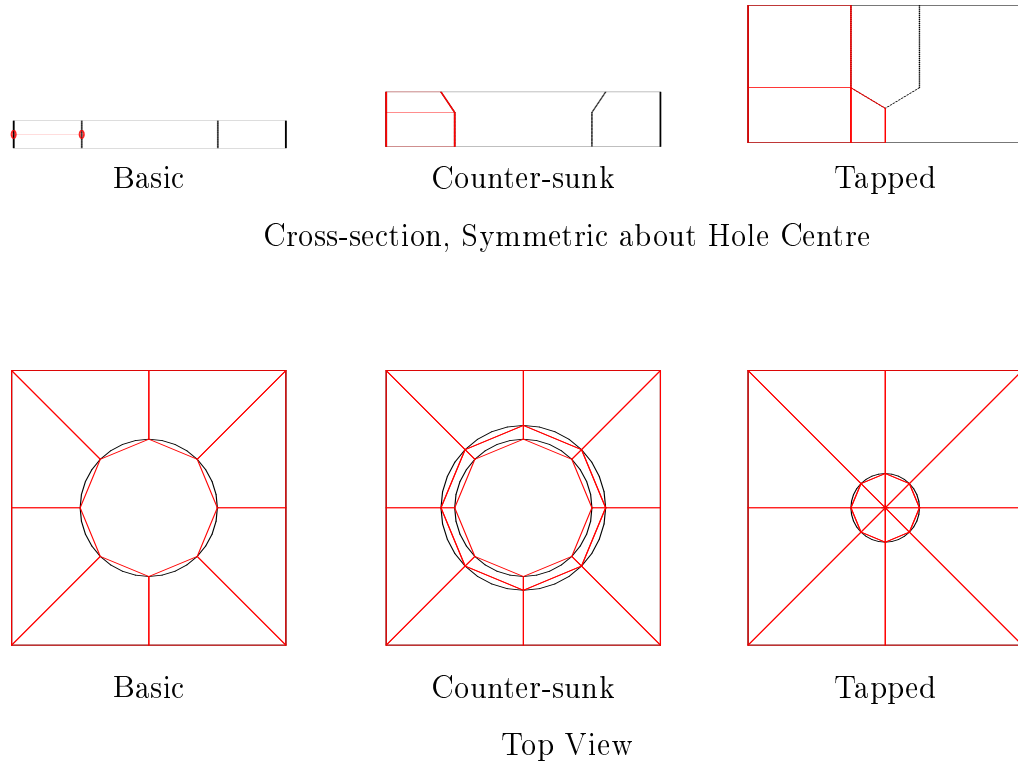


Figure 3.42: FE Models for the Basic Holes

The symmetry of each geometry was used by first modelling the part of each cross-section that is symmetric about the hole centre. This is shown at the top of the Figure by the red lines for each hole geometry. The cross-section models were then spun or replicated about their respective hole centres with 8 nodes and 8 elements around the hole perimeter. The resulting 3-D models are shown in red with a top view at the bottom of the figure. Note that the hexahedron solid elements for the bottom of the tapped hole are now wedge shaped (a hexahedron with two coincident edges). The hexahedron element formulations in most commercial FE programs accept wedge shaped elements as a special case.

3.8.5 Bosses

Bosses are used to provide an interface to attach other components to a structure. They provide three primary functions: (1) a receptive geometry for the mating component, (2) a means of attachment (usually tapped bolt holes) and (3) sufficient load carrying capacity for the mass of the component to be attached. For these reasons bosses are usually about 3 to 5 times thicker than the structure surrounding them.

Figure 3.43 shows both a cross-section view and a top view for two types of basic bosses. The first is a conventional mount pad for attaching accessories and the second is a basic pipe attachment.

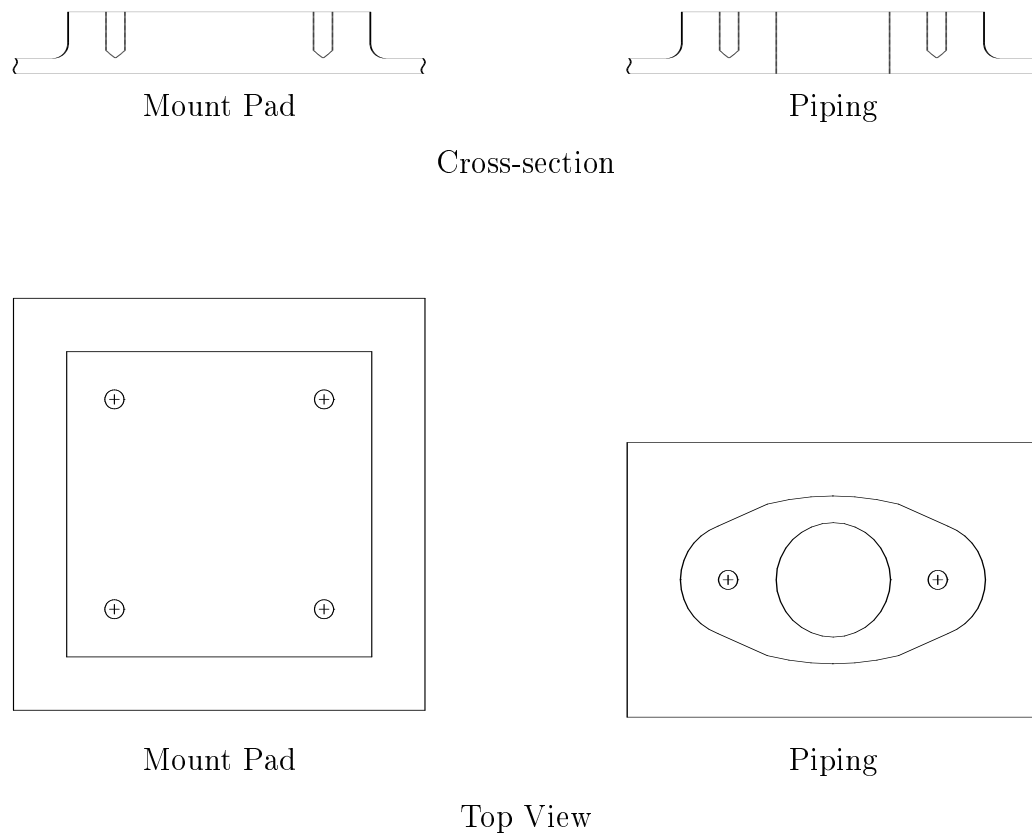


Figure 3.43: Two Types of Basic Bosses

It is often the case that bosses are omitted from the model, unless a very de-

tailed solid model is being constructed. This is especially the case for shell/beam- or shell-element models since bosses cannot, in general, be adequately represented. However, for some bosses, like the first example in Figure 3.43, reasonable results may be obtained using a shell model. Accordingly, the mount pad was modelled with 4-noded shell elements whereas the more complex shape for the pipe attachment required solid elements for which hexahedrons were chosen. The 3-D models will be shown in 2-D with both a cross-section and a top view like the geometry was in Figure 3.43.

Figure 3.44 shows the FE models for the two basic boss geometries. The left

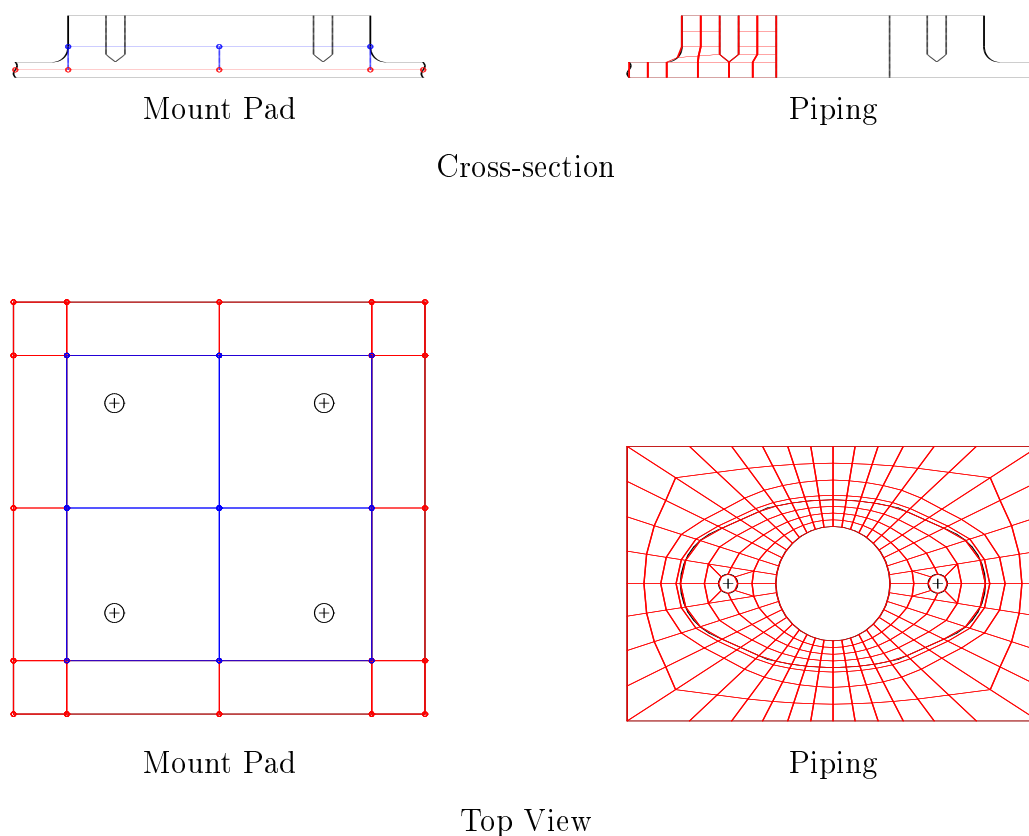


Figure 3.44: FE Models for Two Types of Basic Bosses

hand side of the figure shows that the 4-noded shell FE model for the mount pad boss was generated with nodes along the mean-line of the casing, shown in red,

and with offsets for the nodes corresponding to the boss, shown in blue. This allows for the stiffness and mass to be defined at the proper centroid of the boss. The thicknesses were selected in accordance with section 3.5—using the casing dimension normal to the shell for the casing elements and boss dimension normal to the shell for the boss elements. This model approximates the geometry by ignoring the fillets and tapped holes.

The right hand side of Figure 3.44 shows a very detailed hexahedron solid model for the piping boss which incorporates both the fillets, tapped holes and centre hole. There were 3 nodes along the fillet radii, 8 nodes around the perimeter of the tapped holes and 40 nodes around the centre hole perimeter. Note the significant number of nodes and elements required to model the geometry of the various features. The model contained 766 nodes and 512 elements of which 16 of the elements (at the bottom of the tapped holes) were wedge shaped (a hexahedron solid with two coincident edges). A typical application for say a combustor casing with 8 fuel nozzles would require 8 bosses. Accordingly, using a boss model of this size, the bosses alone would require 6,128 nodes and therefore 18,384 DOFs. The piping boss model has sufficient detail to classify it as a final design model.

If a model with significantly less DOFs were required—say, for an assembly of several components that was to include a reasonable model for the bosses—then an approximate or coarse model like the one shown in Figure 3.45 could be generated. In order to reduce the DOFs from the detailed model for the piping boss, the fillets

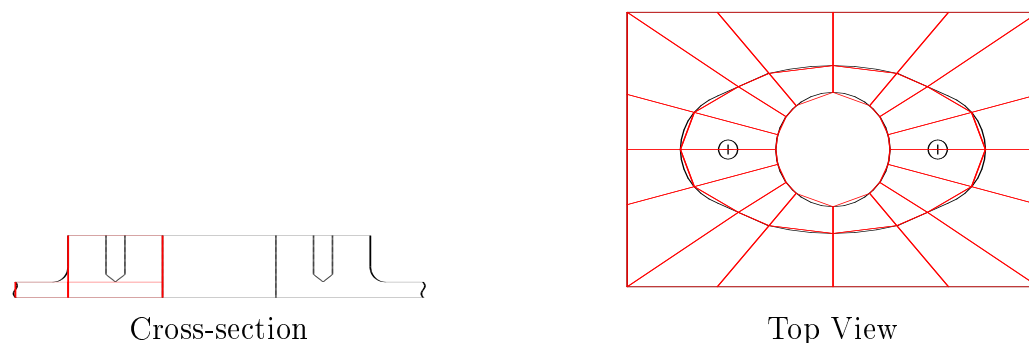


Figure 3.45: Coarse FE Model for Piping Boss

and tapped holes were omitted. However, the primary features—the elliptical boss shape and the centre hole—were retained and modelled with 16 nodes around their respective perimeters. The coarse model for the piping boss contained 128 nodes whereas the detailed model contained 766 nodes, resulting in the coarse model being about 17% of the size of the detailed model. The figure shows that the primary aspects of the geometry—the elliptical boss shape and centre hole—are still reasonably approximated with the reduced mesh.

3.9 Closing Remarks

The fundamentals of finite element modelling for structural dynamic design have been described in a concise and somewhat chronological fashion with emphasis on the practical aspects of modelling and particular relevance to a class of structure found in gas turbines and other machines. At first glance, the number and complexity of the tasks involved in obtaining a sufficiently accurate and robust FE model may seem overwhelming. However, the majority of the tasks have evolved to a state of at least moderate automation. Unfortunately, with the exception of the commercially-available mesh generators, the automation developments remain a protected competitive advantage within the respective companies.

The extensive presentation of approximate modelling methods is in no way intended to contradict the emergence of the super-model concept, which it is envisaged will soon replace the detailed design model for at least a component. The rapid evolution and lack of detail of the design available during the preliminary design stage substantiates using an approximate model instead of a super-model for this stage. Accordingly, the approximate modelling techniques were presented to assist in obtaining both better preliminary design models and better models for assemblies of components, which in general is a major goal for companies that design structures for dynamic environments.

The comparison of the different model types—solid, hybrid, shell and shell/beam—

for the generic turbine casing showed that the approximate models performed reasonably well when compared with the reference or super-model. This is important since it is a necessary condition that the approximate model and the reference or super-model be within a certain threshold of each other in order to be able to update the approximate model as proposed in Chapter 2. Further, the comparison indicates the level of accuracy that may be expected from the different model types when used for preliminary design analysis or for an assembly of component models.

Chapter 4

Assemblies of Components

4.1 Introduction

The accurate modelling of a single component is just the beginning of the model validation process, since the goal is, in general, to model an assembly of components if not an entire system. The modelling of an assembly of components poses an additional challenge to the analyst in how to model the interface between two adjacent components. It is often the case that one can assemble two adjacent component models that individually show good correlation but then obtain an assembly model with relatively poor correlation [34]. For this reason a significant amount of research has focused on the modelling of the interface or joint between two adjacent components [35, 36].

The connection of two adjacent components by means of a joint changes the modal character of both components by introducing additional mass and stiffness to each component from the other component. In general, some of the individual component modes may not be evident in the assembly modes and new modes that do not correspond to any of the component modes, from either component, will be encountered. This behaviour is referred to here as the "interface effect" or the effect the interface has on the component modes. This effect is important since the

goal, as previously stated, is to predict the modes of an assembly of components and therefore it may not be necessary to predict accurately every mode of each component. It may be that only certain modes of each component need to be predicted accurately in order that the modes of the assembly can be predicted accurately.

The modes of each component which are important to the assembly modes are of particular interest when a model reduction is being considered. The degrees of freedom (DOFs) that are to be retained for each component may be selected based on those component modes that are most important for the assembly. In this way a more effective reduction can be obtained by excluding component modes that are not, or at least much less, important. The DOFs that are to be retained have fewer modes to cover and therefore will do a better job representing those modes.

The subsequent sections of this chapter present an overview of the basic joint types found in gas turbine engine components and a review of some currently-available modeling techniques. This is followed by a case study using two real engine casings to illustrate the interface effect. For components or assemblies of components that are considered too large to analyse with current computer capabilities, a physical model reduction technique is proposed and demonstrated using a simple flat plate. As in Chapters 2 and 3, the FMAC, which is presented in detail in Chapter 5, is used to show the correlation for all the analyses either between FE analysis and test data or two different FE analyses.

4.2 Joints

The joint, or place where two structures are connected together, has been known for many years to be a source of difficulty in modelling. This modelling difficulty is characterized by obtaining good correlation for two adjacent structures with data from individual modal tests and then subsequently obtaining poor correlation with modal test data for the assembly. The interaction of two engine casings at a joint is often non-linear due to the directional dependence of the stiffness from the interaction of the two adjacent surfaces. This joint interaction, as shown in Figure 4.1, is sometimes referred to as "heeling and toeing" because it simulates the motion of a person's foot during walking. The linear modelling of such joints for detailed design analysis generally involves simplifying the connection by rigidly joining the two faces together. This precludes taking any account of the "heeling and toeing" effect as well as omitting the flexibility of the bolts that hold the two surfaces together. Accordingly, this type of model is generally considered to be overly stiff and may produce natural frequencies that are considered to be too high.

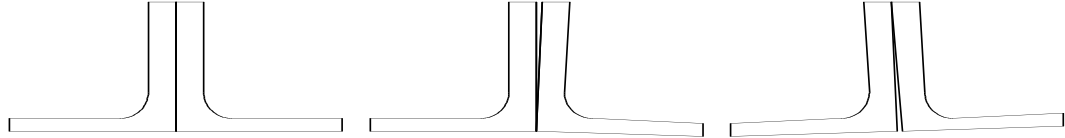


Figure 4.1: Joint Cross-section, Heeling and Toeing

While more sophisticated linear joint models may be attempted, such as modelling the bolts with either spring or beam elements, such models in general have been shown to be overly soft and, consequently, may produce natural frequencies that are considered to be too low. This is again due to the non-linear "heeling and toeing" effect being excluded from the linear model.

4.2.1 Basic Joint Types

The number and variety of joints used to connect adjacent components in industrial structures is quite large. In keeping with the focus of this thesis, the types of joints used to attach adjacent gas turbine engine components are considered here. From this subset of joints, six basic types are shown in Figure 4.2: (a) basic flange, (b) external spigot, (c) internal spigot, (d) double internal spigot, (e) dog-leg and (f) V-band.

The figure shows that the basic flange joint (a) is formed by two 90 degree flanges, with identical bolt hole patterns, that are held together in the axial direction by bolts through their respective holes. In some applications, the two components may be aligned in the circumferential direction, relative to one another, by using close-fitting dowels in the flange of one of the components and corresponding holes in the flange of the other. Although the basic flange has the simplest geometry, it is one of the most difficult to model accurately because with only the bolts to hold the mating flanges together in the axial direction the mating surfaces away from the bolts are free to engage in heeling and toeing.

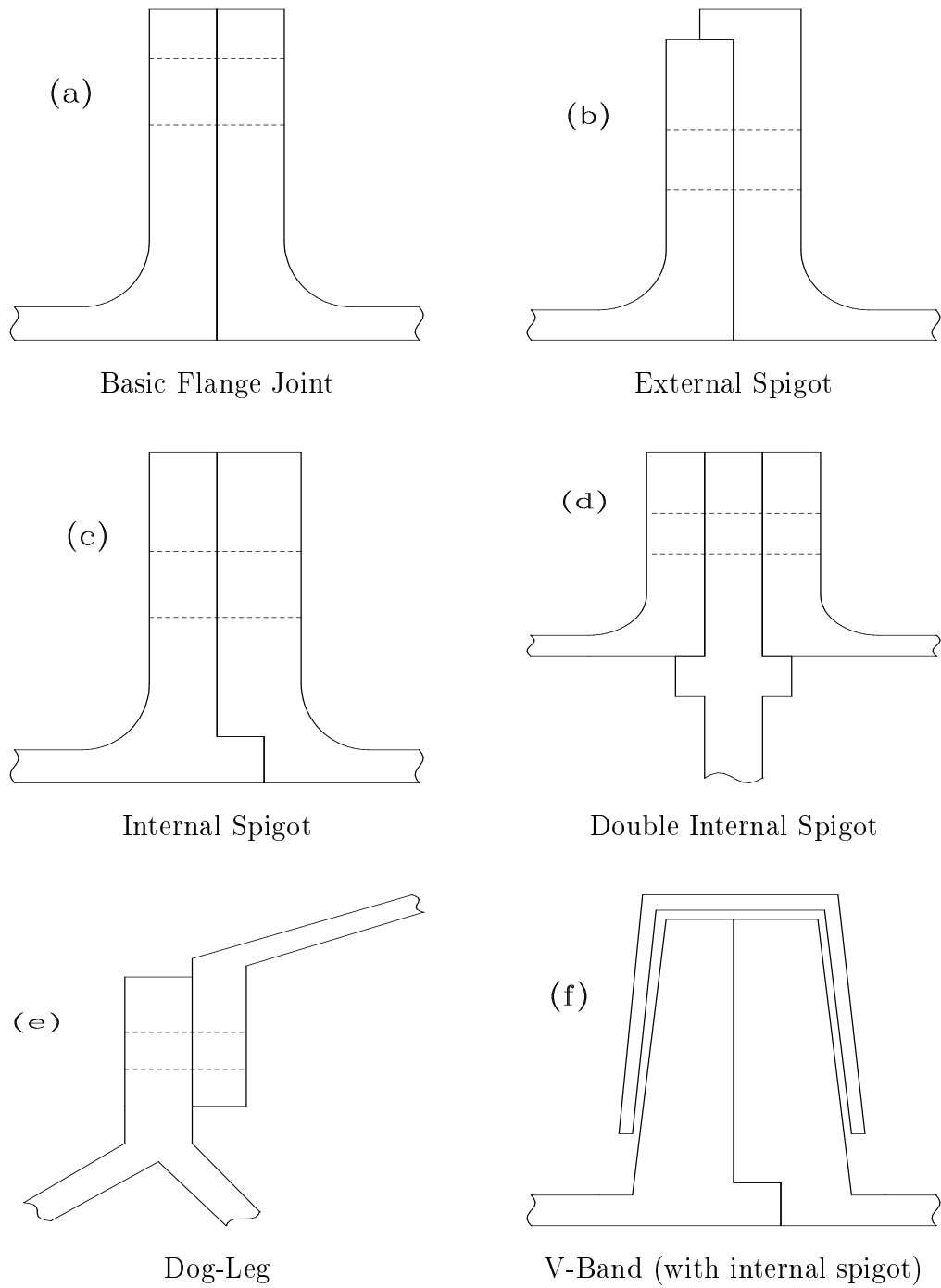


Figure 4.2: Basic Joint Types

The external spigot joint is shown in the figure (b) to be similar to the basic flange but with one of the flanges—the one on the right side in this example—having overlapping material at the outside diameter (OD) of the other flange. In this way the bolts through the respective holes of the two flanges hold them together in the axial direction, while the flange on the right side holds the flange on the left side on the same centre-line. As with the basic flange, the mating surfaces away from the bolts are free to engage, however to a lesser degree than the basic flange. Consequently, the external spigot poses less of a problem for modelling accurately than the basic flange.

The figure shows that the internal spigot joint (c) is similar in concept to the external spigot but with the overlapping material—in this case from the flange on the left—at the inside diameter (ID) as opposed to the OD. Accordingly, the left flange holds the right flange on the same centre-line while the bolts hold the two flanges together in the axial direction. This is the easiest of the joint types presented here to model accurately due to the fact that the combined restraints of the bolts and the spigot prohibits the heeling and toeing of the ID of the mating flanges. Consequently, the internal spigot can be modelled quite accurately by rigidly connecting the two mating flanges as will be demonstrated in the case study in Chapter 6.

The double internal spigot joint (d) can be seen in the figure to consist of two 90 degree flanges that are both mated to a third flange between them that has material that overlaps both of the 90 degree flanges at their ID. With this arrangement the double internal spigot holds all three flanges on the same centre-line while the bolts hold all three flanges together in the axial direction. Like the internal spigot, the double spigot combined with the bolts prohibits the heeling and toeing of both the 90 degree flanges, thereby allowing rigid connections between the three mating surfaces to be used to model the joint quite accurately.

The figure shows that the dog-leg joint (e) is formed, in this example, by a flange on the left that is part of an upside-down V-shaped casing and an internal

flange on the right that is part of a conical casing. With only the bolts to hold the two flanges together, this type of joint is prone to heeling and toeing in a similar manner to the basic flange. Accordingly, an accurate model is difficult to obtain for the dog-leg joint.

The V-band joint is shown in the figure (f) to consist of an internal spigot but with both the flanges having a taper in the radial direction. The V-band is formed around the exterior of the two flanges so as to hold them together in the axial direction while the spigot holds the two casings on the same centre-line. There is a gap in the V-band in the circumferential direction that has an integral nut on one side and an integral bolt on the other side. The joint can be tightened by contracting the V-band by twisting the bolt into the nut which through the tapered flanges will increase the clamp load between the two flanges in the axial direction. This is the most difficult of the joint types presented here to model accurately due to the interaction of the V-band with the two flanges. A mistake that is often made is to ignore the V-band and treat the joint like an internal spigot. However, this approach has been shown in general to be overly stiff and may produce natural frequencies that are considered to be too high, thereby making it necessary to include the V-band in the model.

4.2.2 Overview of Basic Joint Modelling Methods

The models for joints can be divided into several categories but, for the purpose of a general discussion here, the following were selected: (1) linear, (2) non-linear and (3) micro-detail. The first two categories—linear and non-linear—are defined here as those which consider the macro modelling of the joint and, accordingly, ignore the highly localised effects—material non-linearity and plasticity—of the contacting surfaces. The micro-detail modelling of a joint is defined here as that which attempts to include all physical effects of the interacting surfaces using a very detailed, non-linear, contact model.

The linear modelling of joints using springs or beams is the most common approach for detailed design where the desire is to use linear analysis. In general, such linear models attempt to approximate only the non-linear joint stiffness for the computation of the undamped modal data and consequently the damping is not considered. While a reasonable approximation to the non-linear behaviour of a joint can be obtained with this approach, as shown in [37], in general it is only possible for a limited number of modes. Another approach for a linear model is to use generic elements in the form of stiffness matrices as in [38] or flexibility matrices as in [39], where it is claimed that generic elements can be less complex to specify compared with spring or beam elements. In order to improve the joint parameters, model updating was used in [40, 41, 42] for a spring element joint model and in [43] for a generic element joint model.

The desire to include the damping and/or non-linear stiffness characteristics from the interaction of the mating surfaces is the goal behind the non-linear modelling of joints. Due to the complexity of the task, it is often the case that as a first step a non-linear static analysis of the joint is performed, as in [44, 45], in order to first obtain an understanding of the joint stiffness. There are many approaches to including the damping in the joint model but most of them are based on a lumped Coulomb friction model with a combination of spring and damping elements as in [46]. However, it is claimed in [47] that lumped Coulomb damping models can only determine the global state of slip/stick and proposes a new method to help in the understanding of the different slip/stick mechanisms in the contact area.

The micro-detail non-linear joint model takes the next step beyond the non-linear model (as categorised here) by using a very detailed model of the contact areas and by including other effects, such as bolt preload and surface finish, as in [48]. Other models, like those in [39, 35], have sufficient detail so as to include the threads in both the bolt and nut, whereas, the material non-linearity of the contacting surfaces is considered in [49].

4.2.3 Modelling Joints with Beam and Shell Element Flange Models

If beam or shell (finite) elements are used to model the mating structures' flanges, the analyst must be careful in how the spatial separation or gap between the respective flange FE nodes is modelled. Consider the basic flange joint shown in Figure 4.3 (a) along with three modelling approaches (b, c, d) using, for example, shell elements. The geometry is shown by the black lines and the FE model is

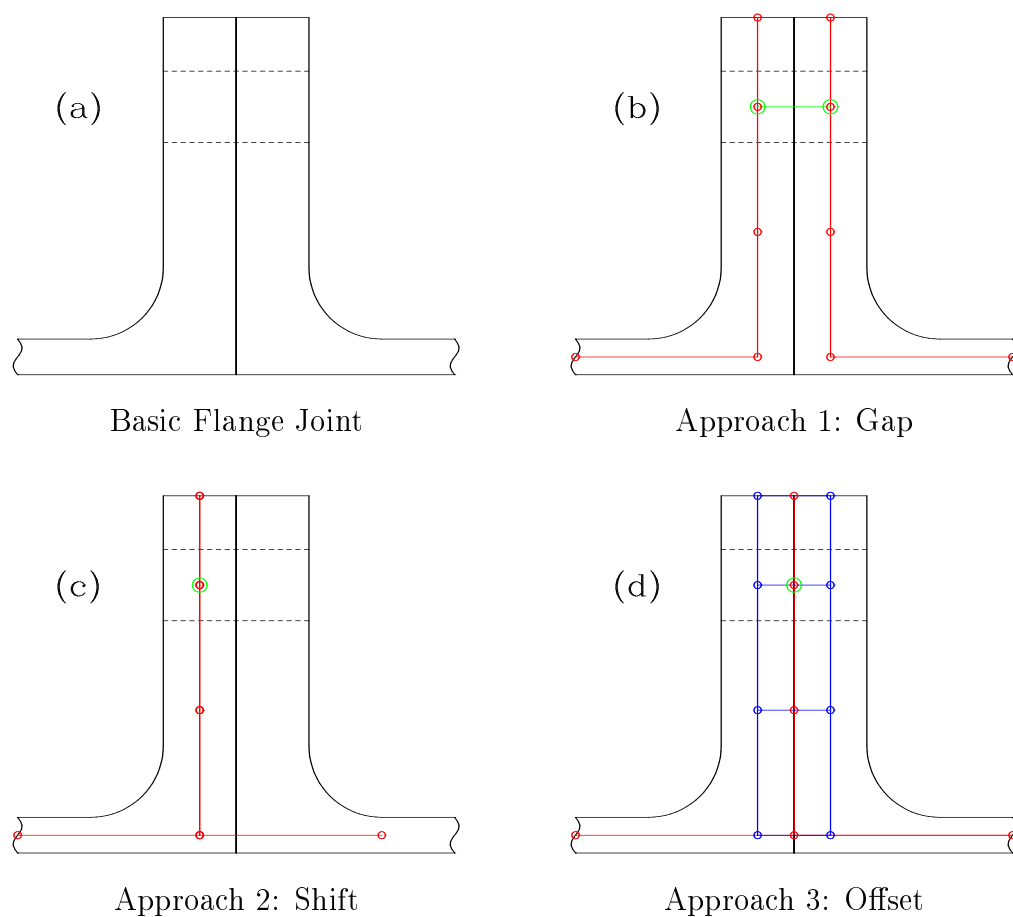


Figure 4.3: Basic Flange Joint Shell Models

shown by the red lines with red circles for the node locations.

The first approach, shown in the figure (b), is to connect the nodes across the

gap from the mating flanges rigidly that are at the centre-line of the bolt holes. This is shown by the green line and green circles concentric with the corresponding nodes to be attached. However, if this is done in all 6 DOFs, the flanges may experience significant rotational deflections due to the relative translation of the two flanges which are separated by the distance across the gap. This introduces an artificial local distortion in each flange that has been shown sometimes to produce unexpected characteristics in the mode shapes and a scattering effect on the natural frequencies. Accordingly, the rotational DOFs are sometimes removed in order to alleviate this problem, leaving a joint model that no longer physically represents a bolt and that has been shown to be overly soft (natural frequencies considered to be too low).

A simple but very effective solution to the gap problem, shown in Figure 4.3 (c), is to displace or shift one of the structures in the axial direction so that the FE nodes of the two mating flanges coincide. The corresponding nodes at the bolt hole centre of each flange, again shown by the green circles, are then rigidly connected in all 6 DOFs. This approach has been shown to be a marked improvement on the first approach. However, for system models formed by assembling multiple component models, the shifts may cause problems in other areas of the system model such as interference with other attachments or misalignment of other interfaces.

The third approach uses the offset capability of the shell element shown by the blue lines in Figure 4.3 (d). In this approach both the flanges have their FE nodes physically located and coincident at the mating surface. The element neutral axes for each flange are then offset to their respective mean-lines providing for the proper specification of their mass and stiffness properties. The corresponding nodes of each flange at the bolt centre-line are again rigidly connected in all 6 DOFs. This approach removes both the gap problem from the first approach and the shift problem from the second approach, thereby yielding the best overall model of the joint.

4.3 Interface Effects

The effects of the interface on the dynamics of assembled components has been a source of problems for many years. It is often the case that an assembly of two independently validated components results in a model that has worse correlation than either of the two components had individually. This, as discussed in the previous section, can usually be attributed to the inadequacy of the joint model since it is the only addition to the assembly model. Having already discussed the modelling of the joints in some detail in the previous section, the focus here is on illustrating the interface effect problem and developing a qualitative method for assessing the effects on the component modes by the joining of the two component models together.

The FMAC can be used to determine which modes of the component models correspond to which modes of the assembly model in both mode shape and frequency. This is referred to as "mode tracking" and demonstrates a unique capability of the FMAC. While a form of "mode tracking" has been performed for years, for example when tuning gas turbine compressor blade modes (by manual stiffness adjustments to shift certain modes out of the operating speed range), in general it has been done visually and for at most a few modes. However, the FMAC provides for the quantitative tracking of several modes simultaneously.

4.3.1 Example of the Interface Effect Problem

In order to illustrate the interface effect problem, the turbine casing described in Chapter 2 was used along with an adjacent (upstream) casing section to form an assembly. For clarity, the casing from Chapter 2 is referred to here as the "aft-casing" and the adjacent (upstream) casing as the "forward-casing". The test data for both casings separately were taken for free-free conditions and consisted of 18 measurements of radial accelerations equally-spaced about the circumference at 2 axial locations (near the forward and aft flanges). The test frequency range for the

individual casings was between 0 and 700 Hertz for which modal analysis of the measured FRFs produced 10 forward-casing modes and 9 aft-casing modes. The assembly test data were taken in a similar manner but the two axial locations at the mating flanges were replaced with a single location on the forward flange of the aft-casing, thereby providing 3 axial locations. The frequency range for the modal test of the assembly was also between 0 and 700 Hz for which the modal analysis produced 20 modes. All of the test data were provided by Rolls-Royce.

The forward-casing was modelled in the same way as the aft-casing from Chapter 2. The cross-section models consisted of 97 nodes, 49 elements and 124 nodes, 69 elements respectively. The 3-D models for both casings had 216 elements in the circumferential direction in order to adequately model the different features (flange holes and scallops). Accordingly, the forward-casing had 20,952 nodes, 10,584 elements and 62,856 DOFs whereas the aft-casing had 26,784 nodes, 14,904 elements and 80,352 DOFs.

The cross-section solid element FE models and corresponding FMAC plots for both the aft- and forward-turbine casings are shown in Figure 4.4 and Figure 4.5, respectively. The FE model and corresponding FMAC plot shown in Figure 4.4 were previously shown in Chapter 2 as Figures 2.6 and 2.8, respectively.

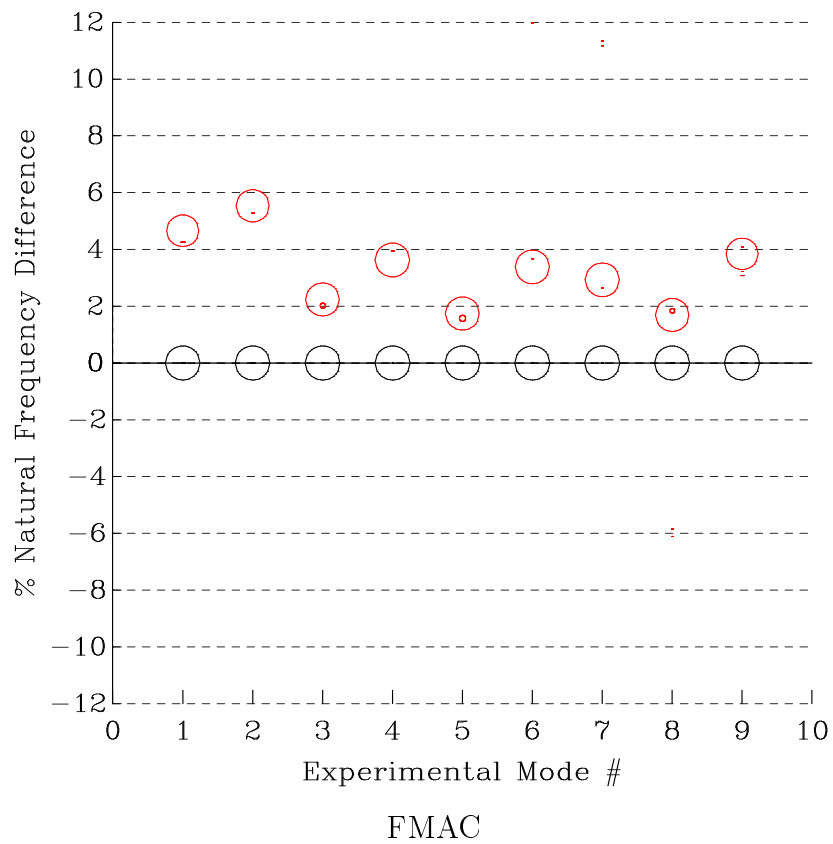
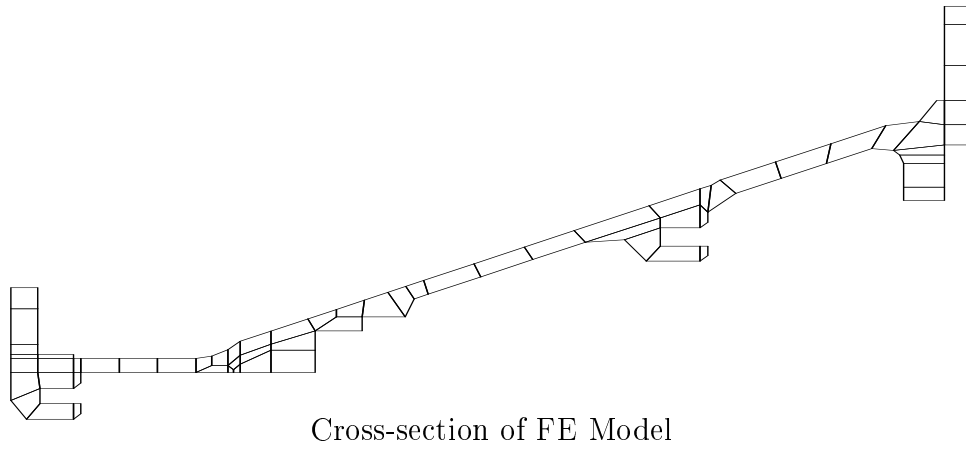


Figure 4.4: Cross-section FE Model and FMAC for Aft-turbine Casing

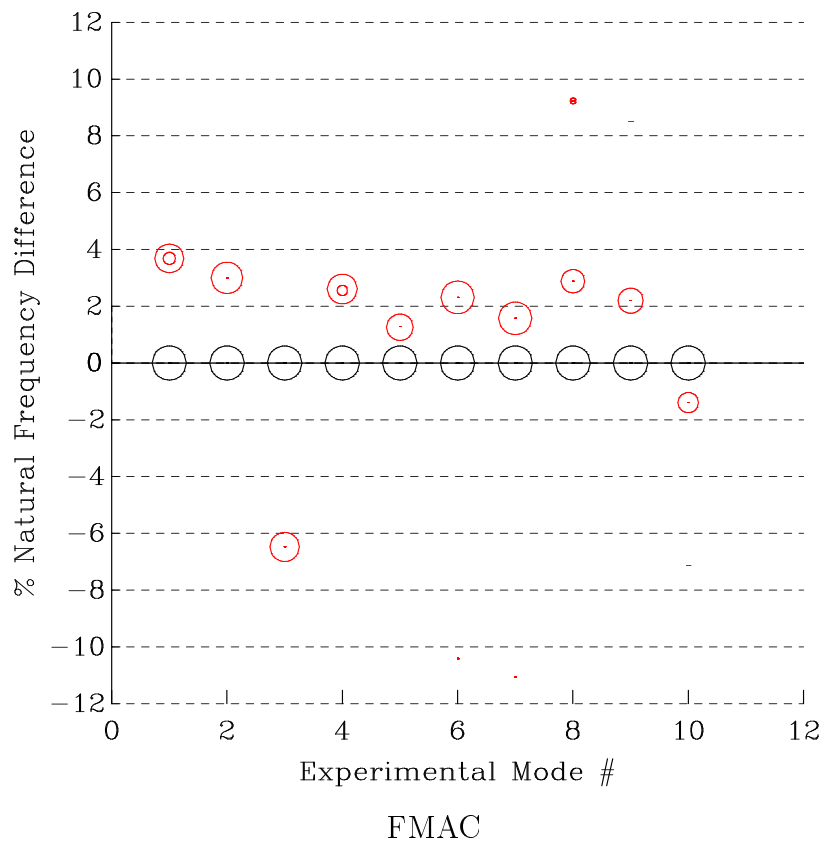
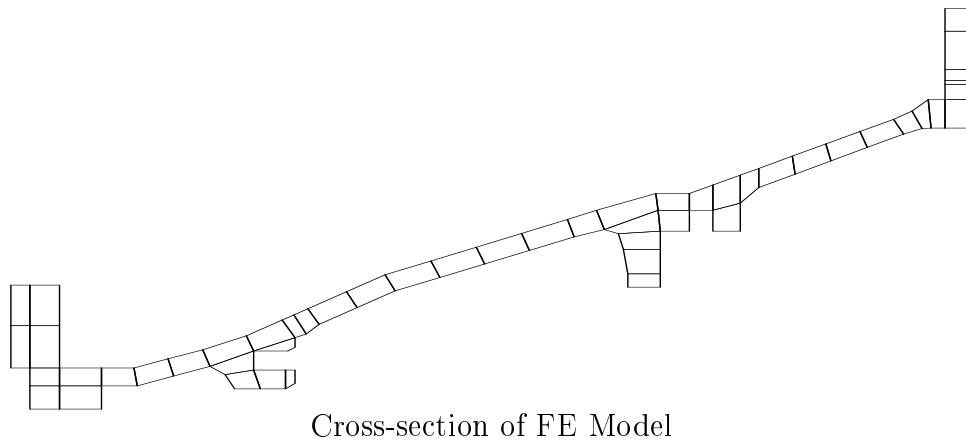


Figure 4.5: Cross-section FE Model and FMAC for Forward-turbine Casing

Figure 4.4 shows that the correlation for the aft-casing is very good with MAC values very close to 1.0 and natural frequency differences between about +1.5% and +5.5% for all 9 of the experimental modes. Although the correlation for the forward-casing, shown in Figure 4.5, is seen to be not as good as for the aft-casing, it is considered to be good with MAC values for 6 of the first 7 experimental modes in excess of 0.70 and natural frequency differences between about +1% and +3.5%.

The forward- and aft-casing solid FE models were attached at their common interface to form a model of the assembly as shown in Figure 4.6. The forward-casing is shown by the black lines and the aft-casing is shown by the red lines.

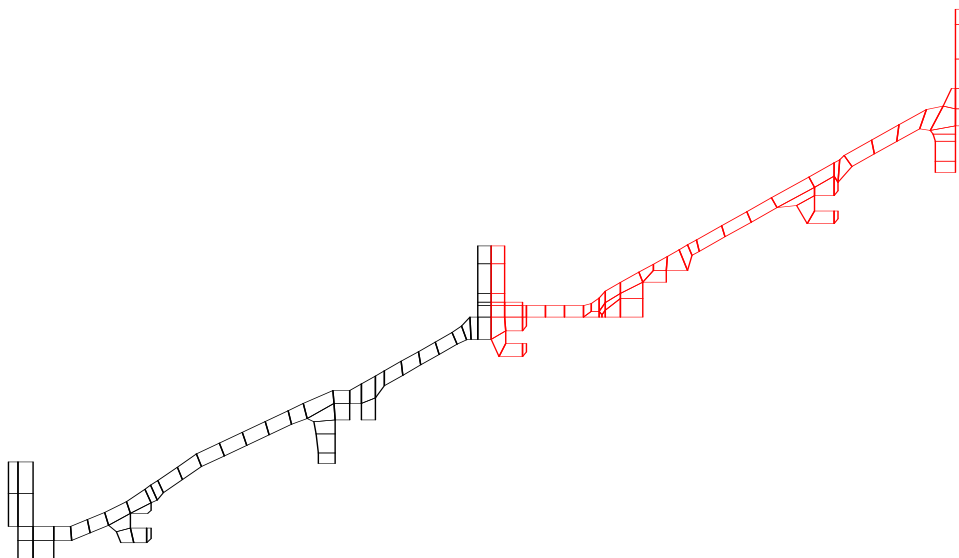


Figure 4.6: Cross-section FE Model for the Assembly

The interface between the forward- and aft-casing cross-section FE models is shown in detail in Figure 4.7. The forward-casing part is shown by the black lines and the aft-casing part is shown by the blue lines. The nodes from the forward-casing on the line of contact are coincident with the corresponding nodes from the

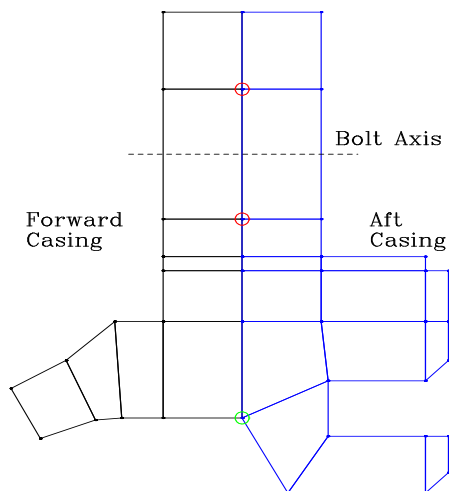


Figure 4.7: Interface of the Forward and Aft-casing Cross-section FE Models

aft-casing. As a first approach to a joint model, the nodes from each component corresponding to the bolt holes, shown by the red circles, were rigidly attached.

The results for applying this first approach for the joint model—attaching at the bolt holes only—to the assembly model are shown in Figure 4.8. The figure

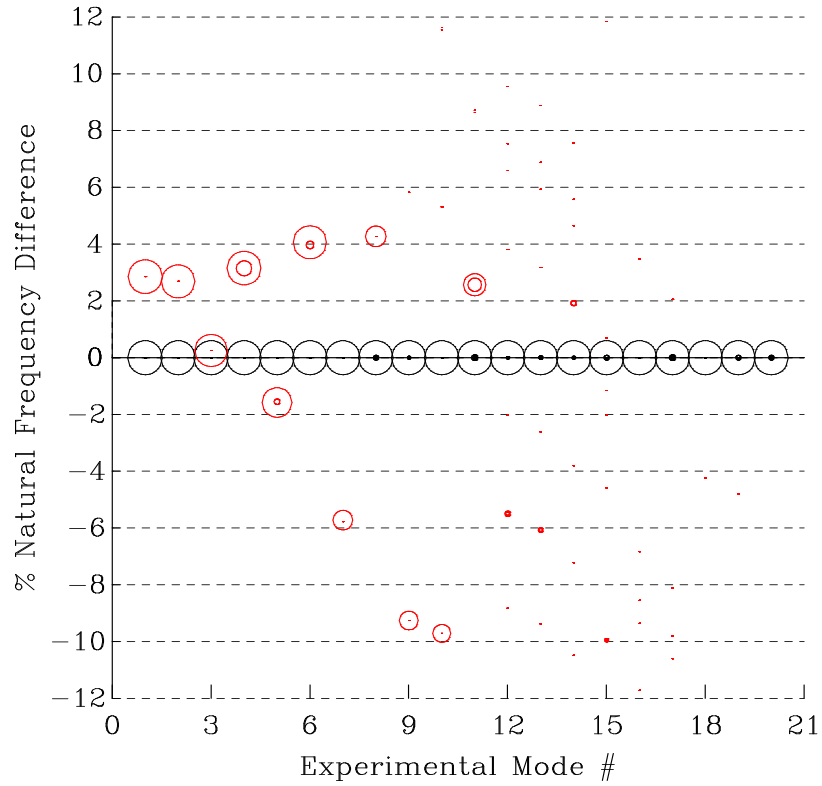


Figure 4.8: FMAC for Assembly using Bolt Only Joint Model

shows that the overall correlation is not very good and is much worse than either of the components individually. Although the correlation for the first 6 experimental modes is considered very good with MAC values in excess of 0.80 and frequency differences between -1.5% and +4.0%, the higher modes (7-20) are shown to have very poor correlation. This is generally attributed to the inadequacy of the joint model. Since the joint model only attached together the corresponding nodes at the bolt holes, leaving the rest of the mating surface free, it is inferred from the poor correlation that the rest of the interface is in reality engaged and not free.

In an attempt to improve the joint model, a second approach added a rigid attachment between the coincident nodes from both components at the ID of the mating flanges, as shown by the green circle in Figure 4.7, to the joint model from the first approach. The results for this second joint model were compared with the

first joint model as shown in Figure 4.9. The correlation results for the first and second joint model approaches are shown by the red and blue circles, respectively. The figure shows that by adding the attachment of the nodes at the ID of the

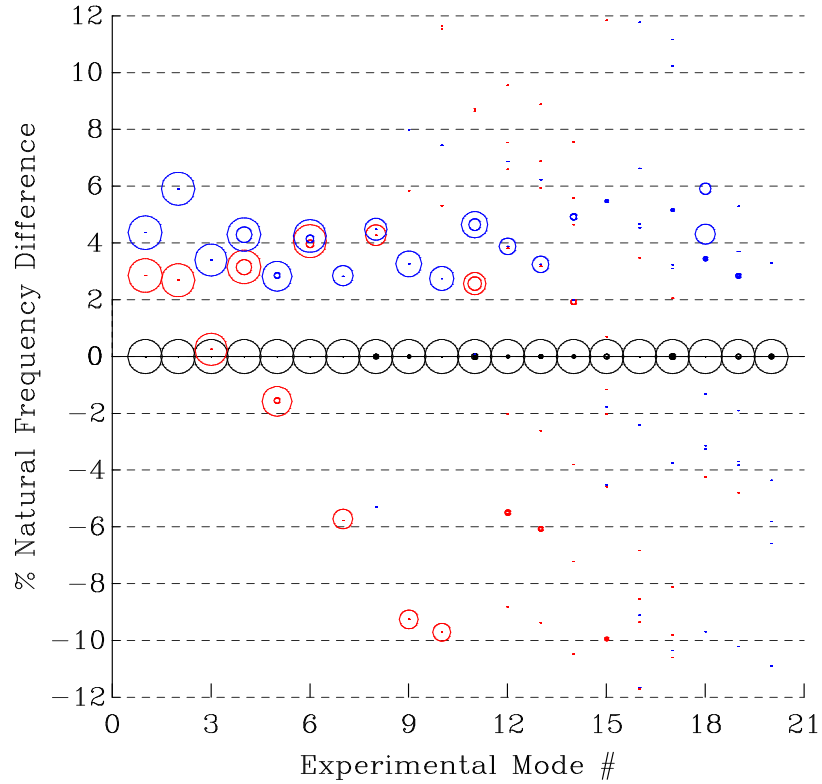


Figure 4.9: FMAC for Assembly using Bolt and ID Joint Model

mating flanges the overall correlation improved significantly, especially in terms of the natural frequency differences. Although the correlation was improved, the lack of correlation for experimental modes 13 through 17 indicates that the joint model remains deficient. However, the example clearly illustrates the interface effect problem that has plagued analysts for many years and has spawned much research.

4.3.2 Mode Tracking

The development in the previous section of the two component FE models—forward-casing and aft-casing—lends itself to further analysis. One such analysis is to compare the analytical modes from the components with the experimental modes of the assembly. This is done to gain an understanding of the effects that assembling the two components have on each other and to determine which modes of the component models correspond with which modes of the assembly in both mode shape and frequency. This is referred to here as "mode tracking" as it is an attempt to track the modes, using the FMAC, of each component by both their shape and frequency to the modes of the assembly [50].

Figure 4.10 shows the FMAC plot that compares the analytical modes of each of the components with the experimental modes of the assembly. The red circles are for the forward-casing and the blue circles are for the aft-casing. The black circles are for the auto-MAC of the experimental modes of the assembly. The figure shows that nearly all the modes of the forward-casing have positive natural frequency differences when compared with those of the assembly. This suggests that the aft-casing had a softening effect on the forward-casing, resulting in a frequency decrease for the assembly modes compared with the forward-casing. Likewise, nearly all the modes of the aft-casing have negative frequency differences when compared with the assembly modes. This implies that the forward-casing had a stiffening effect on the aft-casing, resulting in a natural frequency increase for the assembly modes when compared to the aft-casing.

It can also be seen from the figure that the first 4 assembly modes correspond to modes of each component about equally, with positive frequency shifts for the forward-casing and negative frequency shifts for the aft-casing as previously noted. However, the aft-casing modes are seen to be dominant in modes 6 through 14 of the assembly with the exception of mode 7. The assembly modes 12 and 13 are shown to correspond very well with two modes of the aft-casing, while modes 15

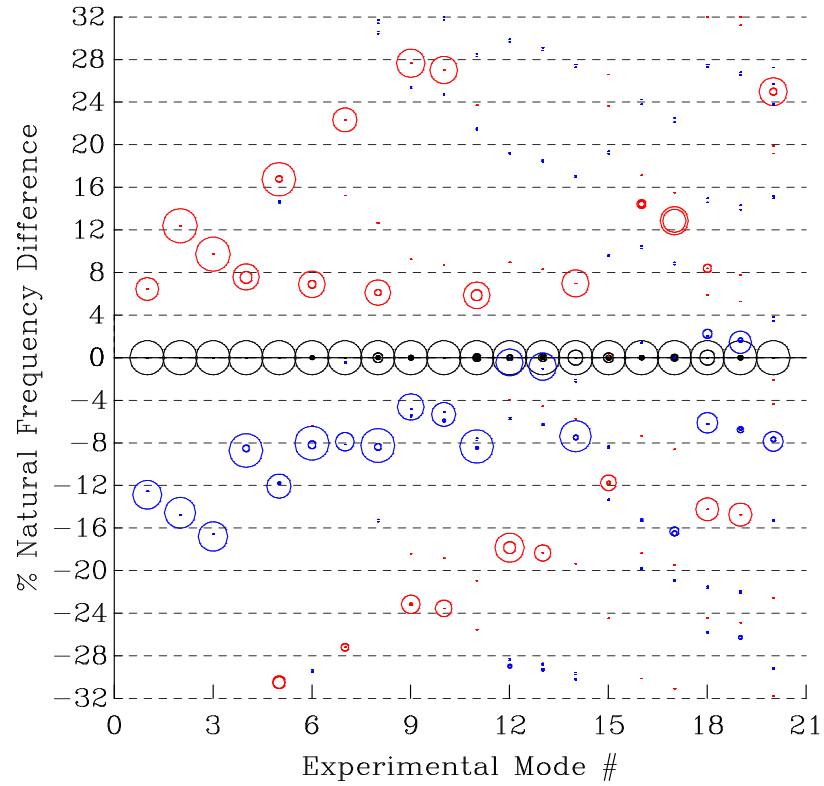


Figure 4.10: FMAC Comparing Component Analytical Modes to Experimental Assembly Modes

and 16 are seen to have almost no correspondence to modes of either component.

4.4 Model Reduction

The current design analysis cycle poses a limit on the number of DOFs of the FE model in terms of the time required for completion of the analysis. Furthermore, current computer capability poses a limit on the maximum number of DOFs of the FE model. Accordingly, the joining of multiple "super-models" to form an assembly may result in a model that is currently too large to analyse, thereby making it necessary to reduce the component "super-models" to a more practical size before assembly.

The model reduction methods are separated here into two groups: (1) matrix and (2) physical. The matrix methods, as referred to here, are those which reduce the physical system matrices—stiffness, mass and damping—to much smaller non-physical matrices. Whereas the physical methods are those which reduce the FE model of the system to a much smaller FE model but one that is a reasonable approximation of the full model for a selected set of modes. A significant amount of research has been documented for the matrix methods but very little has been documented for the physical methods. Accordingly, the next section presents an overview of the matrix model reduction methods followed by the introduction of a new physical model reduction method.

4.4.1 Overview of Matrix Model Reduction Methods

The most common reduction method used in both industry and commercial FE programs is Guyan reduction (GR) (sometimes called Guyan/Irons) [51, 52]. Guyan reduction is often referred to as "static" reduction or condensation since it ignores the inertia effects of omitted DOFs. If there are applied loads on any eliminated DOFs, it is an approximate reduction of the stiffness matrix, otherwise it is an exact reduction. In order to be able to apply loads to omitted DOFs the improved reduced system (IRS) method was introduced as an enhancement to the GR method [53]. Another improvement on the GR method is the extended Guyan reduction (EGR) method which is claimed to decrease the errors in the eigenvectors when compared with the GR method while not requiring any matrix inversions [54]. The succession-level approximate reduction (SAR) method uses a recurrence relation which has GR and IRS as its first and second levels, respectively, where the third level, SAR, is claimed to be more accurate than the IRS method [55]. The extension of the IRS method by introducing an iterative algorithm is also claimed to improve the accuracy when compared with the IRS method alone [56]. The dynamic reduction (DR) method has the advantage of explicitly including an

approximation of the inertia effects but is more computationally intense than the GR method and its derivatives [57, 58].

Another approach to model reduction is to use the system eigenvectors to reduce the system mass and stiffness matrices. Accordingly, such methods are called "modal" methods for which the modal reduction (MR) method is the most common [59]. The MR method is exact for the modes included in the reduction process. The system equivalent reduction expansion process (SEREP) is identical to the MR method for reduction but differs in how the expansion to the full set of DOFs is performed (however, expansion is not the subject of concern here) [60]. The MR and SEREP methods are claimed to be affected by mode truncation and, consequently, less accurate than the complete mode-type reduction (CMR) method which was developed to eliminate the mode truncation problem [61]. The observance of large off-diagonal terms during orthogonality checks of systems that have been reduced using the MR method led to the development of the hybrid reduction (HR) method [62]. The HR method is claimed to improve the off-diagonal terms of the orthogonality check by including the effects of the residual modes (modes outside the frequency range of consideration) in the reduction.

With the significant number of model reduction methods available it is often a useful exercise to compare the different methods using a common structural model and/or test data. The GR, IRS, SEREP and DR model reduction methods are compared in [63]. Whereas the DR, ERS, EGR and IRS reduction methods are compared in [64]. In [65], a comparison of the MR, SEREP and HR methods is presented.

4.4.2 Physical Model Reduction

The physical reduction of a system is defined here as a process that reduces an FE model of a system to a much smaller FE model that approximates the full-size FE model with reasonable accuracy for a selected number of modes. This was

demonstrated in [66] with the reduction of a relatively complex shell-element FE model to a system of spring-mass models. However, the lack of literature available for physical model reduction is an indication that it is a reasonably new concept.

There are advantages to using physical model reduction over the more common matrix methods discussed above. It is often the case that multiple companies participate in producing different parts of a structure and consequently must produce an FE model for their part which will be incorporated into a model of the whole structure. An example of this is in the gas turbine engine industry where a whole engine model (WEM) must be provided to the aircraft maker to incorporate into their model of the entire aircraft. Contained within the FE models for both the engine and aircraft may be several models of components that were provided by sub-contractors. The assembly of all the FE models can be a very cumbersome task and may require slight modifications to where the individual models interface. For such modifications, the use of physical models rather than mass and stiffness matrices is preferred to provide the analyst with a qualitative measure of how the changes will effect the structure. Making such modifications with mass and stiffness matrices generally requires the originator of the model to impose the changes on their physical FE model and to perform the reduction again, which can be a very time consuming process.

4.4.2.1 Modal Average Strain Energy Density

The key to physical model reduction as presented here is to determine, for a selected number of modes, what regions of the FE model are the most important in which to concentrate the elements. The method proposed here is to use the elemental strain energy density averaged over the selected number of modes, which is given by:

$$U_i = \frac{1}{m} \sum_{r=1}^m w_r u_{ir} \quad (4.4.1)$$

where u_{ir} is the strain energy density for element i , mode r and w_r is the weighting factor for mode r . The FE model is then subdivided into a selected number of regions, N , of elements with equal accumulative strain energy, which is given by:

$$U_k = \sum_{i=NE_a}^{NE_b} U_i v_i \quad (4.4.2)$$

where v_i is the volume of element i , NE_a and NE_b are the beginning and ending element numbers for the region and k is the region index with values between 1 and N inclusive. In practice, the user need only select the value for N , which is effectively the number of elements desired in the reduced model. From this selection a reduction ratio can be defined as the initial number of elements divided by the reduced number of elements. The ability to select different weighting factors for each mode provides for a means of emphasizing modes of interest. This capability can be especially useful when combined with mode tracking for assemblies to emphasise the modes of each component that are the most important to the modes of the assembly.

Consider the initial FE model for a flat plate as shown in Figure 4.11. The figure shows that the shell-element model has a mesh with 40 elements horizontally by 40 elements vertically, for a total of 1600 elements. The commercial program MSC/NASTRAN was used to obtain the free-free natural frequencies, mode shapes and corresponding element strain energy densities for the first 10 (non-rigid body) modes.

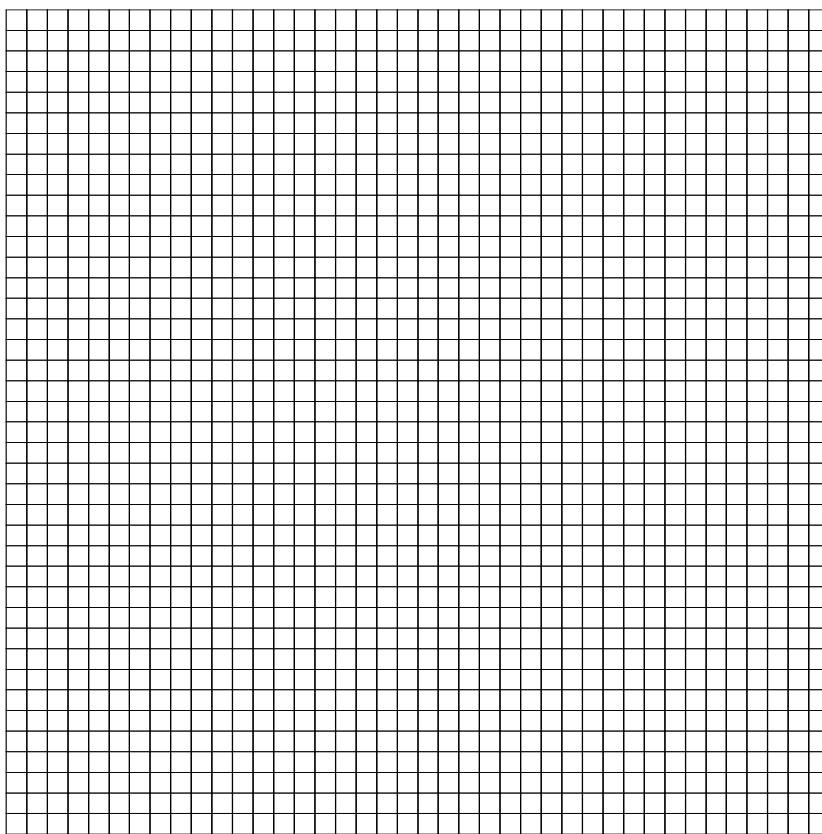


Figure 4.11: Initial Flat Plate 40x40 Shell-Element FE Model

Figure 4.12 shows the modal average strain energy density (MASED) distribution for the first 10 modes with weighting factors of 1.0 for all modes. The figure shows that the MASED is symmetric about the plate centre in both the x and y axes. This is to be expected since the plate is symmetric and contained within the first 10 modes were two sets of orthogonal mode pairs.

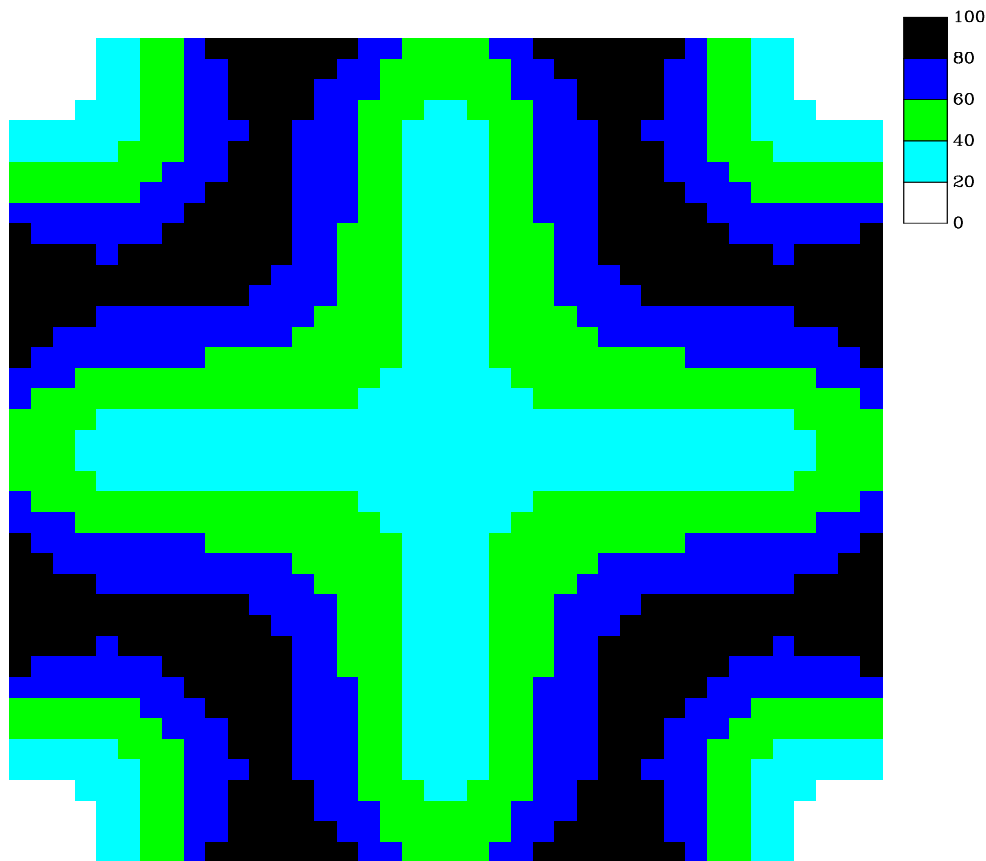


Figure 4.12: Flat Plate Modal Average Strain Energy Density for 10 Modes

The initial model was reduced using the MASED method with the reduced size selected to be 121 (11 horizontal by 11 vertical) elements or a reduction ratio of about 13. The 11x11 element reduced model is shown in Figure 4.13.

The figure shows that the mesh of the reduced model is symmetric about the plate centre in both the x and y axes which is consistent with the MASED in Figure 4.12. Note that the regions of high MASED have a higher mesh density than the regions of low MASED. This is particularly evident near the corners of the plate which have very low MASED. The commercial FE program MSC/NASTRAN was again used to determine the free-free natural frequencies and corresponding mode shapes for the first 10 modes.

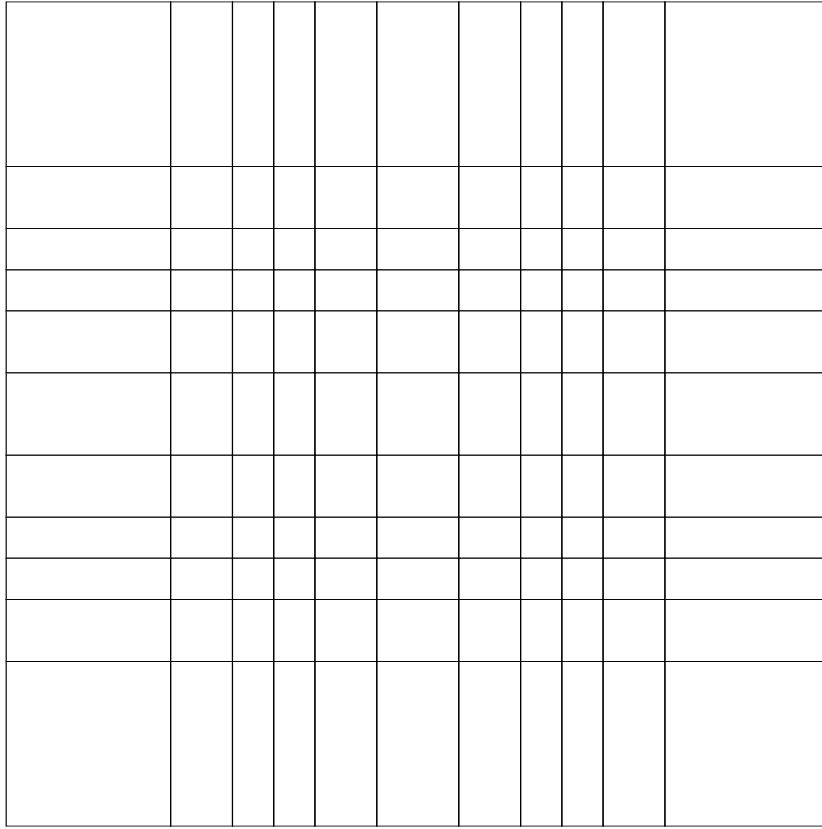


Figure 4.13: Reduced 11x11 Shell-Element FE Model

In order to show the effect of the reduction on the modal characteristics, the FE analysis results of the initial model were used as a reference against which the reduced model FE results were compared. Additionally, to show the benefit of using MASED to select the mesh topology, the results for an equally-spaced element mesh with the same number of elements as the reduced mesh was also compared with the reference.

Figure 4.14 shows the FMAC plot for the correlation comparison of the two reduced models—MASED selected topology and equally-spaced—with the reference. The red circles are for the equally-spaced reduced mesh and the blue circles are for the MASED reduced mesh. The black circles are for the auto-MAC for the reference model. The figure shows that the MASED mesh in general performed

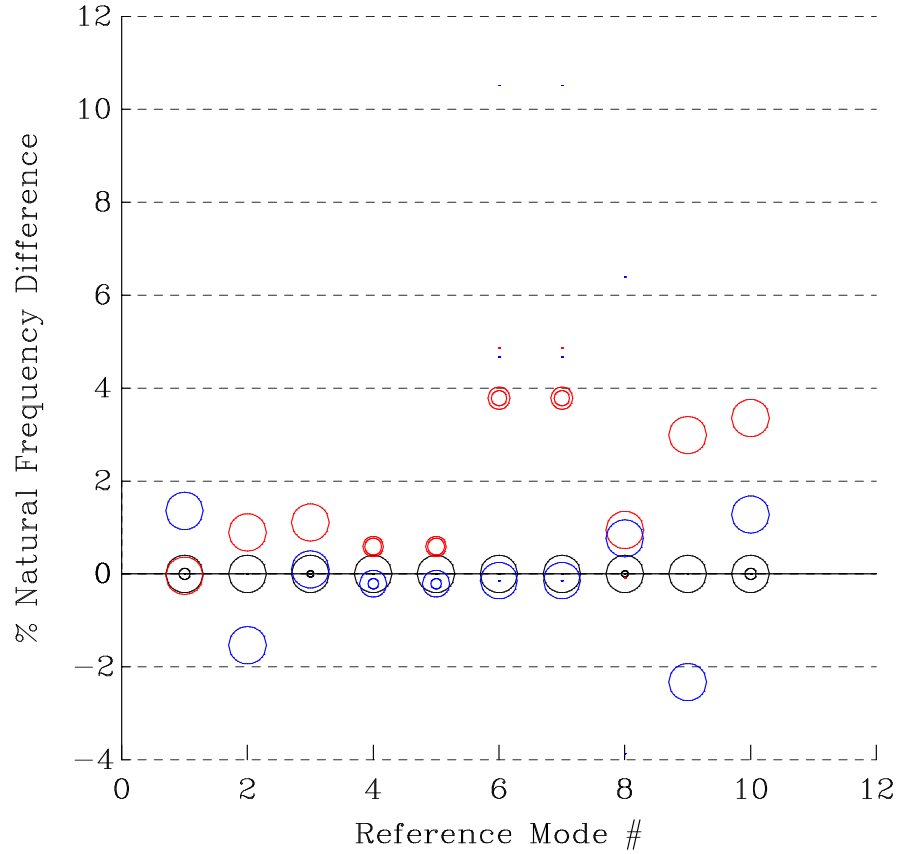


Figure 4.14: FMAC for Reduced 11x11 Element FE Model

better than the equally-spaced mesh. The MAC values for modes 4 through 7 are significantly better and the natural frequency differences for modes 6, 7 and 10 are also significantly better. However, the natural frequency difference increased by about 1.5% for the first mode.

In order to determine the sensitivity of the modal characteristics to the change in mesh size and topology, a second reduction was performed using a reduced mesh size of 36 elements (6 elements horizontally by 6 elements vertically) or reduction ratio of about 44. The 6x6 element reduced mesh is shown in Figure 4.15. Note

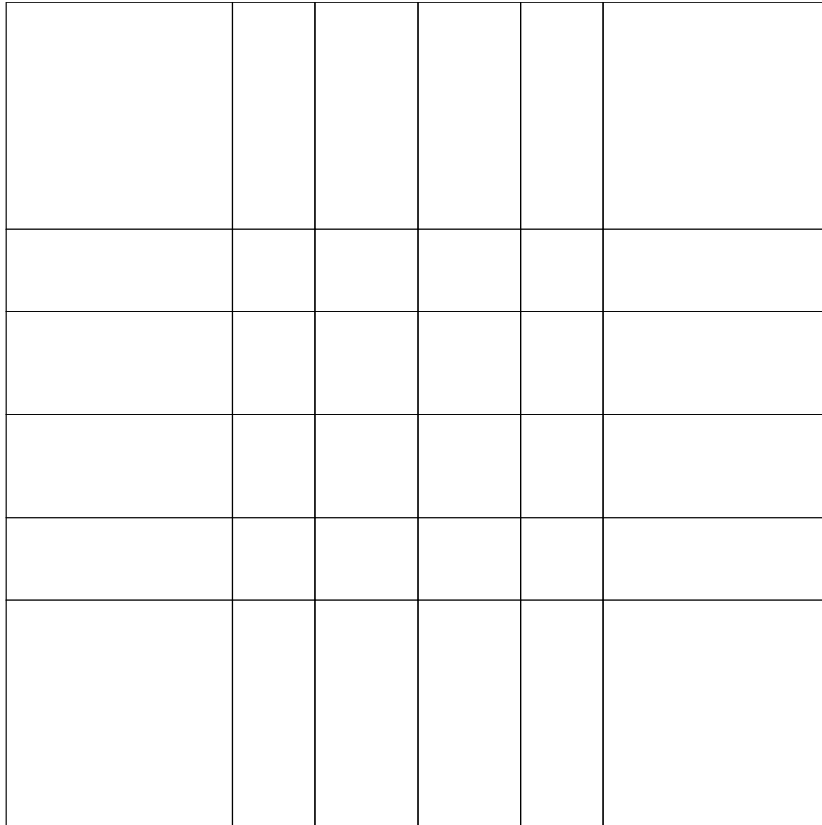


Figure 4.15: Reduced 6x6 Shell-Element FE Model

again that the mesh is concentrated in the regions of high MASED.

The FMAC plot comparing the correlation of both the 6x6 MASED reduced model and 6x6 equally-spaced model is shown in Figure 4.16. The figure shows

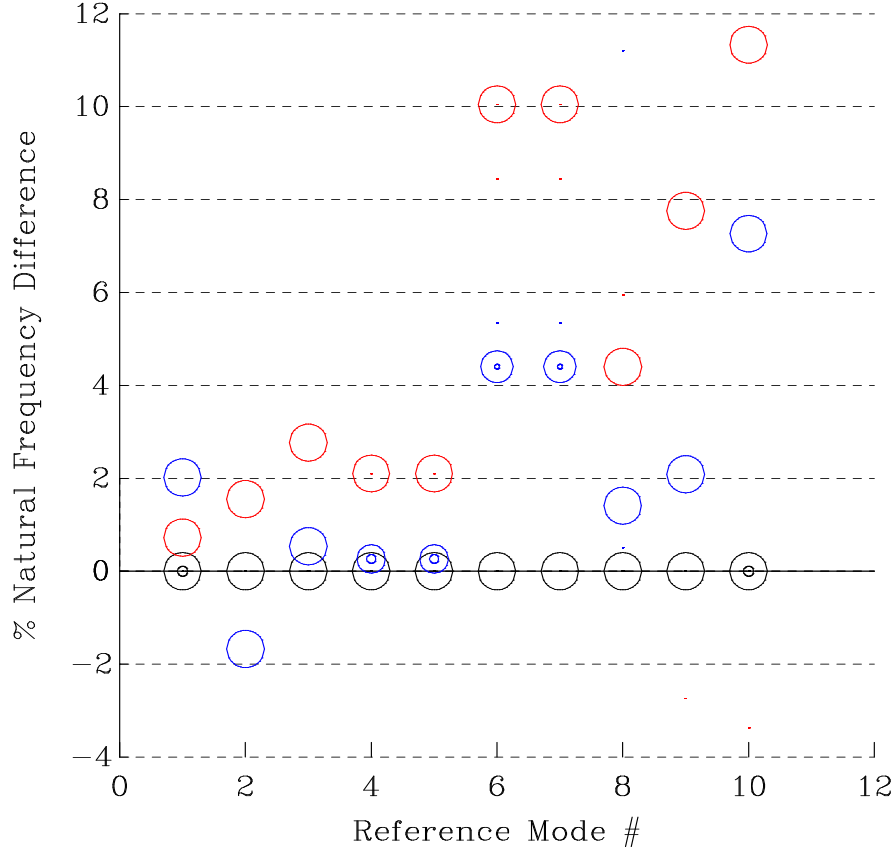


Figure 4.16: FMAC for Reduced 6x6 Element FE Model

that the MASED-reduced model again performed much better than the equally-spaced model. Although the MAC values decreased slightly for modes 4 and 5 the natural frequency differences for modes 3 through 10 are significantly better than those of the equally-spaced model by as much as about 6% for modes 6, 7 and 9. Note again that the natural frequency difference for the first mode increased by about 1.5%.

The correlation of the 11x11 and 6x6 MASED reduced models were both compared with the reference model and each other, as shown in Figure 4.17, to show the change in modal characteristics between the two reduced models. The figure

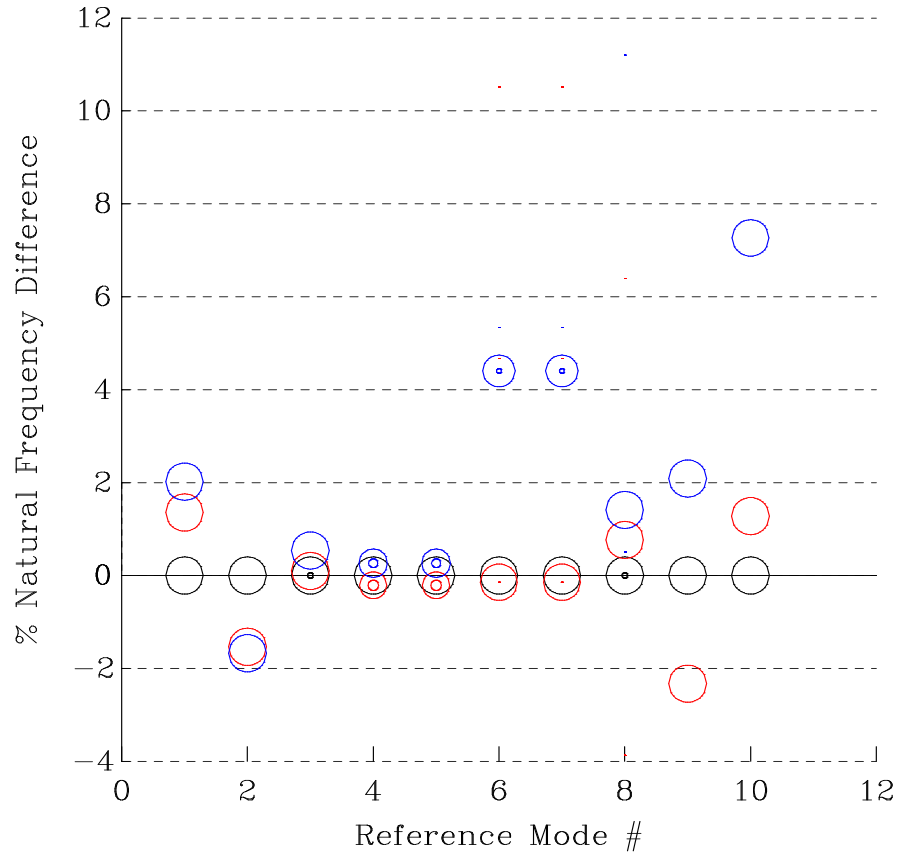


Figure 4.17: FMAC Comparing 11x11 Reduced Mesh with 6x6 Reduce Mesh

shows, as expected, that the 11x11 mesh (red) in general performed better than the 6x6 mesh (blue). This is particularly the case for modes 6, 7 and 10 where the natural frequency differences improved by as much as about 6% for mode 10. However it is noted that the 6x6 mesh performance is quite good when considering it has more than 3 times the reduction ratio of the 11x11 mesh.

4.5 Conclusions

A concise review of the basic problems encountered when connecting adjacent component FE models together to form an assembly model has been presented. Although the review of the types of joints and currently-available modelling tech-

niques focused on gas turbine engine hardware, it is envisaged that the basic understanding and general approach are applicable to a wide range of industrial structures. Despite the presentation in the literature of a few effective linear joint modelling techniques for specific joint types, it is evident that further research is needed to develop a more general linear joint modelling method.

The importance of the joint model for the accurate prediction of the assembly modal characteristics has been demonstrated by a case study using two real engine casings. The assembly modal characteristics were shown to be quite sensitive to the assumptions used in the bolted-flange joint model for the interaction of the mating flange surfaces away from the bolt location. The ability to determine which component modes correspond to which assembly modes, referred to as mode tracking, using the FMAC provided insight into the effects that assembling the two components had on each others modal characteristics. It is envisaged that further research into mode tracking may provide a guide for the improvement of joint models.

The new physical model reduction technique, based on the modal average strain energy density (MASED), was shown to produce a more accurate FE mesh when compared with an equally-spaced mesh with the same number of DOFs. An FE model for a simple flat plate was reduced by a factor of about 44 while a reasonable approximation of the modal characteristics for the full model was obtained. Although the method was demonstrated on a simple flat plate, it will be used in Chapter 6 (Case Study) to reduce the FE models of two real engine casings.

Chapter 5

Model Correlation

5.1 Introduction

Correlation plays a key role in the model validation process because the initial FE model cannot be updated or improved without first performing correlation. Furthermore, for each iteration of the updating task the correlation must be obtained. The first result from performing correlation is to establish the correspondence between modes from the analysis set and modes from the test data which are usually referred to as the "correlated mode pairs (CMPs)". The correlation techniques used must be able to determine the CMPs despite the existence of noise and other errors inherent in the testing process. Further, reliable correlation techniques for other quantities, such as frequency response functions (FRFs), must be available when the test data are too noisy for accurate mode shape extraction.

The modal assurance criterion (MAC, [67]) is the most widely-used method for correlation measure of mode shapes between those from the finite element model and those from the modal test. However, it has been shown that it can sometimes be quite misleading by indicating poor correlation between modes that appear visually to be the same and, conversely, by indicating good correlation between modes that appear visually to be different. This behaviour has led to the devel-

opment of numerous variations of the MAC, either as stand-alone improvements or to be used in conjunction with the MAC to aid in correlation, with the goal of making assistance from mode shape animation unnecessary. Although there has been much work performed in this area since the MAC's presentation in 1982 and its previous form called the mode shape correlation coefficient (MSCC) presented in 1977, a robust correlation tool is still to be found.

After discussion of the different correlation methods available, some examples of the methods are shown using a simple beam. This is followed by the presentation of three new developments. The first is a new plot format that allows for the simultaneous display of the mode shape correlation, the degree of spatial aliasing and the natural frequency comparison (section 5.3). The second is an extension of the new plot format to display the correlation of test frequency response functions (FRFs) with analytical mode shapes (also section 5.3). The third is to compensate for the particular difficulties that arise in performing correlation for axisymmetric structures (section 5.4). The chapter ends with some general conclusions about the new developments presented.

5.2 Overview of Correlation Methods

In this review, the MAC and its related correlation methods have been separated into three categories, and are presented in the following three sub-sections. The first section is for the MAC and related methods which perform vector correlation and therefore only require the mode shapes or eigenvectors to be compared. The second section is for the methods which employ a mass or pseudo-mass matrix to obtain different orthogonality checks. The last section is for the techniques used to correlate frequency response functions (FRFs).

5.2.1 Vector Correlation

This section describes various methods for assessing the degree of correlation between two vectors or, in the case of mode shapes, two sets of eigenvectors. While it is easier to obtain mode shapes from the analytical model than FRFs, the converse is true for the experimental data, which require significant processing of numerous FRFs in order to extract the mode shapes. However, acquiring experimental mode shapes has become less labour-intensive and more reliable through the development of advanced modal analysis software. This, along with the ready availability of analytical mode shapes, has led to the popularity of vector correlation methods.

5.2.1.1 Modal Assurance Criterion

The modal assurance criterion (MAC) between two modes ϕ_i^a and ϕ_j^x is given by [67]:

$$MAC(\phi_i^a, \phi_j^x) = \frac{\sum_{k=1}^N \phi_{ki}^a \phi_{kj}^{x*}{}^2}{\sum_{k=1}^N \phi_{ki}^a \phi_{ki}^{a*} \sum_{k=1}^N \phi_{kj}^x \phi_{kj}^{x*}} \quad (5.2.1)$$

where the modes to be compared need not be similarly scaled (or normalized). The MAC has been described as the coherence of two vectors or a measure of the least-squares deviation about a straight-line plot of two vectors. A result of $MAC = 1$ indicates perfect correlation, while 0 indicates no correlation.

Some of the deficiencies of the MAC, which have been described by various authors, are: Lieven and Ewins [68] point out that the MAC gives no information as to why the correlation is poor; Mitchell [69] conveys that the MAC is not sensitive to small but significant changes in mode shape; Blaschke and Ewins [70] state that the MAC is not sufficient for locating modeling errors; and Brechlin, Bendel and Keiper [71] point out that the MAC can yield misleading results when using rotational DOFs.

The MAC has been found by this author to be sensitive to node lines or near-null deflections. For example: when comparing two modes that appeared visually to be well correlated but dominated by Y and Z motion, a MAC of 0.2 was obtained using X, Y and Z components. However, when the near null X motion terms were removed, a MAC of 0.8 was obtained. This behaviour leads the analyst to trust in the MAC only when it renders relatively high values, say greater than 0.6, and to rely on backup methods, such as visualization, when lower MAC values are obtained.

5.2.1.2 Modal Scale Factor

The modal scale factor (MSF) between two modes ψ_i^a and ψ_j^x is given by [67]:

$$MSF(\psi_i^a, \psi_j^x) = \frac{\sum_{k=1}^N \psi_{ki}^a \psi_{kj}^x}{\sum_{k=1}^N \psi_{ki}^a \psi_{ki}^a} \quad (5.2.2)$$

where the modes to be compared must be of like scale. It is described as the slope of the best straight line fit through a plot of the modal coefficients, but gives no indication of the quality of the fit to the straight line. Where the MAC gives a quantitative comparison of two mode shapes, the MSF gives a qualitative comparison and therefore is not useful for assessing the degree of correlation.

5.2.1.3 Coordinate Modal Assurance Criterion

The coordinate modal assurance criterion (COMAC) for a degree of freedom (DOF) k is given by [68],

$$COMAC_k = \frac{\sum_{j=1}^m \phi_{kj}^a \phi_{kj}^x}{\sum_{j=1}^m \phi_{kj}^a \phi_{kj}^a \sum_{j=1}^m \phi_{kj}^x \phi_{kj}^x} \quad (5.2.3)$$

The modes used may be arbitrarily scaled but first the MAC must be used to determine the correlated mode pairs. The COMAC can be described as the MAC with a rearrangement of the vectors to be compared. Where the MAC compares two modes at specific DOFs, the COMAC compares a DOF for specific correlated mode pairs. It is an attempt to identify the DOFs of the structure which have relatively poor correlation for all correlated mode pairs and which therefore contribute to low MAC values. A result of COMAC=1 for a particular DOF means that DOF has perfect correspondence for all the correlated mode pairs. A result of COMAC=0 for a particular DOF means that that DOF has no correspondence for any of the correlated mode pairs and therefore may be contributing to low MAC values.

5.2.1.4 Extended Coordinate Modal Assurance Criterion

Hunt [72] asserts that the COMAC cannot detect common test data errors such as scaling or polarity and therefore the extended coordinate modal assurance criterion (ECOMAC) was developed to overcome these deficiencies. The ECOMAC is given by,

$$ECOMAC_k = \frac{\sum_{j=1}^m \psi_{kj}^a \psi_{kj}^x}{2m} \quad (5.2.4)$$

Like the COMAC, the modes to be compared must first be paired by the MAC but conversely, must be of unit scale. Where the COMAC weighted each DOF the same regardless of magnitude, the ECOMAC considers the relative magnitudes of each DOF and thus the modes with the larger deflections will dominate the value of the ECOMAC. The numerical interpretation is the opposite of that which applies to the COMAC. A result of ECOMAC=0 for a particular DOF means that DOF has perfect correspondence for all correlated mode pairs. A result of ECOMAC=1 for a particular DOF means that DOF has no correspondence for any of the correlated mode pairs and therefore may be contributing to low MAC values.

Another form of the ECOMAC, which was also named COMAC, is described by [70],

$$COMAC_k = 1 - \frac{\sum_{j=1}^m \psi_{kj}^a \psi_{kj}^x}{2m} \quad (5.2.5)$$

where the requirements and characteristics are identical to the ECOMAC, but the numerical interpretation is the same as the original COMAC. Therefore, a result of COMAC=1 for a particular DOF means that DOF has perfect correspondence for all correlated mode pairs. A result of COMAC=0 for a particular DOF means that DOF has no correspondence for any of the correlated mode pairs and therefore may be contributing to low MAC values.

5.2.1.5 Coordinate Modal Error Function

The coordinate modal error function (COMEF) for a degree of freedom (DOF) k is given by [73],

$$COMEF_k = \frac{1}{m} \sum_{j=1}^m (WM_{kj}) (EM_{kj}) \quad (5.2.6)$$

$$WM_{kj} = \psi_{kj}^a \sum_{l=1}^m \psi_{kl}^a \quad (5.2.7)$$

$$EM_{kj} = \frac{\psi_{kj}^a \psi_{kj}^x}{\psi_{kj}^a} 100 \quad (5.2.8)$$

The modes used must be consistently scaled and must have been pre-determined to be correlated mode pairs using the MAC. Like the COMAC, it is an attempt

to identify the degrees of freedom of the structure which yield poor correlation and therefore contribute to low MAC values. However, this method attempts to weight small deflections with relatively small factors such that node lines and near boundary nodes have less effect than in the COMAC. The numerical result is in % error and can be positive or negative. The larger the absolute number, the greater the error, with the sign indicating the direction of the error away from the chosen reference mode set.

5.2.1.6 Inverse Modal Assurance Criterion

Mitchell [69] observes that the MAC is dominated by the anti-nodes of the mode shapes and therefore is not sensitive to small mode shape changes. To overcome this, he proposes the inverse MAC (IMAC) which is given by,

$$IMAC(\phi_i^a, \phi_j^x) = \frac{\sum_{k=1}^N \phi_{kj}^a{}^{-1} \phi_{kj}^x{}^{-1}{}^2}{\sum_{k=1}^N \phi_{kj}^a{}^{-1} \phi_{kj}^a{}^{-1} \sum_{k=1}^N \phi_{kj}^x{}^{-1} \phi_{kj}^x{}^{-1}} \quad (5.2.9)$$

where, like the MAC, the modes to be compared need not be similarly scaled. This is an attempt to focus the MAC on the node lines and away from the anti-nodes or maximum deflections by using the numerical inverse of each discrete DOF of the eigenvector. The IMAC is useful for detecting differences in nodal line position and therefore differences in that feature of the mode shapes. However, it is not a straight forward measure of correlation but could be interpreted as a nodal line motion index. Additional work is necessary to relate the IMAC value to the physical mode shape changes.

5.2.1.7 Scaled Modal Assurance Criterion

Brechlin, Bendel and Keiper [71] state that the MAC does not adequately handle modes which contain both translational and rotational DOFs. They defined the

scaled modal assurance criterion (SMAC) between two modes ϕ_i^a and ϕ_j^x as:

$$SMAC(\phi_i^a, \phi_j^x) = \frac{\phi_i^a{}^T [S] \phi_j^x}{(\phi_i^a{}^T [S] \phi_i^a)^{1/2} (\phi_j^x{}^T [S] \phi_j^x)^{1/2}} \quad (5.2.10)$$

specifically, to handle a mixture of translational and rotational DOFs. Because rotational deflections are of different units to translational deflections, and as a result the numerical values of the corresponding elements of the vector can be very different in magnitude, the MAC tends to be dominated by one or the other of the DOF types. This is overcome by using a weighting matrix $[S]$ which effectively resolves the magnitude differences between the translational and rotational deflections.

Due to the difficulty in measuring rotational DOFs, current industry practice is to use translational DOFs only when performing correlation between experimental and analytical modes. Therefore, the SMAC would most likely be used to compare only analytical mode shapes. However, the SMAC may prove quite useful when comparing mode shapes between two FE models modeled with shell elements because of the significant extra information provided by the rotational deflections.

5.2.1.8 New Modal Assurance Criterion

The new modal assurance criterion (NMAC) [70] starts with the MAC as given in Equation 5.2.1 and determines which DOF contributes the most to reducing the MAC value for each mode pair. This is done by removal of successive DOF and monitoring for the greatest increase in MAC value. The result is improved MAC values because the DOFs which contributed the most to lowering the MAC values, have been removed.

The NMAC, while aiding in improving the MAC values, also identifies the DOFs which contribute to low MAC values as does the COMAC and ECOMAC. However, the NMAC has the advantage of not requiring normalization of the mode

shapes or prior determination of correlated mode pairs.

5.2.2 Orthogonality

This section describes various methods that use orthogonality in comparing two mode sets. A basis for convergence of an eigensolution is to check that the eigenvectors obtained are orthogonal with respect to the mass matrix as given by:

$$[\phi^a]^T [M] [\phi^a] = [I_N] \quad (5.2.11)$$

where $[I_N]$ is the "numerical" identity matrix. In practice, $[I_N]$ will differ from the "true" identity matrix $[I]$ with the off-diagonal terms being relatively small numerical values rather than zero. The allowable size of the off-diagonal terms is set by the eigensolver's convergence criteria.

In an analogous computation, the correlation between two sets of eigenvectors can be assessed by determining $[I_N]$ and setting correlation criteria for the allowable size of the off-diagonal terms. The analytical mass matrix is generally used since it is much easier to obtain than is the experimental mass matrix.

The number of measured DOFs is usually much smaller than that for the analytical model. Therefore, an expansion of the experimental eigenvectors to analytical size or a reduction of the analytical mass matrix to experimental size, using a technique such as SEREP [60], is required to obtain eigenvectors and a mass matrix which have comparable DOFs. Although SEREP does not explicitly require a mass matrix, the expansion-reduction procedure makes orthogonality checks more computationally-intensive than vector correlation methods.

5.2.2.1 Normalized Cross Orthogonality

The normalized cross orthogonality (NCO) check [74] is given by:

$$NCO(\phi_i^x, \phi_j^a) = \frac{\phi_i^{x\ T}[M_A] \ \phi_j^a \ ^2}{(\phi_i^{x\ T}[M_A] \ \phi_i^x) \ \phi_j^{a\ T}[M_A] \ \phi_j^a} \quad (5.2.12)$$

where $[M_A]$ is an analytical mass matrix that has been either retained at "a" analytical size or reduced to "x" experimental size. Similar to the MAC, the modes to be compared need not be similarly scaled (or normalized). The results are values between 0 and 1, with NCO=1 indicating perfect correlation and 0 indicating no correlation. Ideally, for good correlation the off-diagonal terms should approach zero.

5.2.2.2 Pseudo Orthogonality Check

The pseudo orthogonality check (POC) is given by [75, 76, 77],

$$POC_{ij} = \sum_{k=1}^n \sum_{l=1}^n \phi_{ki}^x m_{kl}^a \phi_{lj}^a \quad (5.2.13)$$

The POC uses an analytical mass matrix and can be done at either "x" experimental DOFs or at the "a" analytical DOFs. For either set of DOFs a reduction or expansion process such as SEREP must be used to achieve the proper reduced mass matrix or expanded eigenvectors. Ideally, all off-diagonal terms must be very near null for perfect correlation but values as high as 0.1 are accepted for some applications. In practice, off-diagonal terms may be quite small (less than 0.05) and the vectors still may be relatively uncorrelated.

5.2.2.3 Coordinate Orthogonality Check

Avitabile and Pechinsky [78] developed the coordinate orthogonality check (CORTHOG) to identify how the individual DOFs contribute to the orthogonality check produced by the POC. This is achieved by taking the element-by-element

difference between the POC and the expected values obtained from analytical orthogonalization and normalizing by the maximum difference between them. The CORTHOG is given by:

$$CORTHOG_{ij}^{kl} = \frac{\frac{\phi_{ki}^x m_{kl}^a \phi_{lj}^a}{\sum_{k=1}^n \sum_{l=1}^n \phi_{ki}^x m_{kl}^a \phi_{lj}^a}}{\frac{\phi_{ki}^a m_{kl}^a \phi_{lj}^a}{\sum_{k=1}^n \sum_{l=1}^n \phi_{ki}^a m_{kl}^a \phi_{lj}^a}} \quad (5.2.14)$$

where kl defines the DOF pair and ij defines the mode pair.

The CORTHOG is claimed to provide insight into the DOFs which are the best and least correlated between two mode sets. It is asserted that near-null modal deflections may have a large effect on the POC off-diagonal terms and that obtaining POC off-diagonal terms near null does not necessarily indicate true correlation.

5.2.2.4 SEREP-Based Normalized Cross Orthogonality

The SEREP mass matrix reduced cross orthogonality (SCO) is given by [79]:

$$SCO(\phi_i^x, \phi_j^a) = \frac{\phi_i^{x\ T} ([\phi^a]^+)^T [\phi^a]^+ \phi_j^a}{\left(\phi_i^{x\ T} ([\phi^a]^+)^T [\phi^a]^+ \phi_i^x \right) \phi_j^{a\ T} ([\phi^a]^+)^T [\phi^a]^+ \phi_j^a} \quad (5.2.15)$$

where $[\phi^a]^+$ is the generalized pseudo inverse of $[\phi^a]$. This is similar to the NCO with the exception that the analytical mass matrix is not explicitly used in favour of the SEREP-reduced mass matrix. Therefore, like the MAC, only the eigenvectors are required and this makes the SCO much easier to implement than other orthogonality methods. While either the analytical or experimental mode shapes may be used for the SEREP-reduced mass, the analytical mode shapes are usually chosen to avoid the introduction of noise and other test uncertainties from the experimental mode shapes into the computation.

The SCO is claimed to be more sensitive than the MAC to actual differences in

mode shapes, by yielding higher values when comparing two similar mode shapes and lower values when comparing two dissimilar mode shapes.

5.2.3 Frequency Response Function Correlation

This section describes the methods used for correlating frequency response functions (FRFs). The use of FRFs for correlation instead of eigenvectors is attractive because experimental FRFs are much more easily obtainable than *experimental* eigenvectors, which require significant data processing of numerous FRFs. Further, the data processing (curve fitting) performed by the modal analysis can introduce significant errors into the resulting mode shapes, especially when the modal density is high. However, since FRFs contain the responses from many experimental modes simultaneously, a significant frequency shift from the experimental to analytical frequencies for just a few of the modes may result in poor correlation.

5.2.3.1 Frequency Domain Assurance Criterion

The frequency domain assurance criterion (FDAC) is given by [80]:

$$FDAC(\omega^a, \omega^x)_k = \frac{\sum_{j=1}^n H_{jk}^a(\omega^a) H_{jk}^x(\omega^x)^*}{\sqrt{\sum_{j=1}^n H_{jk}^a(\omega^a) H_{jk}^a(\omega^a)^* \sum_{j=1}^n H_{jk}^x(\omega^x) H_{jk}^x(\omega^x)^*}}^2 \quad (5.2.16)$$

where $H^a(\omega^a)$ is the analytical FRF at the analytical frequency ω^a , $H^x(\omega^x)$ is the experimental FRF at experimental frequency ω^x and k is the excitation DOF for both the analytical and experimental FRFs.

The FDAC is analogous to the MAC and therefore yields values between 0 and 1. A result of $FDAC = 1$ indicates perfect correlation, while 0 indicates no correlation.

Pascual, Golinval and Razeto [81] point out that a shortcoming of the FDAC is that it allows the pairing of FRFs that are 180 degrees out-of-phase and in order to have any physical meaning the two FRFs should be at least in the same semi-plane as the excitation force. They propose a new FDAC as the cosine between two FRFs which is given by,

$$FDAC(\omega^a, \omega^x) = \frac{H^a(\omega^a)^T H^x(\omega^x)}{H^a(\omega^a) H^x(\omega^x)} \quad (5.2.17)$$

The new FDAC has values between -1 and 1, with a negative value indicating the two FRFs are out-of-phase. An FDAC=1 indicates perfect correlation between the two FRFs.

5.2.3.2 Frequency Response Scale Factor

The frequency response scale factor (FRSF) is given by [81]:

$$FRSF(\omega^a, \omega^x) = \frac{H^a(\omega^a)^T [W] H^x(\omega^x)}{H^a(\omega^a)^T [W] H^a(\omega^a)} \quad (5.2.18)$$

where $H^a(\omega^a)$ is the analytical FRF at analytical frequency ω^a , $H^x(\omega^x)$ is the experimental FRF at the experimental frequency ω^x and $[W]$ is a weighting matrix.

The FRSF is analogous to the MSF and therefore yields values between -1 and 1. Where the FDAC gives a quantitative comparison of two FRFs, the FRSF gives a qualitative comparison and therefore is not useful for assessing the degree of correlation.

5.2.3.3 Frequency Response Assurance Criterion

The frequency response assurance criterion (FRAC) is given by [82, 83]:

$$FRAC(j)_k = \frac{\sum_{i=1}^m H_{jk}^a(\omega_i) H_{jk}^x(\omega_i)^*}{\sum_{i=1}^m H_{jk}^a(\omega_i) H_{jk}^a(\omega_i)^*} \frac{\sum_{i=1}^m H_{jk}^x(\omega_i) H_{jk}^x(\omega_i)^*}{\sum_{i=1}^m H_{jk}^x(\omega_i) H_{jk}^x(\omega_i)^*} \quad (5.2.19)$$

where $H^a(\omega_i)$ is the analytical FRF at frequency ω_i , $H^x(\omega_i)$ is the experimental FRF also at frequency ω_i , j is the response DOF and k is the excitation DOF.

The FRAC is analogous to the COMAC and therefore yields values between 0 and 1 for each DOF. A result of FRAC=1 indicates perfect correlation, while 0 indicates no correlation. Heylen and Avitabile [83] point out that interpretation of FRAC values can be difficult. For lightly damped structures, which exhibit large maximum to minimum amplitude ratios, the FRAC may yield relatively low values while visually the FRFs appear to correlate quite well. To help compensate for this they suggest the use of the logarithm or absolute value of the FRAC.

5.2.4 Examples

The following four figures show examples of the correlation methods—vector, orthogonality and FRF—discussed in the previous sections.

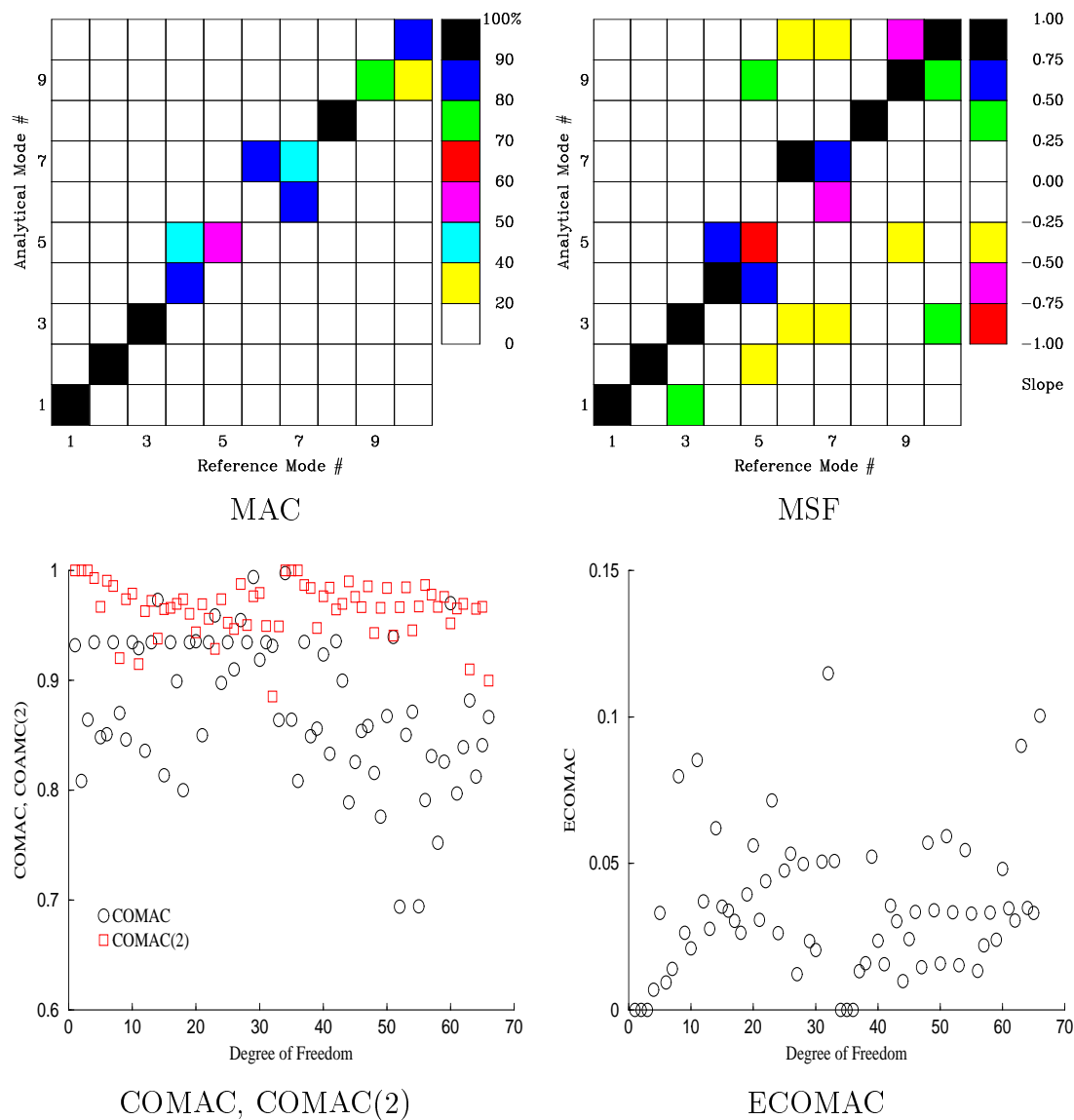


Figure 5.1: Vector Correlation Examples

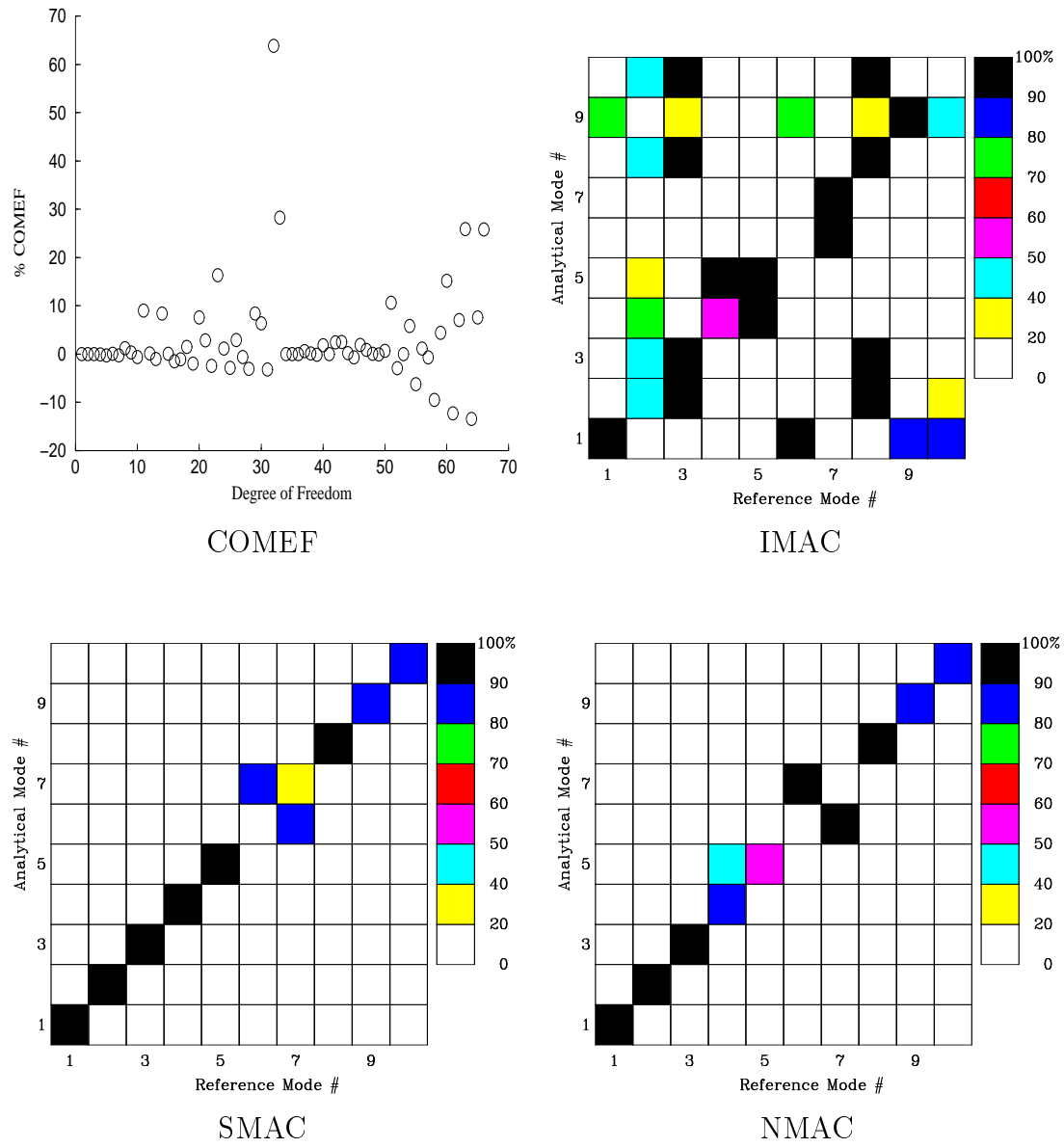


Figure 5.2: Vector Correlation Examples (Continued)

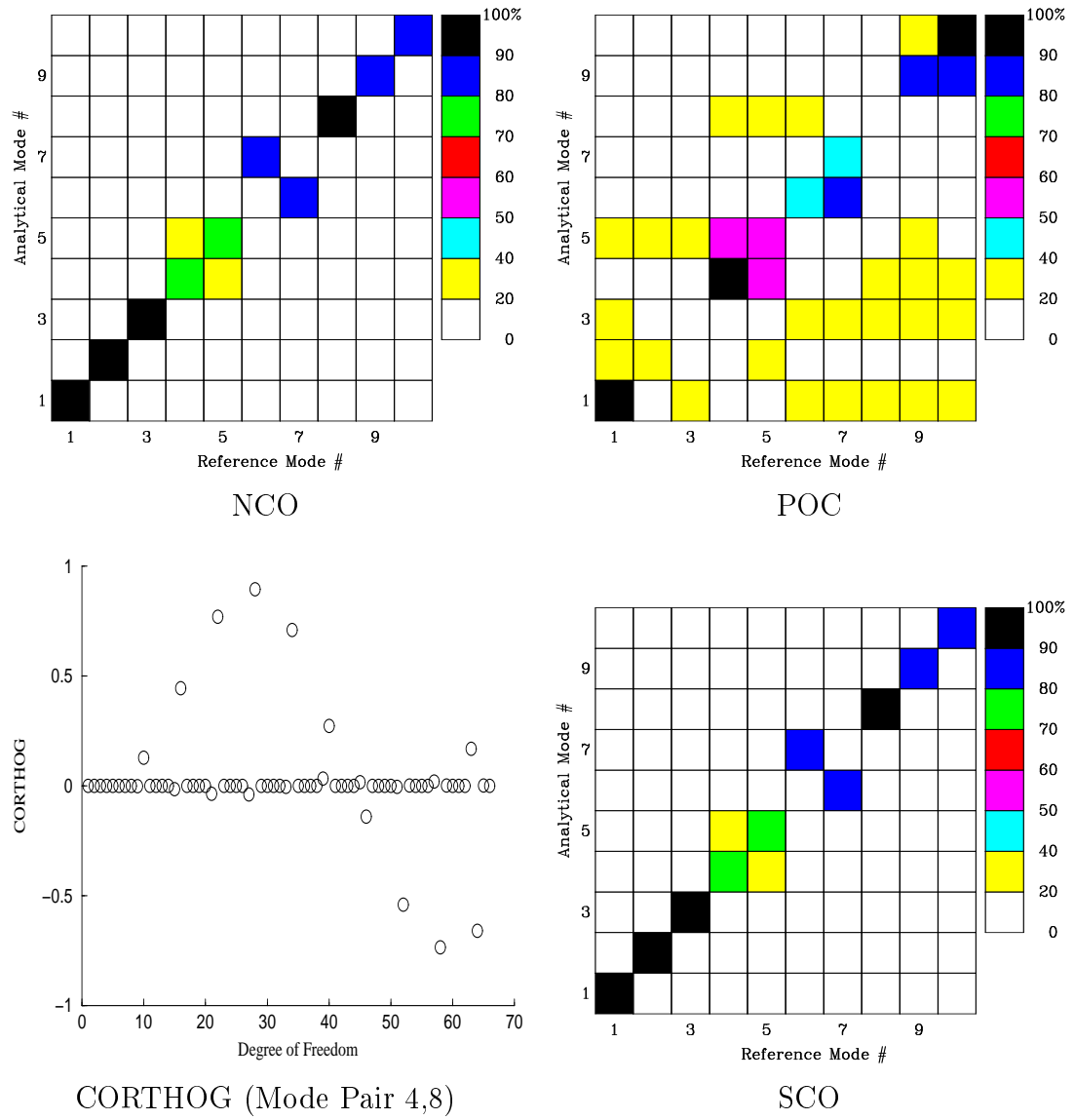


Figure 5.3: Orthogonality Examples

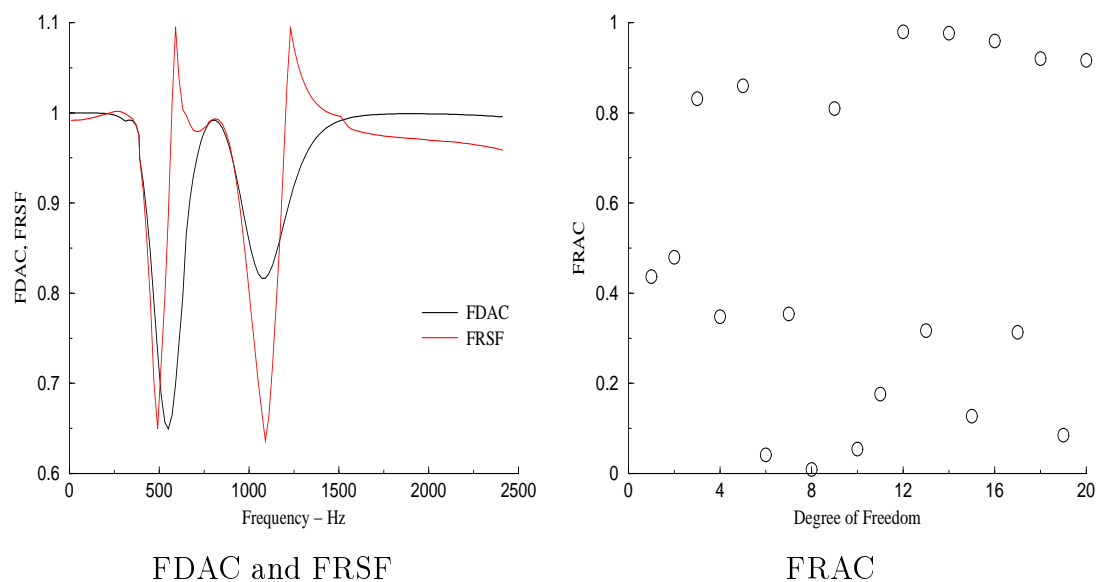


Figure 5.4: FRF Correlation Examples

A simple cantilevered beam FE analysis was used to produce the analytical data and a slightly perturbed (from the reference) cantilevered beam FE analysis was used to provide the reference (pseudo experiment) data.

The next two sections—MAC in the Frequency Domain and Axisymmetric Structures—present the three new correlation developments.

5.3 MAC in the Frequency Domain

The Modal Assurance Criterion (MAC [67]) has been used as a measure of correlation between test-derived and analytically-predicted mode shapes for many years. The fact that the MAC considers only mode shapes usually means that a separate natural frequency comparison must be used in conjunction with the MAC values in order to determine the correlated mode pairs. The mode shape correlation has generally been displayed as a MAC matrix plotted against experimental mode number on the horizontal axis and analytical mode number on the vertical axis. The frequency correspondence is usually displayed with a separate plot such as the experimental natural frequency versus the analytical natural frequency.

The auto-MAC, which compares a set of mode shapes with themselves, is used to determine if the number and/or selection of the chosen measurement DOFs are sufficient to be able to distinguish the modes from each other. The existence of off-diagonal correlation terms in the auto-MAC is an indication of spatial aliasing. If the MAC shows off-diagonal correlation it cannot be determined without the auto-MAC whether this is due to spatial aliasing or to genuine correspondence between the two modes. Thus, the MAC, the auto-MAC and the natural frequency comparison plots are all used to determine the overall correlation/correspondence of the modes.

This thesis presents a way of plotting the MAC, auto-Mac and natural frequency comparison simultaneously such that the mode shape correlation, the degree of spatial aliasing and the natural frequency comparison can all be obtained from one plot. The new plot format, called the FMAC, is naturally extended to the correlation of frequency response functions (FRFs) using the Frequency Domain Assurance Criterion (FDAC, [81]). The advantages of the new plot method are shown by a case study of a real structure.

5.3.1 Evolution of the FMAC: MAC Plot with Frequency Scales

An example of a conventional MAC plot for a simple plate is shown in Figure 5.5. The use of the different colour-filled or shaded rectangles to indicate the MAC values is shown to be quite useful. Since the MAC gives no information about the natural frequency correspondence and can sometimes show good correlation between modes that have significant frequency separation, a natural frequency comparison plot is used as shown in Figure 5.6. Accordingly, the two plots are

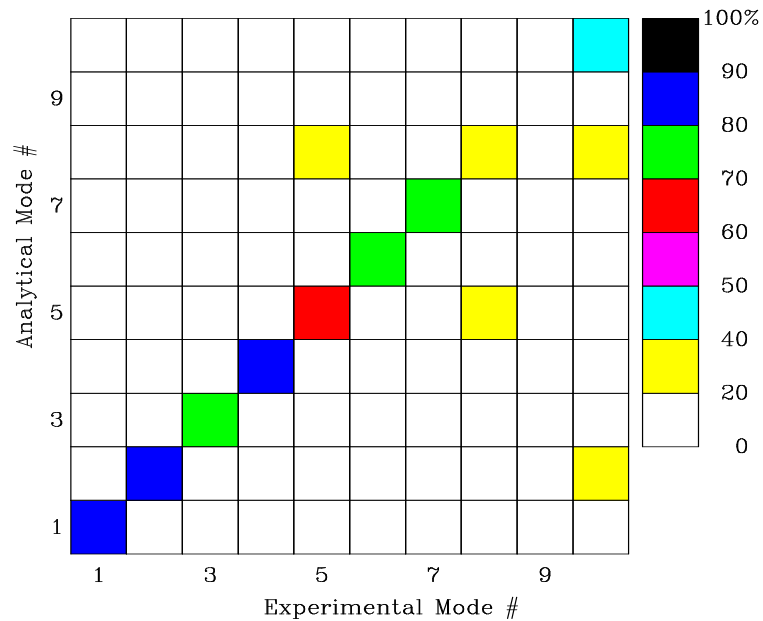


Figure 5.5: Original MAC plot

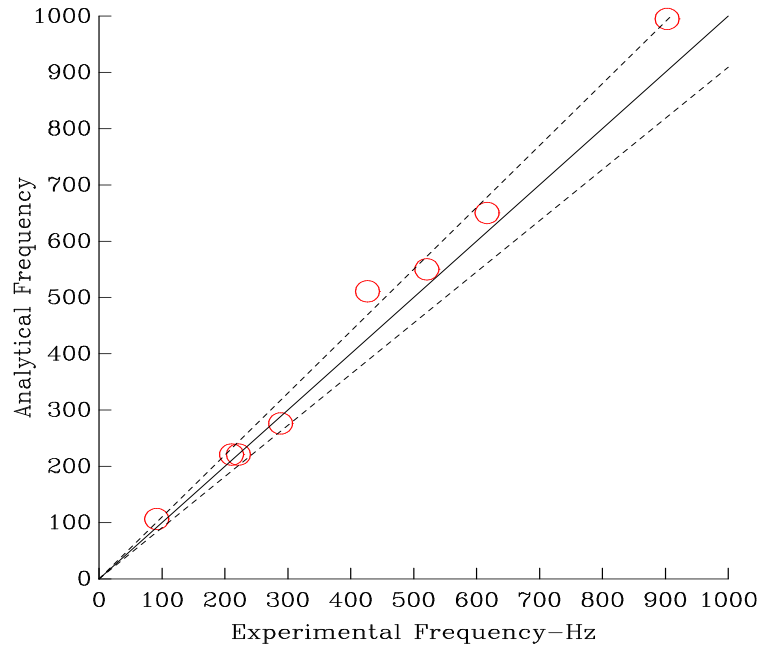


Figure 5.6: Frequency Comparison

used together to determine the mode shape correlation and natural frequency comparison for each mode. However, neither the MAC in Figure 5.5 or the natural frequency comparison in Figure 5.6 indicates which mode pair corresponds to which natural frequency pair.

Further, the MAC can show correlation between off-diagonal mode pairs such as experimental mode 5 and analytical mode 8 in Figure 5.5. In order to determine whether the off-diagonal correlation is real or is due to spatial aliasing (if the number and location of the chosen measurement points are sufficient to be able to distinguish the modes) the auto-MAC, shown in Figure 5.7, is used.

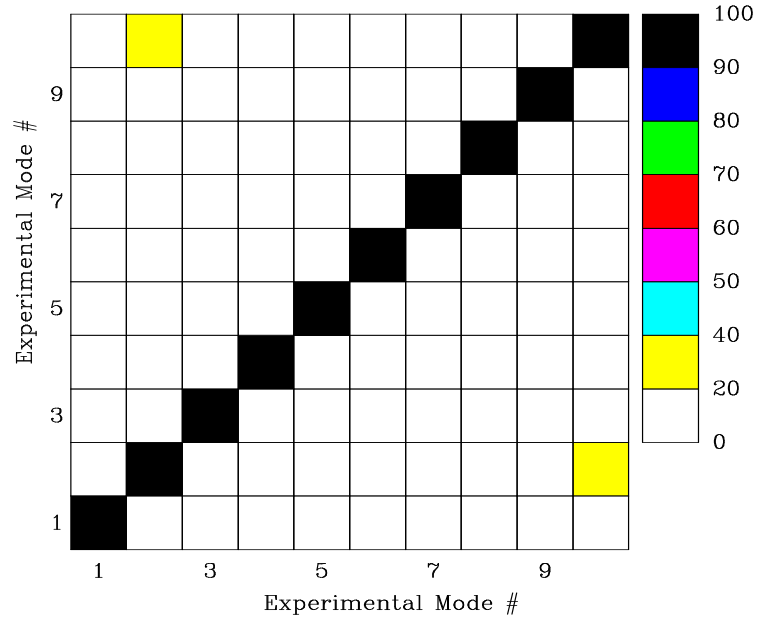


Figure 5.7: Auto-MAC of Experimental Modes

In reference [84] it was shown that it was necessary to be able to compare two different sets of MAC values, which led to a "new" MAC plot that used symmetric symbols with a size proportional to the MAC value instead of the colour-filled or shaded rectangles. The first version of the "new" MAC plot is displayed in the conventional way with the experimental mode number on the horizontal axis and the analytical mode number on the vertical axis as shown in Figure 5.8. However, centred on the coordinates of each mode number pair a circle is drawn with a radius proportional to the value of the relevant MAC. Additionally, to provide a visual scale, a dashed box representing perfect correlation ($\text{MAC} = 1$) is plotted for each mode number pair. The relative size of the circle to that of the dashed box illustrates the MAC value relative to a perfect value of 1. This proved very useful for overlaying MAC plots for comparison, as is shown in Figure 5.8 with the auto-MAC of the experimental modes represented by the black circles and the MAC represented by the red circles.

It has been a goal of many researchers in the area of model correlation to find

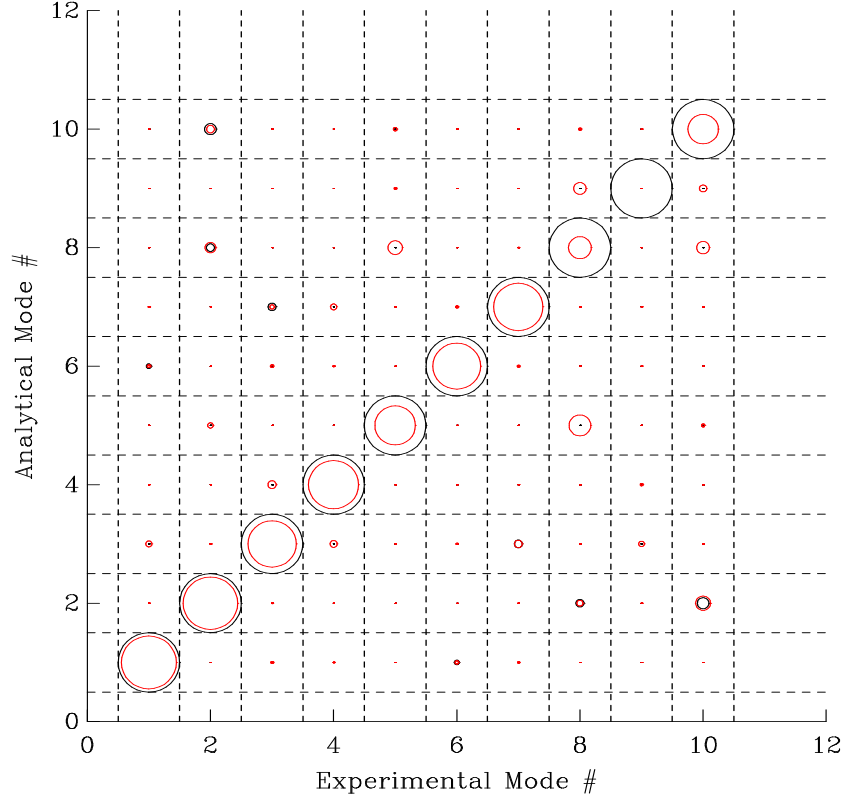


Figure 5.8: The New MAC plot

a way to display the natural frequency information along with the MAC values to get an immediate measure of both the mode shape correlation and natural frequency comparison. This new way of displaying the MAC values, as shown in Figure 5.8, led to replacing the mode numbers on the horizontal and vertical axes with their respective natural frequencies, resulting in the type of MAC plot shown in Figure 5.9 called the FMAC. With the auto-MAC for the experimental modes being represented by the black circles and the MAC by the red circles, the natural frequency separation is shown by the vertical separation between the black and the red circles. The addition of the frequency separation lines, in this case 10%, gives a visual scale for the amount of frequency difference between the test and analytical modes. The change in circle size from the black to the red circles gives a visual measure of the change in the MAC value from the perfect value of $\text{MAC}=1$. The figure also shows the modal density or the relative frequency spacing of the

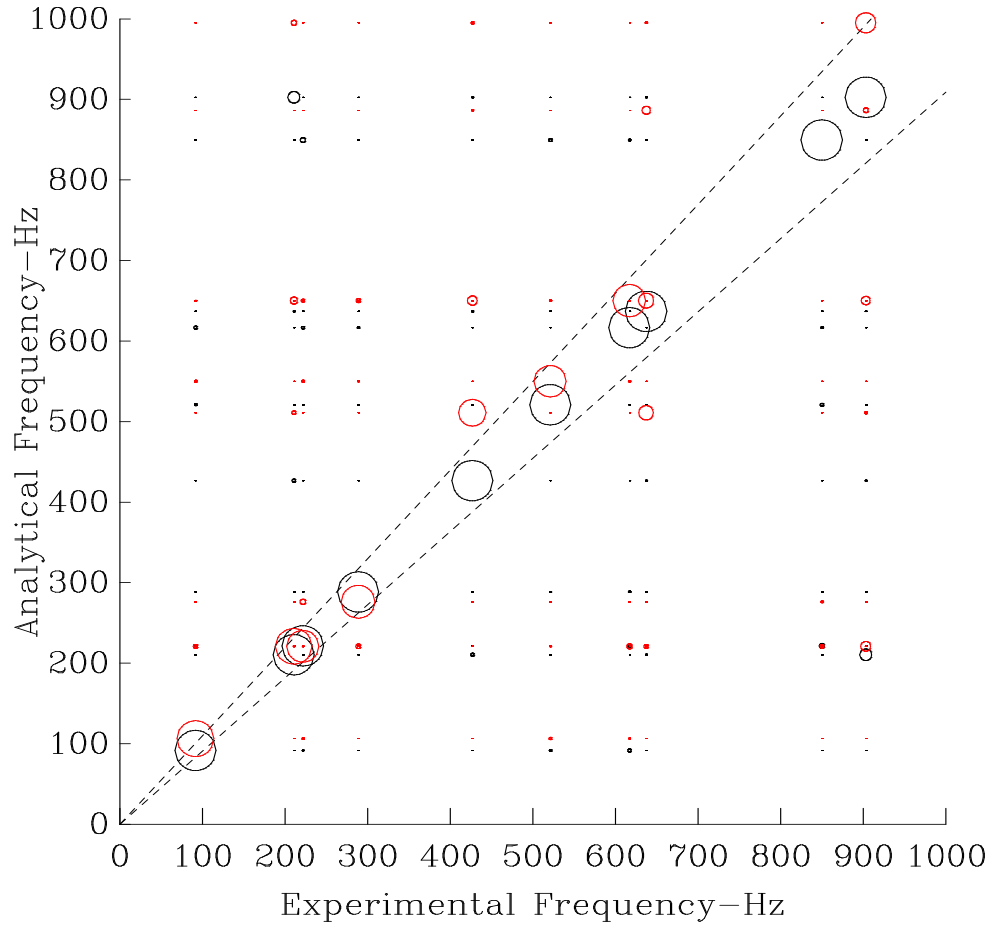


Figure 5.9: FMAC: MAC plot with frequency scales

modes. In addition to assisting in the display of frequency separation between the test and analytical modes, the auto-MAC shows the extent of the spatial aliasing [85]. Note that double modes are shown by concentric circles.

The FMAC plot as shown in Figure 5.9 displays all the information needed to assess the correlation. However, when considering a large frequency range (containing a large number of modes) it may be difficult to judge the natural frequency separation at the lower end of the range for example, between 0 and 300 Hz in Figure 5.9. For this reason an alternative FMAC plot was developed using a percentage frequency difference scale on the y-axis in place of the analytical frequency.

Figure 5.10 is an FMAC plot with percentage frequency difference plotted on the y-axis for the same flat plate used in the FMAC plot of Figure 5.9. The figure shows that the frequency separation of the measured and predicted modes can be determined quite accurately. However, it should be noted that, in general, as the frequency resolution is increased (the y-axis scale is decreased) the amount of aliasing information that can be shown is decreased.

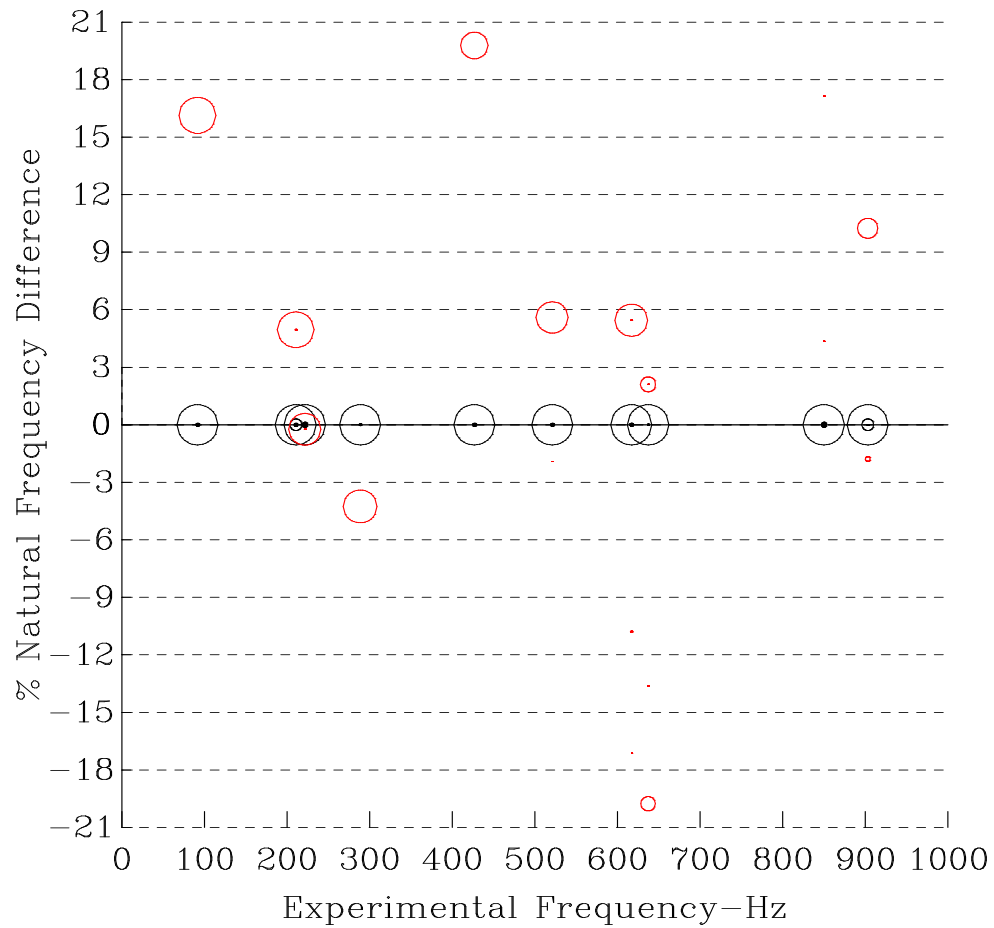


Figure 5.10: FMAC with natural frequency difference on the y-axis

In the particular case of structures with modes that have close natural frequencies (high modal density), or for structures with double modes from symmetry, a plot of the FMAC shows the modes nearly on top of each other. For this reason, a further variation of the FMAC with natural frequency difference on the y- axis was developed with the measured mode number on the x-axis. Figure 5.11 shows

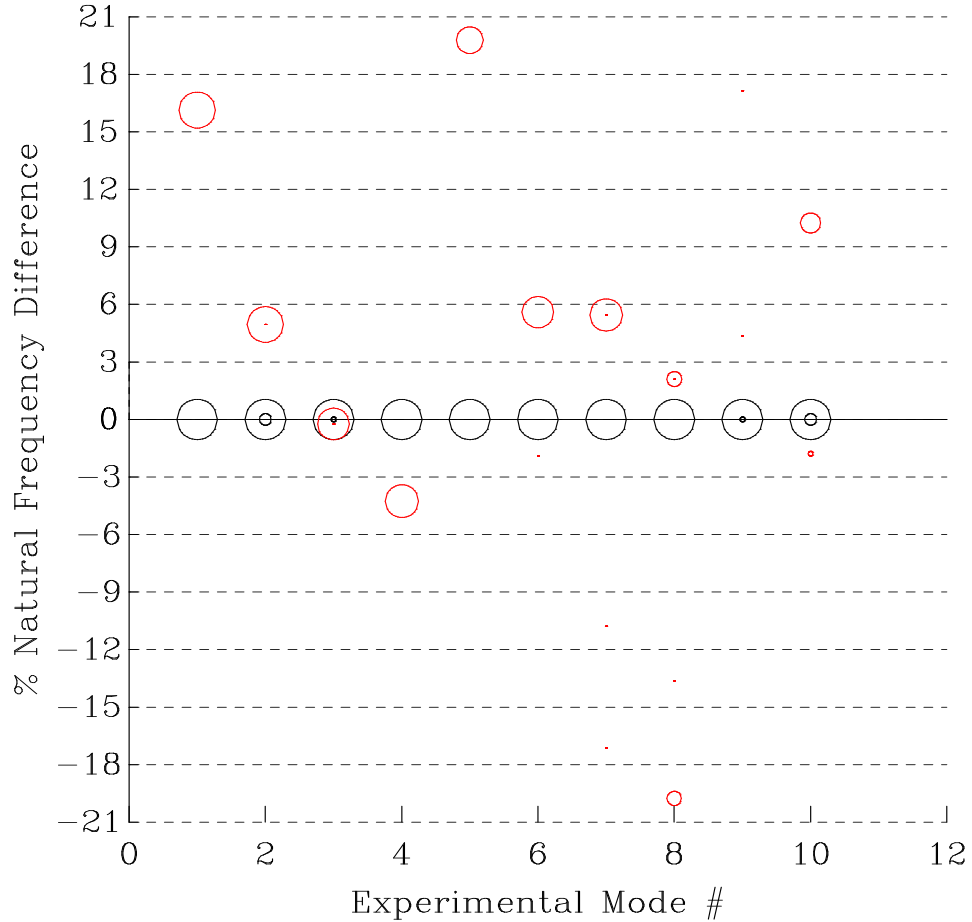


Figure 5.11: FMAC with natural frequency difference on the y-axis and measured mode number on the x-axis

the FMAC with natural frequency difference on the y- axis and measured mode number on the x-axis for the flat plate example. The figure shows that all the modes can now be clearly distinguished and that again the frequency separation can be determined quite accurately. This form of the FMAC can be very useful

for axisymmetric structures that have multiple sets of orthogonal mode pairs [50].

5.3.2 Frequency Domain Correlation

The use of frequency response functions (FRFs) for correlation instead of eigenvectors is attractive because experimental FRFs are more easily obtainable than eigenvectors, which require significant data processing of numerous FRFs. Such data processing (curve fitting), performed by the modal analysis, may introduce significant errors into the resulting mode shapes, which is particularly the case when the modal density is high. Further, there are occasions when test data are too noisy to extract the mode shapes accurately leaving only the FRFs available for correlation. The primary tools used for the correlation of FRFs are the Frequency Response Assurance Criterion (FRAC) and the Frequency Domain Assurance Criterion (FDAC). However, a third tool introduced here as the Modal FRF Assurance Criterion (MFAC) can be used as an intermediate step between the MAC and FDAC.

The FRAC is defined by [82, 83]:

$$FRAC(j)_k = \frac{\sum_{i=1}^m H_{jk}^a(\omega_i) H_{jk}^x(\omega_i)^*}{\sqrt{\sum_{i=1}^m H_{jk}^a(\omega_i) H_{jk}^a(\omega_i)^*} \sqrt{\sum_{i=1}^m H_{jk}^x(\omega_i) H_{jk}^x(\omega_i)^*}} \quad (5.3.1)$$

where $H^a(\omega_i)$ is the analytical FRF at frequency ω_i , $H^x(\omega_i)$ is the experimental FRF also at frequency ω_i , j is the response DOF and k is the excitation DOF. The FRAC is analogous to the COMAC [68] and therefore yields values between 0 and 1 for each DOF. A result of FRAC=1 indicates perfect correlation, while 0 indicates no correlation. Since FRFs contain the responses from many experimental modes simultaneously, a significant discrepancy in natural frequency between the experimental and analytical values for just a few of the modes may result in poor FRAC values.

The FDAC is given by [81]:

$$FDAC(\omega^a, \omega^x)_k = \frac{\sum_{j=1}^n H_{jk}^a(\omega^a) H_{jk}^x(\omega^x)^*}{\sqrt{\sum_{j=1}^n H_{jk}^a(\omega^a) H_{jk}^a(\omega^a)^* \sum_{j=1}^n H_{jk}^x(\omega^x) H_{jk}^x(\omega^x)^*}}^2 \quad (5.3.2)$$

where $H^a(\omega^a)$ is the analytical FRF at the analytical frequency ω^a , $H^x(\omega^x)$ is the experimental FRF at experimental frequency ω^x and k is the excitation DOF for both the analytical and experimental FRFs. The FDAC is analogous to the MAC and therefore yields values between 0 and 1. A result of $FDAC = 1$ indicates perfect correlation, while 0 indicates no correlation.

The MFAC is introduced here with the following definition [85]:

$$MFAC(\omega^a, \omega^x)_k = \frac{\sum_{j=1}^n \phi_j^a(\omega^a) H_{jk}^x(\omega^x)^*}{\sqrt{\sum_{j=1}^n \phi_j^a(\omega^a) \phi_j^a(\omega^a)^* \sum_{j=1}^n H_{jk}^x(\omega^x) H_{jk}^x(\omega^x)^*}}^2 \quad (5.3.3)$$

where $\phi^a(\omega^a)$ is the analytical mode shape at any analytical frequency, ω^a , and $H^x(\omega^x)$ is the experimental FRF at any experimental frequency, ω^x . The MFAC is analogous to the MAC and therefore yields values between 0 and 1. A result of $MFAC = 1$ indicates perfect correlation, while 0 indicates no correlation.

The MFAC and FDAC have a distinct advantage over the FRAC in that they allow for the spatial comparison of the analytical mode shapes to the experimental FRFs and the analytical FRFs to the experimental FRFs, respectively, at different frequencies and therefore the frequency shift does not affect the correlation. The MFAC and FDAC plotted with frequency scales are natural extensions of the FMAC plot.

The MFAC has a distinct advantage over both the FDAC and the MAC in that it allows for the comparison of the two data sets with the greatest fidelity—the analytical mode shapes and the experimental FRFs. The analytical mode shapes,

unlike the corresponding FRFs, require no assumptions about damping. Similarly, the experimental FRFs, unlike the corresponding mode shapes, require no post-processing of the measured data. However, the MFAC is only useful for relatively lightly damped modes since the analytical mode shapes are real quantities from an undamped eigen-solution and the experimental FRFs are complex quantities due to the inherent damping in the structure.

The MFAC and FDAC plotted with frequency scales are natural extensions of the FMAC plot. Accordingly, both the FDAC and MFAC were compared to the FMAC in the case study that follows.

5.3.3 Case Study: Combustor Casing

The case study is for a combustor casing for which an FE model and both mode shape and FRF test data were available. Figure 5.12 shows the MSC/NASTRAN finite element model for the combustor casing. The shell model contained about 3700 nodes (18,500 DOFs) and was used to calculate the first 19 modes. Test data were taken (previously at Imperial College) for 2 rings of 12 equally-spaced points in the radial direction and 1 ring of 12 equally-spaced points in both the radial and axial (along the engine axis) directions. Therefore, a total of 48 FRFs were taken from which 14 mode shapes were generated. The corresponding analytical FRFs were generated using the FE model.

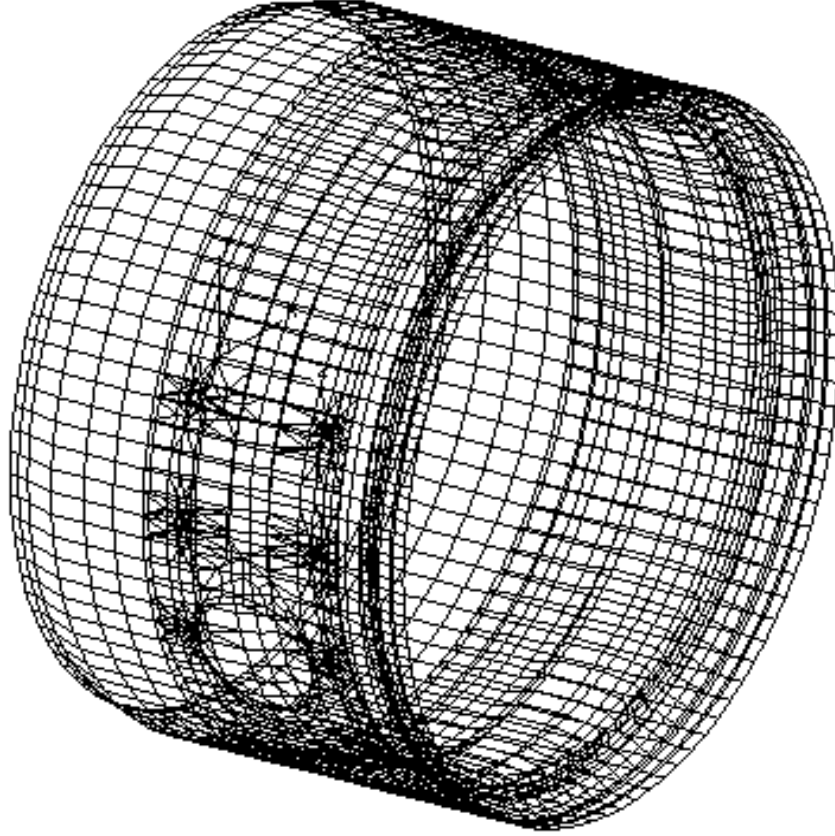


Figure 5.12: MSC/NASTRAN Model of Combustor Casing

The FMAC plot is shown in Figure 5.13. The auto-MAC for the experimental modes is shown by the black circles, the MAC is shown by the red circles and the frequency lines are for a spread of $\pm 10\%$. The frequency shift (vertical from the black to the red circles) is within $\pm 10\%$ for all modes except the mode at about 100 Hz. A degree of spatial aliasing is shown by the auto-MAC at experimental frequencies of about 70 Hz, 170 Hz and 260 Hz. The corresponding MAC values, with respective frequency shifts, show that it is indeed aliasing and not genuine correspondence.

Figure 5.14 shows the Frequency Domain Assurance Criterion (FDAC), in the new plot format, for the FRF correlation in this case. The FDAC values were determined by comparing the analytical FRFs at their resonant frequencies to the experimental FRFs at their resonant frequencies, a response vector which is

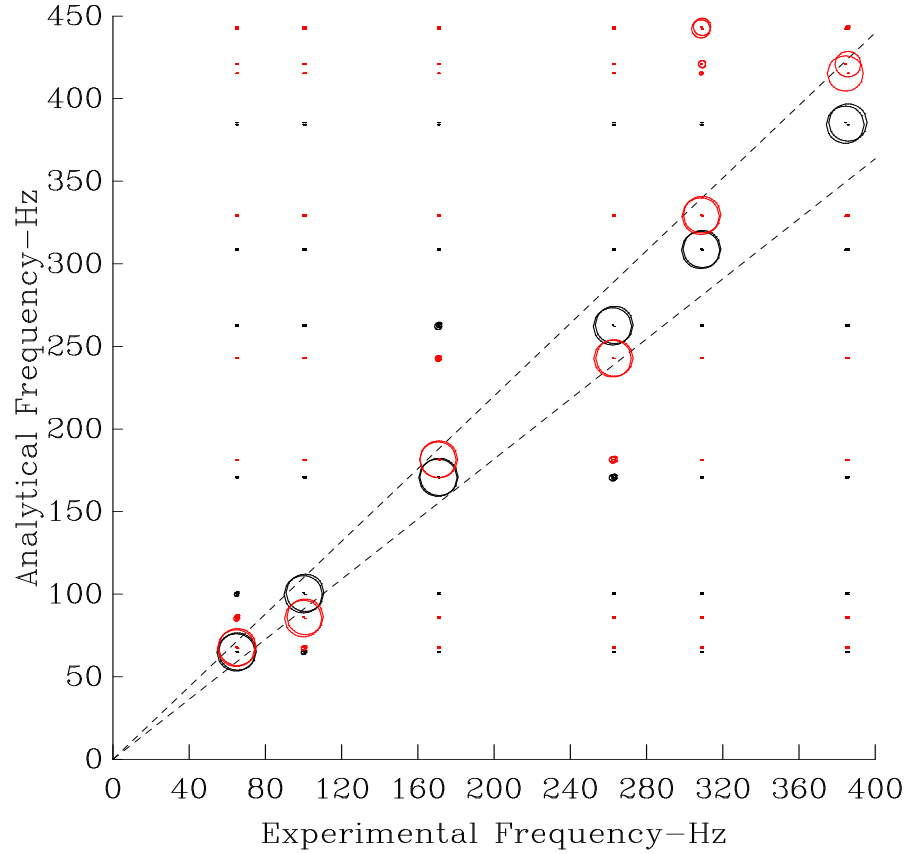


Figure 5.13: FMAC plot for Combustor Casing

sometimes referred to as the Operating Deflection Shape (ODS). The auto-FDAC for the experimental ODSs is shown by the black circles, the FDAC is shown by the red circles and the frequency lines are for a spread of 10%. Note the resemblance to the FMAC plot shown in Figure 5.13. The correlation is comparable to the FMAC. The auto-FDAC shows the spatial aliasing and for the experimental frequencies at about 70Hz, 170 Hz and 260 Hz the corresponding FDAC values confirm that it is aliasing and not genuine correlation. The frequency shift (vertical from the black to the red circles) is within 10% for all ODSs except at about 100 Hz.

The Modal FRF Assurance Criterion (MFAC) plot is shown in Figure 5.15. The MFAC values were determined by comparing the analytical mode shapes at

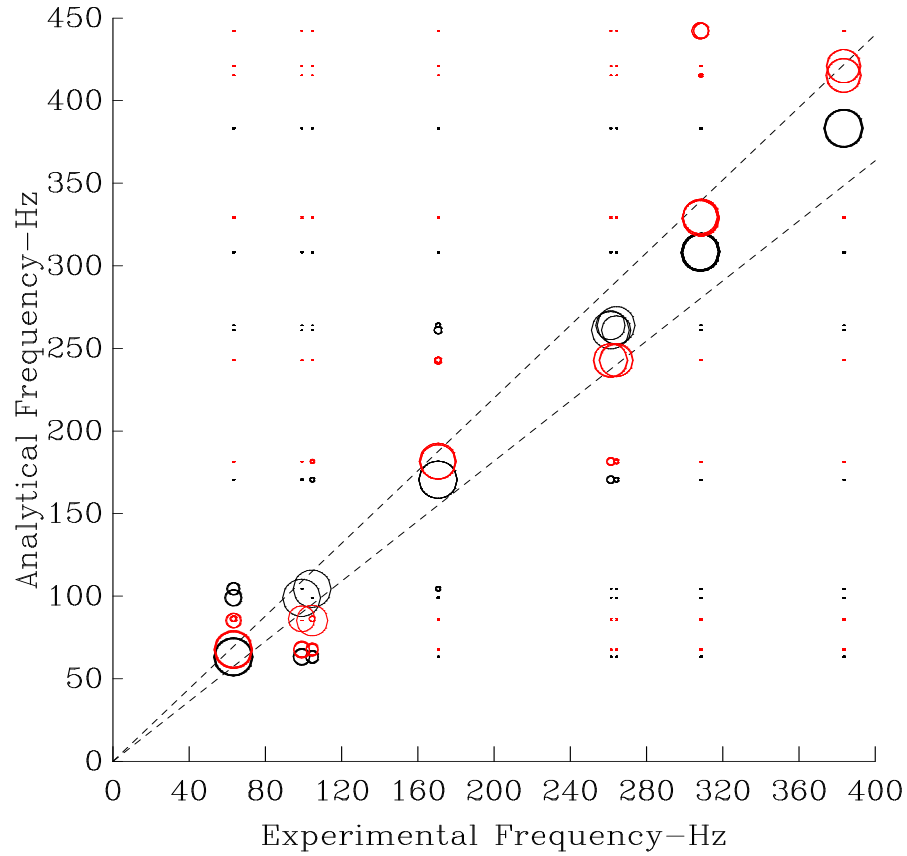


Figure 5.14: New Plot Format for FDAC of FRFs

their natural frequencies to the experimental FRFs at their resonant frequencies (ODSs). The auto-MFAC for the experimental mode shapes is shown by the black circles, the MFAC between the analytical mode shapes and the experimental ODSs is shown by the red circles and the frequency lines are for a spread of $\pm 10\%$. Note the resemblance to both the FMAC plot shown in Figure 5.13 and the FDAC plot shown in Figure 5.14. The correlation is comparable to both (the FMAC and FDAC) and for frequencies at about 100 Hz, 170 Hz, 260 Hz and 310 Hz it is not as good as the FMAC or FDAC, which is probably due to the damping present in the FRFs and not in the mode shapes. The off-diagonal correlation shown by the auto-MFAC for the experimental frequencies at about 70 Hz, 170 Hz and 260 Hz is again confirmed to be aliasing and not genuine correlation by the corresponding

MFAC values. The frequency shift (vertical from the black to the red circles) is again within 10% for all frequencies except at about 100 Hz.

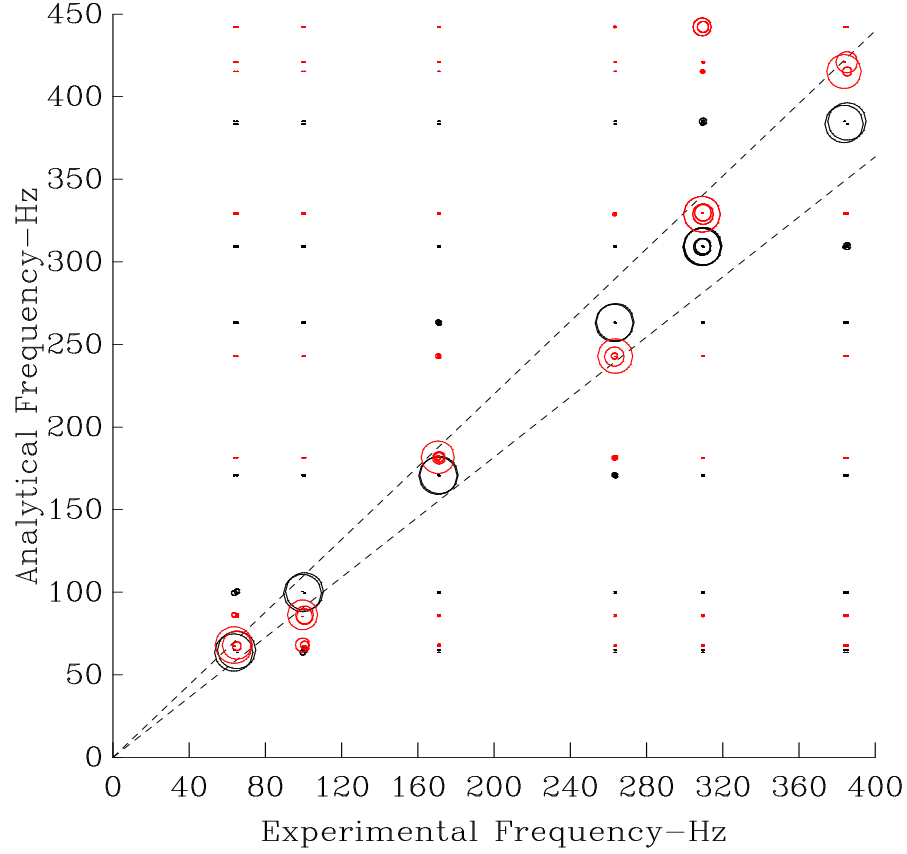


Figure 5.15: MFAC of Mode Shapes versus FRFs

Note that the lack of spatial aliasing (off diagonal correlation) shown in Figures 5.13 through 5.15 indicates that the use of 2 axial (and 12 circumferential) stations was sufficient to distinguish the modes from one another. This is also demonstrated in the case study in Chapter 6 where 3 and 2 axial stations were used for the combustor and turbine casings, respectively.

5.4 Axisymmetric Structures

The prediction of the vibration properties for an axisymmetric structure using an FE model will result in most of the modes existing as orthogonal pairs. The two modes of each orthogonal pair will have identical natural frequencies and mode shapes of the same basic pattern but with different spatial phase angles of the diametral nodal lines that make the modes orthogonal. The spatial phase relationship between any two pairs of orthogonal modes will be arbitrary. However, the actual physical or "real" structure is usually only quasi-axisymmetric due to its inherent geometric or material imperfections. The modes of the "real" structure will contain considered-to-be-orthogonal mode pairs: the modes of each pair will have relatively close frequencies and mode shapes whose spatial phase angles make the modes effectively orthogonal. However, the spatial phase relationship between any two pairs of considered-to-be-orthogonal modes will be fixed. This arbitrary versus fixed spatial phase relationship for the analytical versus experimental modes, respectively, can cause relatively low MAC values to be obtained for modes that appear to be well correlated in a visual comparison.

The imperfections of the "real" structure, as well as test data noise, may produce measured modes that are dominated by one or two diametral orders but which also have non negligible contributions of other diametral orders. However, the modes predicted by the axisymmetric FE model will by definition contain only one diametral order. This difference in diametral order content can also cause relatively low MAC values for modes that visually appear to be well correlated.

Two methods are presented below to help improve the numerical correlation of the MAC for quasi-axisymmetric structures. The first method, mode shape rotation, addresses the arbitrary FE spatial phase angle problem and was first presented in [86]. The second method, Fourier decomposition, addresses the presence of multiple harmonics in test data mode shapes and was developed in this research. Both methods were presented in [87]. For quasi-axisymmetric structures

that exhibit both characteristics, the two methods are combined.

5.4.1 Mode Shape Rotation

This method advocates rotating the analytical mode shape of each mode pair about the axis of axisymmetry by an amount such that the MAC between the experimental and analytical mode gives a maximum value. By using trigonometric functions to describe the mode shapes, and decomposing each mode into its harmonic components, the initial spatial phase angle of each component for each mode can be determined. The rotation about the axis of axisymmetry of the analytical mode shapes is obtained by shifting the initial spatial phase angle of the primary diametral component for each mode shape. For a pair of considered-to-be-correlated modes, a shifted spatial phase angle can be calculated in order to maximise the MAC value between the modes. For further details see reference [86, 87].

5.4.2 Fourier Decomposition

This method proposes Fourier decomposition of the analytical and experimental mode shapes, respectively, and performing a MAC correlation on a reduced set of the Fourier indices instead of the individual displacement amplitudes at measured DOFs. The quasi-axisymmetric imperfections can be removed by using only the indices with the dominant amplitudes for each mode.

Consider a set of eigenvectors described in a cylindrical coordinate system with the DOFs equally spaced around the circumference of one ring. The discrete Fourier series for the eigenvectors, ψ_{ir} , where i defines the DOF and r defines the mode number, is given by [88]:

$$\psi_{ir} = a_{0r} + \sum_{k=1}^{[N/2]} a_{kr} \cos(k\theta_i) + \sum_{k=1}^{[N/2]} b_{kr} \sin(k\theta_i) \quad (5.4.1)$$

Here, N is the number of discrete DOFs, θ_i is the circumferential location of the i^{th}

DOF and k is the harmonic number or index. The upper summation limit $[N/2]$ is interpreted as $N/2$ if N is even and $(N-1)/2$ if N is odd. Further, if N is even, $b_{N/2}$ is omitted. The a and b coefficients are called the discrete Fourier cosine and sine transforms respectively, and for **equally-spaced** θ_i are defined for each mode by:

$$a_{0r} = \frac{1}{N} \sum_{i=1}^N \psi_{ir} \quad (5.4.2)$$

$$a_{N/2r} = \frac{1}{N} \sum_{i=1}^N (-1)^{i-1} \psi_{ir} \quad (5.4.3)$$

$$a_{kr} = \frac{2}{N} \sum_{i=1}^N \psi_{ir} \cos(k\theta_i) \quad (5.4.4)$$

$$b_{kr} = \frac{2}{N} \sum_{i=1}^N \psi_{ir} \sin(k\theta_i) \quad (5.4.5)$$

where $1 \leq k < N/2$. The MAC between the Fourier indices of two modes—one from analysis, A_r^a , and the other from experiment, A_r^x —is given by:

$$MAC(A_r^a, A_s^x) = \frac{A_r^{aT} A_s^x}{(A_r^{aT} A_r^a)(A_s^{xT} A_s^x)} \quad (5.4.6)$$

where

$$A_r^{aT} = [a_{0r}, \dots, a_{N/2r}, b_{1r}, \dots, b_{N/2r-a}] \quad (5.4.7)$$

and

$$A_s^{xT} = [a_{0s}, \dots, a_{N/2s}, b_{1s}, \dots, b_{N/2s-x}] \quad (5.4.8)$$

When the a and b coefficients for all indices are used, the discrete Fourier series are exact representations of both the amplitude and phase of the original mode shapes at the discrete locations θ_i . Therefore, using all the Fourier indices in

the MAC or Fourier MAC results in an identical solution to the MAC obtained using the mode shape deflections directly. Test experience has shown that quasi-axisymmetric structures can occasionally have two different nodal diameter orders present in one mode. Thus, only the two indices with the largest amplitudes for each mode are retained for use in the Fourier MAC, while the exclusion of the other indices serves to filter out the asymmetric imperfections of the "real" structure as well as test data noise.

The DOFs to be used by the Fourier MAC are first separated into rings of equally-spaced points around the circumference as shown on the left side in Figure 5.16. The DOFs in each ring are then grouped by cylindrical coordinate direction as shown on the right side in Figure 5.16. Each group of DOFs is decomposed separately into its Fourier indices. The Fourier MAC uses both a and b coefficients so that both the amplitude and phase of the modes are represented. Otherwise, modes of the same diametral order could not be distinguished.

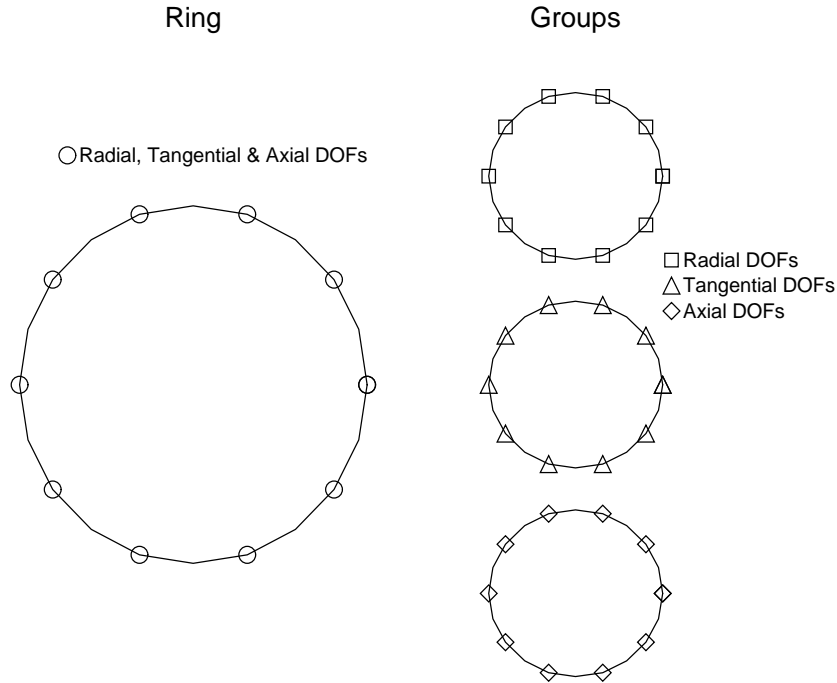


Figure 5.16: One ring of measured DOFs separated into groups by DOF type

Using the amplitudes of the indices given by,

$$AMP_{kr} = \sqrt{a_{kr}^2 + b_{kr}^2} \quad (5.4.9)$$

where k defines the harmonic number and r defines the mode number, the first two primary indices can be determined for each test and analytical mode. The retained indices for all DOFs and all rings can then be assembled into one vector for each of the test and analytical mode shapes. The assembly order (both sequence and total number of elements) must be consistent, for both test and analytical mode shapes, with respect to Fourier index, DOF and ring.

5.4.3 Case Study: Assembly of Two Turbine Engine Casings

The case study is for an assembly of a front and middle turbine engine casing for which an FE model and extensive test data (provided by Rolls- Royce) were readily available. Figure 5.17 shows the MSC/NASTRAN finite element model for the front and middle casing assembly. The shell model contained 10 rings of 60 nodes each (600 total nodes) and was used to calculate the first 20 modes. Test data were taken for 3 rings of 20 **equally-spaced** points in the radial direction but only for the first 20 modes.

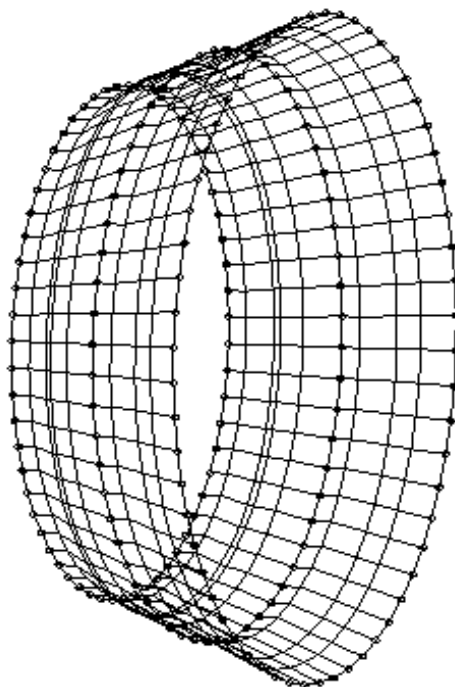


Figure 5.17: MSC/NASTRAN Model for Assembly of Two Casings

The Fourier decomposition was performed for both analytical and experimental mode sets using the experimental locations and radial deflections for each ring. The results, shown in Figures 5.18 and 5.19, are displayed on a plot of mode number versus Fourier index number or diametral order.

Figure 5.18 illustrates the harmonic content and relative participation of each ring for the first 20 analytical modes. Note the relatively large magnitude of the indices for modes 13 and 14. This is because the analytical mode shapes were normalized including all translational DOFs instead of just the radial deflections and it illustrates that modes 13 and 14 have more motion in the radial direction compared with the rest of the modes. The figure also shows which of the modes are orthogonal pairs. By matching the Fourier index value for adjacent modes and then comparing the relative symbol sizes for the respective rings, the orthogonal modes can be determined.

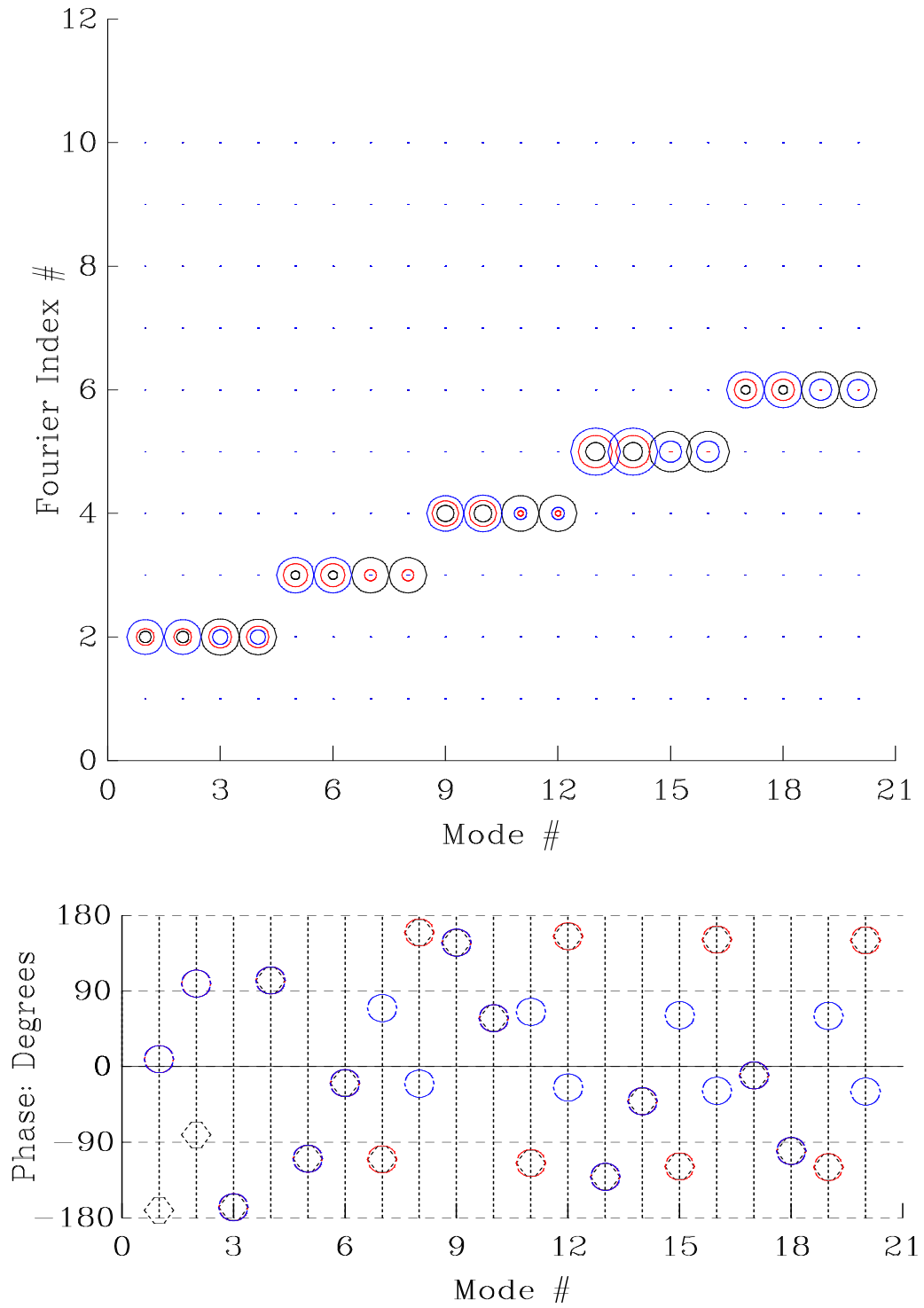


Figure 5.18: Fourier indices for the analytical modes

Figure 5.19 illustrates the harmonic content and relative participation of each ring for the first 20 experimental modes. Since only the radial DOFs were measured, the relative size of the symbols indicate the harmonic content of the radial deflection of the mode shape for each ring. The figure shows a significant increase in noise for the test data modes compared with the analytical modes by multiple indices having contributions to most of the modes.

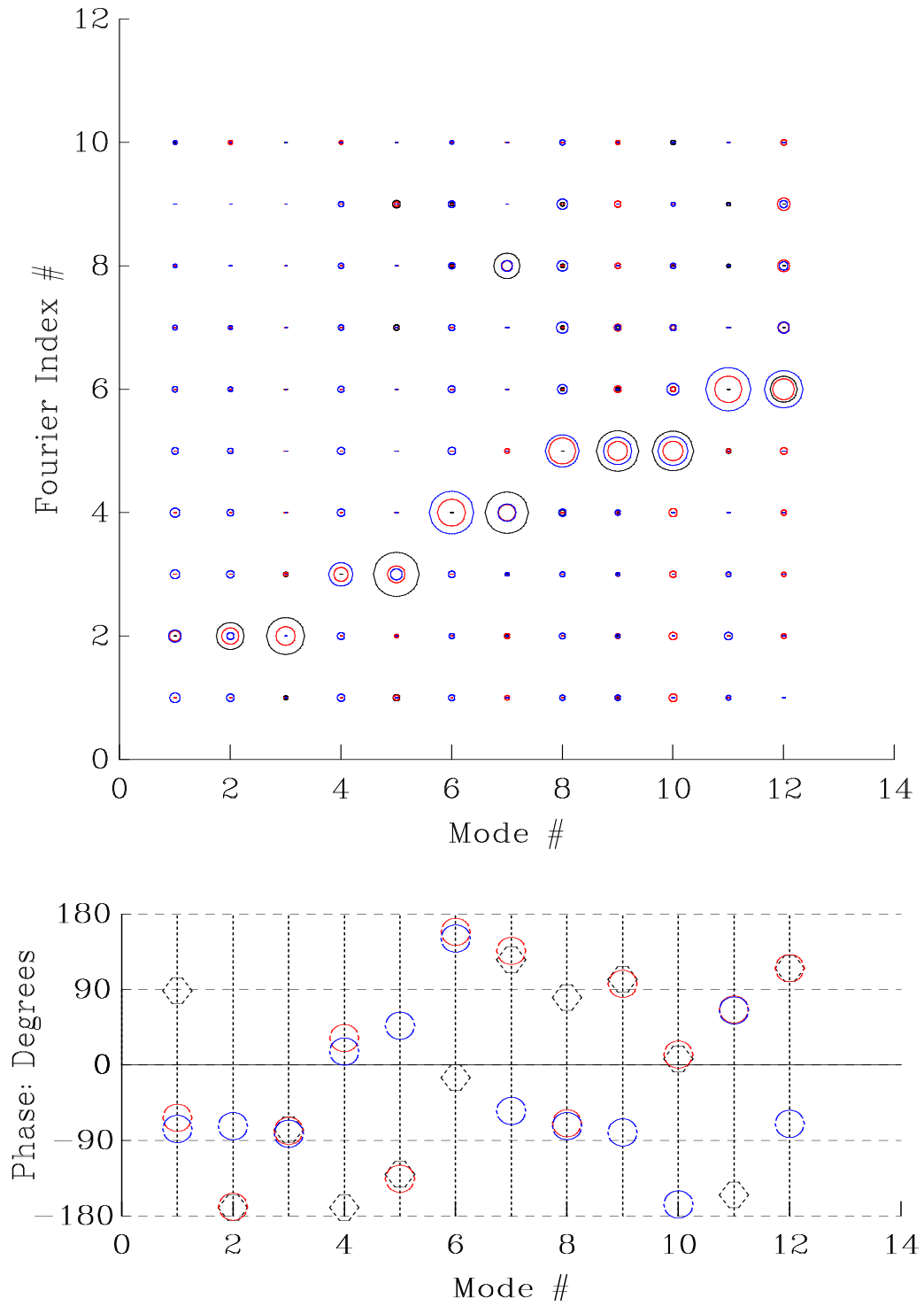


Figure 5.19: Fourier indices for the experimental modes

The comparison between the standard MAC and the MAC with mode shape rotation is illustrated in Figure 5.20. The figure shows a definite improvement in the correlation for experimental modes 4, 9 and 10 with respective increases in MAC values of from 0.35 to 0.61, 0.45 to 0.77 and 0.44 to 0.71. This demonstrates that mode shape rotation helped to improve the correlation by aligning the spatial phases between the analytical and experimental modes.

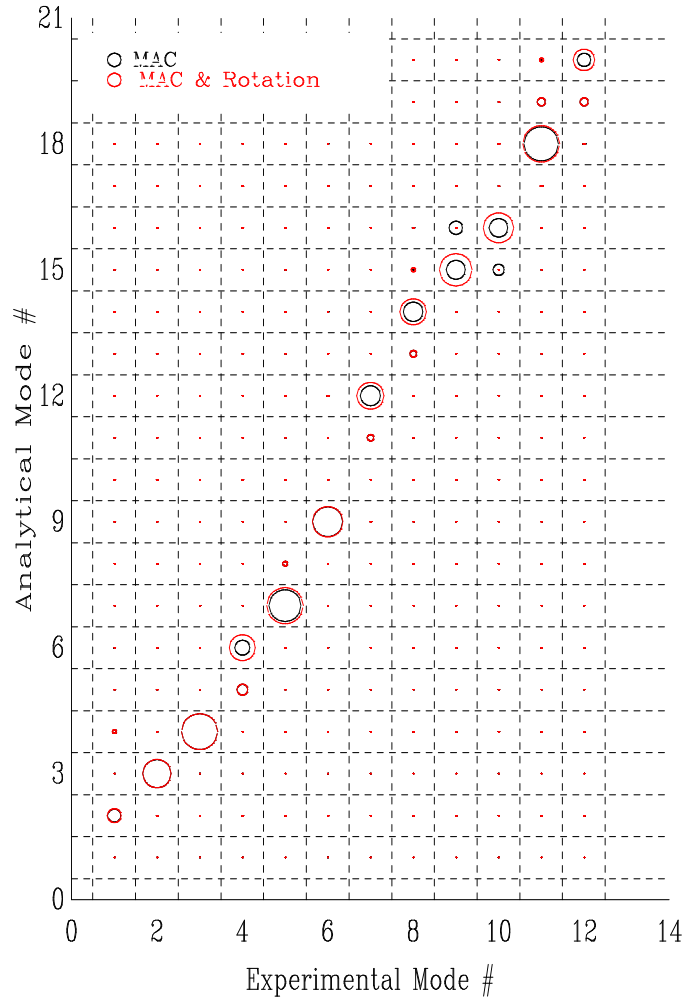


Figure 5.20: Comparison of MAC versus MAC with mode shape rotation

Figure 5.21 illustrates the comparison between the MAC and the Fourier MAC using the first two primary indices. The figure illustrates that the Fourier MAC

improved the correlation for most of the experimental modes. Modes 1, 2, 4 and 8 showed the greatest improvement with respective increases in MAC values of from 0.35 to 0.61, 0.67 to 0.79, 0.35 to 0.50 and 0.46 to 0.61. This is supported by Figure 5.19, which shows that most of the experimental modes have contributions from multiple indices. The truncation effectively removed noise and other associated test errors from the mode shapes which can have significant impact on the MAC values. For further details on how noise and test errors can effect the MAC see reference [84].

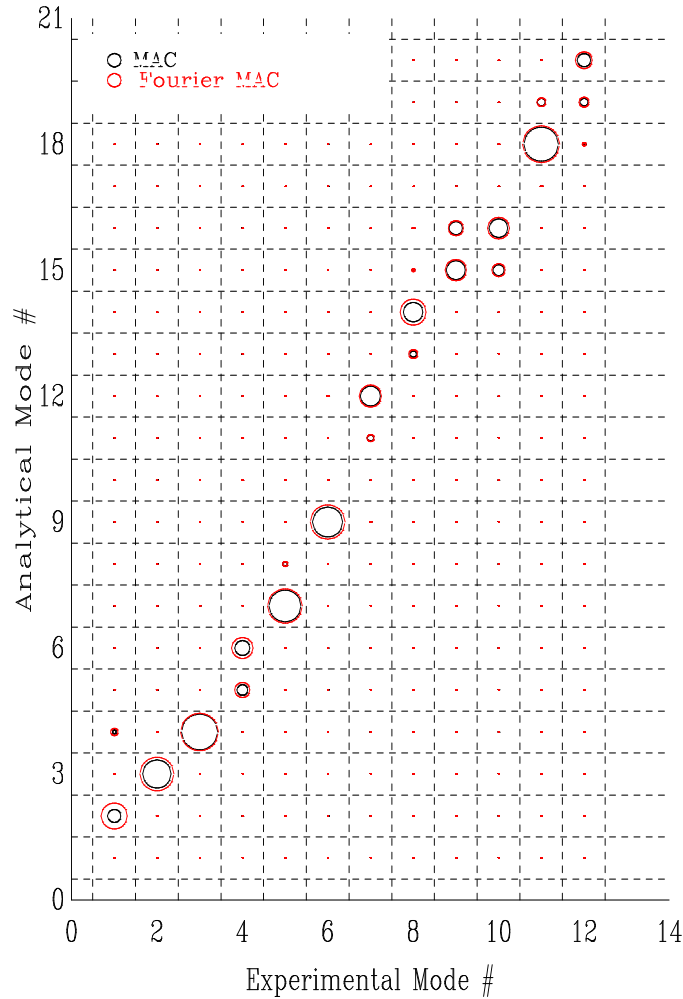


Figure 5.21: Comparison of MAC versus Fourier MAC using 2 indices

The comparison between the MAC and the Fourier MAC (using the first two primary indices) plus mode shape rotation is shown in Figure 5.22. This Figure shows that the combination of mode shape rotation with Fourier truncation increased the MAC values for all mode pairs with one exception, experimental mode 3 and analytical mode 4. The modes most affected were 1, 4, 8, 9 and 10 with respective increases in MAC values of from 0.31 to 0.63, 0.35 to 0.85, 0.46 to 0.82, 0.45 to 0.86 and 0.44 to 0.82. This clearly demonstrates the benefits of combining the two methods to help improve correlation.

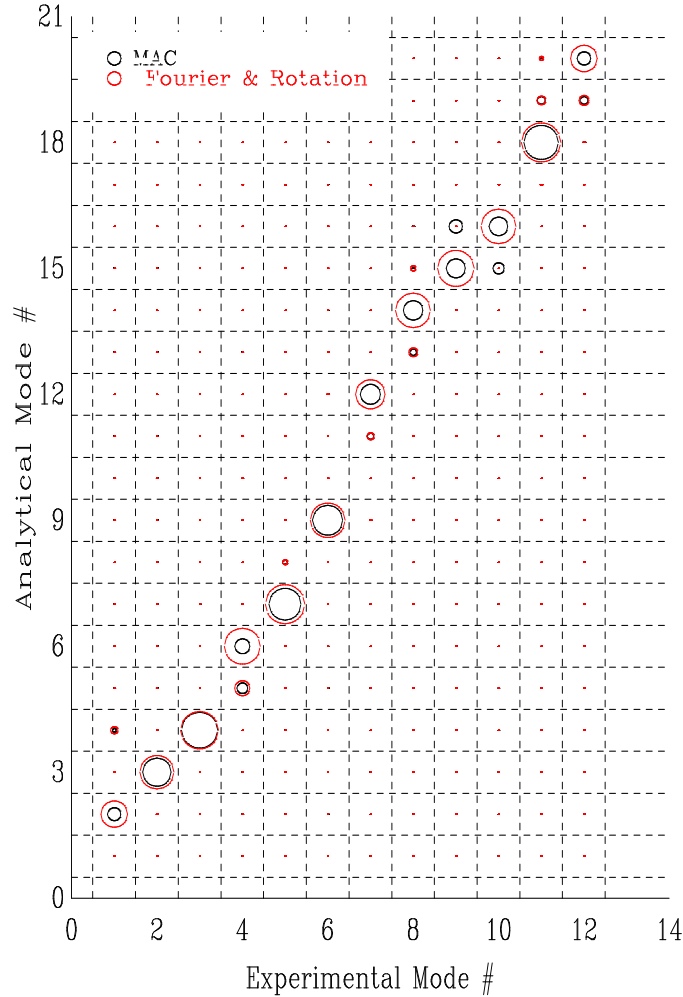


Figure 5.22: Comparison of MAC versus Fourier MAC using 2 indices plus rotation

5.5 Conclusions

The review of the available correlation methods highlighted some of the advantages and disadvantages of the various methods. Although orthogonality and FRF methods were discussed, vector methods remain the most widely used because they require only the mode shapes as input. This is aided by the development of advanced modal analysis software which makes obtaining experimental mode shapes much more reliable and efficient. In certain circumstances some of the stand-alone vector methods may prove superior to the MAC for mode shape correlation, but in general no clear successor to the MAC has been found.

The new format for displaying correlation, the FMAC, was shown to be very useful in combining the information from the frequency comparison with that of the MAC and the auto-MAC. In addition to combining the three sources of information (MAC, natural frequency and auto-MAC) onto one plot, the new plot format also shows modal density and helps to determine whether the high off-diagonal MAC values are from true correlation or spatial aliasing. The two alternative forms of the FMAC plot (with natural frequency difference on the y-axis) were shown to enhance the FMAC so that the frequency error could be shown very accurately and modes very close in frequency (high modal density and double modes for symmetric structures) could be distinguished from each other. It is envisaged that the FMAC may be used very effectively whenever there is a need to compare two or more sets of modal data (natural frequencies and mode shapes) with a reference set of modal data.

The extension of the new plot format to the correlation of FRFs using both the FDAC and the newly-introduced MFAC was also shown to be quite promising. In the industrial case study shown, both the FDAC and MFAC correlation yielded comparable information to the MAC correlation. This result is significant in that if either the FDAC or MFAC correlation can be used instead of the MAC then the costly post-measurement modal analysis, which can introduce significant errors, of

the experimental FRFs to determine the mode shapes can be avoided. Additionally, for lightly damped modes the MFAC could be used instead of the FDAC to avoid the analysis and assumptions required for determining the analytical FRFs, thereby using the data with the greatest fidelity from both test and analysis for correlation.

In the case study shown to illustrate the problems associated with validating (quasi) axisymmetric structures, Fourier analysis of mode shapes using the first two primary indices was shown to help to improve the correlation between test and analytical mode shapes significantly. Mode shape rotation was also shown to help improve the correlation, as previously documented in reference [86, 87]. However, the combination of Fourier analysis and mode shape rotation was shown to be the most effective option to the extent that their combined use is highly recommended for the correlation of the modes of axisymmetric structures. Accordingly, the combination of the two techniques were used for all the FMAC plots shown in the case study in Chapter 6.

Chapter 6

Case Study

The contributions of this research will be demonstrated with a case study for an assembly of two real gas turbine engine casings. The first is a combustor casing that is considered to have a very complex geometry and the second is a turbine casing that has a geometry that is considered to be moderately complex. The two casings will be first considered individually and then as an assembly. A super-model for each component will be generated and validated using test data. Then, the two component models will be assembled using a joint model and also validated using test data.

Having validated the super-models for both the components and the assembly, the analytical modes of each component will then be compared to the experimental modes of the assembly to determine how the component modes track to the assembly. This will be followed by a study to determine the effects that the different features—flange holes, scallops and casing holes with bosses—have on the correlation. These are valuable uses for the super-model as much insight can be gained about which component is the most dominant in the assembly and which features are the most important to either of the components or to the assembly. Both of these can be used to help guide the development of an approximate design size model either directly or by reducing the super-model.

The reduction of each component super-model will be presented next in order to demonstrate the physical model reduction technique. The knowledge gained from the mode tracking exercise will be used to guide the choice of the reduction targets for each of the components. The reduction will be done for the components individually which will consider only their respective component modes with weighting factors of 1.0. This will be followed by the connection of the two reduced models together using a joint model to form a reduced model of the assembly.

The FMAC will be used throughout to demonstrate its ability to show clearly the mode shape correlation, frequency correspondence and the degree of spatial aliasing simultaneously. Further, the FMAC will be used to compare the multiple correlations for the convergence checks and to show the effects that the different features have on the correlation.

6.1 Combustor Casing

The cross-section geometry for the combustor casing is shown in Figure 6.1. The holes are shown by the red lines and the scallops by the blue lines. The figure

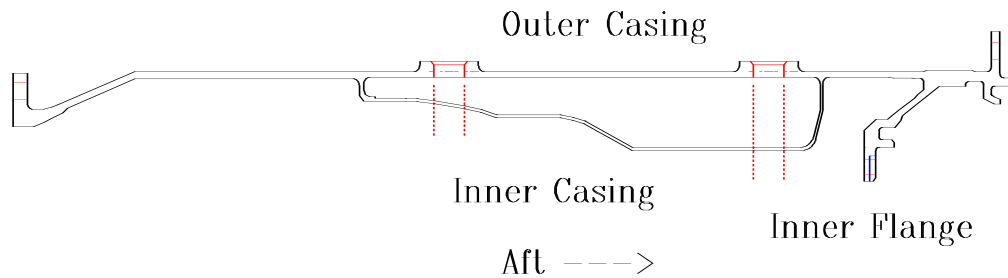


Figure 6.1: Cross-section of Combustor Casing Geometry

shows that the combustor casing has both an outer and inner casing. The outer casing is relatively cylindrical and the inner casing spans about the middle third of the outer casing. The forward flange is a basic or straight type and the aft flange has both an internal spigot and a C channel (with a fish mouth shape) on

its inside diameter. There is an inner flange just forward of the aft flange that also has a C channel just above the radial part of the flange which is scalloped. The outer casing has two rows of piping type bosses, each equally-spaced around the circumference, that have holes which go through both the outer and inner casings as shown by the red dashed lines. All three flanges have bolt holes.

Figure 6.2 shows the geometry of the features with four different views. The axial view, looking forward to aft, of a section of the forward flange shows some of the 120 bolt holes that span its circumference. The axial view, looking aft to forward, of a section of the aft flange shows some of the 120 bolt holes that span its circumference. Further, the view shows some of the inner flange scallops and bolt holes which numbered 36 around the circumference. The last two views are from the radial direction in which the aft direction is towards the top of the page. The two rows of bosses which numbered 18 and were equally-spaced around the circumference are shown with a radial inward view of a section of the outer casing. The radial outward view of the inner casing section shows the casing hole pattern that repeats around the circumference. The total number of holes for the forward pattern (bottom in view) was 18 small holes, 9 mid-size holes and 4 large holes. The total for the aft pattern (top in view) was 18 small holes.

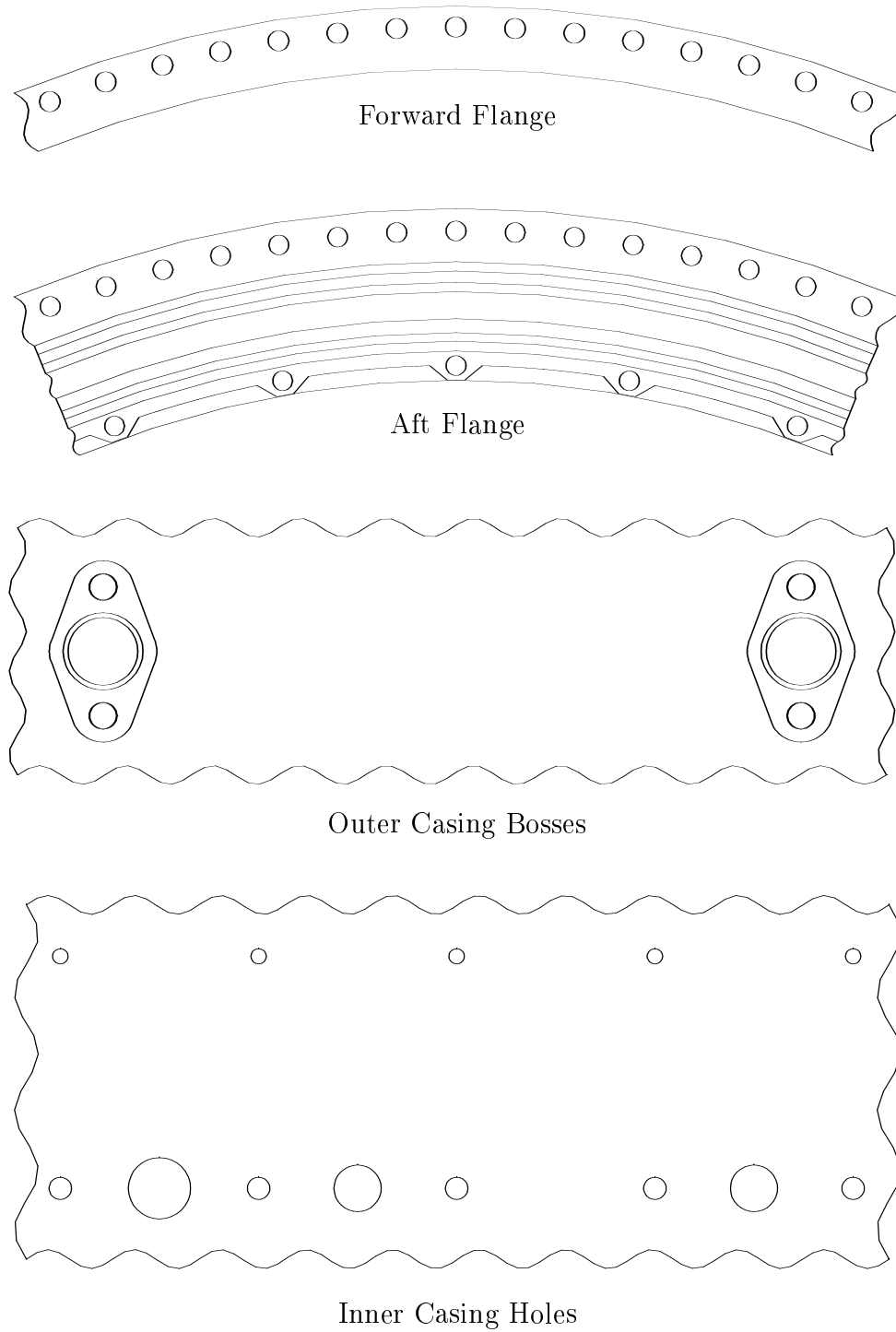
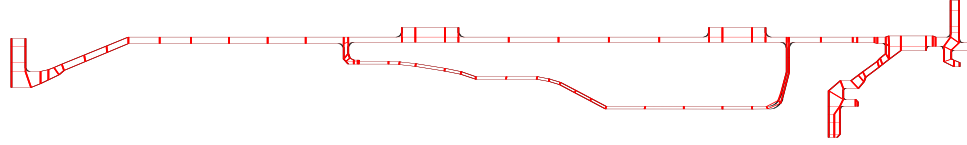
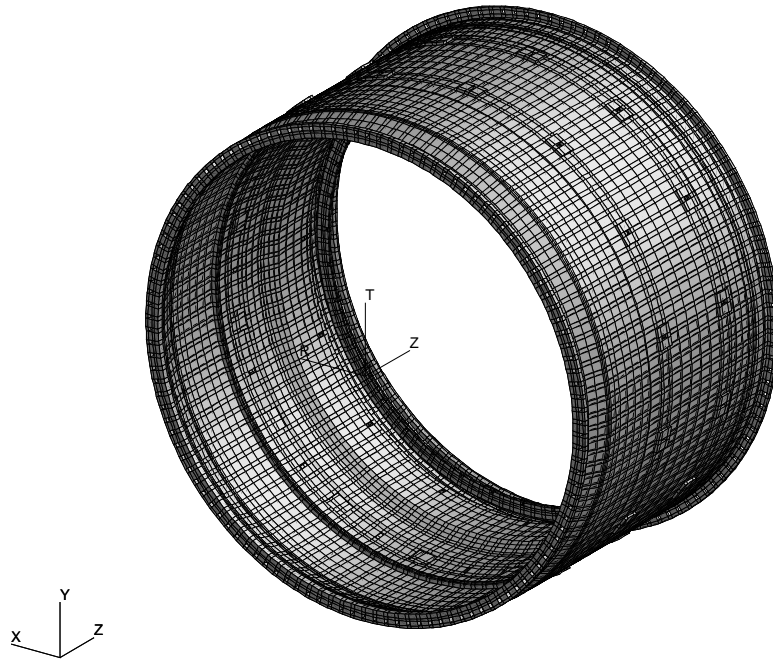


Figure 6.2: Combustor Casing Feature Geometry

The super-model was generated using hexahedron solid elements for which the cross-section model is shown with red lines at the top in Figure 6.3. The geometry is shown by the black lines. The cross-section model contained 211 nodes and 111,



Cross-section Model



3-D Model

Figure 6.3: Combustor Casing Super Model

4-noded elements which was then spun about the axis of axisymmetry with 240 nodes and elements in the circumferential direction. The features were incorporated next by removing elements for both the holes and scallops. The resulting 8 noded hexahedron solid model, shown at the bottom in Figure 6.3, contained 51,840 nodes, 25,365 elements and 155,520 DOFs. MSC/NASTRAN was used to extract the first 20 free-free natural frequencies and mode shapes.

The modal test data was taken (previously at Imperial College) at three rings of 12 equally-spaced transducers in the radial direction. The first ring was located on the outside diameter of the forward flange. The second ring was located on the outside diameter of the outer casing at the forward junction of the inner and outer casings. The third ring was located on the outside diameter of the aft flange. The modal test produced 36 FRFs from which the modal analysis was able to determine contained 12 modes.

Figure 6.4 shows the FMAC plot (in percentage frequency difference versus experimental mode number format) for the correlation of the combustor casing super-model with the test data. The black circles are for the auto-MAC of the experimental modes and the red circles are for the MAC between the experimental and analytical mode shapes. The figure shows that the correlation is excellent

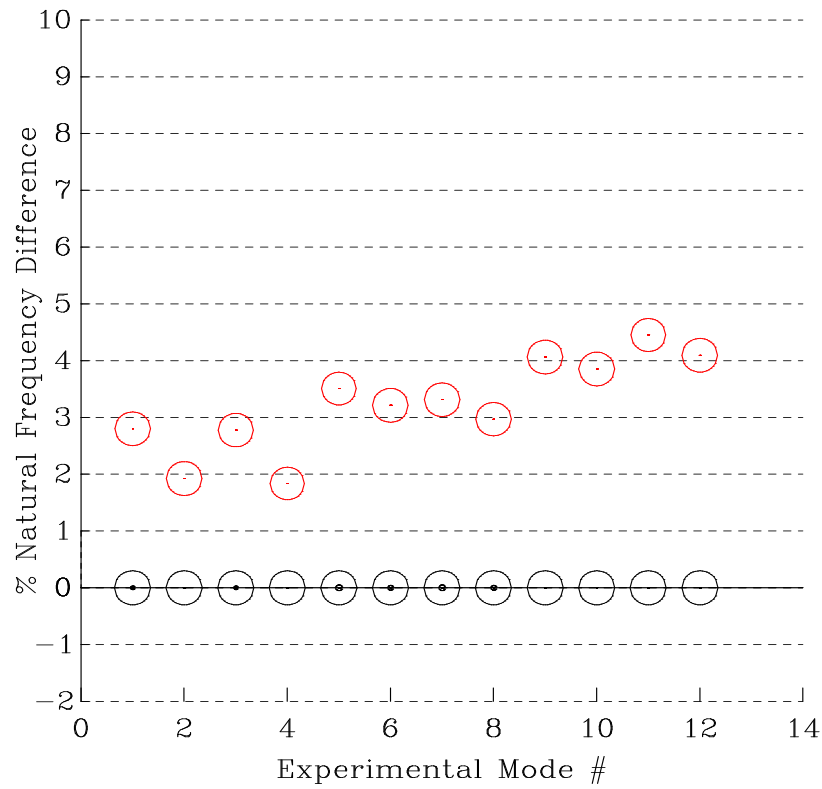


Figure 6.4: FMAC Plot for Combustor Casing Super Model

with MAC values for all modes very near 1.0 and with frequency differences for all modes between about +1.7% and +4.3%. Note the consistency of the frequency differences with a variation of about $\pm 1.3\%$ about a line at +3%.

In order to check the convergence of the model for the combustor casing, a second model was created by refining the first model with two elements through the thickness and a general increase in mesh density. The cross-section of the refined model is shown in Figure 6.5.

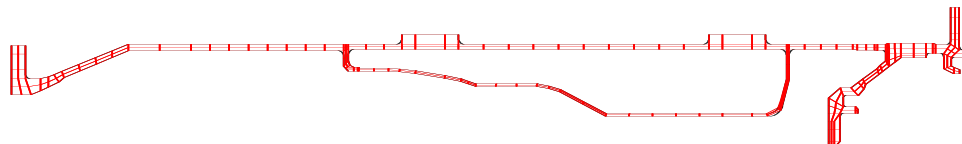


Figure 6.5: Cross-section of Combustor Casing Refined Super Model

The refined cross-section model contained 403 nodes and 273, 4-noded elements which was again spun about the axis of axisymmetry with 240 nodes and elements in the circumferential direction and then the holes and scallops added. Figure 6.6 shows the resulting 8 noded hexahedron solid model which contained 99,600 nodes, 64,930 elements and 298,800 DOFs. MSC/NASTRAN was again used to extract the first 20 free-free natural frequencies and mode shapes.

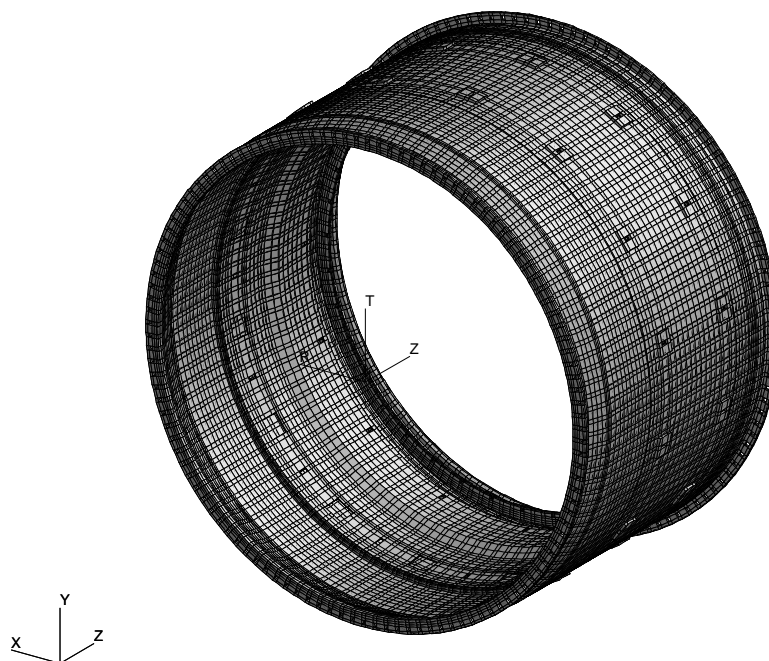


Figure 6.6: Refined Combustor Casing 3-D Super Model

Figure 6.7 shows the FMAC plot for both the initial and the refined super-models. The black circles are for the auto-MAC of the experimental modes, the

red circles are for the initial super-model and the blue circles are for the refined super-model.

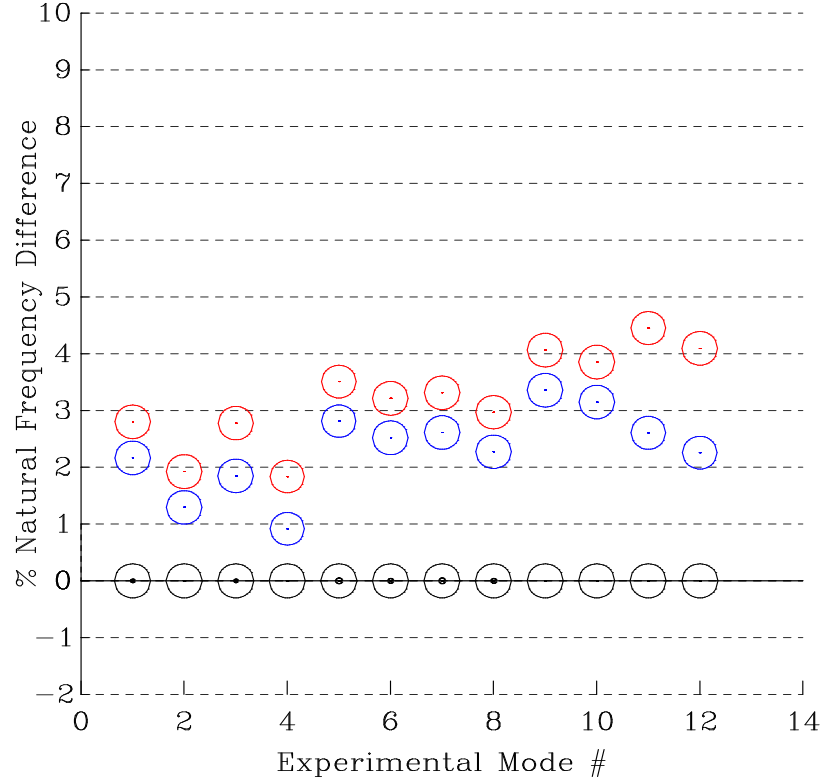


Figure 6.7: FMAC Plot for Initial and Refined Combustor Casing Super Models

The figure shows that the frequency differences decreased from the initial to the refined model between about 1% to 2% while the MAC values remained very near 1.0 for all modes. The frequency differences for all modes of the refined model were between about +1.0% and +3.2%. Note again the consistency of the frequency differences with a variation of about $\pm 1.1\%$ about a line at +2.1%. Further, the decrease in variation from $\pm 1.3\%$ for the original mesh to $\pm 1.1\%$ for the refined mesh is indicative of convergence.

6.2 Turbine Casing

Figure 6.8 shows the cross-section of the geometry for the Turbine casing. The red lines show the bolt hole locations. The figure shows that the turbine casing is

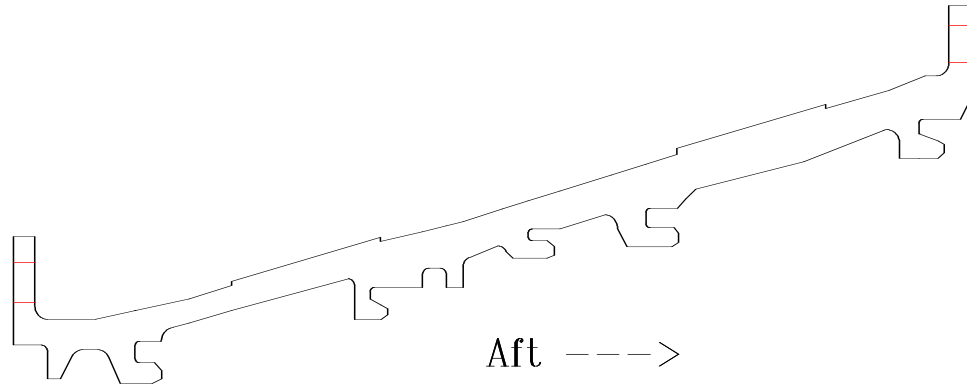


Figure 6.8: Cross-section of Turbine Casing Geometry

conical with an increasing radius from forward to aft. The forward and aft flanges are both of the basic or straight type and both have bolt holes with their locations indicated by the red lines. There are five C channels on the inside diameter of the casing. There are also two radial ribs on the inside diameter of the casing—one near the forward flange and the other about midway between the forward and aft flanges. The outside diameter of the casing has two stiffening rings—the first is at about one quarter axial span and the second is at about three quarters axial span.

The geometry of the features is shown in Figure 6.9 with two different views. The axial view, looking forward to aft, of a section of the forward flange shows some of the 120 bolt holes that span its circumference. The axial view, looking aft to forward, of a section of the aft flange shows some of the 120 bolt holes that span its circumference.

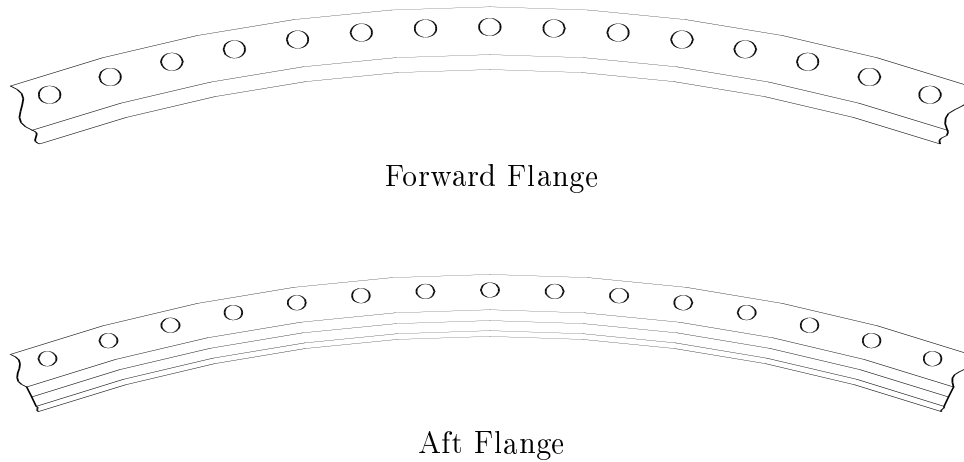
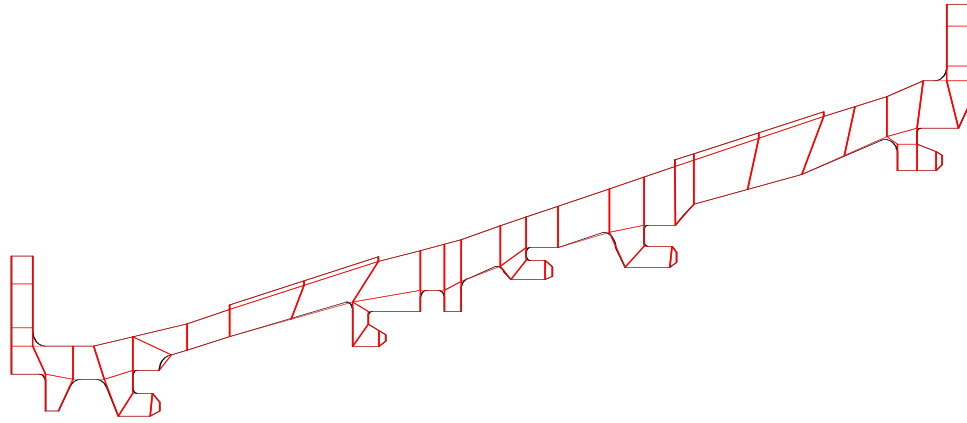
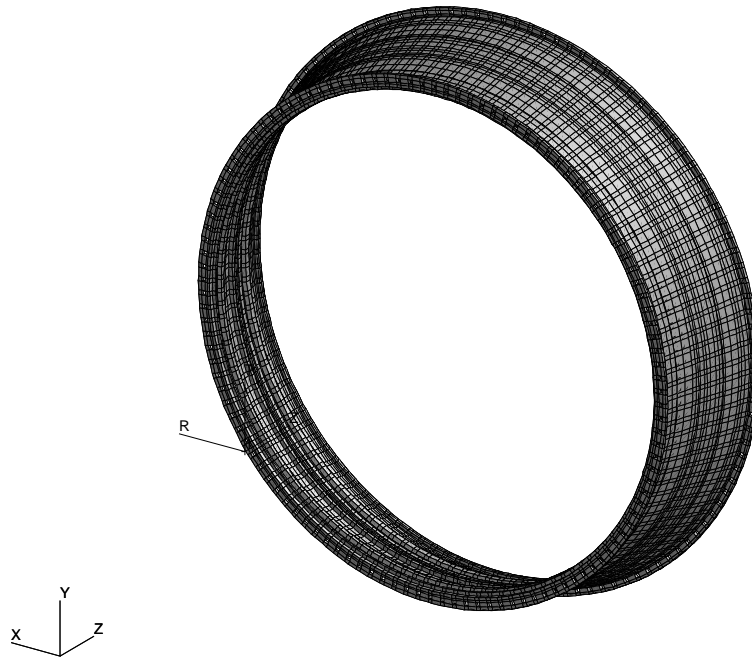


Figure 6.9: Turbine Casing Feature Geometry

The cross-section of the hexahedron solid element super-model is shown at the top of Figure 6.10 with red lines and the geometry with black lines.



Cross-section Model



3-D Model

Figure 6.10: Turbine Casing Super Model

The cross-section model contained 112 nodes and 56, 4-noded elements which was then spun about the axis of axisymmetry with 240 nodes and elements in the circumferential direction. Next, the flange holes (the only non-continuous features) were added by removing the appropriate elements. The resulting 8-noded hexahedron solid model, shown at the bottom of Figure 6.10, contained 26,640 nodes, 13,200 elements and 79,920 DOFs. The first 20 free-free natural frequencies and mode shapes were extracted using MSC/NASTRAN.

The modal test data were taken (previously at Imperial College) using two rings of unequally-spaced radial transducers that were chosen by test planning. The first ring had 8 locations and was located on the outside diameter of the forward flange. The second ring had 11 locations and was located on the outside diameter of the aft flange. The modal test produced 19 FRFs from which the modal analysis determined that there were 11 modes.

The FMAC plot (in percentage frequency difference versus experimental mode number format) for the correlation of the Turbine casing super-model with the test data is shown in Figure 6.11.

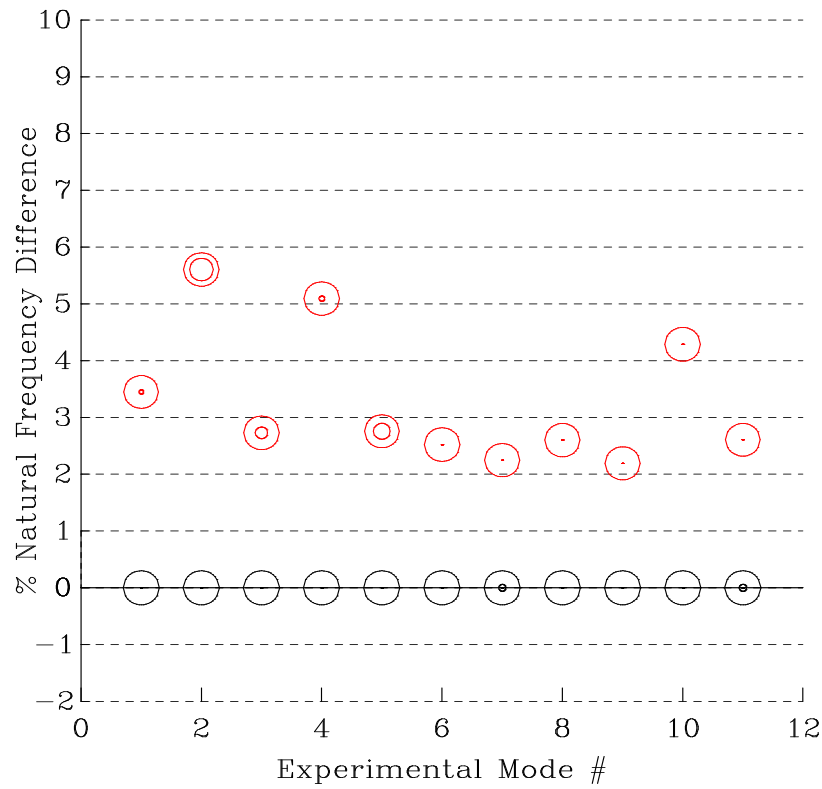
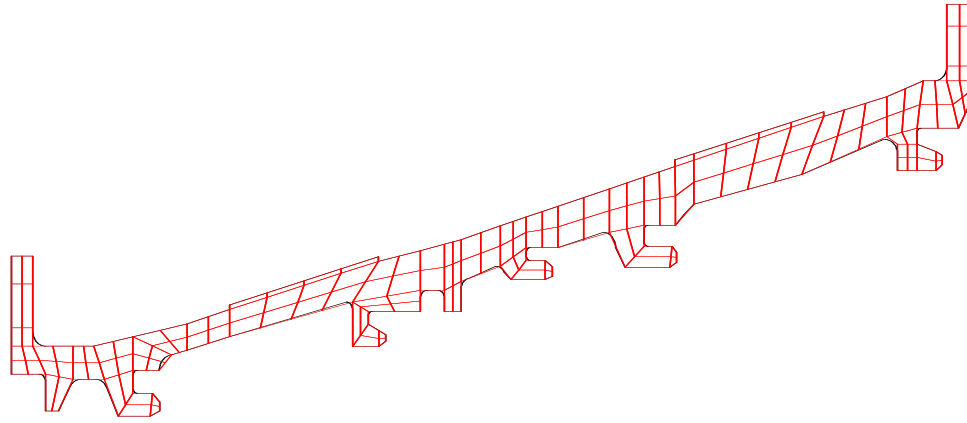


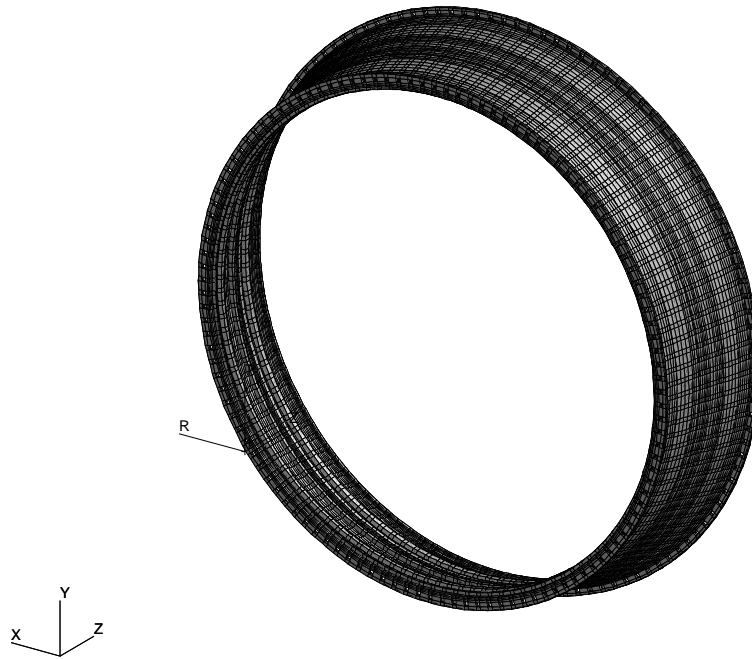
Figure 6.11: FMAC Plot for Turbine Casing Super Model

The figure shows that the correlation is again excellent with MAC values for all modes very near 1.0 and with frequency differences for all modes between about +2.2% and +5.6%. The consistency of the frequency differences is again very good with a variation of about 1.7% about a mean at +3.9%.

The convergence of the model for the turbine casing was also checked by refining the first model with two elements through the thickness and a general increase in mesh density. The cross-section of the refined model is shown at the top of Figure 6.12.



Cross-section Model



3-D Model

Figure 6.12: Refined Turbine Casing Super Model

The refined cross-section model contained 242 nodes and 161, 4-noded elements

which was spun about the axis of axisymmetry with 240 nodes and elements in the circumferential direction and then the flange holes were added. Shown at the bottom of Figure 6.12 is the resulting 8 noded hexahedron solid model which contained 58,080 nodes, 38,160 elements and 174,240 DOFs. MSC/NASTRAN was used to extract the first 20 free-free natural frequencies and mode shapes.

The FMAC plot for both the initial and the refined super-models is shown in Figure 6.13. The red circles are for the initial super-model and the blue circles are for the refined super-model.

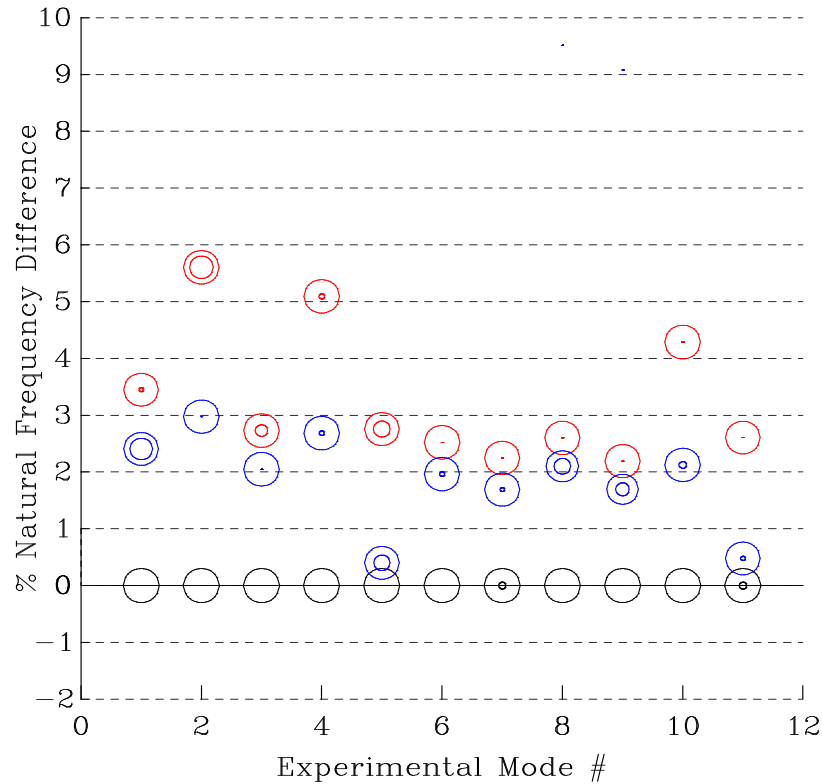


Figure 6.13: FMAC Plot for Initial and Refined Turbine Casing Super Models

The figure shows that the frequency differences decreased between about 1% to 2.5% from the initial to the refined model while the MAC values remained very near 1.0 for all modes. The frequency differences for all modes of the refined model were between about +0.4% and +3.0%. Note the consistency of the frequency

differences with a variation of about 1.3% about a line at +1.7%. Further, the decrease in variation from 1.7% for the original mesh to 1.3% for the refined mesh is indicative of convergence.

6.3 Assembly of Combustor and Turbine Casings

The initial hexahedron solid element super-models for the combustor and turbine casings were connected together at their mating flanges to form the model for the assembly. The cross-section for the assembly model is shown in Figure 6.14. The combustor casing is shown by the black lines and the turbine casing by the red lines.

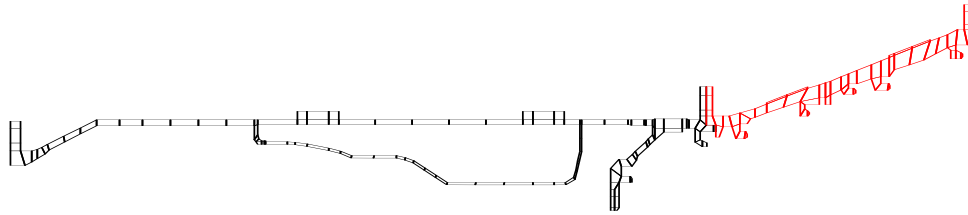


Figure 6.14: Assembly Cross-section Super Model

The cross-section model contained 323 nodes and 167, 4-noded elements which was then spun about the axis of axisymmetry with 240 nodes and elements in the circumferential direction. The features were incorporated once again by removing elements for both the holes and scallops. The resulting 8-noded hexahedron solid model, shown in Figure 6.15, contained 78,480 nodes, 38,565 elements and 235,440 DOFs.

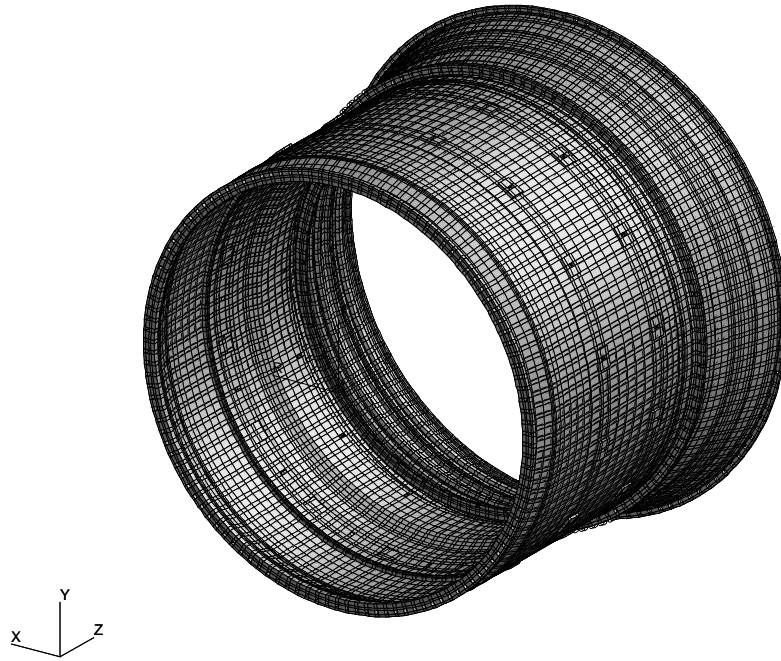


Figure 6.15: Assembly 3-D Super Model

The cross-section of the joint model between the internal spigot of the aft flange for the combustor casing and the forward flange for the turbine casing is shown in Figure 6.16. The combustor casing is shown by the black lines, the turbine casing by the red lines and the centre line through the bolt holes by the black dashed line. The joint model was constructed by rigidly connecting the coincident nodes shown encircled in blue. The coincident nodes at the top and bottom of the bolt holes were connected in all three DOFs for every node around the circumference (square holes). The coincident nodes in the corner of the internal spigot and the corner of the radial rib were connected in the radial and axial DOFs only, also for every node around the circumference. The rigid connections decreased the total number of DOFs by 2,400 (2 cross-section nodes at 3 DOFs and 2 cross-section nodes at 2 DOFs both by 240 circumferential nodes) to 233,040. The first 20 free-free natural

frequencies and mode shapes were extracted using MSC/NASTRAN.

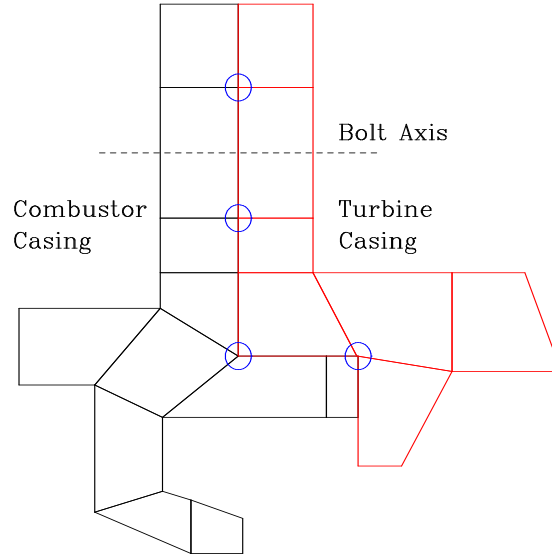


Figure 6.16: Assembly Cross-section Joint Model at the Mating Flanges

The modal test data were taken (previously at Imperial College) using three rings of 12 equally-spaced transducers in the radial direction. The first ring was located on the outside diameter of the forward flange of the combustor casing. The second ring was located on the outside diameter at the aft flange of the combustor casing. The third ring was located on the outside diameter of the aft flange of the turbine casing. The modal test produced 36 FRFs from which the modal analysis was able to determine 12 modes.

Figure 6.17 shows the FMAC plot (in percentage frequency difference versus experimental mode number format) for the correlation of the assembly super-model with the test data. The black circles are for the auto-MAC of the experimental modes and the red circles are for the MAC between the experimental and analytical mode shapes.

The figure shows that the correlation is excellent with MAC values for all modes very near 1.0 except for experimental mode 10 with about 0.90. The frequency differences for all modes were between about +1.3% and +4.3%. The consistency

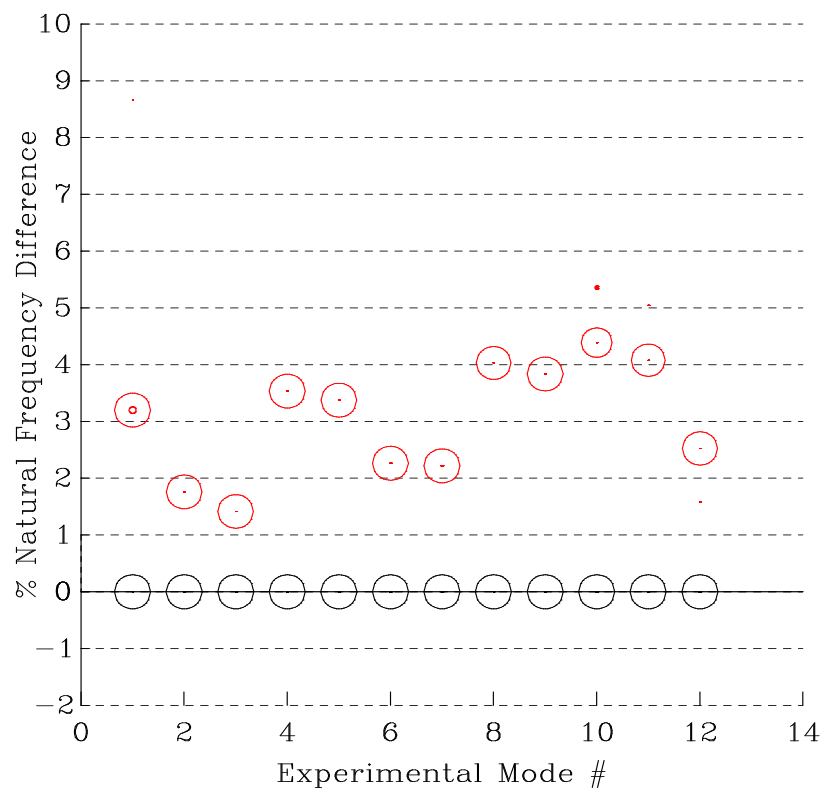


Figure 6.17: FMAC Plot for Assembly Super Model

of the frequency differences is excellent with a variation of about $\pm 1.5\%$ about a line at $+2.8\%$.

The refined model of the assembly for the convergence check contained 151,440 nodes, 90,295 elements and 454,320 DOFs. Unfortunately, the model proved too large to run on the computers available. However, from the correlation for the initial assembly model and the convergence of the individual component models, it is envisaged that the convergence of the assembly model would yield MAC values unchanged from the initial model and frequency differences with a variation of about $\pm 1\%$ about a line at $+2\%$.

6.3.1 Mode Tracking

A useful means for understanding the modal behaviour of both the components and the assembly is to use the FMAC to track the modes of the component structures to the corresponding modes in the assembly, which was referred to in Chapter 4 as "mode tracking". This gives insight into how important each of the components is to the modes of the assembly and can be used as a guide for creating design-size models, either directly or by reducing the super-model. In this way the most important components can be given the greatest attention in modelling or reduction, resulting in a better and more efficient assembly model than would normally be obtained from giving equal attention to all components.

Figure 6.18 shows the comparison of the analytical combustor and turbine casing component modes with the experimental modes of the assembly. The combustor-to-assembly correlation is shown in red and the turbine-to-assembly correlation is shown in blue. It can be seen from the figure that 6 of the combustor casing modes correlate very well with modes of the assembly with MAC values 0.9 and natural frequency differences between about +3% and +6%. The turbine casing is shown to correlate well with 4 modes of the assembly with MAC values 0.9 but with natural frequency differences between about -18% to -24%. However, assembly modes 2, 3, 6 and 7 are seen to not correlate very well with modes of either of the components. The combustor casing is considered to be dominant in the assembly because 6 of the 12 modes were predicted quite accurately with just the model of the combustor casing.

The figure also shows that nearly all the modes of the combustor casing have positive natural frequency differences when compared with those of the assembly. This suggests that the turbine casing had a softening effect on the combustor casing resulting in a frequency decrease for the assembly modes when compared with the combustor casing. Likewise, nearly all the modes of the turbine casing have negative frequency differences when compared with the assembly modes. This

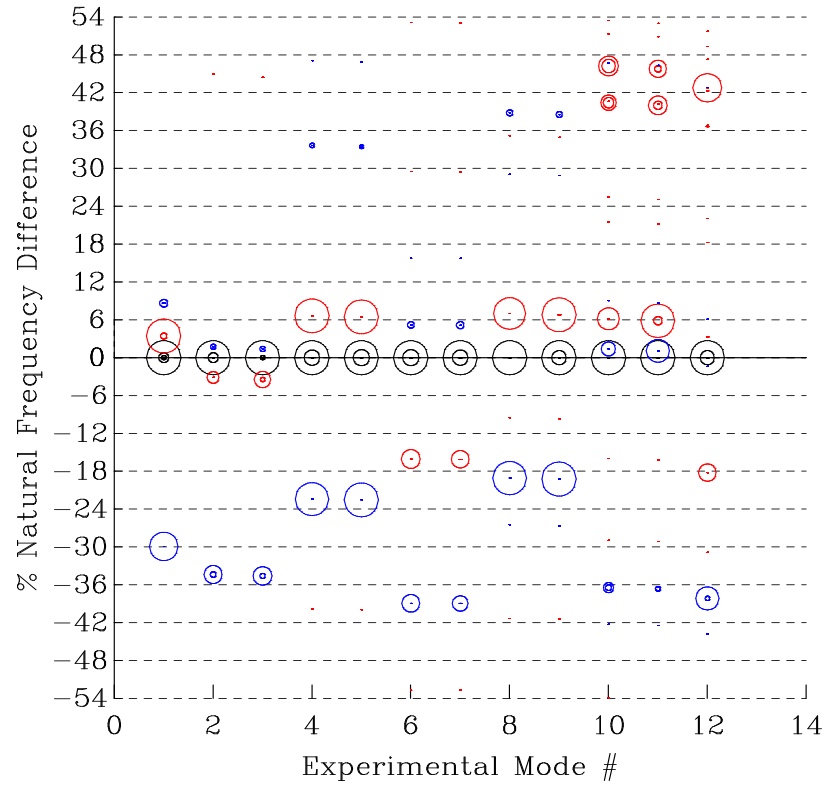


Figure 6.18: FMAC Plot for Mode Tracking Component Modes to Assembly

implies that the combustor casing had a stiffening effect on the turbine casing resulting in a natural frequency increase for the assembly modes when compared to the turbine casing.

6.4 Effects of Features on Modal Characteristics

In order to show how the addition of the different structural features (such as flange holes, scallops and casing holes with bosses) affects the correlation, an analysis was performed with all the features removed (axisymmetric) and then each feature was added individually for subsequent comparisons with the one with no features. The flange and casing holes were removed from the model by including the appropriate elements that were previously removed to create the holes. The scallops and bosses were removed from the model by deleting the appropriate elements. Finally, an analysis including all the features was compared with the analysis with no features. This was done for each component individually as well as for the assembly of the two. The FMAC was used to show the correlation between each analysis and the test data as well as the change in the correlation between the different analyses.

6.4.1 Combustor Casing

The FMAC plot for the model with no features is shown in Figure 6.19. The Figure shows that the correlation is quite good with MAC values very close to 1.0 for all experimental modes and natural frequency differences between about +5.2% and +9.2%. The frequency differences were very consistent with only a 2% variation about a mean at +7.2%.

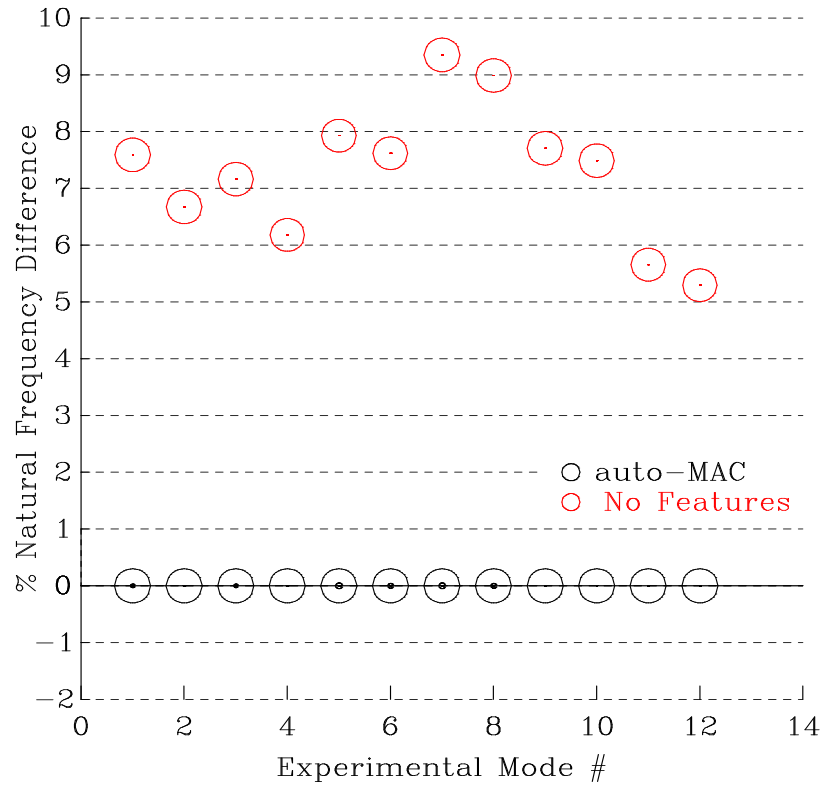


Figure 6.19: FMAC Plot for the Combustor Casing: No Features

Figure 6.20 compares the model with the flange holes added (both flanges) to the (axisymmetric) model with no features. This figure shows that including of the flange holes significantly decreases the natural frequencies, up to about 4% for modes 5 and 6, of 6 of the 12 modes. The correlation is shown to be good with MAC values very close to 1.0 for all experimental modes and natural frequency differences of between +4% and +9%. Note that by adding the flange holes alone the frequency difference variation increased to about 2.5% while the mean decreased to +6.5%.

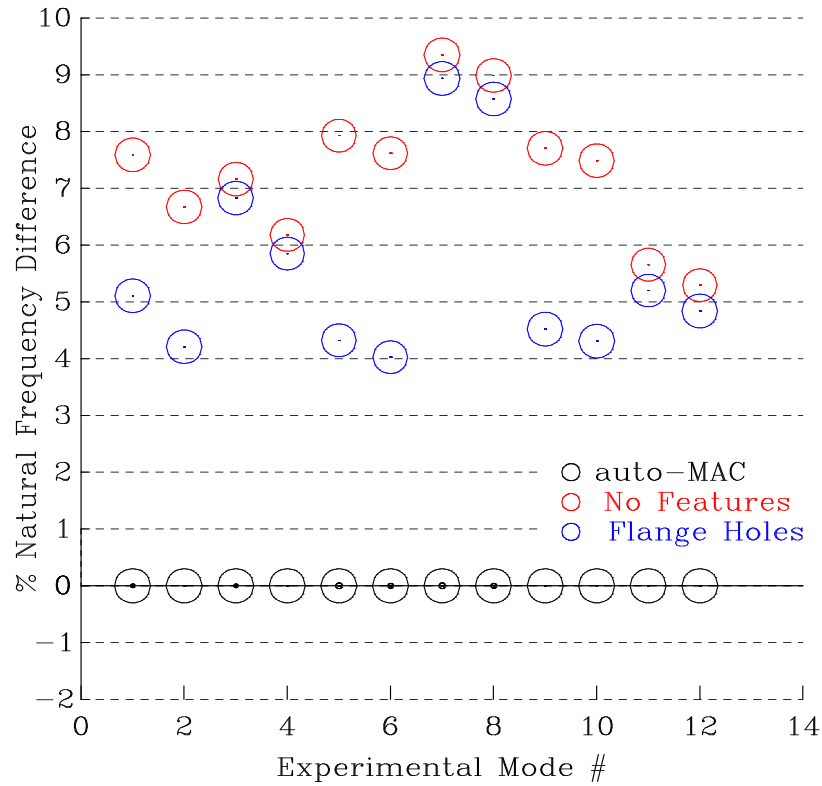


Figure 6.20: FMAC Plot for the Combustor Casing with Flange Holes

The FMAC plot comparing the model with the scallops added (inner flange) to the (axisymmetric) model with no features is shown in Figure 6.21. The figure shows that the scallops significantly decreased the frequencies of 6 of the 12 modes (up to about 4.5% for modes 7 and 8). However, the scallops had nearly no effect on modes 11 and 12. The correlation is shown to be good with MAC values very close to 1.0 for all experimental modes and natural frequency differences between +3.8% and +7.2%. Adding the scallops alone decreased both the frequency difference variation to about 1.7% and the mean to about +5.5%.

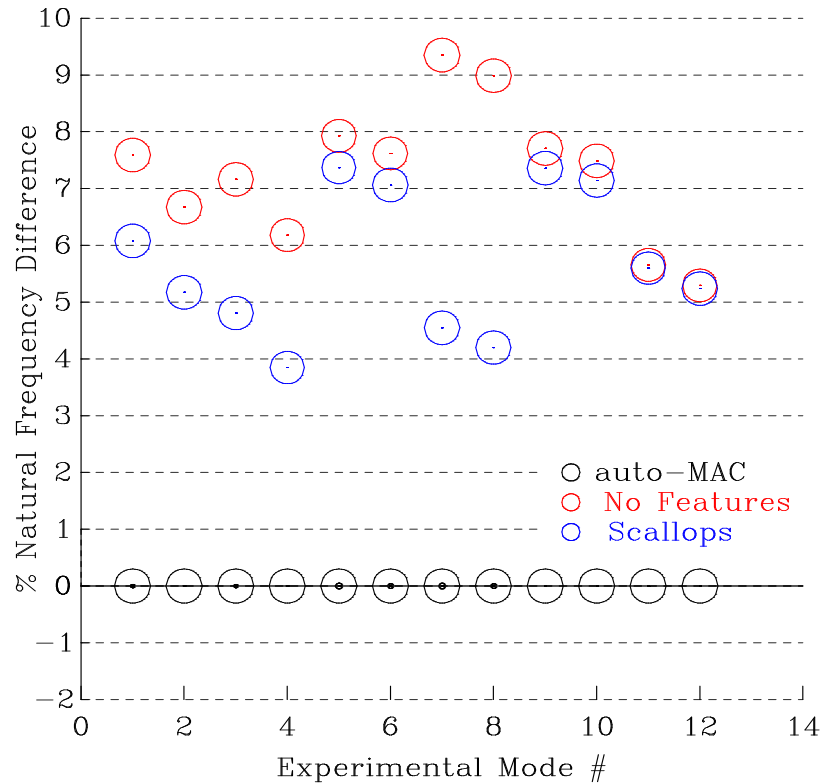


Figure 6.21: FMAC Plot for the Combustor Casing with Scallops

Figure 6.22 compares the model with the case holes (through both inner and outer casings) and bosses added to the (axisymmetric) model with no features. The figure shows that the correlation is good with MAC values very near 1.0 for all modes but adding the case holes with bosses had minimal effect on the frequencies of the 12 modes. The greatest change was about -1.5% for modes 3 and 4. However, there was almost no effect ($< 0.5\%$) on modes 5, 6, 9 and 10. The addition of the casing holes and bosses decreased the mean frequency difference to about +6.7% while the variation remained unchanged at about 2%.

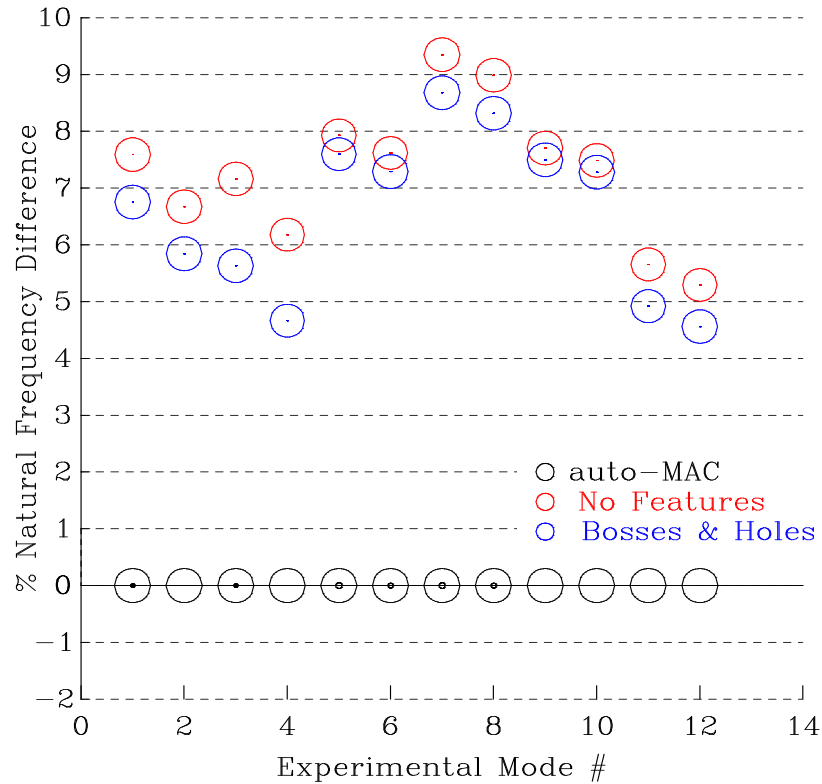


Figure 6.22: FMAC Plot for the Combustor Casing with Holes and Bosses

The model with all the features compared with the (axisymmetric) model with no features is shown in Figure 6.23. The figure shows that the addition of all the features significantly decreased the natural frequencies, up to about 6% for modes 7 and 8, of 10 of the 12 modes. However, the natural frequencies for modes 11 and 12 only decreased by about 1%. Note that adding the features had nearly no effect on the MAC values. The resulting correlation with all the features added is excellent, as mentioned above.

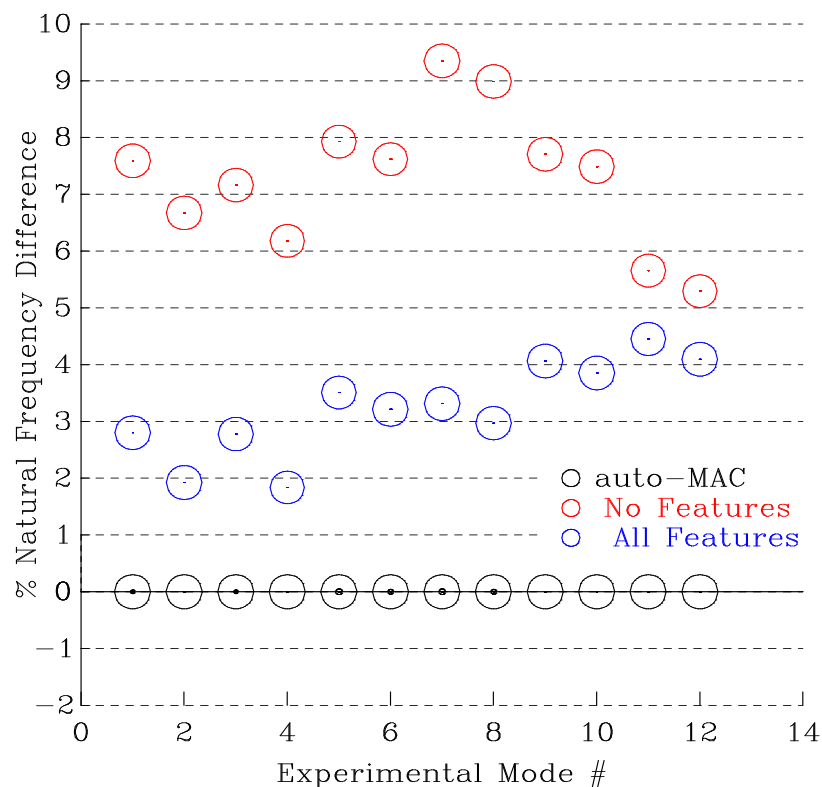


Figure 6.23: FMAC Plot for the Combustor Casing: None and All Features

6.4.2 Turbine Casing

The FMAC plot for the model with no features (axisymmetric case) is shown in Figure 6.24. The figure shows that the correlation is quite good with MAC values very close to 1.0 for all experimental modes, except mode 5 with a MAC value of about 0.5. The frequency differences are between +4.2% and +7% and are very consistent with only about a 1.4% variation about a line at +5.6%.

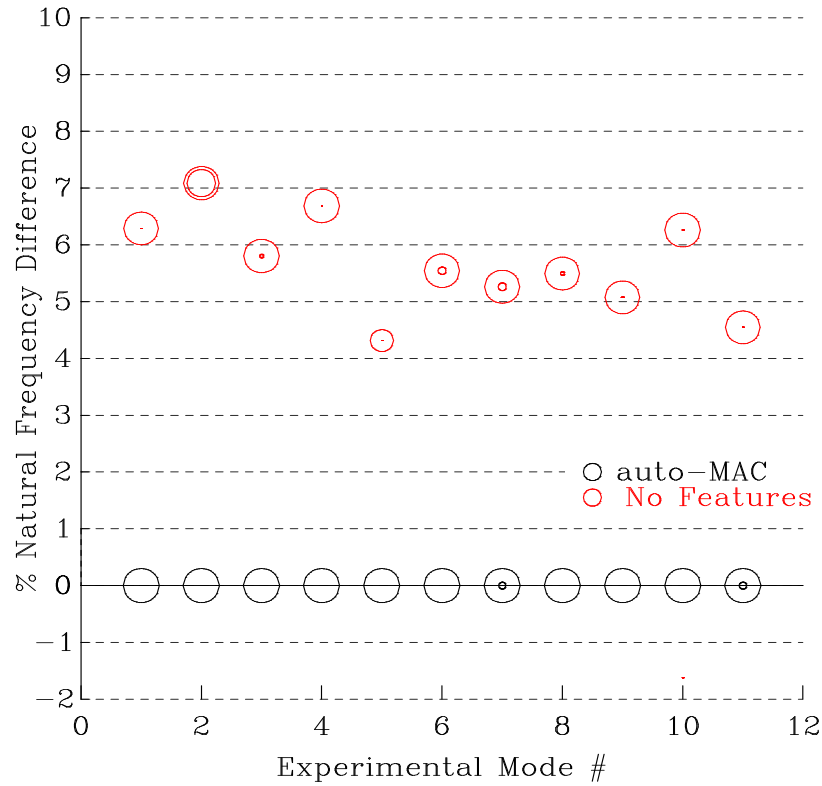


Figure 6.24: FMAC Plot for the Turbine Casing: No Features

Figure 6.25 compares the model with the flange holes added, which were the only features, with the (axisymmetric) model with no features. The figure shows that the flange holes significantly decreased the frequencies of 6 of the 12 modes, by up to about 3.5% for modes 3 and 6 through 9. Note that the MAC value for mode 5 increased to about 1.0 from the value of 0.5 obtained with no flange holes. The resulting correlation with the flange holes added is very good, as mentioned above.

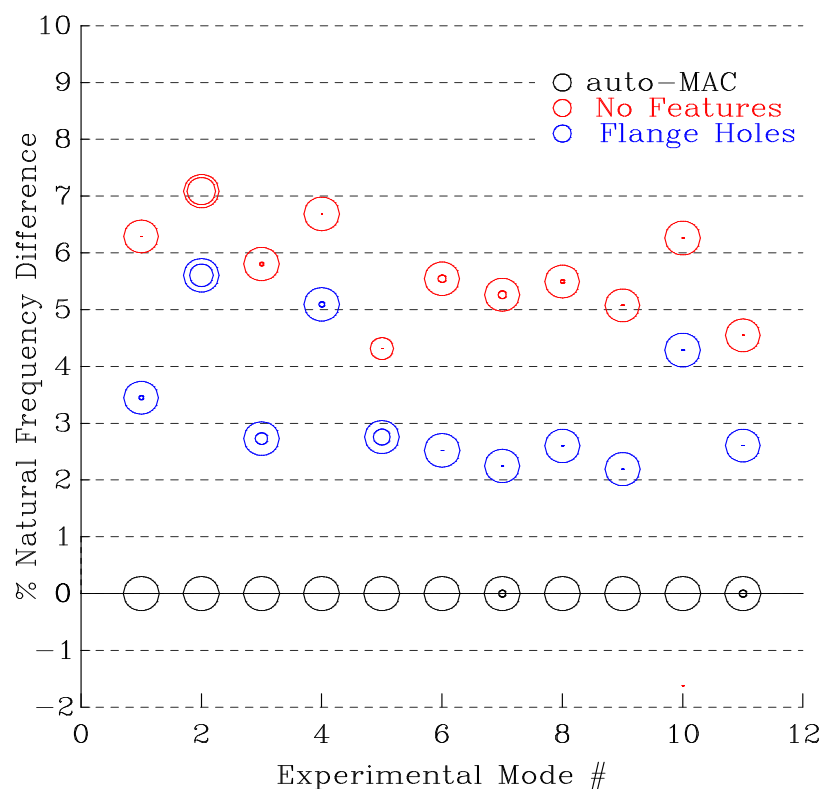


Figure 6.25: FMAC Plot for the Turbine Casing with Flange Holes

6.4.3 Assembly of Combustor and Turbine Casings

The FMAC plot for the model with no features (axisymmetric case) is shown in Figure 6.26. This figure shows that the correlation is very good with MAC values very close to 1.0 for all experimental modes, except mode 10 with a MAC of about 0.8. The frequency differences are between about +5.2% to +7.8% and are very consistent with only a 1.3% variation about a line at +6.5%.

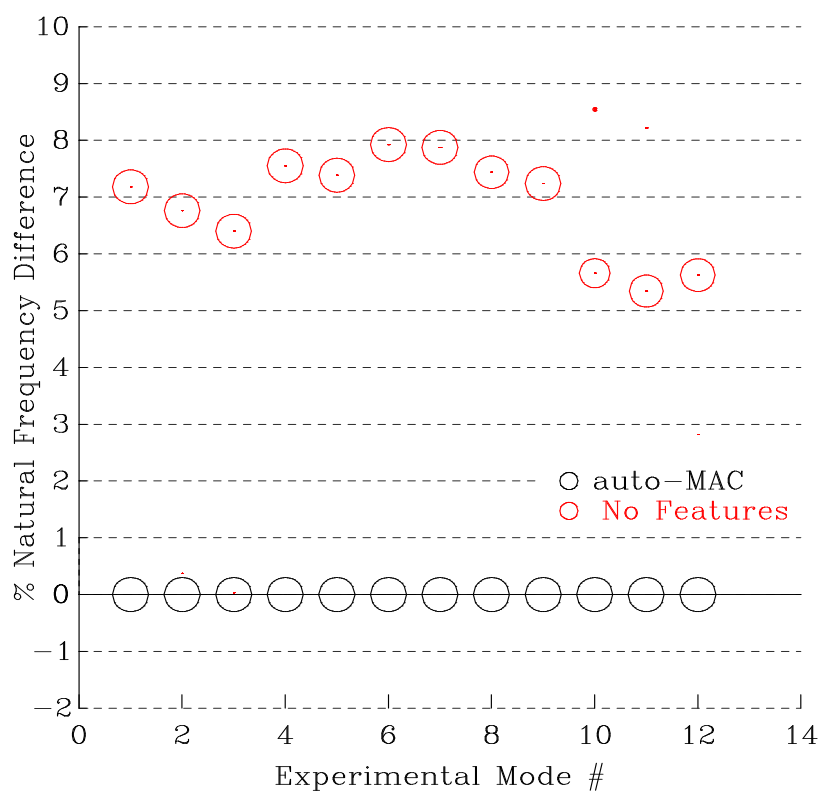


Figure 6.26: FMAC Plot for the Assembly: No Features

Figure 6.27 compares the model with the flange holes (all four flanges) added to the initial (axisymmetric) model with no features. The figure shows that the addition of the flange holes significantly decreased the frequencies, by up to about 3.5% for modes 4 and 5, of 5 of the 12 modes. The MAC values remained near 1.0 for all modes except modes 10 and 11 with values of about 0.5 and 0.7 respectively. Adding the flange holes alone decreased the mean frequency difference to about +5.2%, however the variation increased to about 1.5%.

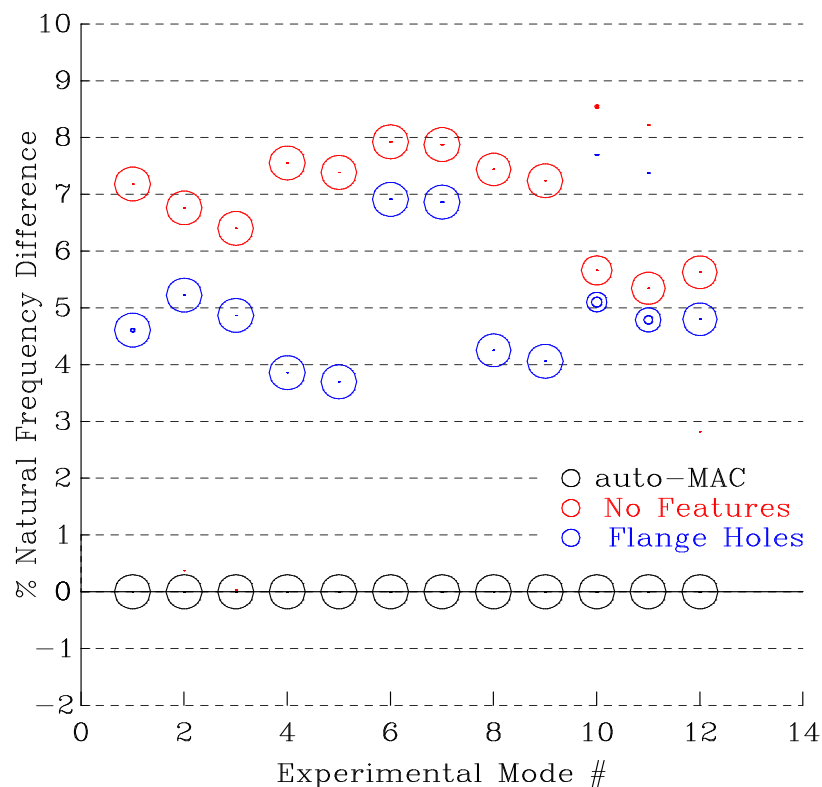


Figure 6.27: FMAC Plot for the Assembly with Flange Holes

The comparison between the model with the combustor scallops added (inner flange) and the (axisymmetric) model with no features is shown in Figure 6.28. The figure shows that the scallops significantly decreased the frequencies, by up to about 4.5% for modes 6 and 7, of 5 of the 12 modes. However, the scallops had nearly no effect on modes 4, 5 and 8 through 10. Note that the MAC values remained about the same for all modes. The addition of the scallops increased the frequency difference variation to about 2.1% but decreased the mean to about +5.4%.

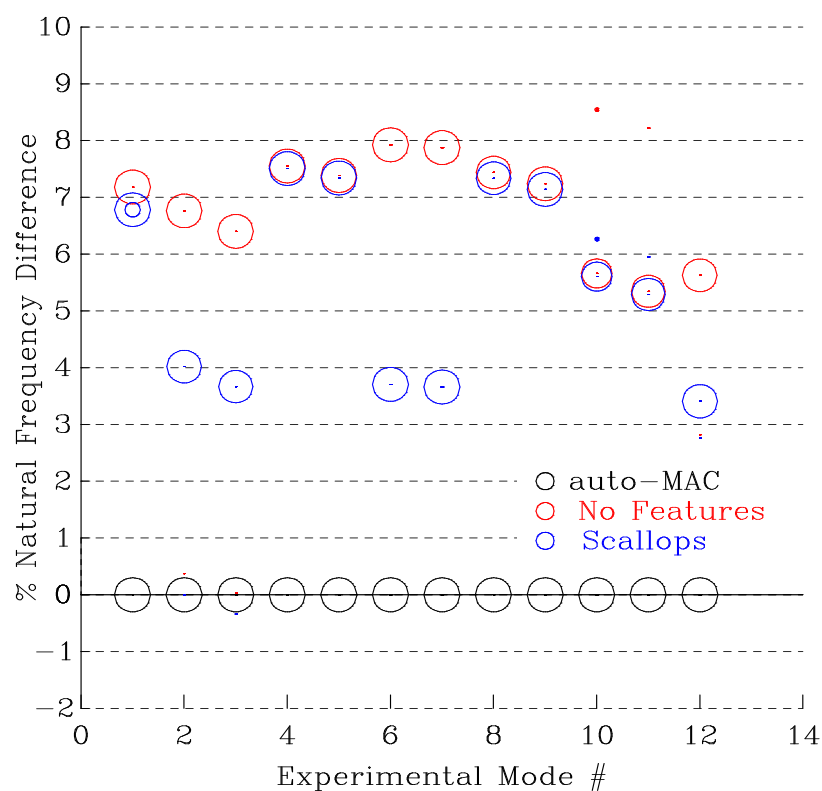


Figure 6.28: FMAC Plot for the Assembly with Scallops

Figure 6.29 compares the model with the case holes (through both inner and outer casings of the combustor) with bosses added to the (axisymmetric) model with no features. The figure shows that the case holes with bosses had minimal effect on the frequencies of the 12 modes. The greatest change was about 1% for mode 1. However, the case holes with bosses had no effect on mode 12 and nearly no effect on modes 8 and 9. The MAC values again remained about the same for all modes. Adding the case holes and bosses decreased the mean frequency difference to about +6.1% and increased the variation to about 1.5%.

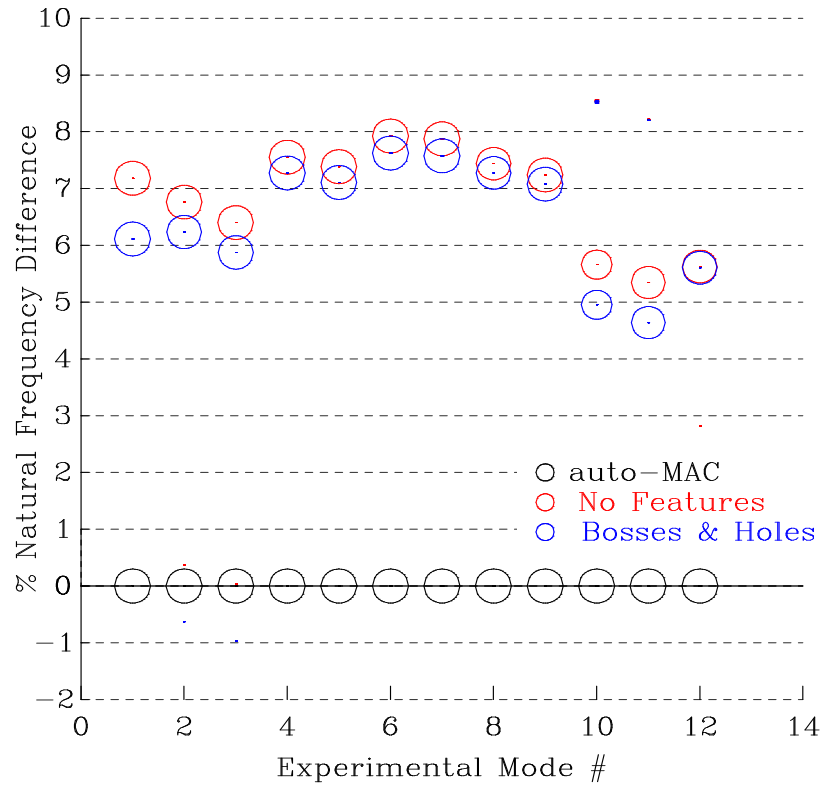


Figure 6.29: FMAC Plot for the Assembly with Holes and Bosses

The comparison between the model with all the features and the (axisymmetric) model with no features is shown in Figure 6.30. The figure shows that with all the features added the frequencies decrease significantly, by up to about 6% for modes 7 and 8, of 10 of the 12 modes. However, the frequency for modes 10 and 11 only decreased by about 1.5%. The MAC values remained unchanged for all modes. The resulting correlation with all the features added is excellent, as mentioned above.

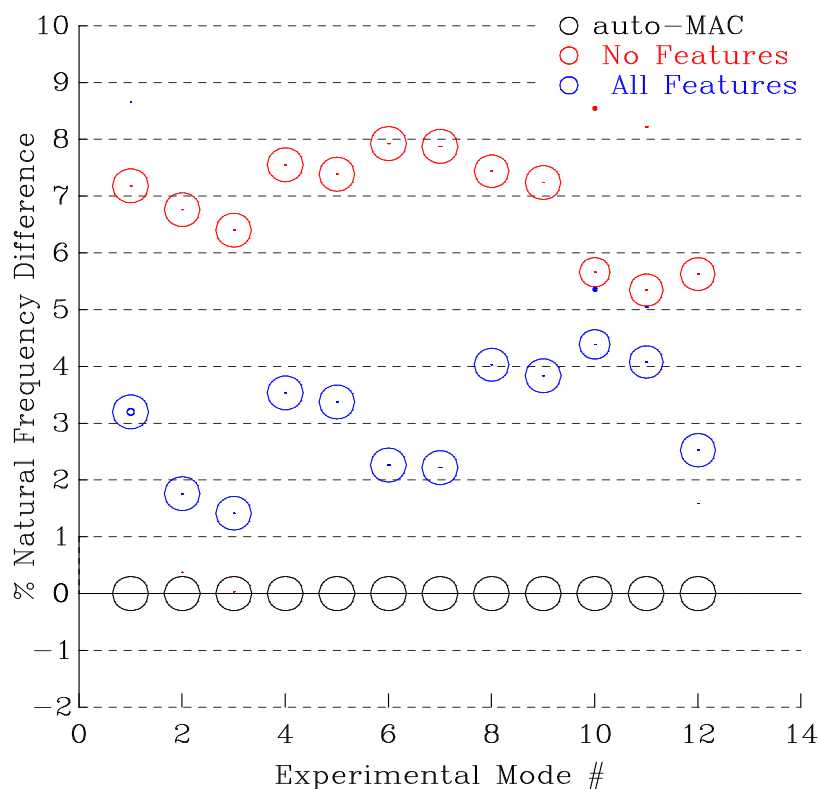


Figure 6.30: FMAC Plot for the Assembly: None and All Features

6.4.4 Summary of Feature Effect Results

The results of the effects of the different structural features on the correlation are summarised in Figure 6.31. The figure lists the natural frequency difference variation and mean for each model that was analysed. In order to display clearly all the results, it was necessary to separate the data into two parts. However, note that the "no features" and "all features" columns are provided in both parts of the summary to simplify the task of making comparisons.

Natural Frequency Differences (variation, mean)				
<u>Model</u>	No <u>Features</u>	Flange <u>Holes</u>	<u>Scallops</u>	All <u>Features</u>
Combustor	2.0%, +7.2%	2.5%, +6.5%	1.7%, +5.5%	1.3%, +3.0%
Turbine	1.4%, +5.6%	1.7%, +3.9%	<i>NA</i>	1.7%, +3.9%
Assembly	1.3%, +6.5%	1.5%, +5.2%	2.1%, +5.4%	1.5%, +2.8%

<u>Model</u>	No <u>Features</u>	Casing Holes <u>and Bosses</u>		All <u>Features</u>
Combustor	2.0%, +7.2%	2.0%, +6.7%		1.3%, +3.0%
Turbine	1.4%, +5.6%	<i>NA</i>	—————	1.7%, +3.9%
Assembly	1.3%, +6.5%	1.5%, +6.1%		1.5%, +2.8%

Figure 6.31: Summary of the Feature Effect Results

6.5 Physical Model Reduction of Engine Casings

The reduction of any model generally requires certain compromises, some of which are the exclusion of selected features and geometry approximations. While there are many ways to generate approximate models of complex structures, as was shown in Chapter 3, the combination of beams, for the features, and shells, for the casings, has been used here. As this modelling approach was shown in Chapter 3 to be the least favourable, in terms of correlation, it is an ideal choice to demonstrate the benefits of selecting the best possible DOFs for a given mesh size. While the super-model may represent the maximum number of DOFs for the model of a given structure, the beam/shell model may represent the least number of DOFs for the same structure. In this way the physical model reduction technique was given the greatest possible challenge.

The application of the modal average strain energy density (MASED) reduction technique presented in Chapter 4 to either of the rather complex casings considered here, in their entirety, may yield results that are not very useful. This is because the modal average strain energy density tends to concentrate in the areas of the major features, such as the flanges and channels, and consequently very few elements would be left for the major casing sections. Accordingly, the technique was applied to the major sections of the casings since the geometry of the included features demands sufficient detail that if decreased may cause significant compromises to the geometry.

It is important to mention that the MASED method, in its current form, selects a subset of the elements considered for reduction without regard for the type of element. Accordingly, the reduction of the solid-element super-models to beam/shell models is a three-step process of which the MASED method is one of the steps. The MASED was first used to determine the subset of the super-model elements to retain for the desired reduced size. Next, the subset or reduced set of solid elements was converted to shell elements using the methods presented in Chapter 3. The

last step was to determine the section properties of the solid-element features—flanges and channels—for the beams. This can be achieved in numerous ways but was accomplished here by using the computational capability in MSC/NASTRAN, called the grid point weight generator, to determine the section properties of the cross-section model for each of the features.

By converting the different features from solid elements to beam elements it was necessary to omit certain features, such as the flange holes, scallops and casing holes. Although the study presented above makes a case for including at least the flange holes and scallops in a super-model, it is generally an unavoidable consequence that they are omitted for a reduced model. However, since the MASED method was applied to the super-model that contained all the features, the effect the features had on the modal average strain energy density will be present in the reduced model. This is referred to here as the "residual" feature effect and is another advantage of the MASED method.

6.5.1 Combustor Casing Model Reduction

The modal strain energy density for each element of the combustor casing super-model was computed using MSC/NASTRAN for the first 20 flexural modes for the free-free condition. The MASED for the first 20 modes is shown in Figure 6.32.

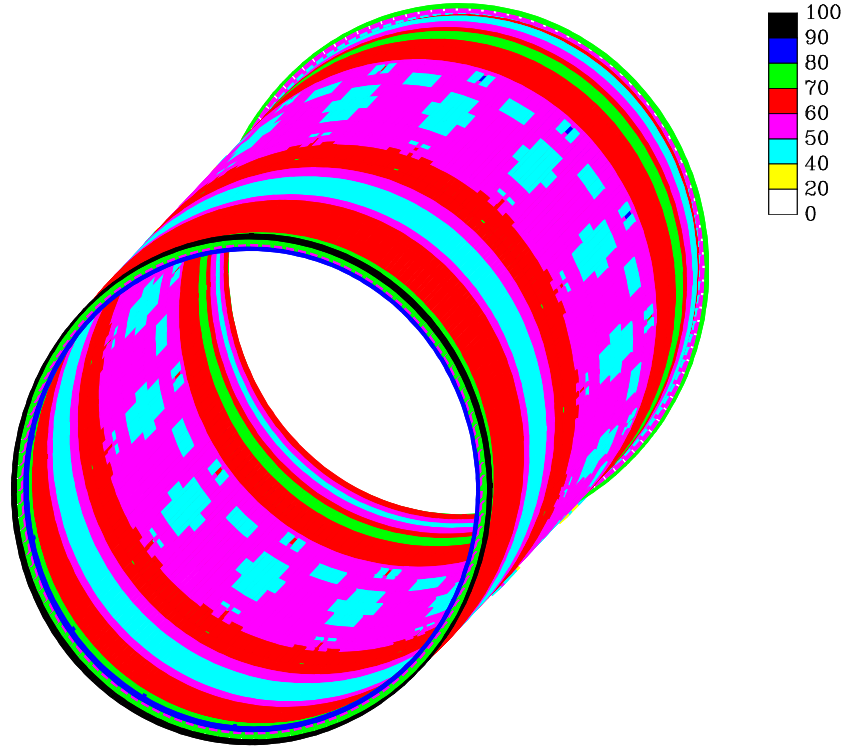


Figure 6.32: MASED for Combustor Casing Super Model

The figure shows that by including 20 modes in the modal average, the MASED distribution in the circumferential direction is very close to uniform for elements that are away from the casing holes. However, there is a moderate axial variation with the maximum being at the forward flange.

The physical model reduction was performed using the MASED approach with a weighting factor of 1.0 used for each of the 20 modes. Since the flanges were to be modeled with beam elements, they were excluded from the reduction. Because of the complexity of the geometry the reduction was performed in three stages. The super-model was first divided into three zones, as shown in Figure 6.33. The target reduction ratio was chosen to be between 10 to 20 for each zone. Selecting a greater reduction ratio, especially for zones B and C, would be most likely to result in compromises made to the geometry. Furthermore, the mode tracking

results described above showed that the combustor casing was dominant in the assembly modes, which suggests that a less aggressive reduction ratio than might ordinarily be used would be prudent to maintain a higher level of accuracy.

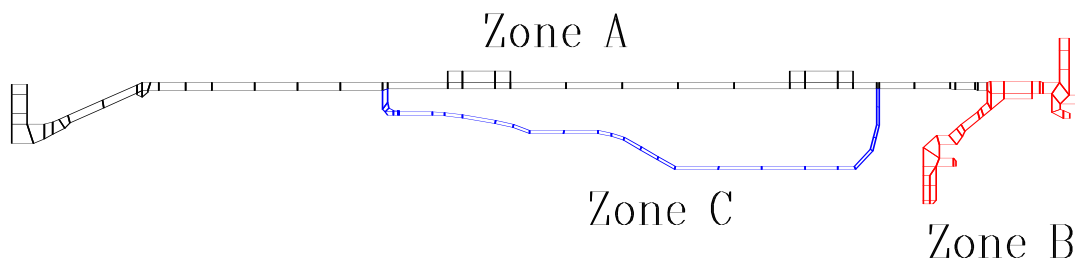


Figure 6.33: Combustor Casing Cross-section Super Model Reduction Zones

The reduced beam/shell model cross-section for the combustor casing is shown in Figure 6.34 superimposed on the super-model. The casing shell-elements are shown in red and the beam centroids are shown by the blue circles with the offsets represented by the blue lines. The cross-section of the super-model is shown by the black lines.

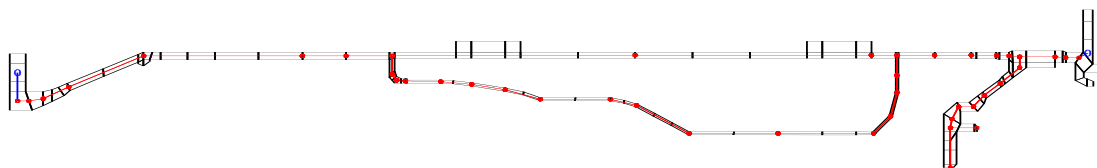


Figure 6.34: Combustor Casing: Cross-section of Reduced and Super Models

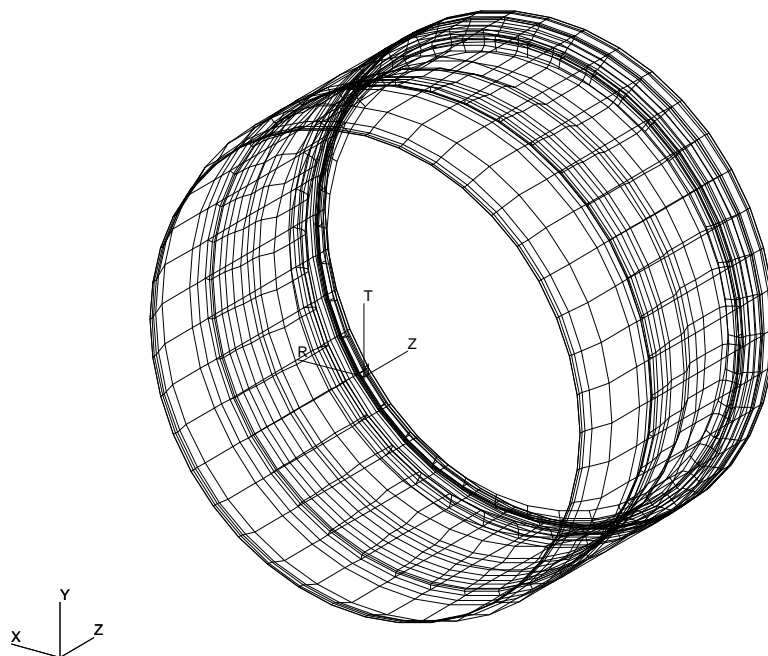


Figure 6.35: Combustor Casing Reduced Beam/Shell 3-D Model

Figure 6.35 shows the resulting 3-D model with 40 circumferential elements. The figure shows that the mesh is nearly equally-spaced in the circumferential direction but has a moderate spacing variation in the axial direction. This is consistent with the MASED distribution as shown in Figure 6.32.

The super-model for the combustor casing had 216 cross-section nodes and 240 circumferential nodes, whereas the reduced beam/shell model had 43 and 40 nodes respectively. Considering the difference in the number of DOFs per node, between the solid-element super-model with 3 and the beam/shell-element model with 6, the total number of DOFs was decreased from 155,520 to 10,320, giving a reduction ratio of about 15.

The FMAC plot in Figure 6.36 shows a comparison of the correlation with the test data for both the reduced model, in blue, and the super-model in red. The

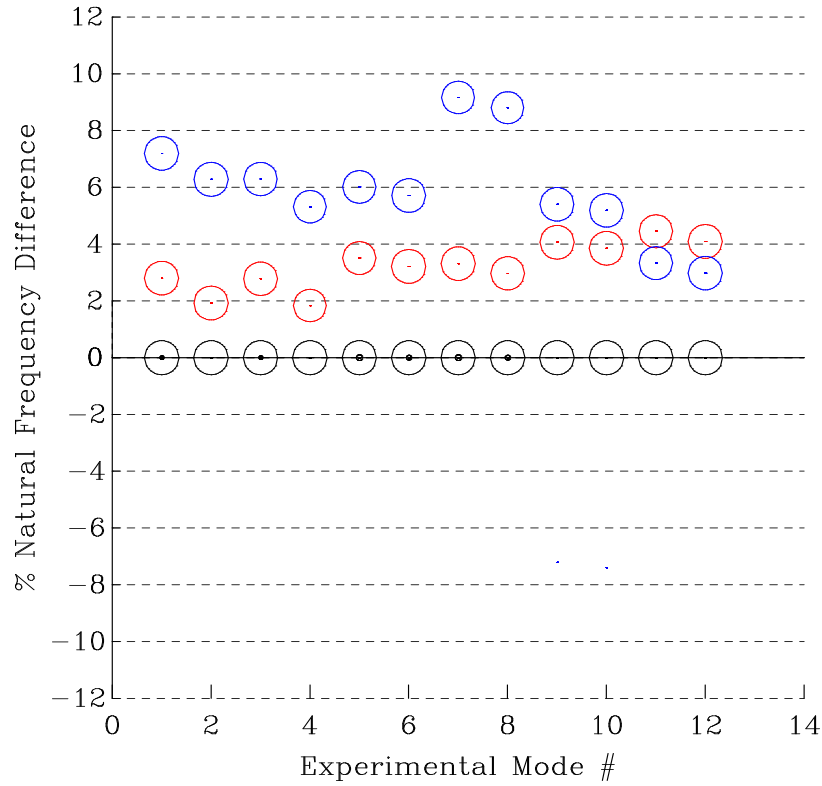


Figure 6.36: FMAC Plot for the Combustor Casing Reduced and Super Models

figure shows that the correlation for the reduced model is good with MAC values 0.9 for all modes but with natural frequency differences of between about +3% and +9%. The super-model is seen to have a much smaller natural frequency variation of between about +1.7% and +4.3%. However, when considering that the super-model had about 15 times the number of DOFs, the natural frequency variation for the reduced model is considered to be very good and can be understood by reviewing Figure 6.21 of the feature effects study above. From that figure it can be seen that by including the scallops on the aft inner flange, the natural frequencies for the first 8 modes of the combustor casing decreased significantly, by up to about 5% for modes 7 and 8. Accordingly, the natural frequency variation in the reduced model can be attributed largely to the omission of the scallops from the model.

6.5.2 Turbine Casing Model Reduction

MSC/NASTRAN was again used to determine the modal strain energy density for each element of the turbine casing super-model for the first 20 flexural modes for free-free boundary conditions. The modal average strain energy density for the first 20 modes of the turbine casing super-model is shown in Figure 6.37. This figure

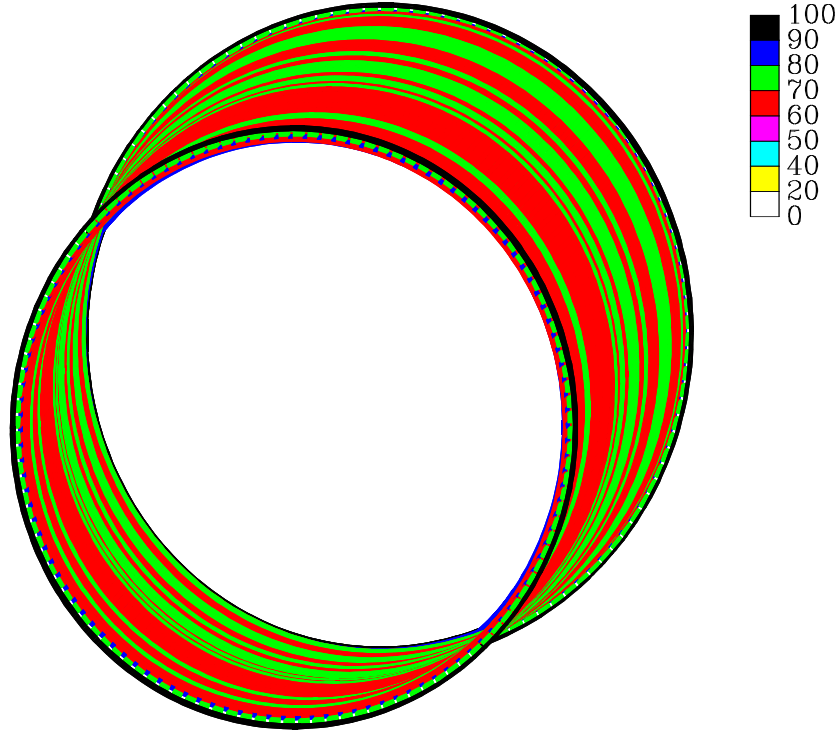


Figure 6.37: MASED for Turbine Casing Super Model

shows that by using 20 modes in the modal average, the MASED distribution in the circumferential direction is again very close to uniform. The axial variation is again moderate, with the maxima occurring at the forward and aft flanges.

The physical model reduction was performed using the MASED approach with weighting factors of 1.0 for each mode. The flanges and channels were to be modelled using beam elements and, consequently, were excluded from the reduction. With moderate geometry variation, the goal for the reduction ratio was set to

be between 25 and 35. Although this is more aggressive than that used for the combustor casing, the mode tracking results from above indicate that the turbine casing modes contribute much less to the assembly when compared with the combustor casing. Accordingly, a greater reduction of the turbine casing model should be possible with less risk of decreasing the accuracy of the assembly model.

The reduced beam/shell model cross-section for the turbine casing is shown in Figure 6.38 on top of the super-model. The casing shell-elements are shown in red and the beam centroids are shown by the blue circles with the offsets represented by the blue lines.

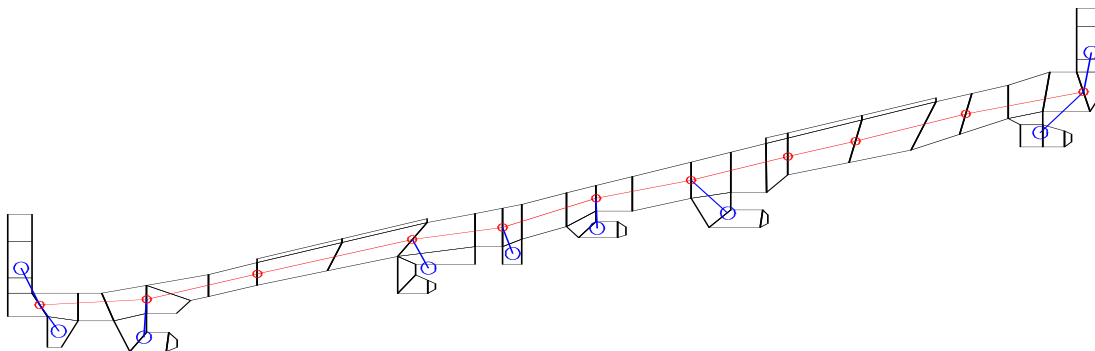


Figure 6.38: Turbine Casing: Cross-section of Reduced and Super Models

The 3-D model with 40 circumferential elements is shown in Figure 6.39. The figure shows that the mesh has a moderate axial spacing variation but is nearly equally-spaced in the circumferential direction. This is again consistent with the MASED distribution as shown in Figure 6.37.

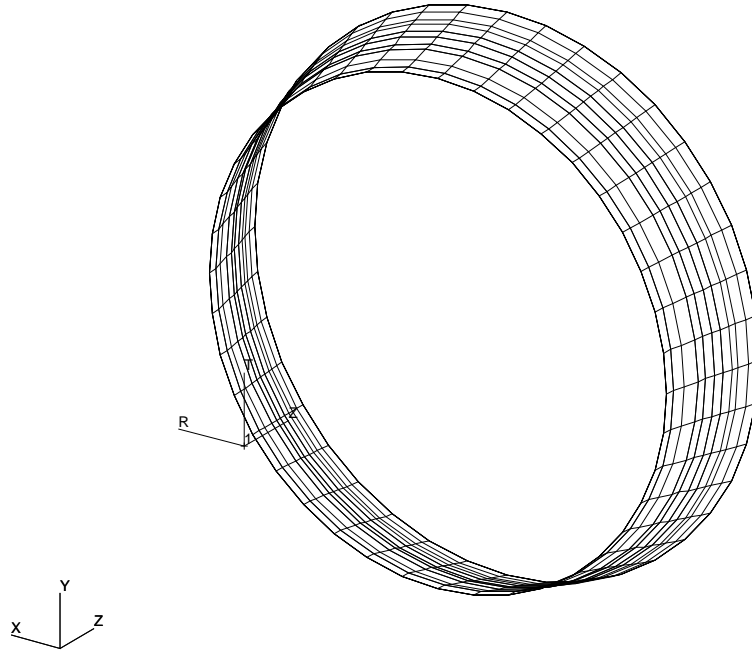


Figure 6.39: Turbine Casing Reduced Beam/Shell 3-D Model

The super-model from above had 111 cross-section nodes and 240 circumferential nodes compared with the reduced model with 11 and 40 nodes, respectively. Taking into account the difference in the number of DOFs per node, the decrease in the total number of DOFs was from 79,920 to 2,640 for a reduction ratio of about 30.

Figure 6.40 shows the FMAC plot which compares the correlation with the test data for both the reduced model, in blue, and the super-model in red. The correlation is seen in the figure to be good with MAC values > 0.8 for all modes and natural frequency differences of between about -3.5% and +5.5%. The figure shows again that the super-model had a much smaller natural frequency variation of between about +2.2% and +5.6%. However, the natural frequency variation for the reduced model is still considered to be very good, especially when taking account

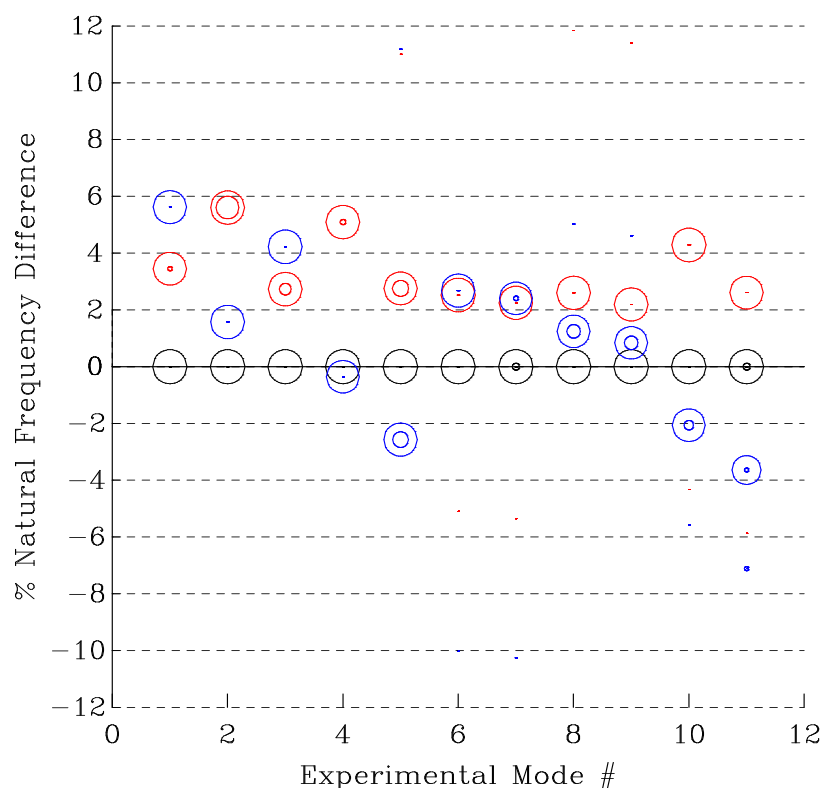


Figure 6.40: FMAC Plot for Turbine Casing Reduced and Super Models

of that the super-model had about 30 times the number of DOFs. An explanation of the reduced model frequency variation can be obtained by reviewing Figure 3.25 from Chapter 3. That figure compares, for a generic casing with two flanges, three different modelling methods—shell/beam, shell alone and hybrid—against a very detailed reference solid model. From the figure it can be seen that, when compared with the reference solid model, the shell/beam model demonstrated very similar natural frequency variations to those from the comparison shown here for the reduced model compared with the super-model. Accordingly, the increase in the natural frequency variation is attributed mostly to the change from a solid to a shell/beam type model for the reduced model.

6.5.3 Assembly of the Reduced Component Models

The reduced model for the assembly was obtained by attaching the two reduced component models together at their mating flanges using a rigid joint model. However, since the reduced mating flanges were represented by beam elements, the mating nodes had a gap between them making it necessary to add rigid elements to bridge the gap.

Figure 6.41 shows a cross-section of the joint model between the aft flange of the combustor casing and the forward flange of the turbine casing. The model for the reduced casings is superimposed on the joint model that was used for the assembly super-model. The shell models are shown by the lines and circles that coincide with the mean-line of the casings. The off-set beam element centroids are shown by the dashed lines and the two circles with the "X" in the middle. The rigid elements are shown by the green lines connecting the shell nodes to the extra node, also shown in green, at the bolt hole centre-line.

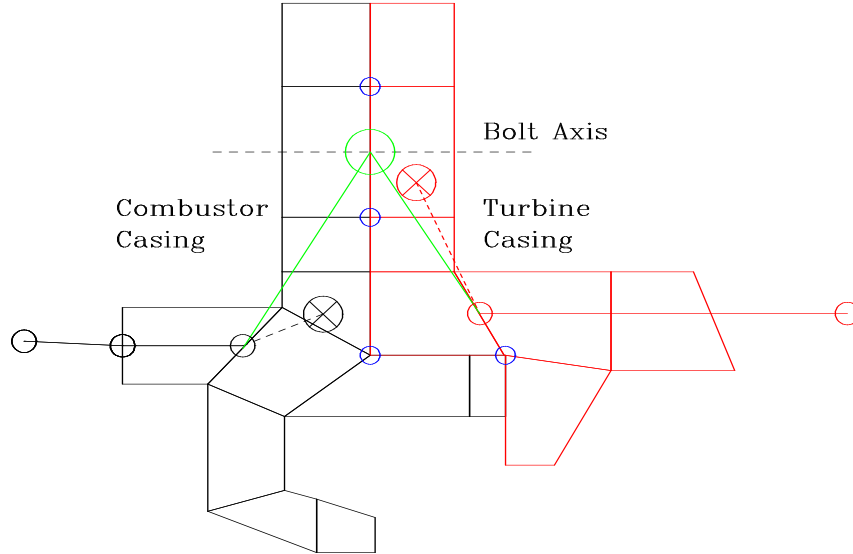


Figure 6.41: Cross-section of Joint Model for the Reduced Assembly

All 6 DOFs (3 translations and 3 rotations) of each node of the rigid elements were used so that the physical joint, which can transmit both translational and

bending loads, could be modelled adequately. The reduced assembly model had 12,960 DOFs compared with the super-model which had 235,440 DOFs, reflecting a reduction ratio of about 18.

The correlation for both the reduced and super-models of the assembly are compared in the FMAC plot in Figure 6.42. The figure shows that the correlation

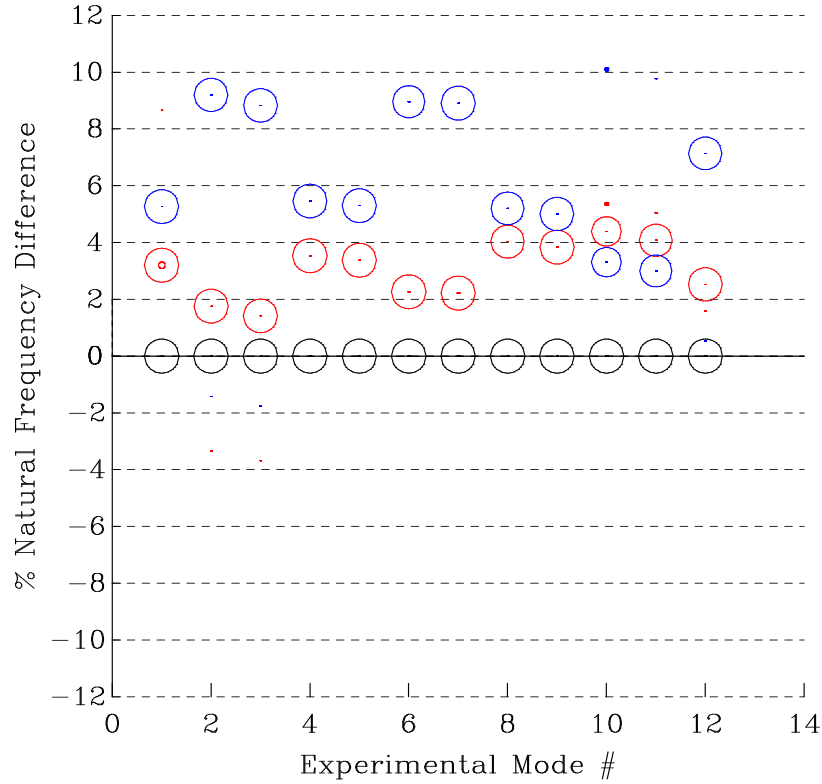


Figure 6.42: FMAC Plot for Assembly Reduced and Super Models

for the reduced model is good with MAC values > 0.8 for all modes and with natural frequency differences of between about +3% and +9%. The super-model is seen to have a much smaller natural frequency variation (between about +1.3% and +4.3%) as was previously noted for the individual component super-models. However, when considering that the super-model had about 18 times the number of DOFs, the natural frequency variation for the reduced model is considered to be very good. As for the component reduced models, the natural frequency variation

here can be attributed to the omission of certain features from the reduced model. From Figure 6.28 of the feature effects study above, it can be seen that by adding the scallops to the aft inner flange of the combustor casing part of the assembly model, the natural frequencies for modes 2, 3, 6, 7 and 12 all decreased significantly, by up to about 4% for modes 6 and 7. Consequently, the omission of the scallops can be identified as a possible cause for the largest part of the greater natural frequency variation for the reduced model. It is no coincidence that the assembly model comparison parallels that of the combustor casing alone, as the mode tracking study indicated that the combustor casing was the dominant component in the assembly.

6.6 Residual Modes and Reduced Assemblies

One of the advantages of the new model validation strategy presented in Chapter 2 is that once the super-model has been obtained, it can be used to overcome some of the limitations of a conventional modal test. The test frequency range is one of the limitations that it is often desired to overcome. The lack of correlation of an assembly is often attributed to the inability of the component FE models to predict certain high-frequency modes, some of which may get driven to much lower frequencies in the assembly as a result of connecting the mating components. It is argued in [32], that the component FE models are less accurate for the higher modes due to their limited mesh densities. Accordingly, the super-model can be used as a reference or virtual test data set and the modes for any desired frequency range can be generated. In this way, the reduced models can be compared with the reference for a much larger frequency range than would be afforded by a conventional modal test. This comparison can give insight into what is termed the "residual mode" effect.

Figure 6.43 shows the FMAC plot that compares the reduced model for the combustor casing with its corresponding super-model for the first 26 modes.

The figure shows that the reduced model performs quite well for about the first 16 modes. However, for the higher modes (17-26), the correlation becomes much worse and is very poor for modes 24 through 26. This clearly shows the limits of the reduced model for the prediction of the higher frequency modes.

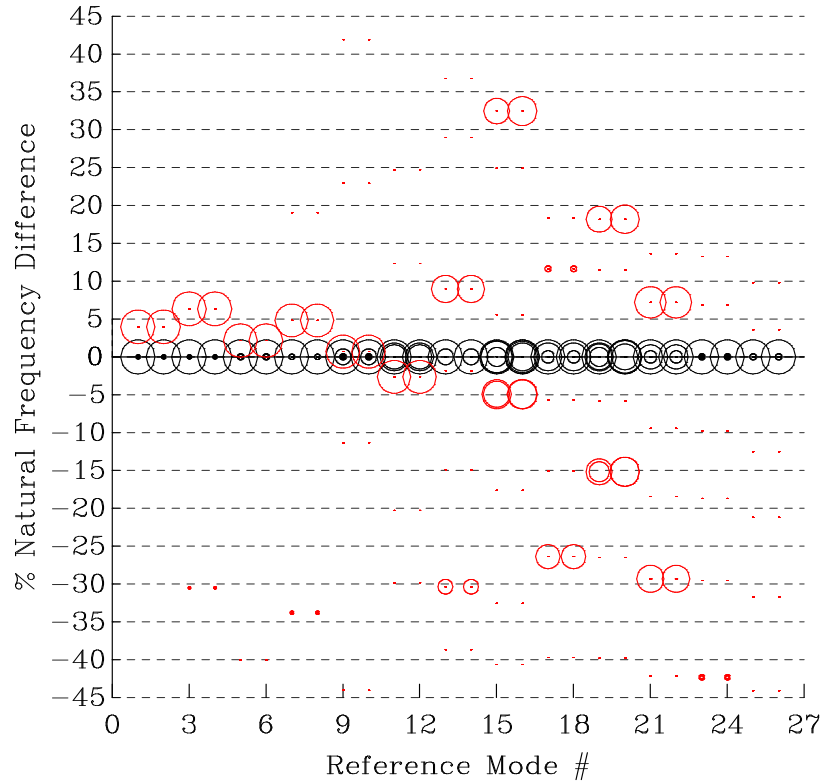


Figure 6.43: FMAC: Combustor Casing Reduced and Super Models, Higher Modes

Similarly, for the turbine casing the FMAC plot in Figure 6.44 shows the comparison between the reduced and super-models for the turbine casing for the first 26 modes. In this figure, the correlation is seen to be very good for the first 20 modes but for modes 21 through 26, is almost non-existent. Again, the high frequency limits of the reduced model have been clearly shown.

It is important to mention that this is not a reflection on the performance of

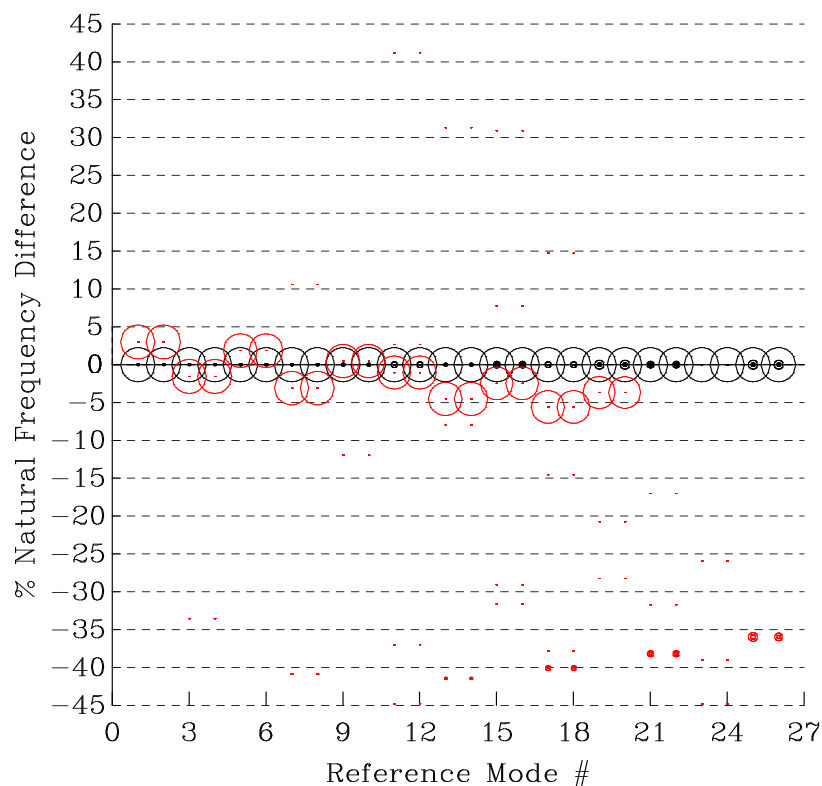


Figure 6.44: FMAC: Turbine Casing Reduced and Super Models, Higher Modes

the reduced models. This study is intended to lend support to the lack of the high-frequency or residual mode capability of the reduced models being at least part of the cause for the increase in the natural frequency differences for the reduced assembly model. However, it can be said that the two comparisons in Figures 6.43 and 6.44 further illustrate that the reduced models performed very well when one considers only the first 20 modes were used in the MASED, and reduction ratios of 15 and 30 were achieved for the combustor and turbine casings respectively.

6.7 Conclusions

6.7.1 Super Models

The ability to reproduce the test data using a super-model was clearly demonstrated for two adjacent real turbine engine casings. Further, the two casings were connected using a rigid joint model to form an assembly model that was also shown to reproduce the test data with excellent accuracy. The convergence of the refined component models to a higher degree of accuracy than the initial models demonstrated the robustness of the models. The consistency of the natural frequency variations in all cases is attributed to the models possessing accurate geometry, adequate mesh density and details of the most significant features.

6.7.2 Effects of Features on Correlation

In the study presented here, the effects of the different detail design features on the degree of correlation was clearly shown. It is important to mention that the MAC values were in general unchanged by the addition of the different features but that the natural frequency differences were affected, in some cases significantly. The flange holes and scallops had the greatest effect by decreasing the natural frequencies of some modes by between about 2% and 4%. The case holes with bosses had a lesser effect by showing natural frequency decreases of about 1%. However, when all the features were included, the natural frequencies decreased between about 4% and 6% for more than half the modes considered. The features affected the assembly properties by about the same amount as they affected the components individually. With a goal of predicting natural frequencies to within, say, 5%, it is clear that features such as flange holes and scallops should be considered, either directly with a detailed model or approximately with an enhanced coarse (shell) model. However, an argument could be made that casing holes with bosses could be ignored, at least for casings with similar geometries to those presented in this

study.

6.7.3 Physical Model Reduction

The reduction of the super-models using the MASED physical model reduction technique was shown to be very effective. While the omission of most of the features in the reduced models was necessary, the degree of correlation obtained remained high with MAC values ≥ 0.8 and natural frequency differences $< 10\%$ for the modes considered. An important point to make is that the reduction used the modal average strain energy from the super-models which did, of course, include all the features. Consequently, the FE mesh topology had a built-in "residual feature effect" from the features, even though they were not physically included in the reduced models. The high degree of correlation that was obtained is attributed, in part, to this advantageous characteristic of the method.

Chapter 7

Conclusions and Future Work

The ability to generate an accurate FE model for structural dynamic analysis at any phase of the design process may be thought to be a relatively simple task. Some might believe that as computer power grows so must the modelling capability. However, in practice this is not generally the case as most analysts, at least in the aerospace industry, will confirm that their models for large structures have not improved significantly in the last 5 years or so. This unfortunate circumstance is attributed, at least in part, to deficiencies in the model validation process that this thesis seeks to remedy.

The tasks for developing valid FE models for structural dynamic design using the proposed new model validation strategy—the super-model—have been developed and presented in a concise and logical manner. This was done to emphasise the inter-dependence of the two primary tasks—FE modelling and correlation—and to illustrate how important they are, together, to the success of the model validation process.

The detailed conclusions for the research topics considered in this thesis have already been presented at the end of each chapter. The following three sections present the overall conclusions, summarise the contributions of this work and offer suggestions for future work. This is followed by some closing remarks.

7.1 Conclusions

7.1.1 New Model Validation Strategy

The success of the new model validation strategy proposed in this work relies on the ability to match the test data accurately using a super-model. This ability has been clearly demonstrated for three different gas turbine engine casings with relatively complex geometries. Each of the casings was modelled from design drawings without any geometric measurements being taken from the physical structure. This is important since during the design process the physical hardware will generally not be available at the stage when the models must be constructed. The correlation results showed that the test data could be consistently matched by predictions based on the model with excellent accuracy. This achievement is significant in that it allows for the validation of the FE model within the design process (without recourse to measurements) so that it can be used to better guide the design of the physical structure.

7.1.2 FE Modelling

The modelling techniques for both approximate and super-models were presented in some detail to illustrate the number and importance of the choices that are necessary to create an accurate FE model. It was emphasised that it is important for the analyst to have a basic understanding of the limitations of each element type in terms of order and distortion tolerance in order to determine how best to use them in practice. The basic techniques presented for using beam and shell elements were shown to help improve the modelled geometry, and therefore the mass and stiffness distributions, to be more representative of the actual structure. Additionally, it was shown that by using the beam and shell element modelling techniques presented that it was possible to represent a reference or super-model with sufficient accuracy, which is necessary for the approximate model to be updated.

7.1.3 Physical Model Reduction

A new physical model reduction technique using the modal average strain energy density has been developed and presented here, and has been shown to be very effective. It was demonstrated that a super-model could be reduced by a factor as high as 30 times while retaining a reasonable approximation of the modal characteristics of the super-model for a significant number of modes (16 to 20 in the case studies shown). The differential reduction of different components, taking account of how these individual component modes are influential in the assembly modes, using mode tracking, was shown to further enhance the reduction process. The ability to determine, using the super-models of the components and of the assembly, which of the components is the most dominant in each of the assembly modes has been shown to allow for the concentration of the most elements in the dominant component, thereby providing a more efficient model.

7.1.4 Model Correlation

The review of the available correlation methods depicted that the vector correlation methods are, in general, more widely used than either orthogonality or FRF-based methods. Furthermore, in certain cases some of the stand-alone vector methods (such as the NMAC) may prove superior to the MAC for mode shape correlation, but in general the MAC parameter remains the method of choice, mainly because it has not been improved upon for general applications.

The FMAC format of presentation of correlation parameters, developed in this thesis, has been shown to be very effective at simultaneously displaying all the necessary correlation information—the MAC, the natural frequency correspondence and the degree of spatial aliasing. Two alternate forms of the FMAC were shown to provide for a more detailed view of the frequency correspondence for modes close in frequency. The ability of the FMAC to display multiple correlations on a single plot was shown to be a very useful and powerful tool for assessing the

change in modal characteristics between the different correlation sets. A natural extension of the FMAC to the correlation of FRFs and mode shapes using the MFAC, introduced in this thesis, was shown to be quite promising in that the data with the most integrity—the test FRFs and the analytical mode shapes—may be used for correlation, thereby avoiding the modal analysis of the test FRFs.

The use of a truncated set of Fourier indices for the correlation of (quasi) axisymmetric structures was shown to help significantly improve the correlation. In some cases, the improvement was shown to be very significant and when combined with mode shape rotation provided a means for extracting the most meaningful correlation possible from (quasi) axisymmetric structures. It was demonstrated that by combining the Fourier truncation and mode shape rotation techniques the MAC values, between test and analysis mode shapes, could be as much as doubled for about half of the experimental modes. This is a significant achievement in that it effectively transforms what appears, at first, to be a poorly-performing model into a good-performing model.

7.2 Summary of Contributions

- (1) A new model validation strategy has been introduced which proposes replacing the traditional modal test data used in the classical model validation process with the analytical results from a very detailed FE model called a super-model. The demonstration that this is possible forms the basis for the improvement of the model validation process and gives rise to new possibilities, some of which are described below.
- (2) The use of the super-model in place of test data removes many of the limitations of a conventional modal test, such as the limited frequency range and number of measured DOFs. Furthermore, multiple boundary conditions can be explored with relative ease. The super-model when used as the refer-

ence for updating a design size model, provides information from significantly more DOFs than a modal test and, accordingly, renders the error location and model updating processes over-determined, which may be a significant advantage for obtaining an updated design model in much less time.

- (3) The current modelling trend is to generate a very detailed or super-model using automated mesh generating software. However, there is still a need for good approximate modelling techniques for preliminary design and early detailed design models when there may be no electronic form of the design available. While there is a significant amount of literature available on the FE method, there is relatively little published information on how to use the available elements and techniques in practice. This unfortunate circumstance is somewhat aided by the automation of mesh generation in commercial software where the ease of use can be misinterpreted by the analyst into meaning reliable and robust, which may not be the case. Accordingly, approximate modelling techniques remain necessary and those presented in this thesis should help to avoid the most common problems associated with most poorly performing models.
- (4) In the analysis of assemblies containing many components it remains important to be able to simulate the modal characteristics of a much larger model using relatively fewer DOFs. The physical model reduction technique using the modal average strain energy density introduced in this thesis provides a means to reduce large super-models to much smaller approximate but physical (as opposed to numerical) models. The technique has been shown to be very effective at making the most efficient use of a reduced number of elements by the reduced model retaining an adequate representation of the modal characteristics of a super-model for a significant number of modes (16 to 20 in the case studies shown).

- (5) The introduction of mode tracking of component modes to corresponding assembly modes has been shown to aid model reduction. By using mode tracking prior to performing reduction to rank the importance of each component to the assembly modes, the reduction ratios for each component can be selected optimally. In this way, the selected reduced number of total elements for the assembly can be placed where they are most needed, resulting in a more efficient model.
- (6) The natural frequency correspondence has often been overlooked in correlation procedures in favour of the mode shape correlation. The introduction of the frequency-scaled modal assurance criterion (FMAC) for performing correlation has remedied this by providing a way of displaying the mode shape correlation, natural frequency comparison and degree of spatial aliasing on a single plot that is relatively simple to construct. Furthermore, the FMAC has been shown to be very useful for comparing multiple correlation sets to gain insight into changes in modal characteristics.
- (7) The development of using a truncated set of Fourier indices for correlation of (quasi) axisymmetric structures was shown to help to eliminate some of the frustration often encountered when performing numerical correlation on such structures. When combined with mode shape rotation, the technique was shown to improve the correlation significantly. Before this development, the numerical correlation of (quasi) axisymmetric structures could often show poor results for modes that visually appeared to be similar or sometimes identical.
- (8) The modal frequency response assurance criterion (MFAC) was introduced so that a direct comparison could be made of the most readily-available information from each source—FRF data from the test and mode shapes from the analysis—and, consequently, the modal analysis of the test FRFs

could be avoided. This can present a significant advantage, especially when the test data are relatively noisy, a situation which tends to introduce errors in the mode shapes resulting from the modal analysis.

7.3 Suggestions for Future Work

Joint Modelling

Although the modelling of joints was not addressed in depth in this thesis, the demonstration of the effects of the interface on the modal characteristics of assembled structures clearly indicates that an accurate joint model is needed. The review of the available literature on joint modelling revealed that in general most of the published work focused on very specific joint types and applications. What is needed is a more general methodology for modelling joints.

Physical Model Reduction

Model reduction was presented in this thesis with the view towards reducing a super-model to a more practical size for use in an assembly of multiple components. However, one could envisage using the reduction techniques in the model validation process to reduce the super-model directly to create a validated design-size model and avoid the task of model updating. For this use, the physical model reduction technique would need to be enhanced to include the preservation of geometric features, such as complex shapes and inter-connections. Other improvements might be to consider the different element types and provide for a direct and possibly more accurate conversion from one element type to another. These improvements could significantly increase the robustness of the technique.

Model Correlation

While the FMAC is considered to be a significant advance in model correlation it still uses the MAC to compare mode shapes. There have been numerous attempts

to improve the MAC with varying success. Although the MAC remains, in general, the most common parameter for comparing mode shapes, it still has weaknesses. Some of these were addressed in this thesis for the particular case of axisymmetric structures. However, more work on correlation is warranted to find a more robust tool to replace the MAC.

7.4 Closure

The overall objective of this research was to improve the model validation process so that the design process could benefit from using a validated FE model. This was accomplished by the introduction of the super-model into the model validation process to replace test data. Further improvements were presented for various tasks within the model validation process for FE modelling and correlation. While even the most well received research is not completely self-contained, it is believed that the research presented in this thesis makes significant steps towards obtaining the efficient and timely development of validated FE models for structural dynamic design.

References

- [1] Lieven, N. A. and Ewins, D. J. A Proposal for Standard Notation and Terminology in Modal Analysis. *Proceedings of the 10th International Modal Analysis Conference*, pages 1414–1419, 1992.
- [2] Yap, K. C. and Zimmerman, D. C. Optimal Sensor Placement for Dynamic Model Correlation. *Proceedings of the 18th International Modal Analysis Conference*, pages 607–612, 2000.
- [3] Schedlinski, C. and Link, M. An Approach to Optimal Pick-up and Exciter Placement. *Proceedings of the 14th International Modal Analysis Conference*, pages 376–382, 1996.
- [4] Kammer, D. C. and Yao, L. Enhancement of On-Orbit Modal Identification of Large Space Structures Through Sensor Placement. *Journal of Sound and Vibration*, 171(1), pages 119–139, 1994.
- [5] Friswell, M. I. and Mottershead, J. E. *Finite Element Model Updating in Structural Dynamics*. Kluwer Academic Publishers, 1995.
- [6] Chen, G. FE Model Validation for Structural Dynamics. *Ph.D. Thesis, Imperial College of Science, Technology and Medicine, Department of Mechanical Engineering*, 2001.
- [7] Yagawa, G., Yoshimura, S. and Nakao, K. Automatic mesh generation of complex geometries based on fuzzy knowledge processing and computational

- geometry. *Integrated Computer-Aided Engineering, Vol. 2, No. 4*, pages 265–280, 1995.
- [8] Nakajima, N. Intelligent mesh generation technique for three-dimensional objects based on the extended oct tree representation method. *Nippon Kikai Gakkai Ronbunshu, C Hen/Transactions of the Japan Society of Mechanical Engineers, Part C, Vol. 57, No. 542, October*, pages 3174–3182, 1991.
- [9] Zienkiewicz and Taylor. *The Finite Element Method, Third Edition*. McGraw-Hill, 1977.
- [10] Megahed, M. M., Sayed, H S. and Hasan, M. Finite element modeling for structural analysis of shells of reduction cells. *Light Metals: Proceedings of Sessions, TMS Annual Meeting, Warrendale, Pennsylvania*, pages 375–381, 1996.
- [11] Cook, R. D. *Concepts and Applications of Finite Element Analysis*. John Wiley and Sons, 1981.
- [12] Petyt, M. *Introduction to Finite Element Vibration Analysis*. Cambridge University Press, 1998.
- [13] Rao, S. S. *The Finite Element Method in Engineering, 3rd Edition*. Butterworth-Heinemann, 1999.
- [14] Li, M. Finite deformation theory for beam, plate and shell. Part III. The three-dimensional beam theory and the FE formulation. *Computer Methods in Applied Mechanics and Engineering, Vol. 162, No. 1-4, August*, pages 287–300, 1995.
- [15] Bouabdallah, M. S. and Batoz, J. L. Formulation and evaluation of a finite element model for panels. *Finite Elements in Analysis and Design, Vol. 21, No. 4, April*, pages 265–289, 1996.

- [16] Lee, D. and Lee, I. Vibration analysis of anisotropic plates with eccentric stiffeners. *Computers and Structures*, Vol. 57, No. 1, October, pages 99–105, 1995.
- [17] Meriam, J. L. *Engineering Mechanics: Statics and Dynamics*. John Wiley and Sons, 1978.
- [18] Kilroy, K. *MSC/NASTRAN Quick Reference Guide, Version 70.5*. The MacNeal-Schwendler Corporation, 1998.
- [19] MacNeal R. H. Perspective on Finite Elements for Shell Analysis. *Finite Elements in Analysis and Design*, Vol. 30, No. 3, pages pages 175–186, 1998.
- [20] Wriggers, P. and Gruttmann, F. Analytical and Computational Models of Shells. *Presented at the Winter Meeting of the ASME (code 13093), December*, 1989.
- [21] Fox, D. D. and Simo, J. C. Drill rotation formulation for geometrically exact shells . *Computer Methods in Applied Mechanics and Engineering*, Vol. 98, No. 3, August, pages 329–343, 1992.
- [22] Soh, A. K., Soh, C. K. and Pey, L. P. On the compatibility conditions for modeling tubular joints using different types of elements. *Computers and Structures*, Vol. 62, No. 5, March, pages 935–942, 1997.
- [23] Krueger, R. and O'Brien, T. K. Shell/3D modeling technique for the analysis of delaminated composite laminates. *Composites - Part A: Applied Science and Manufacturing*, Vol. 32, No. 1, January, pages 25–44, 2001.
- [24] Aaghaakouchak, A. A. and Dharmavasan, S. Stress analysis of unstiffened and stiffened tubular joints using an improved finite element model of intersection. *Proceedings of the International Offshore Mechanics and Arctic Engineering Symposium*, Vol. 3, Pt. A, pages 321–328, 1990.

- [25] SRS IP, Inc. *ANSYS On-line Reference Guide, Version 5.5*. Swanson Analysis Systems, Murray, Pennsylvania, 1998.
- [26] Raj, D. M., Narayanan, R., Khadakkar, A. G. and Paramasivam, V. Effect of ring stiffeners on vibration of cylindrical and conical shell models. *Journal of Sound and Vibration, Vol. 179, No. 3, January*, pages 413–426, 1995.
- [27] Timoshenko, S. P. *History of Strength of Materials*. Dover Publications, 1953.
- [28] Timoshenko, S. P. *Mechanics of Materials, 3rd Edition*. Chapman and Hall, 1995.
- [29] Destuynder, P. and Salaun, M. Mixed finite element for shell model with free edge boundary conditions. Part 3. Numerical aspects. *Computer Methods in Applied Mechanics and Engineering, Vol. 136, No. 3-4, September*, pages 273–292, 1996.
- [30] Zienkiewicz, O. C. and Taylor, R. L. Finite element patch test revisited. A computer test for convergence, validation and error estimates. *Computer Methods in Applied Mechanics and Engineering, Vol. 149, No. 1-4*, pages 223–254, 1997.
- [31] Imamovic, N. and Ewins, D. J. Model Validation of an Aerospace Structure. *Proceedings of the 17th International Modal Analysis Conference*, pages 470–474, 1999.
- [32] Buehrle, R. D., Fleming, G. A., Pappa, R. S. and Grosveld F. W. Finite Element Model Development and Validation for Aircraft Fuselage Structures. *Proceedings of the 18th International Modal Analysis Conference*, pages 356–362, 2000.
- [33] Jeong, J. D., Yoo, S. W., Choi, H. G., Ahn, C. G. and Lee, J. M. Acoustic Mode Control Method using Additional Cavity and Holes. *Proceedings of the 18th International Modal Analysis Conference*, pages 1737–1742, 2000.

- [34] Reece, C. A. Model Correlation Applied to Mechanical Couplings for Weapon Structure Design. *Proceedings of the 16th International Modal Analysis Conference*, pages 394–398, 1998.
- [35] Butler, T. A., Hemez, F. M., Schultze, J., Sohn, H. and Doebling, S. W. Model Validation for a Complex Jointed Structure. *Proceedings of the 19th International Modal Analysis Conference*, pages 1318–1324, 2001.
- [36] Moon, Y. M., Jee, T. H. and Park, Y. P. Development of an Automotive Joint Model using an Analytical Based Formulation. *Journal of Sound and Vibration*, 220(4), pages 625–640, 1999.
- [37] Jarvis, B. P., Tomlinson, G. R. and Chance, J. E. Linear Modelling of A Non-Linear Joint. *Proceedings of the 2nd International Conference on Structural Dynamics Modelling*, pages 209–218, 1996.
- [38] Wang, D. , Friswell, M. I., Nikraves, P. E. and Kuo, E. Y. Damage Detection in Structural Joints Using Generic Joint Elements. *Proceedings of the 17th International Modal Analysis Conference*, pages 792–798, 1999.
- [39] Lee, J. W., Ko, K. H., Lee, S. I., Kim, S. K. and Lee, J. M. A Dynamic Analysis of Complex Structures with Joints. *Proceedings of the 13th International Modal Analysis Conference*, pages 331–337, 1995.
- [40] Horton, B., Gurgenci, H., Veidt, M. and Friswell, M. I. Finite Element Model Updating of the Welded Joints in a Tubular H-Frame. *Proceedings of the 17th International Modal Analysis Conference*, pages 1556–1562, 1999.
- [41] Mottershead, J. E. and James, S. Updating Parameters for the Model of a Three Story Aluminium Space Frame. *Proceedings of the 16th International Modal Analysis Conference*, pages 8–11, 1998.

-
- [42] Kim, H., Lee, S. and Park, Y. Structural Joint Characteristic Identification Using Optimal Experiment Design Technique. *Proceedings of the 16th International Modal Analysis Conference*, pages 1388–1394, 1998.
- [43] Ahmadian, H., Mottershead, J. E. and Friswell, M. I. Joint Modelling for Finite Element Model Updating. *Proceedings of the 14th International Modal Analysis Conference*, pages 591–596, 1996.
- [44] Englund, R. B., Johnson, D. H. and Sweeney, S. K. Finite Element Analysis Study of Non-linear Behavior in a Bolted Connection. *American Society of Mechanical Engineers, Vol. 102*, pages 73–79, 1999.
- [45] Varadi, K. and Joanovics, L. Non-linear Finite Element Analysis of the Contact, Strain and Stress States of a Bolt-Nut-Washer-Compressed Sheet Joint System. *American Society of Mechanical Engineers, Vol. 92*, pages 31–36, 1996.
- [46] Gaul, L., Nackenhorst, U., Willner, K. and Lenz, J. Nonlinear Vibration Damping of Structures with Bolted Joints. *Proceedings of the 12th International Modal Analysis Conference*, pages 875–881, 1994.
- [47] Gaul, L. and Lenz, J. Nonlinear Dynamics of Structures Assembled by Bolted Joints. *Acta Mechanica, Vol. 125, N 1-4*, pages 169–181, 1997.
- [48] Simmermacher, T., Segalman, D. and Sagartz, M. A Mechanical Diode: Comparing Numerical and Experimental Characterizations. *Proceedings of the 16th International Modal Analysis Conference*, pages 718–722, 1998.
- [49] Troup, S., Xiao, R. Y. and May, S. S. J. Numerical Modelling of Bolted Steel Connections. *Journal of Constructional Steel Research, Vol. 46, N 1-3*, page 269, 1998.
- [50] Fotsch, D. and Ewins, D. J. Further Applications of the FMAC. *Proceedings of the 19th International Modal Analysis Conference*, pages 635–639, 2001.

- [51] Guyan, R. J. Reduction of Stiffness and Mass Matrices. *AIAA Journal*, Vol. 3, No. 2, February, page 380, 1965.
- [52] Irons, B. M. Structural Eigenvalue Problems: Elimination of Unwanted Variables. *AIAA Journal*, Vol. 3, May, 1965.
- [53] O'Callahan, J. A Procedure for an Improved Reduced System (IRS) Model. *Proceedings of the 7th International Modal Analysis Conference*, pages 17–21, 1989.
- [54] Paz, M. and Malpartida, C. EXTENDED GUYAN REDUCTION METHOD. *Transactions of the International Conference on Structural Mechanics in Reactor Technology*, pages 211–218, 1983.
- [55] Zhang, D. and Li, S. Succession-Level Approximate Reduction (SAR) Technique for Structural Dynamic Model. *Proceedings of the 13th International Modal Analysis Conference*, pages 435–441, 1995.
- [56] Friswell, M. I., Garvey, S. D. and Penny, J. E. T. Using Iterated IRS Model Reduction Techniques to Calculate Eigensolutions. *Proceedings of the 15th International Modal Analysis Conference*, pages 1537–1543, 1997.
- [57] Paz, M. Dynamic Condensation. *AIAA Journal*, Vol. 22, No. 5, May, pages 724–727, 1984.
- [58] Flanigan, C. C. Model Reduction Using Guyan, IRS, and Dynamic Methods. *Proceedings of the 16th International Modal Analysis Conference*, pages 172–176, 1998.
- [59] Kammer, D. C. Test-Analysis Model Development Using an Exact Modal Reduction. *The International Journal of Analytical and Experimental Modal Analysis*, October, pages 174–179, 1987.

- [60] O'Callahan, J., Avitabile, P., Riemer, R. System Equivalent Reduction Expansion Process (SEREP). *Proceedings of the 7th International Modal Analysis Conference*, pages 29–37, 1989.
- [61] Zhang, D. and Wei, F. S. Complete Mode-Type Reduction (CMR) for Structural Dynamic System. *Proceedings of the 13th International Modal Analysis Conference*, pages 616–622, 1995.
- [62] Kammer, D. C. A Hybrid Approach to Test-Analysis-Model Development for Large Space Structures. *Journal of Vibration and Acoustics*, Vol. 113, No. 3, July, pages 325–332, 1991.
- [63] Urgueira, A. P. V., Maia, N. M. M. and Almeida, R. A. B. On the Dynamic Properties of Reduced Systems in Structural Coupling. *Proceedings of the 17th International Modal Analysis Conference*, pages 1445–1450, 1999.
- [64] O'Callahan, J. Reduced Model Concepts). *Proceedings of the 18th International Modal Analysis Conference*, pages 1528–1536, 2000.
- [65] Kammer, D. C. Correlation Considerations - Part 2: Model Reduction using Modal, SEREP and Hybrid. *Proceedings of the 16th International Modal Analysis Conference*, pages 177–184, 1998.
- [66] Roy, N. A., Girard, A. and Bugeat, L. P. Dynamic Reduction of Finite Element Models using Standard Finite Element Capabilities). *Proceedings of the 15th International Modal Analysis Conference*, pages 1959–1965, 1997.
- [67] Allemang, R. J., Brown, D. L. A Correlation Coefficient for Modal Vector Analysis. *Proceedings of the 1st International Modal Analysis Conference*, pages 110–116, 1982.
- [68] Lieven, N. A. and Ewins, D. J. Spatial Correlation of Mode Shapes, the Coordinate Modal Assurance Criterion (COMAC). *Proceedings of the 6th International Modal Analysis Conference*, pages 690–695, 1988.

- [69] Mitchell, L. D. Increasing the Sensitivity of the Modal Assurance Criteria (MAC) to Small Mode Shape Changes: The IMAC. *Proceedings of the 16th International Modal Analysis Conference*, pages 64–69, 1998.
- [70] Blaschke, P. G., Ewins, D. J. The MAC Revisited and Updated. *Proceedings of the 15th International Modal Analysis Conference*, pages 147–154, 1997.
- [71] Brechlin, E., Bendel, K., Keiper, W. A New Scaled Modal Assurance Criterion for Eigenmodes containing Rotational Degrees of Freedom. *International Society for Modal Analysis*, 1998.
- [72] Hunt, D. L. Application of an Enhanced Coordinate Modal Assurance Criteria. *Proceedings of the 10th International Modal Analysis Conference*, pages 66–71, 1992.
- [73] Catbas, F. N., Aktan, A. E., Allemang, R. J., Brown, D. L. A Correlation Function For Spatial Locations of Scaled Mode Shapes (COMEF). *Proceedings of the 16th International Modal Analysis Conference*, pages 1550–1555, 1998.
- [74] Lieven, N. A. J., Waters, T. P. Error Location using Normalised Orthogonality. *Proceedings of the 12th International Modal Analysis Conference*, pages 761–764, 1994.
- [75] Avitabile, P., O’Callahan, J., Milani, J. Model Correlation and Orthogonality Criteria. *Proceedings of the 6th International Modal Analysis Conference*, pages 1039–1047, 1988.
- [76] Avitabile, P., O’Callahan, J. Mass and Stiffness Orthogonality Checks Without a Mass or Stiffness Matrix. *Proceedings of the 13th International Modal Analysis Conference*, pages 1515–1519, 1995.
- [77] O’Callahan, J. Correlation Considerations - Part 4 (Modal Vector Correlation Techniques). *Proceedings of the 16th International Modal Analysis Conference*, pages 197–206, 1998.

- [78] Avitabile, P., Pechinsky, F. Coordinate Orthogonality Check (CORTHOG). *Proceedings of the 12th International Modal Analysis Conference*, pages 753–760, 1994.
- [79] Imamovic, N., Ewins, D. J. An Automatic Correlation Procedure for Structural Dynamics. *CEAS Conference, Manchester, England*, 1995.
- [80] Pascual, R., Golinval, J. C., Razeto, M. Testing of FRF Based Model Updating Methods Using a General Finite Elements Program. *International Conference on Noise and Vibration Engineering, 21th ISMA, Leuven Belgium*, 1996.
- [81] Pascual, R., Golinval, J. C., Razeto, M. A Frequency Domain Correlation Technique for Model Correlation and Updating. *Proceedings of the 15th International Modal Analysis Conference*, pages 587–592, 1997.
- [82] Nefske, D. J., Sung, S. H. Correlation of a Coarse-Mesh Finite Element Model using Structural System Identification and a Frequency Response Assurance Cri. *Proceedings of the 14th International Modal Analysis Conference*, pages 597–602, 1996.
- [83] Heylen, W., Avitabile, P. Correlation Considerations - Part 5 (Degree of Freedom Correlation Techniques). *Proceedings of the 16th International Modal Analysis Conference*, pages 207–214, 1998.
- [84] Fotsch, D. The MAC Revisited: Part 2, A Sensitivity Study. *Rolls-Royce Report No. VUTC/E2/99001*, Jan 1999.
- [85] Fotsch, D. and Ewins, D. J. Application of MAC in the Frequency Domain. *Proceedings of the 18th International Modal Analysis Conference*, pages 1225–1231, 2000.
- [86] Chen, G. Correlation Study on (quasi) Axisymmetric Structures. *Rolls-Royce Report No. VUTC/E2/98008*, May 1998.

- [87] Chen, G., Fotsch, D., Imamovic, N. and Ewins, D. J. Correlation Methods for Axisymmetric Structures. *Proceedings of the 18th International Modal Analysis Conference*, pages 1006–1012, 2000.
- [88] Kahmer, D., Moler, C., Nash, S. Numerical Methods and Software. *Prentice-Hall International Editions*, pages 414–416, 1989.